HELLENIC REPUBLIC

UNIVERSITY OF IOANNINA

SCHOOL OF ENGINEERING

DEPARTMENT OF MATERIALS SCIENCE AND ENGINEERING

Thesis for the degree of Doctor of Philosophy

“*Development of technologies for the utilization of thermoelectric and electrothermal energy from advanced structural multifunctional composite materials*”

George M. Karalis

Materials Engineer, MSc

Ioannina-Greece, 2021

ΕΛΛΗΝΙΚΗ ΔΗΜΟΚΡΑΤΙΑ
ΠΑΝΕΠΙΣΤΗΜΙΟ ΙΩΑΝΝΙΝΩΝ
ΠΟΛΥΤΕΧΝΙΚΗ ΣΧΟΛΗ
ΤΜΗΜΑ ΜΗΧΑΝΙΚΩΝ ΕΠΙΣΤΗΜΗΣ ΥΛΙΚΩΝ

Διδακτορική Διατριβή

«*Ανάπτυξη τεχνολογιών για την αξιοποίηση θερμοηλεκτρικής και ηλεκτροθερμικής ενέργειας από προηγμένα δομικά σύνθετα πολυλειτουργικά υλικά*»

Γεώργιος Μ. Καραλής

Μηχανικός Επιστήμης Υλικών, ΜΔΕ

Ιωάννινα-Ελλάδα, 2021

« The acceptance of Doctoral Dissertation from the Department of Materials Science and Engineering of University of Ioannina, Greece, does not imply the acceptance of the author's opinion. » (Law 5343/1932, article 202).

« Η έγκριση της διδακτορικής διατριβής από το Τμήμα Μηχανικών Επιστήμης Υλικών της Πολυτεχνικής Σχολής του Πανεπιστημίου Ιωαννίνων δεν υποδηλώνει αποδοχή των γνωμών του συγγραφέα Ν. 5343/32, άρθρο 202, παράγραφος 2 ».

Application and Subject appointment date of MSc George Karalis: **28/03/2018**

“Development of technologies for the utilization of thermoelectric and electrothermal energy from advanced structural multifunctional composite materials”

Appointment date for the three-membered advisory committee: **16/04/2018**

Members of the three-membered advisory committee:

Supervisor

Alkiviadis S. Paipetis, Professor at the Dept. of Materials Science and Engineering,
School of Engineering, University of Ioannina

Members

Dimitrios Gournis, Professor at the Dept. of Materials Science and Engineering, School of Engineering, University of Ioannina

Leonidas N. Gergidis, Associate Professor at the Dept. of Materials Science and Engineering, School of Engineering, University of Ioannina

Appointment date for the seven-membered committee: **14/10/2021**

1. **Alkiviadis S. Paipetis**, Professor at the Dept. of Materials Science and Engineering, School of Engineering, University of Ioannina,
2. **Dimitrios Gournis**, Professor at the Dept. of Materials Science and Engineering, School of Engineering, University of Ioannina,
3. **Leonidas N. Gergidis**, Associate Professor at the Dept. of Materials Science and Engineering, School of Engineering, University of Ioannina,
4. **Nektaria-Marianthi Barkoula**, Professor at the Dept. of Materials Science and Engineering, School of Engineering, University of Ioannina,
5. **Michael A. Karakassides**, Professor at the Dept. of Materials Science and Engineering, School of Engineering, University of Ioannina,
6. **Pagona Papakonstantinou**, Professor at the Dept. of School of Engineering, Engineering Research Institute, University of Ulster,
7. **Theodore Matikas**, Professor at the Dept. of Materials Science and Engineering, School of Engineering, University of Ioannina.

The Head of the Department

Apostolos Avgeropoulos

The Secretary of the Department

Maria Kontou

Ημερομηνία αίτησης και ορισμού θέματος του κ. Γεωργίου Καραλή: 28.3.2018

«Ανάπτυξη τεχνολογιών για την αξιοποίηση θερμοηλεκτρικής και ηλεκτροθερμικής ενέργειας από προηγμένα δομικά σύνθετα πολυλειτουργικά υλικά»

Ημερομηνία ορισμού Τριμελούς Συμβουλευτικής Επιτροπής: 16.04.2018

Μέλη Τριμελούς Συμβουλευτικής Επιτροπής:

Επιβλέπων

Αλκιβιάδης Παϊπέτης, Καθηγητής του Τμήματος Μηχανικών Επιστήμης Υλικών της Πολυτεχνικής Σχολής του Πανεπιστημίου Ιωαννίνων

Μέλη

Δημήτριος Γουρνής, Καθηγητής του Τμήματος Μηχανικών Επιστήμης Υλικών της Πολυτεχνικής Σχολής του Πανεπιστημίου Ιωαννίνων,
Λεωνίδας Γεργίδης, Αναπληρωτής Καθηγητής του Τμήματος Μηχανικών Επιστήμης Υλικών της Πολυτεχνικής Σχολής του Πανεπιστημίου Ιωαννίνων.

ΔΙΟΡΙΣΜΟΣ ΕΠΤΑΜΕΛΟΥΣ ΕΞΕΤΑΣΤΙΚΗΣ ΕΠΙΤΡΟΠΗΣ : 14.10.2021

1. **Αλκιβιάδης Παϊπέτης**, Καθηγητής του Τμήματος Μηχανικών Επιστήμης Υλικών της Πολυτεχνικής Σχολής του Πανεπιστημίου Ιωαννίνων,
2. **Δημήτριος Γουρνής**, Καθηγητής του Τμήματος Μηχανικών Επιστήμης Υλικών της Πολυτεχνικής Σχολής του Πανεπιστημίου Ιωαννίνων,
3. **Λεωνίδας Γεργίδης**, Αναπληρωτής Καθηγητής του Τμήματος Μηχανικών Επιστήμης Υλικών της Πολυτεχνικής Σχολής του Πανεπιστημίου Ιωαννίνων,
4. **Νεκταρία-Μαριάνθη Μπάρκουλα**, Καθηγήτρια του Τμήματος Μηχανικών Επιστήμης Υλικών της Πολυτεχνικής Σχολής του Πανεπιστημίου Ιωαννίνων,
5. **Μιχαήλ Καρακασίδης**, Καθηγητής του Τμήματος Μηχανικών Επιστήμης Υλικών της Πολυτεχνικής Σχολής του Πανεπιστημίου Ιωαννίνων,
6. **Παγώνα Παπακωνσταντίνου**, Professor of Advanced Materials Nanotechnology and Integrated Bioengineering Centre (NIBEC), Engineering Research Institute, School of Engineering, Ulster University.
7. **Θεόδωρος Ματίκας,** Καθηγητής του Τμήματος Μηχανικών Επιστήμης Υλικών της Πολυτεχνικής Σχολής του Πανεπιστημίου Ιωαννίνων,

Έγκριση Διδακτορικής Διατριβής με βαθμό **«ΑΡΙΣΤΑ»** στις **3.12.2021**

Ο Πρόεδρος του Τμήματος

Απόστολος Αυγερόπουλος
Καθηγητής

Η Γραμματέας του Τμήματος

Μαρία Κόντου

Abstract

Fiber-reinforced polymer (FRP) advanced composites consist a prominent class of high-demand construction materials with significantly improved specific properties that combine low weight, high mechanical strength and excellent corrosion resistance. Moreover, the relatively easy manufacturing procedures and low maintenance costs are some of the factors that have led composites to rank first among the state-of-the-art advanced structures for a wide range of applications. Additionally, beyond the state-of-the-art, multifunctional structural composites constitute an extremely interesting research field introducing new secondary functions, such as autonomous structural integrity monitoring, temperature control, deformation or damage detection, self-healing, energy harvesting and power generation. The purpose of the present PhD thesis was to unfold technologies for the utilization of thermoelectric (TE) and electrothermal (ET) energy from advanced structural multifunctional composite materials. In this research, hybrid (inorganic-organic) and organic nanomaterials-based inks were developed and extensively characterized in order to produce functional printed films with desired electrical properties via proper solution-processed printing techniques in both planar and fibrous substrates. Thus, the aim of this study was to seamlessly integrate TE and ET functional "system" reinforcing laminae within FRP composite laminates for the realization of thermoelectric element generator (TEG) enabled and electrothermal-enabled multifunctional structures. The thermal energy harvesting performance (taking advantage of the Seebeck effect) and the out-of-oven curing and de-icing efficiency (taking advantage of the Joule effect) exhibited remarkable results at composite demonstrators level.

Keywords: Smart materials, Fiber Reinforced Polymers (FRPs), Multifunctional composites, Seebeck effect, Thermal-energy harvesting, Thermoelectric Generators (TEGs), Structural Health Monitoring (SHM), Self-powered piezoresistive sensors, Thermocouple-based temperature sensors, Joule effect, Electrothermal heating, Temperature resistive sensors, Self-sensing

Περίληψη

Τα προηγμένα ινοενισχυμένα πολυμερικά σύνθετα κατατάσσονται ως μια εξέχουσα κατηγορία κατασκευαστικών υλικών υψηλής ζήτησης με σημαντικά βελτιωμένες ειδικές ιδιότητες που συνδυάζουν χαμηλό βάρος, υψηλή μηχανική αντοχή και εξαιρετική ανθεκτικότητα στη διάβρωση. Επιπλέον, οι σχετικά εύκολες κατασκευαστικές διεργασίες και το χαμηλό κόστος συντήρησης είναι μερικοί από τους παράγοντες που οδήγησαν τα σύνθετα υλικά να συμπεριλαμβάνονται στις πρώτες θέσεις μεταξύ των πιο προηγμένων δομικών στοιχείων για ένα ευρύ φάσμα εφαρμογών. Επιπλέον, τα πολυλειτουργικά δομικά σύνθετα αποτελούν ένα εξαιρετικά ενδιαφέρον ερευνητικό πεδίο, καθώς επιτρέπουν την εισαγωγή νέων δευτερεύουσων λειτουργιών, όπως η αυτο-παρακολούθηση δομικής ακεραιότητας, έλεγχος θερμοκρασίας, ανίχνευση παραμορφώσεων ή αστοχιών, αυτοΐαση, συγκομιδή και παραγωγή ενέργειας. Ο σκοπός της παρούσας διδακτορικής διατριβής ήταν να αναπτυχθούν τεχνολογίες για την αξιοποίηση θερμοηλεκτρικής και ηλεκτροθερμικής ενέργειας από προηγμένα δομικά πολυλειτουργικά σύνθετα υλικά. Σε αυτήν την έρευνα, υβριδικά (ανόργανα-οργανικά) και οργανικά μελάνια νανοσωματιδίων αναπτύχθηκαν και χαρακτηρίστηκαν εκτενώς προκειμένου να παραχθούν λειτουργικά τυπωμένα υμένια με επιθυμητές ηλεκτρικές ιδιότητες μέσω κατάλληλων τεχνικών εκτύπωσης υγρής εναπόθεσης σε επίπεδα και ινώδη υποστρώματα. Έτσι, ο στόχος αυτής της μελέτης ήταν η απρόσκοπη ενσωμάτωση λειτουργικών (θερμοηλεκτρικά και ηλεκτροθερμικά) με ιδιότητες θερμοηλεκτρικής γεννήτριας και ηλεκτροθερμικής απόκρισης «βοηθητικών» εμποτισμένων με εποξειδική ρητίνη ενισχυτικών υφασμάτων εντός σύνθετων πολύστρωτων δομών. Η απόδοση της συγκομιδής θερμικής ενέργειας (επωφελούμενη από το φαινόμενο Seebeck) και η ενεργειακά αποδοτική διαδικασία του πολυμερισμού εκτός φούρνου και διαδικασία απομάκρυνσης επιφανειακά ποσότητας πάγου (εκμεταλλευόμενη το φαινόμενο Joule) παρουσίασαν αξιοσημείωτα αποτελέσματα σε επίπεδο σύνθετων δομών επίδειξης.

Λέξεις κλειδιά: Έξυπνα υλικά, Ινοενισχυμένα πολυμερή, Πολυλειτουργικά σύνθετα, φαινόμενο Seebeck, Συγκομιδή θερμικής ενέργειας, Θερμοηλεκτρικές γεννήτριες, Παρακολούθηση δομικής ακεραιότητας, Αυτο-τροφοδοτούμενοι αισθητήρες πιεζοαντίστασης, Αισθητήρες θερμοκρασίας βάση θερμοστοιχείων, φαινόμενο Joule, Ηλεκτροθερμική θέρμανση, Αισθητήρες θερμοκρασίας βάση αντίστασης, Δομικός αυτοέλεγχος

Acknowledgements

During the progress of this PhD research, I had the opportunity to collaborate with several remarkable people who significantly contributed to the realization of this effort and I would like to dedicate the following paragraphs as an acknowledgement to them.

First and foremost, I would like to express my sincere appreciation and thanks to my supervisor, Alkiviadis Paipetis, Professor of the Dept. of Materials Science and Engineering (MSE) and Lab director of the Composite and Smart Materials Laboratory (CSML) who gave me the opportunity to conduct the current research. I want to kindly thank him for his patience during my early researching steps and his guidance and support through the whole PhD study. I also appreciate the scientific discussions as well as the opportunities he has opened up for me. His advice on both research, as well as on my career have been priceless and without his support it would not be possible to complete successfully this research.

I also wish to thank Dimitrios Gournis, Professor at the MSE, for his participation as a member of the advisory committee. I would also like to thank Leonidas Gergidis, Associate Professor at the MSE for his guidance at crucial points, for the decisive contribution to the experimental findings with the relative modeling results and for his participation as a member of the advisory committee.

At this point, I want to express my gratitude to Nektaria-Marianthi Barkoula, Professor at the Dept. of MSE for her scientific advice, our insightful discussions and for her participation as a member of the examination committee. Her advice and support were always valuable and helpful to me. My sincere appreciation also goes to Michael A. Karakassides, Professor at the Dept. of MSE for the for his participation as a member of the examination committee. I would also like to deeply thank Pagona Papakonstantinou, Professor of Advanced Materials at the School of Engineering, at the Engineering Research Institute of the University of Ulster for honoring me with her participation to the examination committee. My sincere thanks also go to Theodore Matikas, Professor at the Dept. of MSE for his participation in the examination committee.

I want to express my sincere gratitude to Lazaros Tzounis, Associate Professor at the Dept. of Mechanical Engineering at Hellenic Mediterranean University (HMU) for his precious friendship, guidance, and collaboration. Our stimulating discussions cautiously encouraged me to explore novel concepts. His advices were more that valuable.

I also gratefully thank Dr Kyriaki Tsirka for her friendship, support and for the opportunities she gave me during my research. It was a privilege collaborating with her.

Moreover, I have to express my thanks to the PhD candidates Georgios Foteinidis, Maria Kosarli, Christos Mytafides, Lampros Koutsotolis, Ioanna Vareli, Katerina Garavela and Eva Tzouma for their friendship, support, collaboration and of course their patience. It was a great pleasure and a

privilege working with them on a daily basis. I also thank my newer companions who collaborated with me and supported me during the steps of this journey MSc Michaela Konstantinidou, MSc Evangelos Dimos and Anastasia Typou, Ksenia Exarchou, Angelos Voudouris-Itskaras and Alexandros Anastasopoulos for the fruitful discussions and cooperation. I would also like to thank MSc Marilena Georgosopoulou and the Lab technician Christos Drougas for their support and care during the stages of this research.

Finally, I would like to thank my partner in life Giota for her patience, understanding and for always being there for me all the time I was working on my thesis and I entirely appreciate everything she had done for me. I also thank my beloved family, my father Michail, my mother Filitsa and my sister Katerina for their support all these years. I would not be at this position without their infinite support.

The current PhD thesis has been co-financed by the following resources and I gratefully acknowledge the following research projects for the financial support.

«Acknowledgment: This research has been co-financed by the European Union and Greek national funds through the Operational Program Competitiveness, Entrepreneurship and Innovation, under the call RESEARCH – CREATE – INNOVATE (project code: T1EDK 03480)».

«Acknowledgment: DAAD association is gratefully acknowledged for supporting this work under the exchange program great!ipid4all (group2group exchange for academic talents)».

The program great!ipid4all is promoted by the German Academic Exchange Service (DAAD) and funded by the Federal Ministry of Education and Research (BMBF) and the TU Dresden's Institutional Strategy by the Excellence Initiative of the German Federal and State Governments.

«Acknowledgment: This study has been co-financed by the Operational Program "Human Resources Development, Education and Lifelong Learning" and is co-financed by the European Union (European Social Fund) and Greek national funds as part of the project "Advanced structural composites with power generation capabilities in order to supply low power requirements electronic circuits from photo-thermal energy-harvesting (PROMETHEUS)"».

Table of Contents

Nomenclature - Symbols and Abbreviations

GF: Glass Fiber

GFRP: Glass Fiber Reinforced Polymer

CF: Carbon Fiber

CFRP: Carbon Fiber Reinforced Polymer

UD: Unidirectional

FRP: Fiber Reinforced Polymer

FRPCs: Fiber Reinforced Polymer Composites

DGEBA: Diglycidyl ether of bisphenol-A

1D: One-Dimensional

2D: Two-Dimensional

Al: Aluminum

Cu: Copper

Ag: Silver

Pu_{238}: Plutonium-238

N_2: Nitrogen

d-H_2O or DI water: Distilled water

IPA: Isopropyl alcohol

DMSO: Dimethyl sulfoxide

NPs: Nanoparticles

CNTs: carbon nanotubes

SWCNT: Single walled carbon nanotube

MWCNT: Multi walled carbon nanotube

Gr: Graphene

SDBS: Sodium dodecylbenzenesulfonate

CTAB: Cetyltrimethylammonium bromide

CMC: Critical Micelle Concentration

Na_2TeO_3: Sodium tellurite

$Te(OH)_6$: Telluric acid

AA: Ascorbic Acid

CO_2: Carbon dioxide

NH_4OH: Ammonium hydroxide

H_2O_2: Hydrogen peroxide

H: Hybrid

PEDOT:PSS: Poly(3,4-ethylenedioxythiophene) Polystyrene sulfonate

Te NWs: Tellurium nanowires

Te: Tellurium

Bi_2Te_3: Bismuth telluride

Bi_2S_3: Bismuth(III) sulfide

PbTe: Lead telluride

Ag_2Te: Silver telluride

Sb_2Te_3: Antimony telluride

$Bi_{0.5}Sb_{1.5}Te_3$: Bismuth antimony telluride

SiGe: Silicon germanium

PEI: Polyetherimide

PEEK: Polyetheretherketone

PVDF: Poly(vinylidene fluoride)

PET: Polyethylene terephthalate

PDDA: Poly(diallyldimethylammonium chloride)

PANI: Polyaniline

PC: Polycarbonate

PAN: Polyacrylonitrite

PTFE: Polytetrafluoroethylene

M_w: Weight average molecular mass

M_r: Relative molecular mass or molecular weight

RH: Relative Humidity

TE: Thermoelectric

ET: Electrothermal

TEP: Thermoelectric Power

S: Seebeck coefficient

S_m: Measured thermopower or Seebeck coefficient

S_c: Calculated thermopower or Seebeck coefficient

ΔV: Electric potential difference or thermovoltage

ΔT: Temperature difference or temperature gradient

PF: Power factor

σ: Electrical conductivity

ρ: Resistivity

ZT: Dimensionless thermoelectric figure of merit

κ: Thermal conductivity

κ_e: Electrical thermal conductivity

κ_l: Lattice thermal conductivity

R_s: Sheet resistance

t: Thickness

t: Time

d: Distance

θ: Angle

γ: Surface tension

η: Carnot efficiency

n: Carrier concentration

μ: Carrier mobility

τ: Scattering time

m^*: Effective mass of the carrier

K_B: Boltzmann constant

E: Energy state or Electric field

A_{1g}: Out-of-plane phonon vibration mode

E_{1g}: In-plane phonon vibration mode

E_{2g}: Double degenerate active optical vibration-band

N: Atom

h: Plank constant

v: Frequency

ν_0: Excitation light

λ: Wavelength of the light

π: 3.14

r: Radius

L: Length

A: Cross section area

T: Absolute temperature

RT: Room Temperature

T_H: Temperature of the hot side

T_C: Temperature of the cold side

T_g: Glass transition temperature

Btu: British thermal units

CVD: Chemical Vapor Deposition
CCD: Charged Coupled Device
WSN: Wireless Sensor Network
IoT: Internet of Things
LED: Light-Emitting Diode
TRL: Technology Readiness Level
R2R: Roll-to-Roll
DC: Direct Current
EMI: Electromagnetic interference
IR: Infrared
UV: Ultraviolet
RBM: Radial Breathing Mode
SHM: Structural Health Monitoring
NDT: Non-Destructive Testing
FEM: Finite Element Method
ICT: Information and Communication Technology
IDE: Interdigitated electrode
ERCM: Electrical Resistance Change
OOC: Out-of-Oven-Curing
R: Electrical resistance
R_0: Initial electrical resistance
R_{TEG} or R_{in}: Total internal electrical resistance of the TEG device
N: Number of thermoelements or legs
V: Output voltage
I and J: Output current and current density
P: Output power
$\mathrm{I_{sc}}$: Short circuit current
$\mathrm{I_{UV}}$: Photocurrent
$\mathrm{I_D}$: Dark current
R_L or $\mathrm{R_{LOAD}}$: Applied load resistance
I_L: Current passes through applied load resistance
V_L: Voltage passes through applied load resistance
TEG: Thermoelectric Generator
RITEG: Radioisotope Thermoelectric Generator

P_{out} or P_{max}: Maximum output of electrical power
V_{OUT} or V_{TEP} or V_{OC} or V_{TEG}: Open circuit voltage output
H and Q: Heat and heat flow
V_{bias}: Voltage input
R_{heater}: Electrical resistance of the heater device
XRD: X-Ray Diffraction
RS: Raman spectroscopy
CA: Contact Angle
TGA: Thermal Gravimetric Analysis
SEM: Scanning Electron Microscopy
FESEM: Field-Emission Scanning Electron Microscopy
SE: Secondary electrons
BSE: Backscattered electrons
FIB: Focused Ion Beam
TEM: Transmission Electron Microscopy
SAED: Selected Area Electron Diffraction
IR-T: Infrared Thermography
DMA: Dynamic Mechanical Analysis
ASTM: American society for testing and Materials
E: Young’s modulus
F: Applied load
F_{max}: Maximum load prior to the fracture
TS or σ_0: Tensile strength
R^2: Weibull distribution
m: Weibull shape
L_0: Initial length
σ: Applied normal stress
IFSS or σ_{IFSS} or τ_{rz}: Interfacial Shear Strength
SFFT: Single Fiber Fragmentation Test
σ_{fu}: Mean axial fiber tensile strength
l_f : Fragment length
l_c: Critical length
l: Embedded length, including the meniscus
d_f : Fiber diameter

List of Figures

List of Tables

Introduction

Advanced multi-scaled reinforced composite materials (**Figure 1a**) have been studied for several years oriented to the extended employment and proper utilization as structural components for renewable energy, aerospace and automotive industry, as well as in other infrastructure constructions and consumer goods applications (**Figure 1b-c**).

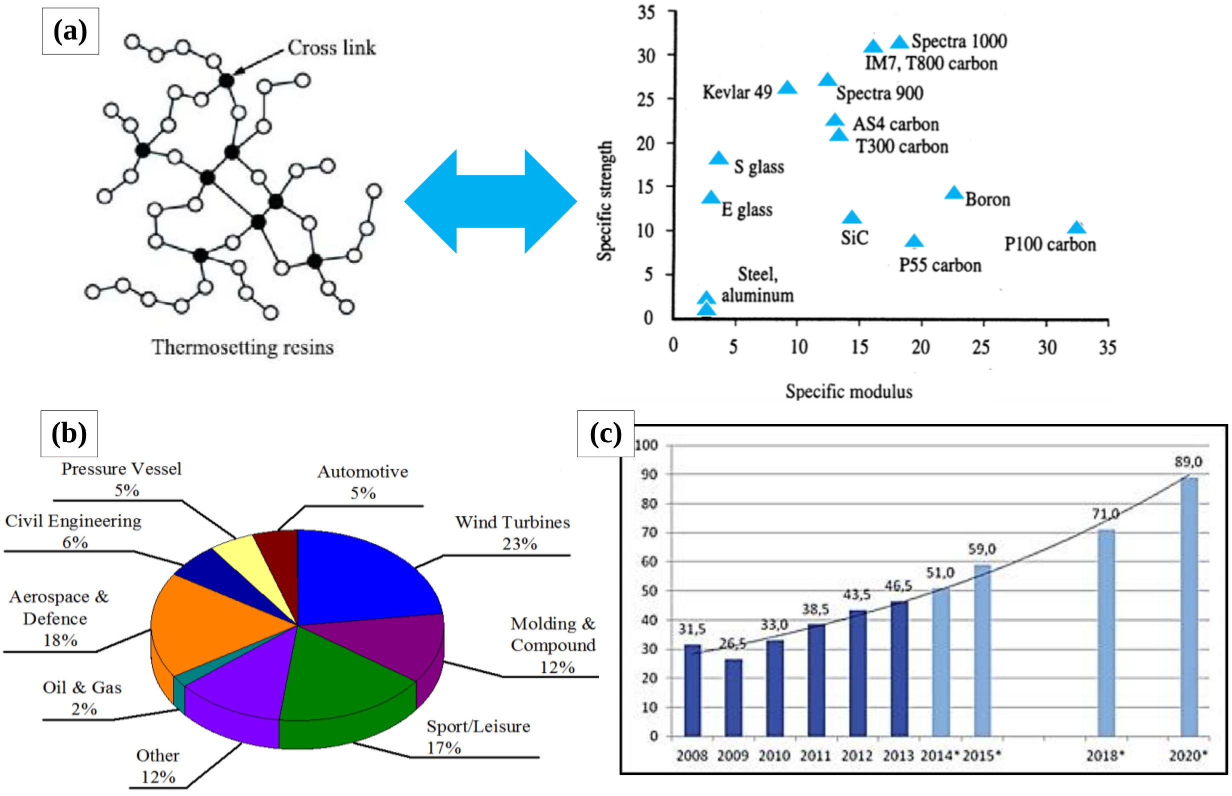

Figure 1. (a) A typical example of a polymer-based structural composite combining an epoxy-based thermoset matrix and possible fillers as reinforcements at different scale (*https://en.wikipedia.org/wiki/Specific_modulus*), **(b)** application sectors for advanced fiber reinforced polymer composites and **(c)** the corresponding market demand increase up to date (Das, T. K.; Ghosh, P.; Das, N. C. Preparation, Development, Outcomes, and Application Versatility of Carbon Fiber-Based Polymer Composites: A Review. Adv. Compos. Hybrid Mater. 2019, 2 (2), 214–233. (*https://doi.org/10.1007/s42114-018-0072-z.*).

The next generation of multifunctional advanced fiber reinforced polymer (FRP) composites enable a notable change in design mentality, due to the flexible engineering and potential for implementation of other nonstructural multiple functions in accordance with structural needs. A typical case study scenario is that of embedding properly dispersed nano / micro-particles into the polymer matrix system with a view to enhance both the matrix dominated properties as well as imparting specific functionalities (**Figure 2a-b**). As already reported in the literature, the additional functionalities provide diverse nonstructural capabilities, such as inherent structural health monitoring (SHM), sensing and actuation-morphing, self-healing, energy harvesting and storage

(**Figure 2c**). The combined structural and nonstructural properties of the next generation composites are expected to further improve product lifespan and increase product utility with a minimum structural aggravation. The imparted functionalities may be passive, active or even adaptive. For instance, when a multifunctional structural composite system is subjected to a certain field during its service life will be enabled to perform the full cycle of sense–evaluate–react, in response to the desired external stimuli (*i.e.*, mechanical, electrical, thermal, *etc*.). Therefore, multifunctionality is the provision of engineering to integrate extra smart properties within the composite structure at a system level, in order to confer additive value and emerge new products for the composites market.

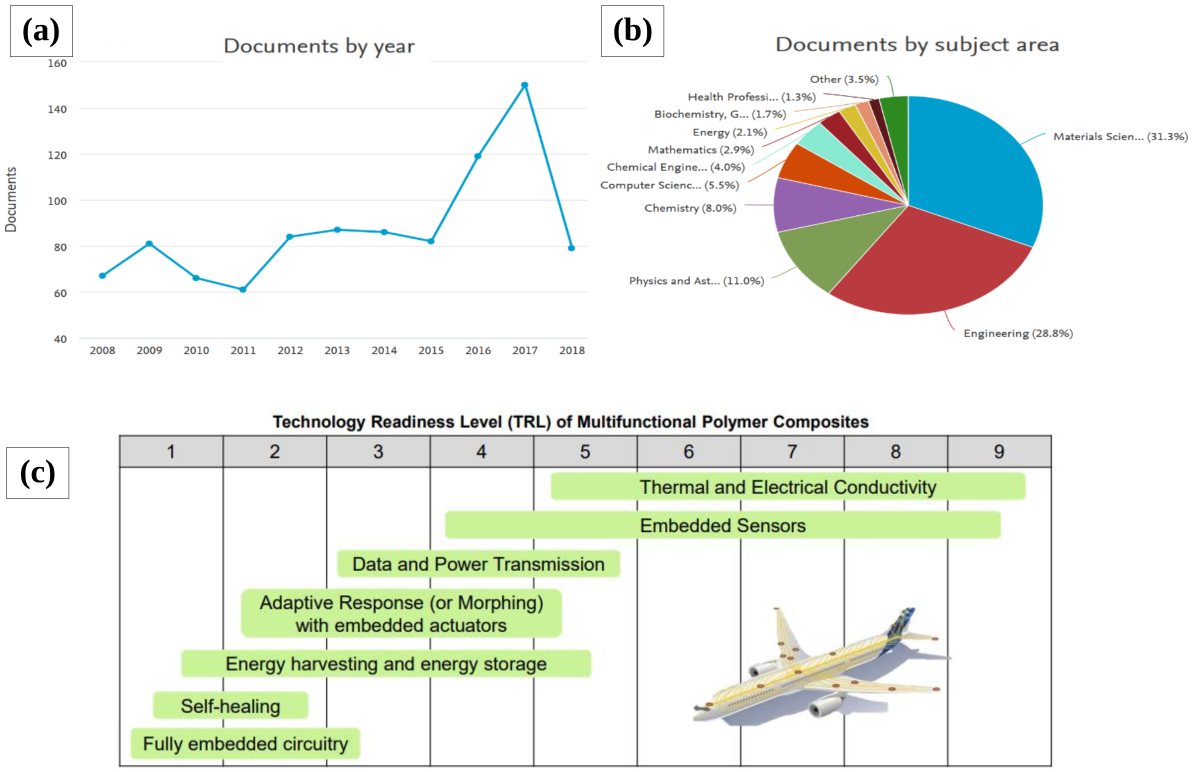

Figure 2. (a, b) Recent impact of multifunctional composites global research and the related scientific fields which are involved (*Scopus*) and **(c)** the corresponding Technology Readiness Level (TRL) as a sign of maturity for multifunctional polymer composites introduction to markets (*https://www.idtechex.com/en/research-report/multifunctional-composites-2019-2029-technology players-market-forecasts/630*).

Motivation: Within the scope of this research was to transform conventional advanced (FRP) composites to multifunctional structural components with thermal energy harvesting and thermal energy management capabilities in order to become capable of micro-power generation and efficiently electrothermal adjustable, respectively.

PhD Thesis Outline: The current PhD thesis contains a representative part of research efforts aimed at producing new knowledge at material level, as well as on the fabrication of efficient thermoelectric (TE) and electrothermal (ET) devices for the proper seamless integration within advanced FRP composites in order to manufacture smart and multifunctional structures (**Figure 3**).

More precisely, **Chapter 1** includes an introductory literature overview on multifunctional structural composites with a main perspective on self-powered and self-sensing capabilities.

Chapter 2 deals with the synthesis and characterization of tellurium nanoparticles (Te NPs) in aqueous medium and the optimized hybridization with conductive polymer - PEDOT:PSS for the production of thermoelectric inks with suitable viscosity and wetting ability in flexible planar surfaces (*e.g.*, polymeric substrates) for their proper deposition in order to create films (p-type semiconductor). Therefore, the most TE efficient films were employed as multiple printed thermoelements and were interconnected with highly conductive single wall carbon nanotube (SWCNT) dispersion printed junctions in order to fabricate a thermoelectric element generator (TEG) device, exploiting the TE effect through the existence of in-plane temperature difference (ΔT).

Chapter 3 consists of the physicochemical and micromechanical characterization of nanostructured interphases resulting from the deposition onto reinforcing glass fiber (GF) tows of efficient Te-based (p-type) and organic-based (p- and n-type SWCNT-molecular doped) TE inks impregnated with epoxy resin matrix. The fabricated model composites were utilized for the purpose of conducting micromechanical tests (single-fiber-fragmentation test – SFFT and tow pull-out tests) to evaluate both the modified interphases and the TE functionality upon the application of ΔT.

Chapter 4 discusses the development and characterization of a structural glass fiber reinforced polymer (GFRP) composite laminate with efficient in-plane thermal energy harvesting properties based on GF hierarchical fabrics with p- and n-type SWCNT-molecular doped TE films. In addition, the relative responsive generated TE power at a specific ΔT during the application of mechanical loads was evaluated as an inherent self-powered damage sensor via on-line monitoring of electrical measurements.

Chapter 5 presents the manufacturing and mechanical assessment of structural GFRP and carbon fiber reinforced polymer (CFRP) composite laminates with through-thickness thermal energy harvesting capabilities based on coated GF fabrics with functional (Te NPs-based) TE inks and pastes. For both cases, the functional GF system laminae transfuse the bulk TE response. In the case of CFRP composite laminates, the unmodified structural part can also act as conductive electrodes for the most efficient transfer of TE carriers to achieve the maximum possible thermoelectric power. Moreover, through the TE effect exploitation is able to be achieved indirect self-powered temperature sensing for the multifunctional structures.

Chapter 6 demonstrates the fabrication of novel designed low-power consuming ET printed devices directly onto GF reinforcing fabrics and the subsequently proper integration of the system laminae within CFRP composite laminates in order to implement out-of-oven curing (OOC) and post-curing of the epoxy resin matrix. Furthermore, the produced multifunctional structures providing additional functions such as de-icing and self-sensing with respect to unique opportunities for large-area applications via multiple interconnected arrays of ET printed devices.

Finally, **Chapter 7** concludes in detail the main experimental findings and summarizes the outcome and the respective prospects derived from the completion of the current PhD thesis.

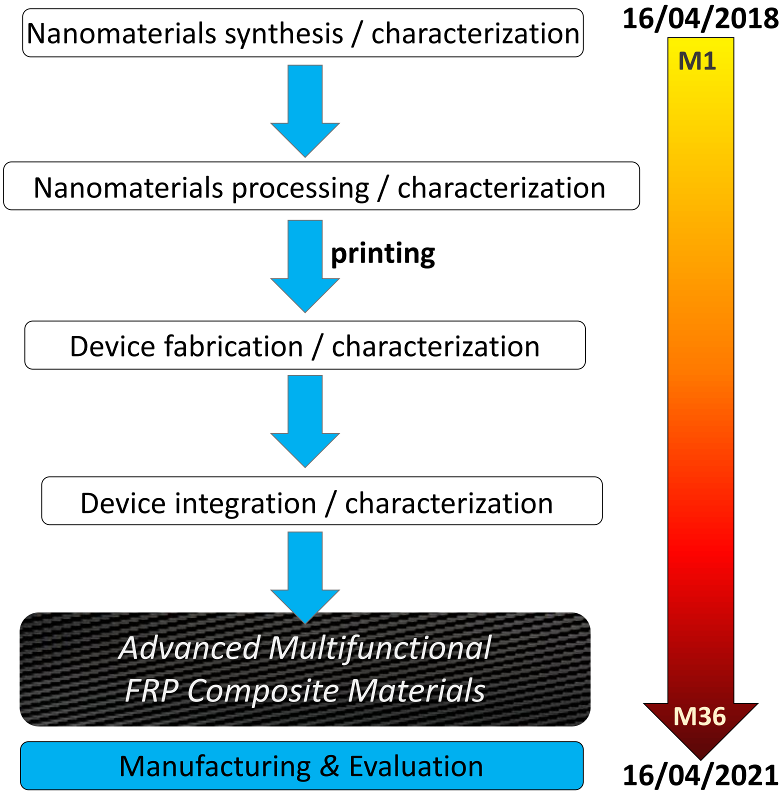

Figure 3. The current PhD thesis outline as a flow chart diagram implemented at the specific and expected timelines.

Principles and theoretical background

The fundamental theory at material level as well as at electronic device level (applications) of both TE and ET effects are comprehensively elaborated within the next subsections.

TE power conversion - Seebeck effect: Any transport phenomenon that implicates an exchange of heat and electrical potential energy can be referred to as TE effect. The process in which system's final state can be restored to its initial state without entropy production or dissipation of energy is defined as thermodynamically reversible. TE phenomena involve the transfer of energy between electric power and thermal gradients, widely used for cooling and heating, including air conditioning, refrigeration, thermal management and the generation of electrical power from waste heat. There exist three reversible TE effects *i)* the Seebeck, *ii)* the Peltier effects used for TE generation and electronic refrigeration respectively and *iii)* the Thomson effect that holds no practicality. At the same time, the performance of a real TE device always remains lower than Carnot efficiency due to two present irreversible processes that include Joule heating and thermal conduction. Since it is virtually impossible to separate reversible and irreversible processes in thermoelectrics, it can only be treated within non-equilibrium thermodynamics. The discovery of the TE effect belongs to Estonian-German physicist Thomas Johann Seebeck, which was made in early 1820 as a result of his experimental investigations into a possible relation between electricity and heat. In that experiment he used an open circuit consisting of two dissimilar materials (standard thermocouple configuration) where the cold junction kept at temperature T_1 and the hot junction at T_2 creating a temperature gradient. Under these conditions an electromotive force (Seebeck voltage) is induced in the circuit. The measured voltage is directly related to temperature gradient by a proportionality coefficient, which is best known as Seebeck coefficient or thermopower. A thermocouple is a TE device that involves a junction between two TE materials with semi-conducting properties. The physics relies on the Seebeck effect, *i.e.,* the movement of the mobile charge carriers from the hot point to the cold point of each TE material and the consequent voltage difference between the hot and cold points of each dissimilar material (**Figure 4**). If the majority of charge carriers are holes the Seebeck coefficient is positive (p-type), otherwise for electrons is negative (n-type).

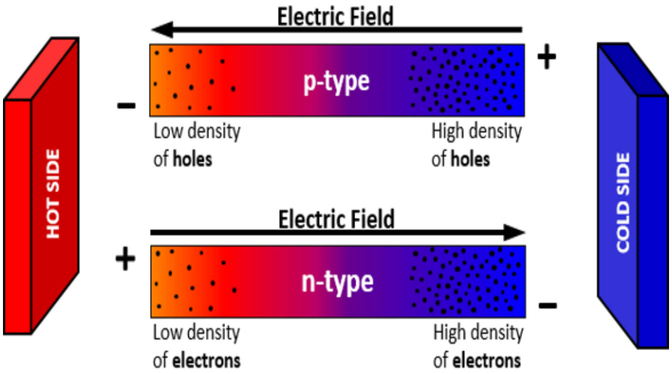

Figure 4. Schematic representation of Seebeck effect mechanism, generating voltage output when semi-conductor materials with p- or n-type behavior exposed in temperature difference (*https://doi.org/10.1016/B978-0-12-815751-0.00009-2*).

From conventional electronics theory, Ohm's Law, the proportionality between unipolar electrical current density *J* and electric field E is derived from Drude's model and written as: $J = q \cdot n \cdot \mu \cdot E = \sigma \cdot E$, where q is the elementary charge, n the carrier concentration, μ the mobility and σ the electrical conductivity. At the atomic level, temperature is a concept that is defined in terms of kinetic energy.

When referring that something is hot, the atoms and electrons have gained high kinetic energy and means that magnitude of the atomic vibrations has increased for atoms and valence electrons occupy higher energetic states. Heat is transported by the collective vibration of atoms, by the scattering of electrons and if electrical current is flowing, by electric current. A short but important note is the interrelation between heat and electronic transport. That means that if a ΔT is applied to a material, heat will flow and (if connected to a load) electricity will flow as well. Vice versa, if a ΔV is applied, electric current will flow and as a consequence heat will flow as well. Hence, in semiconductor materials, heat transport implies electric transport and vice versa.

The TE performance at material level is generally benchmarked by the dimensionless thermoelectric figure of merit (*ZT*), which is composed of the electrical conductivity (σ), the Seebeck coefficient (S), the thermal conductivity (κ) and the absolute temperature (T). The Drude model (electrical conduction theory) provides a very good explanation of DC and AC conductivity, the Hall effect and the magnetoresistance in metals near room temperature. Additionally, it could be explain partially the Wiedemann–Franz law, where the ratio of the electronic contribution of the thermal conductivity to the electrical conductivity of a metal is proportional to the temperature. The Seebeck coefficient is directly related to the density of states, whereas the electrical conductivity can be limited by electronic and morphological defects. Consequently, Seebeck coefficient reflects the average entropy transported per charge carrier and thus decreases with increasing carrier concentration (n). By contrast, the electrical conductivity increases with carrier concentration, fact that derives from the analytical formula of $\sigma = n \cdot e \cdot \mu_e + n \cdot h \cdot \mu_h$ (μ_e: carrier mobility of electrons, μ_h: carrier mobility of holes). The thermal conductivity is composed of the lattice (κ_l) contribution and the electronic (κ_e) contribution ($\kappa = \kappa_l + \kappa_e$), which increases with carrier concentration, as charge carriers can also transport heat.

The efficiency (η) of a TE generator (TEG) device is related to the ZT of the TE material and the Carnot limit. Typical TEG devices consist of 'legs' or thermoelements of multiple single type (p- or n-type) or alternating p- /n-type TE materials that are connected electrically in series and thermally in parallel, as shown in **Figure 5**. Traditional inorganic TEG devices consist of bulk thermoelements tiled in two dimensions over a ceramic substrate that is patterned with electrical contacts, in which the thermal gradient across the material is perpendicular (through-thickness) to the substrate. The aforementioned geometry is not suitable for solution-processed / film-based TE materials, which benefit from an in-plane architecture due to the main in-plane direction of carrier transport, as indicated by the current (I) direction and the thermal gradient across the TEG device is applied parallel to the substrate. Thus, the large-scale exploitation of ambient existing or artificially created thermal gradients is able to recover thermal energy losses and transform sustainably to electrical power by specially designed TEG applications.

The generated voltage-power due to Seebeck effect is single phase DC and is given by $I^2 \cdot R_L$ or $V \cdot I$, where R_L is the load resistance. The output voltage and output power are increased either by increasing the temperature difference between the hot and cold ends or by connecting several heat generators in series. The voltage of this generator is given by $V = \mathrm{S} \cdot \Delta T$, where S is the Seebeck coefficient and ΔT is the temperature difference between hot and cold coupling.

When R_{TEG} is the internal resistance of the thermoelectric generator then the current flowing through the external resistor R_L is given by $I = \frac{V}{R_{TEG}+R_L}$ (**1**). The replacement of the voltage value in equation (**1**) derives the generated current: $I = \frac{\mathrm{S}.\Delta T}{R_{TEG}+R_L}$ (**2**). The power flow in the external load is given by $P_L = I^2 \cdot R_L$. The replacement of the current value in the aforementioned derives the generated power: $P_L = \left(\frac{\mathrm{S}.\Delta T}{R_{TEG}+R_L}\right)^2 . R_L$ (**3**). This power will be maximum when $R_{TEG} = R_L$. Thus, the maximum power is given by $P_{max} = \frac{(\mathrm{S}.\Delta T^2)}{4.R_{TEG}}$ (**4**).

The efficiency of the thermoelectric generator is defined as the ratio of the developed power against load resistance at heat flow, Q from the source: $Efficiency = \frac{I^2.R_L}{Q}$ (**5**).

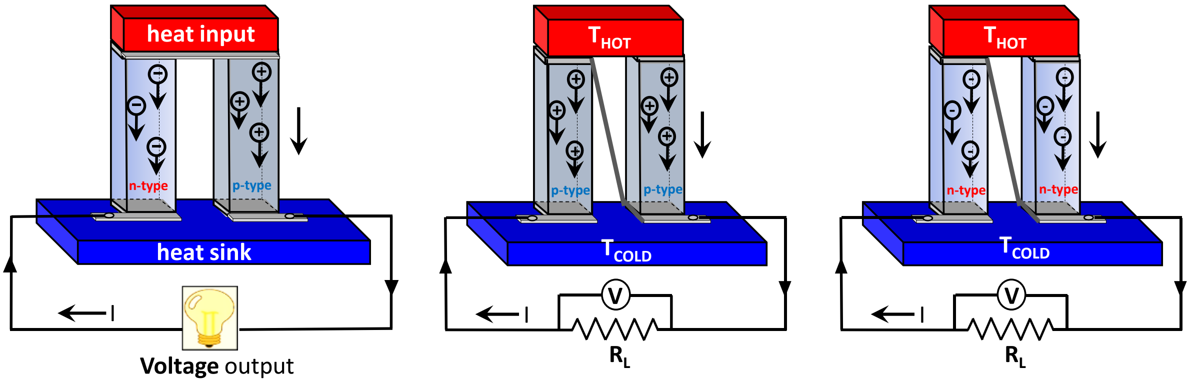

Figure 5. Different TEG assemblies and equivalent circuits depending on the semi-conducting type of the thermoelements interconnection (*https://doi.org/10.1016/B978-0-12-815751-0.00009-2*).

Electrothermal heating - Joule effect: Joule heating, also referred as Ohmic heating or resistive heating, is the phenomenon when an electric current pass through a conductor and produces heat. Joule heating affects the whole electric conductor, unlike the Peltier effect which transfers heat from one electrical junction to another. Joule's first law, indicates that the power (P) of heating which is generated by an electrical conductor is proportional to the material's inherent electrical resistance (R) and the square of the current (I). James Prescott Joule back in 1840, observed that heat (H) could be generated by an electrical current. Joule conducted an experiment where he immersed a wire in a fixed mass of water and measured the temperature rising owing to a known current that was flowing through the wire for a time (t) period of 30 min. By changing the current and the length of the wire subsequently he found that the produced heat was proportional to the square of the current multiplied by the electrical resistance of the immersed wire in accordance with time ($H = I^2 \cdot R \cdot \mathrm{t}$). At atomic level, the inner interactions between electrons and the ions of the conductor resulting in Joule heating effect. When voltage difference is applied between two points of a conductor an electric field is being created that forces and parallel accelerates charge carriers in the direction of the electric field, enhancing the kinetic energy of the system. The collision of electrons within a conductor leading to scattered particles and spontaneously the electrical energy is converted into thermal energy (**Figure 6a)**.

Concerning the applications of resistive heating, various everyday utilities are based on the Joule heating effect and can be found everywhere around from home up to industrial world. Therefore, the sustainable and low-power consuming heat generation remains a desirable technology and is being intended for design in a wide range of applications and sectors. A common electrothermal equivalent circuit is show in **Figure 6b**.

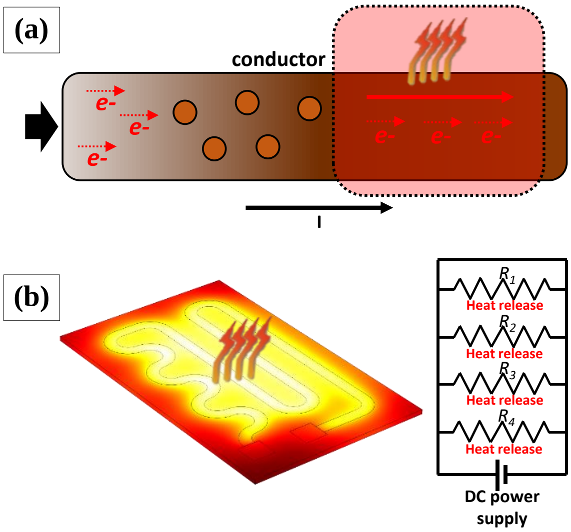

Figure 6. Graphical **(a)** microscopic description of Joule heating within a conductor and **(b)** electrothermal heater device upon operation with an indicative equivalent circuit.

Characterization techniques

The basic principles and the respective instrumentation of the main analytical, morphological and measuring methods which were utilized throughout this research study are briefly described in the sections below.

Raman Spectroscopy: Raman spectroscopy (RS) is an analytic technique that uses scattered light to measure the energy vibrations of a sample. The technique took its name from the Indian physicist C.V. Raman who, together with his colleague K.S. Krishnan, observed the scattering phenomena in 1928. When a beam of monochromatic radiation hits a sample, the light will interact with the sample. It can be reflected, absorbed, scattered or emit secondary radiation. Secondary radiation originates from atoms of matter and is used to determine a number of events, such as fluorescence and Raman scattering. The energy of a photon (E) is equal to the product of the Planck constant (h) and the frequency (v). The interaction of a photon with a molecule can result in absorption, reflection or scattering. Its absorption will take place if the energy of the photon is equal to the energy difference of the two energy levels. If the energy of the photon after its interaction with the sample is equal to the energy difference of the two energy levels, then the photon is reflected. If the energy of the photon is different from the difference between the fundamental energy level and the first excited level, scattering of the photon is observed. When a beam of photons is scattered by a molecule, the electromagnetic field of the photon causes the molecular electron cloud to polarize so that the photon energy is transferred to the molecule. This energy state is unstable and the photon (scattered light) is re-emitted. This type of scattering retains the energy of the molecule unchanged after it interacts with the photon and is called elastic or Rayleigh scattering. Raman scattering is an inelastic type of scattering *i.e.*, there is an energy transfer between the scattered photon and the molecule. If the molecule gains energy during the scattering of the photon (higher vibrational level), then the scattered photon loses energy, its wavelength increases and is called Stokes Raman scattering. Conversely, if the molecule loses energy (lower vibrational level) the scattered photon receives this energy and its wavelength decreases. This type of interaction between the photon and the molecule is known as Anti-Stokes Raman scattering. Stokes and Anti-Stokes scattering are quantum mechanically possible processes. However, according to the Boltzmann distribution, Stokes scattering is statistically more likely, as the majority of molecules are at a lower vibrational level. For this reason, Stokes scattering is more intense than Anti-Stokes and is almost always measured by Raman spectroscopy (**Figure 7a**). The number of active vibrations in Raman spectroscopy is estimated to be equal to (3N-4), where N is the number of carbon atoms in the unit cell of the crystal. According to the rules of group theory, only 15 to 16 types of vibrations are active in Raman (A_{1g}, E_{1g}, E_{2g}). It should also be noted that one type of vibration can be weak enough that it cannot be detected experimentally, although its existence is theoretically predicted. Each molecule can have a number of vibration modes. For nonlinear molecules with N atoms, the number of vibration modes is given by the 3N-6 relation. 3N are the total degrees of freedom of the molecule, 3 metaphorical and 3 rotational degrees of freedom. For linear molecules there is a less rotational degree of freedom and therefore the number of vibration modes of the molecule is calculated from the 3N-5 ratio.

Figure 7b presents a schematical graph of a typical Raman spectroscopy set-up.

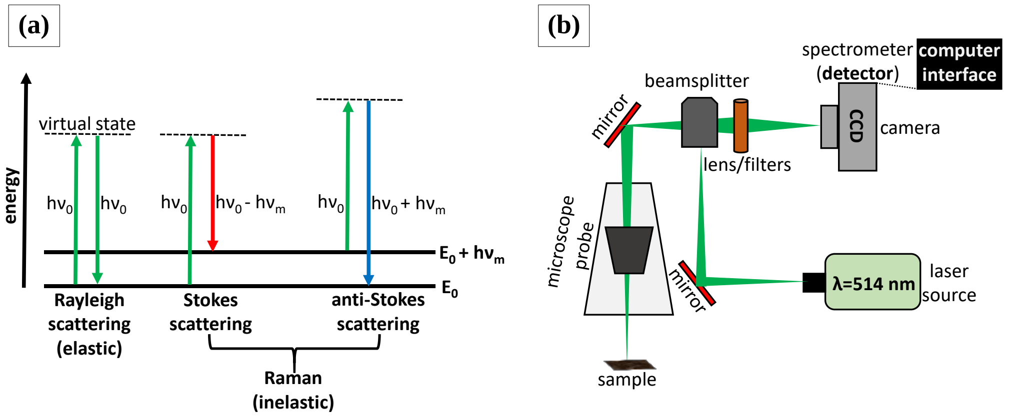

Figure 7. Schematic presentation of **(a)** basic Raman phenomenon theory and **(b)** Raman spectroscopy set-up.

X-Ray Diffraction: X-Ray Diffraction (XRD) is a non-destructive method of characterizing materials to determine the crystalline or amorphous nature of a tested sample. Databases, such as that of the World Bank (Powder Diffraction Data File - PDF), contain tables for thousands of crystalline compounds, with the aim of identifying the components of each sample, the lattice constants and its geometry through a search / identification technique. When X-Rays impinge on a sample, several types of interaction can be occurred *e.g.*, photoelectric effect, fluorescence, production of Auger electrons, Compton scattering and coherent scattering. Only the last one, coherent scattering, leads to the phenomenon of diffraction. In practice, a perfectly elastic collision between a photon and an electron leads to a change of direction of the photon, but preserving its energy and phase (**Figure 8a**).

As illustrated in **Figure 8b**, when X-Rays pass through a crystalline structure (sample), the formed patterns can be captured and then used to determine the crystal's structure.

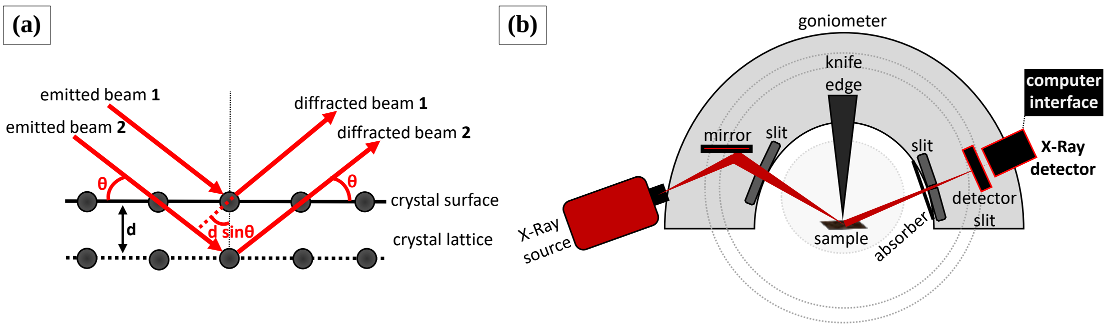

Figure 8. Schematic depiction of XRD principles **(a)** X-Ray interaction with crystal lattice**, (b)** set-up configuration.

Thermogravimetric analysis: Thermogravimetric analysis (TGA) is an analytical method used to determine the thermal stability of a compound, by monitoring the weight change that occurs upon heating. The analyzer usually consists of a high-precision balance with a pan loaded and a furnace. The measurement is normally performed in air or in an inert atmosphere, such as N_2 or Argon and the weight loss of a sample is recorded as a function of temperature (**Figure 9**). It is commonly employed to determine characteristics of materials such as polymers, to determine degradation temperatures, absorbed moisture content of materials, the level of inorganic and organic components in materials, decomposition points and any solvent residues.

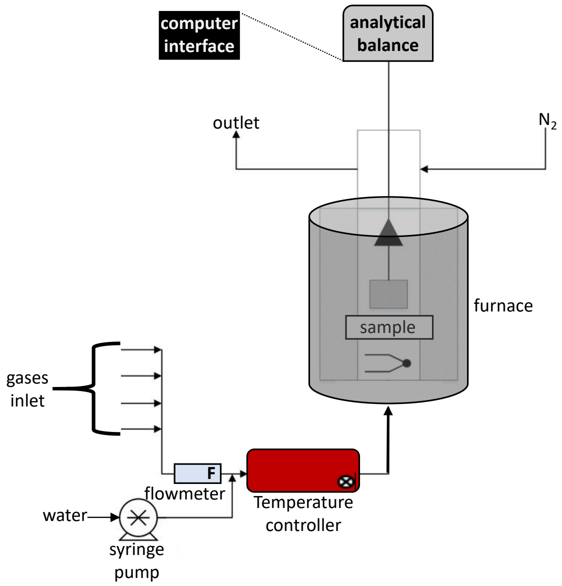

Figure 9. Graphic representation of TGA set-up and operating principle.

Scanning Electron Microscopy and Transmission Electron Microscopy: Scanning Electron Microscopy (SEM) is an instrument used to examine and record the surface topography of a sample. The resolution of this microscope is significantly higher than that obtained with an optical microscope and the image can reveal microscopic information about the shape, size, crystallography and other chemical and physical properties of a sample. The operation principle of SEM is based on the creation of a focused electron beam through emission from an electron source (electron gun). Typically, the energy of the electrons in the beam region is from 0.1 to 30 KeV. The diameter of the emitted electron beam is initially too large (~50 μm) to obtain a high-resolution image. For this reason, electromagnetic lenses and apertures are used resulting in the formation of an electron beam point on the sample (~1-100 nm). In addition, the above procedure is performed in vacuum so that the electrons are not scattered by the air molecules. The formation of the final image depends on the collection of the produced signals, due to the interaction of the electron beam with the sample under examination. These interactions are divided into two categories, elastic and inelastic. The elastic scattering is the result of the deflection of the electron beam from the atomic nucleus or from the electrons of the outer layers of the sample's atoms. These interactions are characterized by negligible loss of energy during impact and a large angle of change of direction of the scattered electrons. The incident electrons that scattered at an angle greater than 90° are called backscattered electrons (BSE) and provide important information for the topography of the sample. As mentioned above, the backscattered electrons are the result of the inelastic interaction of the electron beam and the sample. These electrons escape from the surface of the sample with energies greater than 50 eV. The signal by the back-scattered electrons also contains information from areas below the surface of the sample and concerns both the topography and the composition of the material. Inelastic scattering occurs due to a wide variety of interactions of the incident electrons with the atoms and electrons of the sample. The amount of energy that will be transferred to the sample depends on the individual or collective stimulation of the electrons in the sample and their binding energy to the individual. The ionization of the sample atoms leads to the formation of secondary electrons (SE), which possess energies less than 50 eV and are used to analyze the image of the sample. Secondary electrons are produced both by the primary electron beam and by excitation from the back-scattered electrons and are also produced when the back-scattered electrons escape the surface of the sample which are mainly used to represent the structure and surface roughness of the examined sample. Complementary to the above two signals used to form the image of a sample, when the electron beam interacts with the sample a number of other signals are generated such as X-Ray emission, Auger electrons and cathodoluminescence. Each of these signals confer different information about the sample and originate from different built-in detectors (**Figure 10a**).

Transmission Electron Microscopy (TEM) is an imaging technique based on the irradiation of a sample by a beam of electrons. The image is formed, magnified and detected by a sensor such as charged coupled device (CCD) camera. Contrary to the conventional light microscope where photons are employed, TEM uses electrons as light source (electrons gun). Accordingly, it is possible to get a thousand times higher resolution than with a light microscope due to their much lower wavelength. The filament on the top of the microscope emits electrons that go through vacuum in the column of the microscope. Electromagnetic lenses are used to focus the electrons into a very thin beam. This beam travels through the examined sample. Depending on the density of the sample, some of the electrons are scattered away from the beam. At the bottom of the microscope the un-scattered electrons hit the fluorescent screen and an image of the sample is obtained (**Figure 10b**).

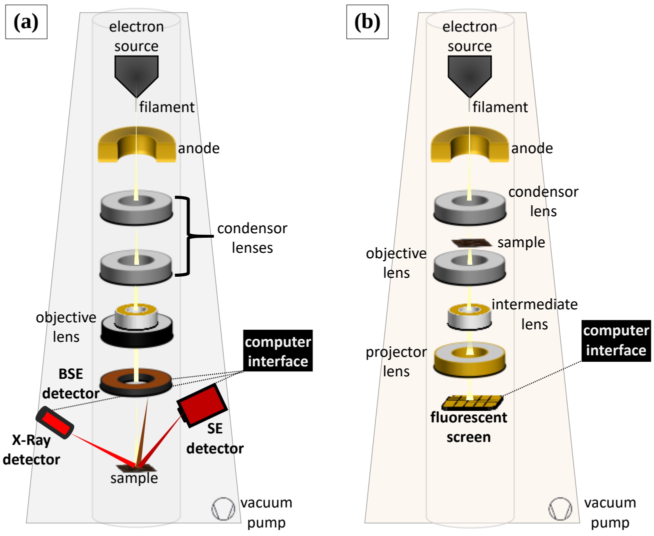

Figure 10. Schematic outline of **(a)** SEM and **(b)** TEM modulation.

Viscosity measurements: A crucial factor that affects the resulting printing films of the prepared functional inks is the rheological behavior. Dynamic viscosity measurements were conducted using a digital rotary viscometer NDJ-9S (**Figure 11a**) at 25 °C in a range of shear rates with the same spindle (**Figure 11b**) for all the examined systems so as to investigate any shear rate dependent phenomena. Apparent each shear rate was applied for approximately 2 min in order to achieve pseudo-equilibrium and ensure data accuracy.

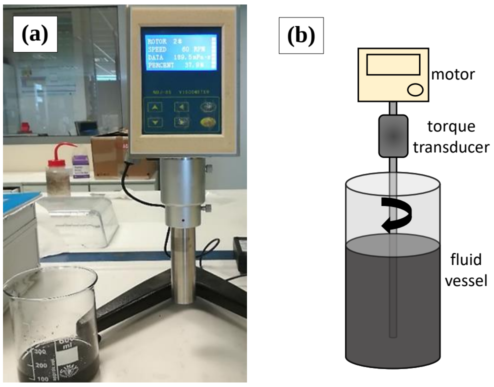

Figure 11. (a) Photo and **(b)** the corresponding schematic depiction of the utilized viscometer.

Contact angle measurements: Wetting is the ability of a liquid to spread over a solid surface. Contact angle (CA) is the measuring technique that investigates and quantify the wetting angle that the liquid forms on a solid surface. The surface tension (γ) of a droplet is determined by the interactions between its constituent molecules. When a drop comes in contact with a solid surface, three interfaces *i)* solid-liquid, *ii*) liquid-vapor and *iii*) solid-vapor. **Figure 12a** represents some indicative interface forces exerted by surface tension. When the system is in equilibrium, the forces can be described by Young's formula: $\gamma_{SV} = \gamma_{LS} + \gamma_{LV} \cdot \cos\theta$, where θ is the wetting angle, γ_{SV} is the force at the solid-vapor interface, γ_{LS} is the force at the liquid-solid interface, γ_{LV} is the force on the liquid-vapor interface. Generally, in the case $\gamma_{SV}<\gamma_{LS}$, $\cos\theta$ will take a negative value and therefore θ will be $<90^{o}$ indicating good wetting properties. On the other hand, in the case $\gamma_{SV}>\gamma_{LS}$, $\cos\theta$ will take a positive value and therefore θ will be $>90^{o}$ indicating poor wetting properties.

The measurement includes the stages of recording and analysis. The most common set-up uses the following three basic elements *i)* a light source, *ii*) a camera and *iii*) an adjustable stage for placing the sample. The measuring process begins by depositing a drop of liquid on the surface, while the base is adjusted so that the drop does not move during deposition. The droplet is then illuminated from behind with a light source and the image is captured by a camera. Finally, the image is further analyzed using a built-up software and thus the wetting contact angle is determined (**Figure 12b**).

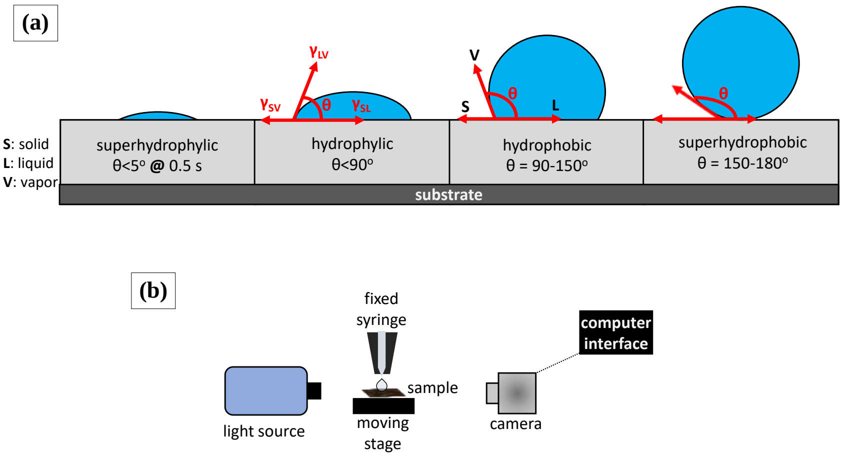

Figure 12. Schematic illustration of **(a)** different contact angle cases and **(b)** contact angle measuring set-up.

Electrical measurements: 4-probe sheet resistance measurements were performed employing a commercial 4-point probe electrical characterization system (Ossila Ltd). As depicted in **Figure 13a**, DC current is applied between the two external electrodes (1 and 4) and the voltage drop between the 2 internal electrodes (2 and 3) is measured through the 4-electrode configuration with the four metallic pins (lined-up in a straight line equidistant from each other). The electrical conductivity of a sample with a known thickness (*t*) derived from the formula: $\sigma = 1/R_s \cdot L/A \cdot (\ln 2/\pi)$, where R_s is the measured 4-probe sheet resistance, L is the length and A is the cross-section area.

2-probe DC-electrical resistance measurements were performed using Agilent 34401A digital multimeter (**Figure 13b**). The Agilent 34401A instrument (measuring unit) provide accuracy of 0.0035 ± 0.0005 and resolution of 6½ digits (sampling rate: 1 reading measure/s) with measuring DC range voltage up to 1 KV and current up to 3 A. All data were automatically transferred to computer and treated with an interfaced data logging software (DMM connectivity utility software).

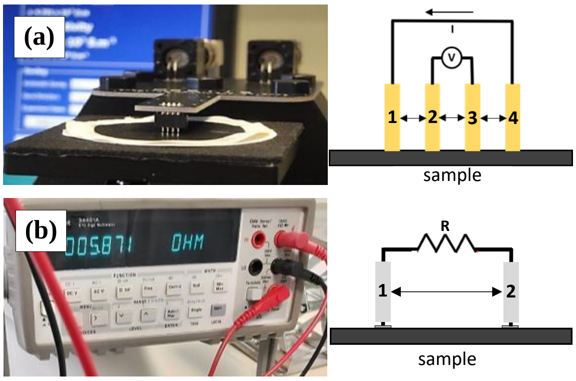

Figure 13. Photo and the corresponding schematic presentation of the **(a)** 4-probe sheet resistance and **(b)** 2-probe electrical resistance measurements.

Hall measurements: Hall-effect measurements were performed at 0.55 T and 1 mA using the Ecopia HMS-3000 system, in order to determine the carrier concentration and mobility of the different semi-conducting films. The Hall effect is the production of a voltage difference (Hall voltage) across an electrical conductor that is transverse to an electric current in the conductor and to an applied magnetic field perpendicular to the current (**Figure 14**). It was discovered by Edwin Hall in 1879. The Hall effect is due to the nature of the current in a conductor. Current consists of the movement of many small charge carriers, typically electrons, holes, ions or all three. When a magnetic field is present, these charges experience a force, called the Lorentz force. When such a magnetic field is absent, the charges follow approximately straight, 'line of sight' paths between collisions with impurities, phonons, *etc*.. However, when a magnetic field with a perpendicular component is applied, their paths between collisions are curved, thus moving charges accumulate on one face of the material. The Hall coefficient is defined as the ratio of the induced electric field to the product of the current density and the applied magnetic field. It is a characteristic of the material from which the conductor is made, since its value depends on the type, number, and properties of the charge carriers that constitutes the current.

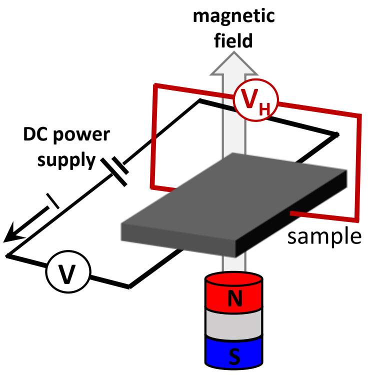

Figure 14. Graphic illustration of Hall measurements.

Chapter 1

Literature Overview –
Towards multifunctional self-powered structural composites

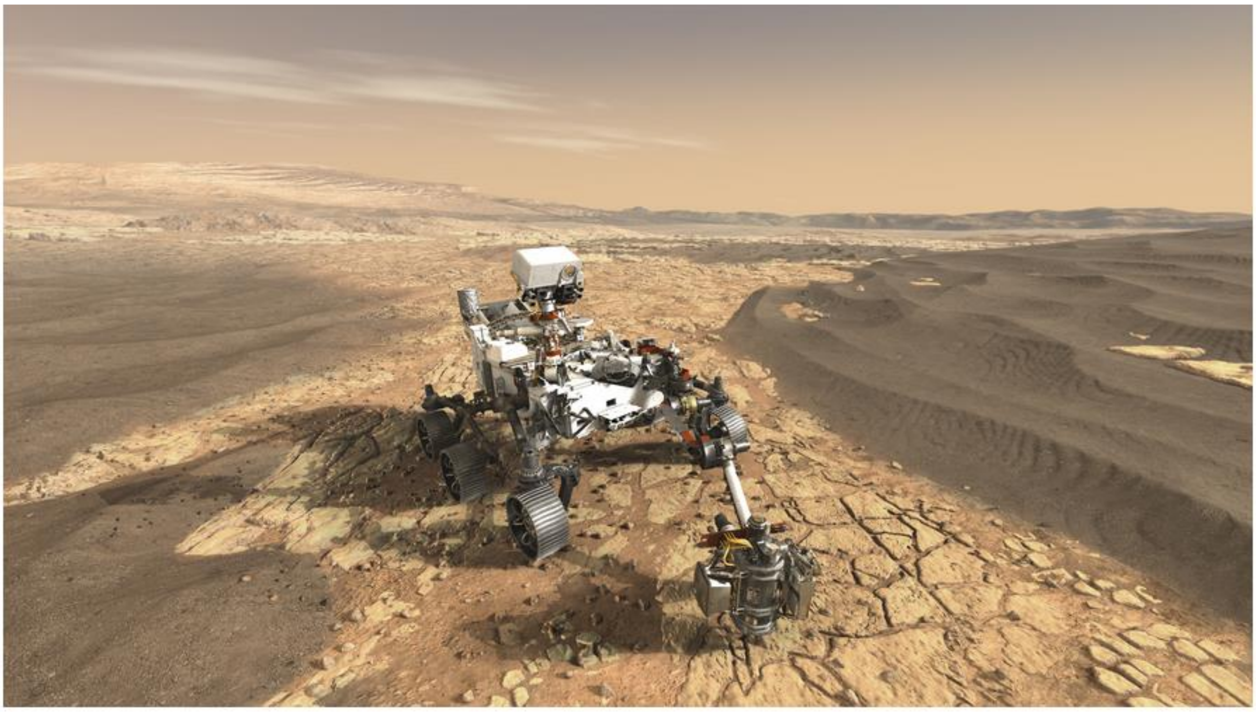

An illustration of NASA's Perseverance rover on the surface of Mars.

The Multi-Mission Radioisotope Thermoelectric Generator (MMRTG) converts heat from the natural radioactive decay of plutonium into electricity. This power system charges the 2 primary batteries of the rover. The heat from the MMRTG is also used to keep the tools of the rover and systems at their correct operating temperatures *https://rps.nasa.gov/missions/14/mars-2020*.

1. Literature Overview – Towards multifunctional self-powered structural composites

The total world energy consumption, otherwise reported as the world power consumption, has shown an increasing trend over the last decades with a present value of about 600 quadrillion British thermal units (Btu). This value is predicted to increase by 28 % rising to 736 quadrillion Btu in 2040. The extreme increase in the consumption of energy resources and especially that of petroleum feedstocks could be attributed mainly to *i)* the industrial development and *ii)* the population growth [1]. The finite supply of fossil fuels, which resulted to the intensified energy crisis in the 21st century, has rendered the demand for alternative energy resources higher than ever [2].

In industrial environments and our daily life, a large amount of generated heat is wasted in the environment as it cannot be effectively used, *e.g.*, emissions of factory boilers, car exhausts, friction, *etc*.. A major contributor to waste heat is in the transport sector. Among developed countries, transportation accounts between 20 and 25 % of the total energy being consumed [3]. Aeronautics and automotive are typical examples of high energy usage with low efficiency, where roughly 75 % of the energy produced during combustion is lost in the turbine / exhaust or engine coolant in the form of heat. At a global scale, approximately 60 % of all energy produced is never utilized, as most of it is dissipated in the form of waste heat [4]. Novel technologies that can harvest energy from the environment as sustainable self-sufficient micro / nano-power sources offer a possible of solution, since the available energy has a wide spectrum of frequencies and time-dependent amplitudes. This type of energy is called random energy and can come from irregular vibrations, light airflow, noise and human activity [5]. Research for alternative energy sources *e.g.*, solar energy, thermal energy, wind energy, hydrogen energy and biomass energy to replace the conventional fossil fuels, is predicted to dramatically improve the current efficiency of the energy usage and emerge viable alternative approaches (**Figure 15**).

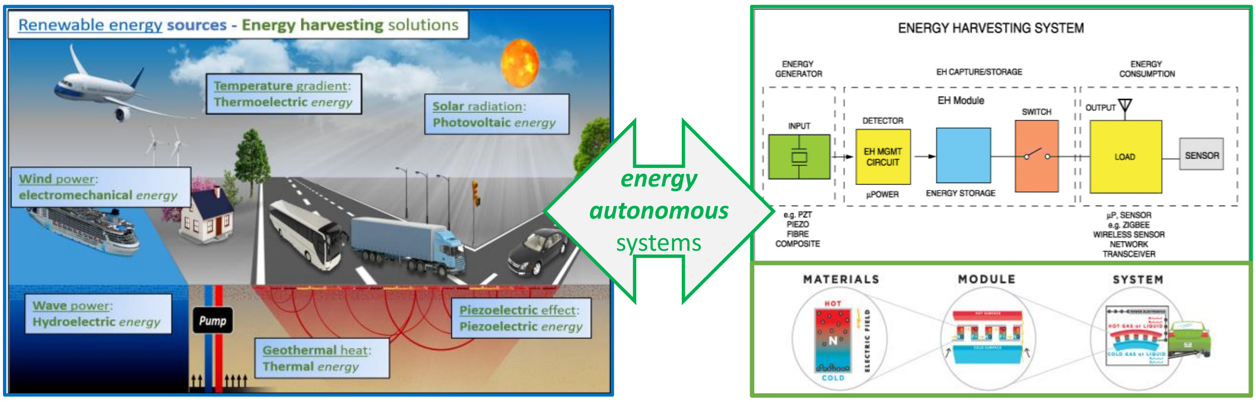

Figure 15. Potential exploitation of ambient energy losses by specially designed advanced structural components.

Nowadays, the energy that is dissipated into the environment as waste heat has become more important as an alternative energy resource. Thermoelectric (TE) materials are a potential candidate for harvesting waste thermal energy, due to their ability to generate electricity even from small temperature gradients often induced by thermal power sources (*e.g.*, combustion engines or power plants). TE materials obey the well-known thermoelectric or Seebeck effect described by the thermoelectric power (TEP), or thermopower, or Seebeck coefficient (S), which is the direct solid-state conversion of thermal to electrical energy [6]. Through the diffusion of charge carriers, either electrons or holes, an electric current is created from the hot side of the material to the cold one. The Seebeck coefficient is defined as: $S = \Delta V/\Delta T$, where ΔV is the electric potential difference or the generated thermovoltage created by a temperature difference, ΔT. The Seebeck coefficient is used for the calculation of the power factor ($PF = \sigma \cdot S^2$, σ is the electrical conductivity), a well-known entity for comparing the efficiency of different thermoelectric materials. The dimensionless figure of merit (ZT), $ZT = (\sigma \cdot S^2) \cdot T/\kappa$, where κ is the thermal conductivity and T is the absolute temperature, is also used to compare the TE efficiency of different materials [7]. The Seebeck coefficient is an intrinsic property of materials related to their electronic properties. Specifically, it does not depend on the geometry, while it has positive values for p-type and negative for n-type semiconductors [8]. A high ZT may be achieved by creating a material exhibiting a high-power factor and low thermal conductivity. However, the direct relationship between the electrical conductivity (carrier mobility) and the charge carrier density (Seebeck) contribution to the thermal conductivity should always be considered. Moreover, for a high ZT, several other important issues such as cost, weight, and processability should also be taken into account. Traditional thermoelectric materials and thermoelectric generator (TEG) devices are based on low band gap semiconductors *e.g.* Bi_2Te_3 [9], Bi_2S_3 [10], PbTe [11], Ag_2Te [12] *etc*..

Conventional TEGs have been reported many times utilized in practical applications for waste thermal energy recovery and conversion. The machine in service is another heat source with temperature differences from the surroundings. Because of the features of safety, reliability and durability, as well as the extensive existence of temperature difference, TEGs have been widely applied in vehicles, aerospace, ships and other industrial operations [13]. Some of the TEGs aim to reduce fuel consumption and CO_2 emissions by converting exhaust heat into an alternative energy as an electric power backup. More specific, TEGs were recently reported for potential fuel saving from the exhaust system of light-duty vehicles, where the TEG integration effects have been analyzed showing that the installation position has significant influence on the fuel saving potential [14]. Others are designed to provide electricity for wireless sensors networks (WSNs) using for structural health monitoring (SHM) or system condition monitoring of machines. It is confirmed that spatial temperature gradients are available, continuous and stable in mechanical systems [15]. More importantly, TE harvesters have characteristics of high stability, durability and safety. One of the most illustrious examples of efficient and reliable power generation are the multi-hundred-Watt radioisotope thermoelectric generators (RITEGs) developed for the Voyager 1 and 2 spacecrafts (1977-today). Each Voyager spacecraft was equipped with three RITEGs-collectively supplied 470 W of electrical power with a total weight of 37.7 kg including about 4.5 kg of Pu238 (four pressed plutonium-238 oxide spheres - halving every 87.7 years) based on conversion of the decay heat of the plutonium to electrical power by exploiting 312 SiGe interconnected TE junctions (**Figure 16**).

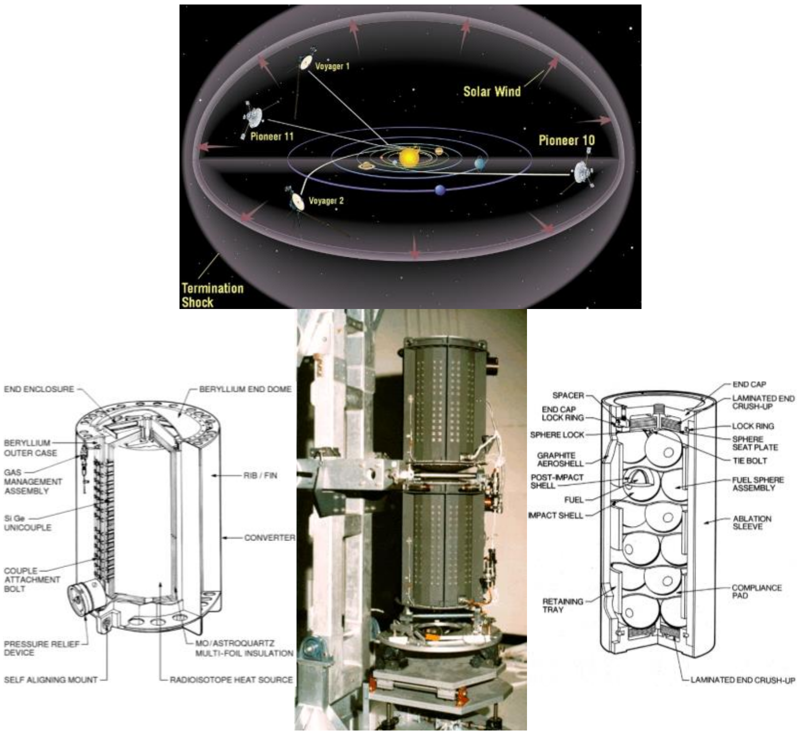

Figure 16. Multi-hundred-Watt radioisotope RITEGs for powering the Voyager 1 and Voyager 2 spacecrafts until nowadays (*https://en.wikipedia.org/wiki/MHW-RTG*).

Another important parameter in TEGs design, otherwise referred as TE modules is the optimization of the individual thermoelement geometrical characteristics, since all the thermoelements are connected serially, while the generated current in each of them is not the same. A novel TEG structure has been proposed, where the cross-sectional area of thermoelements is increasing gradually along with the hot fluid downward flow, with the performance fully corroborating a three-dimensional and fluid-thermal-electric multi-physical model developed [15]. The integration of TE materials in asphalt pavements has been also reported, since pavements are exposed to solar radiation and absorb a large amount of heat that can be harvested. A stacked structure of heat collector / TEG / coolant module has been deployed towards a prototype that generated a power output of approx. 29 mW in field conditions, which is envisaged to be enough power for autonomously driving WSNs and near-field data communications [16].

Such traditional TE materials and devices have been studied and utilized commercially for the last half century [17], while recently they have been developed onto flexible substrates using metallic pastes and inks for the thermoelements interconnection, resulting into flexible TEG devices *i.e.* for wearable applications, *etc*. [18,19]. However, they are expensive for mass production, cannot be deposited on large surfaces for potential large-scale energy harvesting, are often toxic and consist of rare and expensive elements [20]. Recently, Madan *et. al*, reported on printed flexible TEGs for low levels of waste heat recovery, consisting of Se doped Bi_2Te_3 (n-type material) and Te doped $Bi_{0.5}Sb_{1.5}Te_3$ serially interconnected via printed metallic junctions, with a maximum power output 33 μW and power density of 2.8 W/m^2 [21]. In another work, Lu *et. al.* reported on a flexible and wearable TEG on a silk fabric consisting of conventional TE materials (n-type Bi_2Te_3 and p-type Sb_2Te_3), while the fabricated prototype with 12 alternating TE junctions exhibited a maximum voltage and power outputs of ∼10 mV and ∼15 nW, respectively at a temperature difference of 30 K [22].

Recent advances in organic thermoelectrics have shown promising results for their use as an alternative to traditional ones [23]. Although organics typically possess low Seebeck coefficient values, they have the potential to be utilized as thermoelectrics. This results from the inverse relationship between the Seebeck coefficient and electrical conductivity due to charge carrier concentration and mobility [24]. For instance, carbon nanotubes (CNTs) are potential candidates for TE materials due their excellent electrical conductivity, while the thermal conductivity can be adjusted. CNTs are 1D carbon nanomaterials with diameters and thicknesses in the nanoscale region. Regarding the rolling angle of the single graphene sheet, CNTs present chiral and non-chiral configurations. Scientific findings [25,26] reveal that all armchair tubes are metallic-like without a bandgap, while the other chiral tubes are small-bandgap semiconductors (**Figure 17a**). In addition, high mechanical strength and high thermal stability are advantages for the commercialization of flexible TE devices. P- and n-type CNTs can be easily arise based on molecular doping strategies [27]. By oxygen doping it is possible to increase the density of charge carriers (thereby the Seebeck coefficient value) and simultaneously decrease the thermal conductivity due to the defects induced [28]. Another exceptional example of TE candidate material is the well-researched and commercially used PEDOT:PSS (**Figure 17b**) conjugated polymer because of its good electrical conductivity and environmental stability. Although its Seebeck coefficient is relatively low compared with inorganic counterparts and its applications are limited to a lower temperature range, it is relatively low-cost, lightweight, non-toxic, abundant and easily processable with inherently low thermal conductivity [29]. The presence of π–conjugated chain is the first fundamental requirement for a polymer to become conducting. However, the band gaps of conjugated polymers are ranging from 1 to 3 eV, which is consistent with semiconducting or even insulating properties. In order to acquire metallic electronic characteristics, a doping process is used. In contrast to inorganic doping involving atoms replacement, doping in conducting polymers is due to an oxidation (p-type doping) or reduction (n-type doping) process. Oxidation / reduction can be achieved by removing / adding an electron from / to a polymer via an electron transfer reaction with a chemical species (redox reaction) or with an electrode (electrochemical reaction). The doping charge on the polymer is stabilized by a counter ion (cation / anion) to ensure electroneutrality of the materials [30]. The hybrid and nanocomposite approach are highly recommended by the research community, since the organic part offers necessary structure flexibility, fact that enriches the range of potential efficient TE coatings utilization. To explore the feasibility of using polymers as TE materials, researchers have recently focused on polymer / inorganic TE composites because of their synergistic effects [31]. Nano structuring (referring to nano-domains within a crystalline structure bounded by grain boundaries) and/or alloying have allowed to increase the peak of both n-type and p-type, showing a significant improvement in *ZT* values, mainly because of an extended reduction in lattice thermal conductivity. Low-dimensional materials, such as nanowires and nanorods, may possibly decouple electrons and heat transport behaviour by suppressing phonon propagation because of their short mean free path (**Figure 17c**). In particular, carriers with a mean energy substantially below the Fermi level are “filtered” by potential barriers and hence do not contribute to transport. The energy filtering results in electrical conductivity reduction and Seebeck coefficient improvement [32]. As a result, the thermal conductivity of low-dimensional materials can be significantly lower than that of bulk without negatively affecting the electrical conductivity. According to previous research studies [33], environmental-friendly aqueous-processable dispersions / inks have been utilized for the fabrication of different electronic devices offering several advantages such as process versatility and scalability towards R2R continuous large-scale 2D printing production onto various types of substrates (**Figure 17d**).

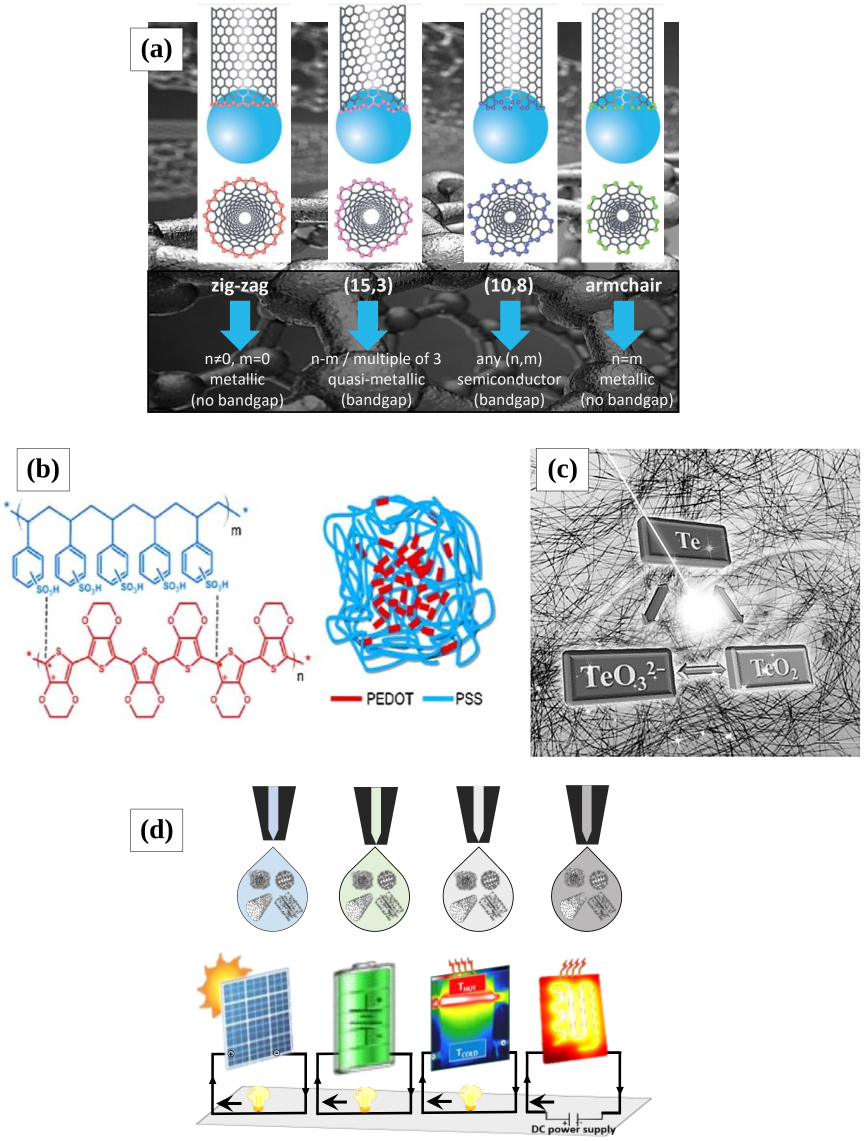

Figure 17. Exceptional nanostructured materials *e.g.*, **(a)** graphitic SWCNT with different chirality, **(b)** organic PEDOT:PSS conductive polymer and **(c)** inorganic Te NPs at diverse aspect ratios, **(d)** for various solution-processed printing applications.

The superiority of carbon fiber (CF) is due to the nature of carbon as an element and the intra-atomic bonds it forms with other carbon atoms. Graphite consists of anisotropic polycrystallites, whose anisotropy depends on the conditions of their synthetical processes based on PAN precursors [34]. The result of the strong orientation of the crystallites along the longitudinal axis of the carbon fibers is the high strength and fracture resistance coupled with low coefficient of thermal expansion in this direction [35]. Within the graphite structure, carbon atoms are arranged very densely in the form of hexagonal planes. The strong bond between the carbon atoms in these flat hexagonal layers results in an extremely high modulus of elasticity. In contrast, the weak Van Der Waals type bond between adjacent layers results in a lower value of a modulus of elasticity in this direction [36]. Carbon fiber reinforced polymer composites (CFRPs) offer the possibility for flexible design approaches for advanced structural materials with significantly enhanced specific properties such as strength and stiffness [37]. Polymer-matrix composites reinforced with a high-volume fraction of continuous aligned CFs are the dominant advanced lightweight structural materials for aircraft, satellites, sporting goods, *etc*.. Recently in the field of advanced composites, multifunctionality is also a topic of active research. Compared to the use of embedded or attached devices within the composite structure, a multifunctional structural composite is advantageous in the low cost, high durability, large functional volume and absence of mechanical property loss. The multifunctional character of composite structures was demonstrated in many different ways, *i.e.* strain / damage monitoring [38], humidity and temperature sensitivity [39], lightning-strike protection and heat dissipation [40], energy storage [41], superior electrical [42] and thermal conductivity [43], temperature management [44], EMI shielding [45], TE and piezoelectric energy harvesting [46,47] as well as colored damage indicating interfaces [48].

In the aeronautics, automotive and renewable energy industry, the employed structural FRPs are often exposed to environments where a temperature difference exists. Therefore, their potential to function as TE materials is a very challenging field of research [49]. TE energy harvesting by FRPs has been seldom reported in literature. Namely, the TE power of short carbon fiber / PC composites [50] and continuous long fiber reinforced laminates have been investigated [46]. The optimization of power factor by increasing both the conductivity, as well as the Seebeck coefficient remains still an open field for investigation. To this end, different approaches could be adopted such as doping of fibers, creating hierarchical nanoparticle-based coatings onto the fibers, *etc*.. TE structural materials are undoubtedly very promising for large-scale thermal energy harvesting, rendering them an attractive technology for the composite market. To achieve this goal, significant challenges are posed, which include the increase in TE efficiency both at material and structural level, as well as the integration of the TE functionality in the structure. In order to produce sufficient power, any TE material needs to be combined into a module, containing alternating p-type and n-type thermoelement junctions (or only p- or n-type) that are connected electrically in series, and thermally in parallel. This arrangement of thermoelements is utilized because it allows for the direct addition of the TE voltage contribution of each thermocouple, while they are subjected to the same maximum available ΔT. The TEG architecture results in the highest attainable TE voltage for a given number of thermoelements or legs (N) subjected to the available ΔT. The creation of a structural TEG based on serially interconnected CF tows, facilitating thus the increase of the total voltage and power output, as well as its integration within a CFRP laminate. Karalis *et al.* [51] reported the fabrication of CF-based TEG and manufacturing of TEG-enabled CFRP involved the exploitation of CF-M40B tows (10 thermocouples) of approximately 33.4 mm length and diameters of 0.156 mm were initially placed in parallel on a flexible Kapton foil at equal distances among them (**Figure 18a**). For the TEG generator based on CF tows, commercial single CF-M40B fiber tows have been used. The widths of the CF tows that can be observed in **Figure 18b** seem to be approx. 0.40 – 0.50 mm. This is due to the fact that the CFs as received from the manufacturer are pre-spreaded CF tows that can help any potential spreading process towards *i.e.* manufacturing of unidirectional (UD) prepregs and/or tapes, filament winding, *etc*.. Copper (Cu) wires of 0.122 mm diameter were utilized then to serially interconnect the adjacent CF tow thermocouples via small droplets of Ag paste (red lines represent the Cu wires in **Figure 18a**). This enabled the fabrication of the TEG module / device with external dimensions of 40 mm×60 mm. **Figure 18a** depicts the cartoon of the CF-based TEG module, while **Figure 18b** the real device that has been fabricated based on CF-M40B tows. **Figure 18c** shows the vacuum bagging process following the previously performed hand-layup in order to manufacture the 8-ply TEG-enabled CFRP laminate, where the supporting Kapton film was finally removed. **Figure 18d** illustrates the manufactured TEG-enabled CFRP laminate that operated as a planar TEG device upon being exposed to the in-plane temperature difference.

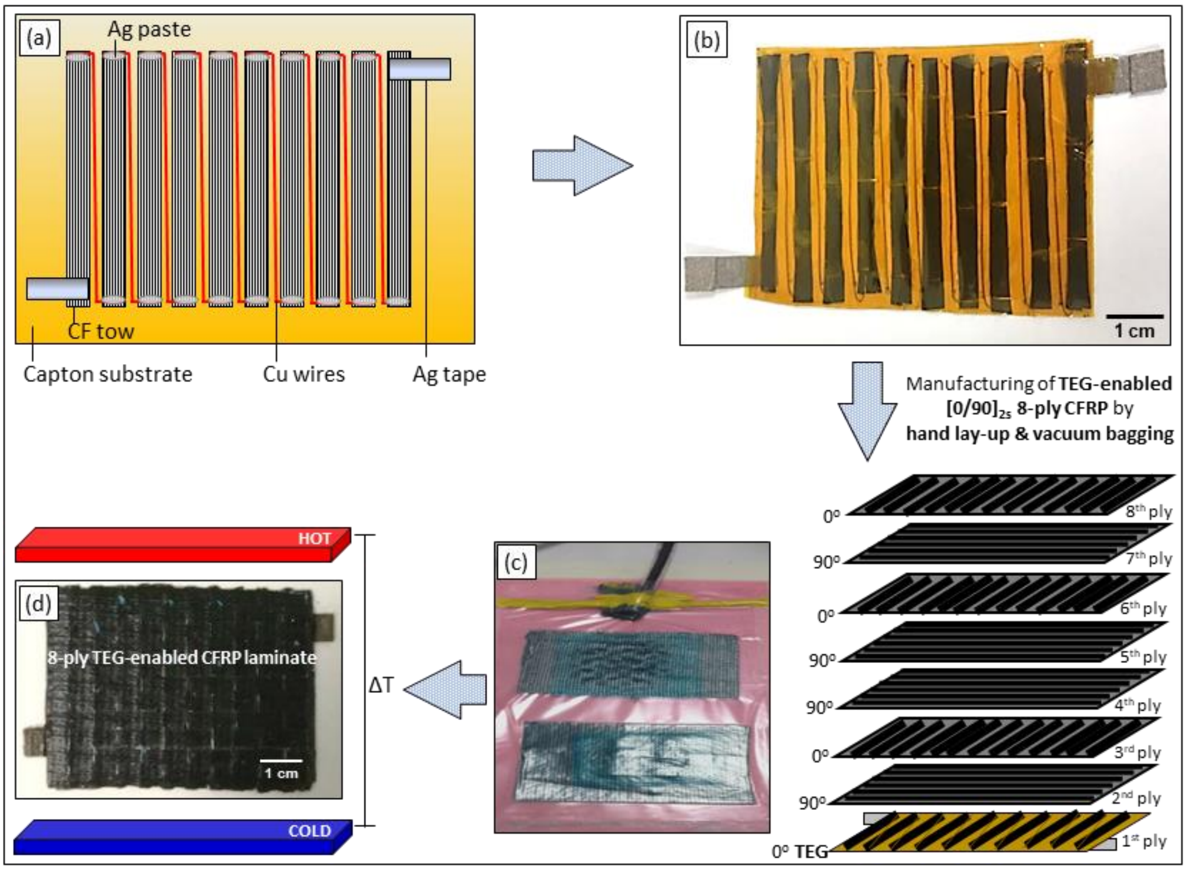

Figure 18. **(a)** Cartoon of the CF-based TEG module with 10 p-type serially interconnected CF-M40B thermocouples, **(b)** the real device on a Kapton substrate, **(c)** the vacuum bagging process for the manufacturing of the TEG-enabled CFRP, followed by thermopressing and curing / post-curing, as well as the cartoon of the TEG-enabled CFRP with a $[0/90]_{2s}$ symmetric configuration, **(d)** the final TEG-enabled CFRP and demonstration of an in-plane temperature difference (ΔT) [51].

The CFRP TEG device yielded a total voltage output of 19.56 mV and a total maximum electrical power output of 0.87 μW, upon being exposed to a temperature difference of 75 K [51].

Table 1. Simulation derived and experimental open circuit voltages (V_{oc}) and maximum output of electrical power (P_{max}) of the TEG-enabled CFRP at ΔT of 35, 55 and 75 K [51].

Temperature difference (ΔT)	V_{oc} simul. (mV)	P_{max} simul. (μW)	V_{oc} exper. (mV)	P_{max} exper. (μW)
35	11.83	0.32	10.19	0.24
55	18.60	0.79	14.44	0.47
75	25.36	1.46	19.56	0.87

It should be highlighted that the structural TEG-enabled CFRP fabricated in this study opens the route towards structural TEGs with increased total voltage and power outputs, as well as the realization of in-field applications and practical utilization of the TEG harvested energy. In order to realize a structural TEG that can power practical low power electronics, at least 20 mV should be generated. This value arises from the fact that the voltage output should be generally enhanced via a voltage step-up converter and further stored in a supercapacitor. Commercially available highly integrated DC/DC step-up converters with no additional power requirements, *e.g.*, the LTC3108 (Linear Tech.) operate at inputs of at least 20 mV to give an output voltage of 2.2 V or even higher. Wei *et. al.* [52] powered a light-emitting diode (LED) via a polymer based TEG containing 300 pieces of parallel connected thermocouples (10 in parallel, 30 in series) generating a maximum power output of ~50 μW with an open circuit voltage higher than 40 mV. Utilizing structural laminate composites as TEGs with a voltage output of 20-50 mV, with or without a step-up boost converter driving the DC voltage produced in a capacitor, could enable the powering of low-consumption electronic devices integrated in aeronautics, aerospace or automotive. *e.g.* ultra-low power microcontrollers, WSNs, *etc.* [53]. When the TEG produces voltage outputs greater than 100 mV, more sophisticated devices in the new era of Internet of Things (IoT) applications could be powered [54]. Furthermore, except for the purpose of energy harvesting, the TEG devices can also function as self-powered temperature sensors [55].

It could be envisaged that the TEG-enabled FRP structural materials could allow the thermal energy harvesting from structural parts *i.e.*, structural parts in automotive chassis close to the exhaust or structural TEG-enabled FRP bonnet harvesting thermal energy “through-thickness” in aeronautics parts exposed to ΔT *e.g.* parts of the fuselage, *etc*.. The harvested energy in such parts could be used then for the SHM of structures decreasing maintenance costs, while improving safety. Also, structural TEGs may enable large-scale thermal energy harvesting, because of the large areas of structural materials where temperature gradients exist. The generation of thermoelectricity using structural engineering materials that can routinely be exposed to high temperatures will represent a breakthrough in multifunctional materials rendering them an attractive technology for future zero energy consumption structures. It could be envisaged that TEG-enabled innovative structural composites will contribute to *i)* the protection of the environment due to the reduction of conventional fuels usage, *ii)* strengthen the interfaces between the energy and transport, transmission and distribution systems and *iii)* promote synergies with the energy / ICT sectors. The further development of innovative structures based on nanotechnology advances can promote the conversion rate to achieve high efficiency, flexibility and conformability in the field of machine condition monitoring. The future of nanotechnology is likely to focus on the areas of integrating individual nanodevices that acts like living specie with sensing, communicating, controlling and responding. A nano system requires a nano-power source to make the entire package extremely small and high performance. The ultimate goal is to establish self-powered nano systems that can operate wirelessly, independently and sustainably. The self-powering approach is a new paradigm for truly achieving self-sufficient systems, which are of critical importance for sensing, medical science, infrastructure / environmental monitoring, defense technology and even personal electronics.

References

1. Zhang, H.; Xing, F.; Cui, H.Z.; Chen, D.Z.; Ouyang, X.; Xu, S.Z.; Wang, J.X.; Huang, Y.T.; Zuo, J.D.; Tang, J.N. A novel phase-change cement composite for thermal energy storage: Fabrication, thermal and mechanical properties. *Appl. Energy* **2016**, *170*, 130–139, doi:10.1016/j.apenergy.2016.02.091.
2. He, W.; Zhang, G.; Zhang, X.; Ji, J.; Li, G.; Zhao, X. Recent development and application of thermoelectric generator and cooler. *Appl. Energy* **2015**, *143*, 1–25, doi:10.1016/j.apenergy.2014.12.075.
3. Oliveira, R.P.; Singh, N.R.; Ribeiro, F.; Delgass, W.N.; Agrawal, R. Sustainable fuel for the Brazilian transportation sector. *AIChE Annu. Meet. Conf. Proc.* **2008**, *2007*.
4. EPSRC Thermoelectric Network UK Thermoelectric Roadmap. Energy Harvesting From Waste Heat. *EPSRC Thermoelectr. Netw. UK* **2018**, 1–69.
5. Dresselhaus Alternative energy technologies M. **2001**, *414*.
6. Vineis, C.J.; Shakouri, A.; Majumdar, A.; Kanatzidis, M.G. Nanostructured thermoelectrics: Big efficiency gains from small features. *Adv. Mater.* **2010**, *22*, 3970–3980, doi:10.1002/adma.201000839.
7. Boukai, A.I.; Bunimovich, Y.; Tahir-Kheli, J.; Yu, J.K.; Goddard, W.A.; Heath, J.R. Silicon nanowires as efficient thermoelectric materials. *Nature* **2008**, *451*, 168–171,

doi:10.1038/nature06458.

8. Cowen, L.M.; Atoyo, J.; Carnie, M.J.; Baran, D.; Schroeder, B.C. Review—Organic Materials for Thermoelectric Energy Generation. *ECS J. Solid State Sci. Technol.* **2017**, *6*, N3080–N3088, doi:10.1149/2.0121703jss.

9. Madan, D.; Wang, Z.; Chen, A.; Juang, R.C.; Keist, J.; Wright, P.K.; Evans, J.W. Enhanced performance of dispenser printed MA n-type Bi2Te 3 composite thermoelectric generators. *ACS Appl. Mater. Interfaces* **2012**, *4*, 6117–6124, doi:10.1021/am301759a.

10. Ge, Z.H.; Qin, P.; He, D.; Chong, X.; Feng, D.; Ji, Y.H.; Feng, J.; He, J. Highly Enhanced Thermoelectric Properties of Bi/Bi2S3 Nanocomposites. *ACS Appl. Mater. Interfaces* **2017**, *9*, 4828–4834, doi:10.1021/acsami.6b14803.

11. Liang, D.; Yang, H.; Finefrock, S.W.; Wu, Y. Flexible Nanocrystal-Coated Glass Fibers for High-Performance Thermoelectric Energy Harvesting. **2012**, 8–13.

12. Chang, Y.; Guo, J.; Tang, Y.Q.; Zhang, Y.X.; Feng, J.; Ge, Z.H. Facile synthesis of Ag2Te nanowires and thermoelectric properties of Ag2Te polycrystals sintered by spark plasma sintering. *CrystEngComm* **2019**, *21*, 1718–1727, doi:10.1039/c8ce01863d.

13. Martín-González, M.; Caballero-Calero, O.; Díaz-Chao, P. Nanoengineering thermoelectrics for 21st century: Energy harvesting and other trends in the field. *Renew. Sustain. Energy Rev.* **2013**, *24*, 288–305, doi:10.1016/j.rser.2013.03.008.

14. Lan, S.; Yang, Z.; Stobart, R.; Chen, R. Prediction of the fuel economy potential for a skutterudite thermoelectric generator in light-duty vehicle applications. *Appl. Energy* **2018**, *231*, 68–79, doi:10.1016/j.apenergy.2018.09.087.

15. Elefsiniotis, A.; Kokorakis, N.; Becker, T.; Schmid, U. A thermoelectric-based energy harvesting module with extended operational temperature range for powering autonomous wireless sensor nodes in aircraft. *Sensors Actuators, A Phys.* **2014**, *206*, 159–164, doi:10.1016/j.sna.2013.11.036.

16. Tahami, S.A.; Gholikhani, M.; Nasouri, R.; Dessouky, S.; Papagiannakis, A.T. Developing a new thermoelectric approach for energy harvesting from asphalt pavements. *Appl. Energy* **2019**, *238*, 786–795, doi:10.1016/j.apenergy.2019.01.152.

17. Hsu, C.T.; Huang, G.Y.; Chu, H.S.; Yu, B.; Yao, D.J. An effective Seebeck coefficient obtained by experimental results of a thermoelectric generator module. *Appl. Energy* **2011**, *88*, 5173–5179, doi:10.1016/j.apenergy.2011.07.033.

18. Suarez, F.; Parekh, D.P.; Ladd, C.; Vashaee, D.; Dickey, M.D.; Öztürk, M.C. Flexible thermoelectric generator using bulk legs and liquid metal interconnects for wearable electronics. *Appl. Energy* **2017**, *202*, 736–745, doi:10.1016/j.apenergy.2017.05.181.

19. Hyland, M.; Hunter, H.; Liu, J.; Veety, E.; Vashaee, D. Wearable thermoelectric generators for human body heat harvesting. *Appl. Energy* **2016**, *182*, 518–524, doi:10.1016/j.apenergy.2016.08.150.

20. Moriarty, G.P.; Wheeler, J.N.; Yu, C.; Grunlan, J.C. Increasing the thermoelectric power factor of polymer composites using a semiconducting stabilizer for carbon nanotubes. *Carbon N. Y.* **2012**, *50*, 885–895, doi:10.1016/j.carbon.2011.09.050.

21. Madan, D.; Wang, Z.; Wright, P.K.; Evans, J.W. Printed flexible thermoelectric generators for use on low levels of waste heat. *Appl. Energy* **2015**, *156*, 587–592, doi:10.1016/j.apenergy.2015.07.066.

22. Lu, Z.; Zhang, H.; Mao, C.; Li, C.M. Silk fabric-based wearable thermoelectric generator for energy harvesting from the human body. *Appl. Energy* **2016**, *164*, 57–63, doi:10.1016/j.apenergy.2015.11.038.

23. Tzounis, L.; Hegde, M.; Liebscher, M.; Dingemans, T.; Pötschke, P.; Paipetis, A.S.; Zafeiropoulos, N.E.; Stamm, M. All-aromatic SWCNT-Polyetherimide nanocomposites for thermal energy harvesting applications. *Compos. Sci. Technol.* **2018**, *156*, 158–165, doi:10.1016/J.COMPSCITECH.2017.12.030.

24. Snyder, G.J.; Toberer, E.S. 1. Complex thermoelectric materials. *Nat Mater* **2008**, *7*, 105–114,

doi:10.1038/nmat2090.

25. Terrones, M. Science and Technology of the Twenty-First Century: Synthesis, Properties, and Applications of Carbon Nanotubes. *Annu. Rev. Mater. Res.* **2003**, *33*, 419–501, doi:10.1146/annurev.matsci.33.012802.100255.

26. Nakai, Y.; Honda, K.; Yanagi, K.; Kataura, H.; Kato, T.; Yamamoto, T.; Maniwa, Y. Giant Seebeck coefficient in semiconducting single-wall carbon nanotube film. *Appl. Phys. Express* **2014**, *7*, doi:10.7567/APEX.7.025103.

27. Nonoguchi, Y.; Ohashi, K.; Kanazawa, R.; Ashiba, K.; Hata, K.; Nakagawa, T.; Adachi, C.; Tanase, T.; Kawai, T. Systematic conversion of single walled carbon nanotubes into n-type thermoelectric materials by molecular dopants. *Sci. Rep.* **2013**, *3*, 1–7, doi:10.1038/srep03344.

28. Dörling, B.; Sandoval, S.; Kankla, P.; Fuertes, A.; Tobias, G.; Campoy-Quiles, M. Exploring different doping mechanisms in thermoelectric polymer/carbon nanotube composites. *Synth. Met.* **2017**, *225*, 70–75, doi:10.1016/j.synthmet.2017.01.002.

29. Wen, N.; Fan, Z.; Yang, S.; Zhao, Y.; Cong, T.; Xu, S.; Zhang, H.; Wang, J.; Huang, H.; Li, C.; et al. Highly conductive, ultra-flexible and continuously processable PEDOT:PSS fibers with high thermoelectric properties for wearable energy harvesting. *Nano Energy* **2020**, *78*, 105361, doi:10.1016/j.nanoen.2020.105361.

30. Tomlinson, E.P.; Mukherjee, S.; Boudouris, B.W. Enhancing polymer thermoelectric performance using radical dopants. *Org. Electron. physics, Mater. Appl.* **2017**, *51*, 243–248, doi:10.1016/j.orgel.2017.09.029.

31. Jin Bae, E.; Hun Kang, Y.; Jang, K.S.; Yun Cho, S. Enhancement of Thermoelectric Properties of PEDOT:PSS and Tellurium-PEDOT:PSS Hybrid Composites by Simple Chemical Treatment. *Sci. Rep.* **2016**, *6*, 1–10, doi:10.1038/srep18805.

32. Zaia, E.W.; Sahu, A.; Zhou, P.; Gordon, M.P.; Forster, J.D.; Aloni, S.; Liu, Y.S.; Guo, J.; Urban, J.J. Carrier Scattering at Alloy Nanointerfaces Enhances Power Factor in PEDOT:PSS Hybrid Thermoelectrics. *Nano Lett.* **2016**, *16*, 3352–3359, doi:10.1021/acs.nanolett.6b01009.

33. Rogdakis, K.; Karakostas, N.; Kymakis, E. Up-scalable emerging energy conversion technologies enabled by 2D materials: from miniature power harvesters towards grid-connected energy systems. *Energy Environ. Sci.* **2021**, doi:10.1039/d0ee04013d.

34. Lee, J.K.; An, K.W.; Ju, J.B.; Cho, B.W.; Cho, W. Il; Park, D.; Yun, K.S. Electrochemical properties of PAN-based carbon fibers as anodes for rechargeable lithium ion batteries. *Carbon N. Y.* **2001**, *39*, 1299–1305, doi:10.1016/S0008-6223(00)00237-2.

35. Xu, Z.; Gao, C. Graphene fiber: A new trend in carbon fibers. *Mater. Today* **2015**, *18*, 480–492, doi:10.1016/j.mattod.2015.06.009.

36. Zhou, G.; Liu, Y.; He, L.; Guo, Q.; Ye, H. Microstructure difference between core and skin of T700 carbon fibers in heat-treated carbon/carbon composites. *Carbon N. Y.* **2011**, *49*, 2883–2892, doi:10.1016/j.carbon.2011.02.025.

37. De Luca, F.; Clancy, A.J.; Carrero, N.R.; Anthony, D.B.; De Luca, H.G.; Shaffer, M.S.P.; Bismarck, A. Increasing carbon fiber composite strength with a nanostructured “brick-and-mortar” interphase. *Mater. Horizons* **2018**, *5*, 668–674, doi:10.1039/c7mh00917h.

38. Tsirka, K.; Tzounis, L.; Avgeropoulos, A.; Liebscher, M.; Mechtcherine, V.; Paipetis, A.S. Optimal synergy between micro and nano scale: Hierarchical all carbon composite fibers for enhanced stiffness, interfacial shear strength and Raman strain sensing. *Compos. Sci. Technol.* **2018**, *165*, 240–249, doi:10.1016/j.compscitech.2018.07.003.

39. Zhuang, R.C.; Doan, T.T.L.; Liu, J.W.; Zhang, J.; Gao, S.L.; Mäder, E. Multi-functional multi-walled carbon nanotube-jute fibres and composites. *Carbon N. Y.* **2011**, *49*, 2683–2692, doi:10.1016/j.carbon.2011.02.057.

40. Chakravarthi, D.K.; Khabashesku, V.N.; Vaidyanathan, R.; Blaine, J.; Yarlagadda, S.; Roseman, D.;

Zeng, Q.; Barrera, E. V. Carbon fiber-bismaleimide composites filled with nickel-coated single-walled carbon nanotubes for lightning-strike protection. *Adv. Funct. Mater.* **2011**, *21*, 2527–2533, doi:10.1002/adfm.201002442.

41. Senokos, E.; Ou, Y.; Torres, J.J.; Sket, F.; González, C.; Marcilla, R.; Vilatela, J.J. Energy storage in structural composites by introducing CNT fiber/polymer electrolyte interleaves. *Sci. Rep.* **2018**, *8*, 1–10, doi:10.1038/s41598-018-21829-5.

42. Pozegic, T.R.; Hamerton, I.; Anguita, J. V.; Tang, W.; Ballocchi, P.; Jenkins, P.; Silva, S.R.P. Low temperature growth of carbon nanotubes on carbon fibre to create a highly networked fuzzy fibre reinforced composite with superior electrical conductivity. *Carbon N. Y.* **2014**, *74*, 319–328, doi:10.1016/j.carbon.2014.03.038.

43. Pozegic, T.R.; Anguita, J. V; Hamerton, I.; Jayawardena, K.D.G.I.; Chen, J.; Stolojan, V. Multi-Functional Carbon Fibre Composites using Carbon Nanotubes as an Alternative to Polymer Sizing. *Nat. Publ. Gr.* **2016**, 1–11, doi:10.1038/srep37334.

44. Kim, M.; Sung, D.H.; Kong, K.; Kim, N.; Kim, B.J.; Park, H.W.; Park, Y. Bin; Jung, M.; Lee, S.H.; Kim, S.G. Characterization of resistive heating and thermoelectric behavior of discontinuous carbon fiber-epoxy composites. *Compos. Part B Eng.* **2016**, *90*, 37–44, doi:10.1016/j.compositesb.2015.11.037.

45. Micheli, D.; Vricella, A.; Pastore, R.; Delfini, A.; Giusti, A.; Albano, M.; Marchetti, M.; Moglie, F.; Primiani, V.M. Ballistic and electromagnetic shielding behaviour of multifunctional Kevlar fiber reinforced epoxy composites modified by carbon nanotubes. *Carbon N. Y.* **2016**, *104*, 141–156, doi:10.1016/j.carbon.2016.03.059.

46. Han, S.; Chung, D.D.L. Through-thickness thermoelectric power of a carbon fiber/epoxy composite and decoupled contributions from a lamina and an interlaminar interface. *Carbon N. Y.* **2013**, *52*, 30–39, doi:10.1016/j.carbon.2012.08.071.

47. Narita, F.; Nagaoka, H.; Wang, Z. Fabrication and impact output voltage characteristics of carbon fiber reinforced polymer composites with lead-free piezoelectric nano-particles. *Mater. Lett.* **2019**, *236*, 487–490, doi:10.1016/j.matlet.2018.10.174.

48. Deng, Y.; Gao, S.; Liu, J.; Gohs, U.; Mäder, E.; Heinrich, G. Variable structural colouration of composite interphases. *Mater. Horizons* **2017**, *4*, 389–395, doi:10.1039/c6mh00559d.

49. Liebscher, M.; Petra, P.; Voit, B.; Heinrich, G.; Stamm, M. Influence of a cyclic butylene terephthalate oligomer on the processability and thermoelectric properties of polycarbonate / MWCNT nanocomposites. **2014**, *55*, 5381–5388, doi:10.1016/j.polymer.2014.08.048.

50. Saq'an, S.; Zihlif, A.M.; Al-Ani, S.R.; Ragosta, G. Thermoelectric power and AC electrical properties of PAN-based carbon fiber composites. *J. Mater. Sci. Mater. Electron.* **2008**, *19*, 1079–1085, doi:10.1007/s10854-007-9470-7.

51. Karalis, G.; Tzounis, L.; Lambrou, E.; Gergidis, L.N.; Paipetis, A.S. A carbon fiber thermoelectric generator integrated as a lamina within an 8-ply laminate epoxy composite: Efficient thermal energy harvesting by advanced structural materials. *Appl. Energy* **2019**, *253*, doi:10.1016/j.apenergy.2019.113512.

52. Wei, Q.; Mukaida, M.; Kirihara, K.; Naitoh, Y.; Ishida, T. Polymer thermoelectric modules screen-printed on paper. *RSC Adv.* **2014**, *4*, 28802–28806, doi:10.1039/c4ra04946b.

53. Samson, D.; Otterpohl, T.; Kluge, M.; Schmid, U.; Becker, T. Aircraft-specific thermoelectric generator module. *J. Electron. Mater.* **2010**, *39*, 2092–2095, doi:10.1007/s11664-009-0997-7.

54. Lu, X.; Yang, S.H. Thermal energy harvesting for WSNs. *Conf. Proc. - IEEE Int. Conf. Syst. Man Cybern.* **2010**, 3045–3052, doi:10.1109/ICSMC.2010.5641673.

55. Shi, Y.; Wang, Y.; Deng, Y.; Gao, H.; Lin, Z.; Zhu, W.; Ye, H. A novel self-powered wireless temperature sensor based on thermoelectric generators. *Energy Convers. Manag.* **2014**, *80*, 110–116, doi:10.1016/j.enconman.2014.01.010.

Chapter 2

Development of functional nanoparticle-based inks for printed electronic devices

---

The results included in **Chapter 2** have been published at the *Applied Energy* peer-reviewed scientific journal as part of the study "A high performance flexible and robust printed thermoelectric generator based on hybridized Te nanowires with PEDOT:PSS" and can be found under *https://doi.org/10.1016/j.apenergy.2021.117004*.

2. Development of functional nanoparticle-based inks for printed electronic devices

2.1 A high performance flexible and robust printed thermoelectric generator based on hybridized Te nanowires with PEDOT:PSS

Abstract

In this work, we demonstrate a water-based scalable synthetic method of Te nanowires (NWs) and formulation of hybrid thermoelectric (TE) inks utilizing poly(3,4-ethylenedioxythiophene) polystyrene sulfonate (PEDOT:PSS), towards the fabrication of high performance and flexible printed thermoelectric generators (TEGs). X-Ray diffraction (XRD) and Raman spectra confirm the high crystallinity of Te NWs nanocrystals with hexagonal lattice. Scanning Electron Microscopy (SEM) and Transmission Electron Microscopy (TEM) illustrated the microstructural features of the produced nanostructures, as well as the monocrystalline nature of the synthesized Te NWs. Hall-effect measurements determined the carrier density and mobility of Te NWs and their hybrid materials. According to the thermoelectric response and best power factor (*PF*) of the hybrid inks measured in solid-state of pre-fabricated films (max. PF = 102.42 μW/m · K^2), a flexible TEG has been fabricated with a power output (P_{out}) of ~4.5 μW upon being exposed to ΔT = 100 K. The fabricated TEG demonstrated herein can be produced in a continuous and scalable roll-to-roll (R2R) printing process using *i.e.,* slot die, gravure, *etc*. printing technologies towards the realization of large-scale flexible TEG production and future large scale thermal energy harvesting by printed TEG devices.

Keywords: Hybrid thermoelectric materials; Inorganic-organic hybrids; Solvothermal reaction-synthesis; Energy filtering; Seebeck effect; Thermal energy harvesting; Printed thermoelectric generators (TEGs); Flexible TEGs

Highlights:

- Aqueous-green and ambient synthesis of TeNW@PEDOT:PSS core@shell hybrids
- TE hybrid ink with optimum energy filtering effect
- Low temperature sintering-annealing process of the hybrid thermoelectric films
- 102.42 μW/m · K^2 max. power factor of the flexible hybrid film
- Flexible TEG device with ~4.5 μW max. power output and 2.57 W/m^2 power density

Graphical Abstract

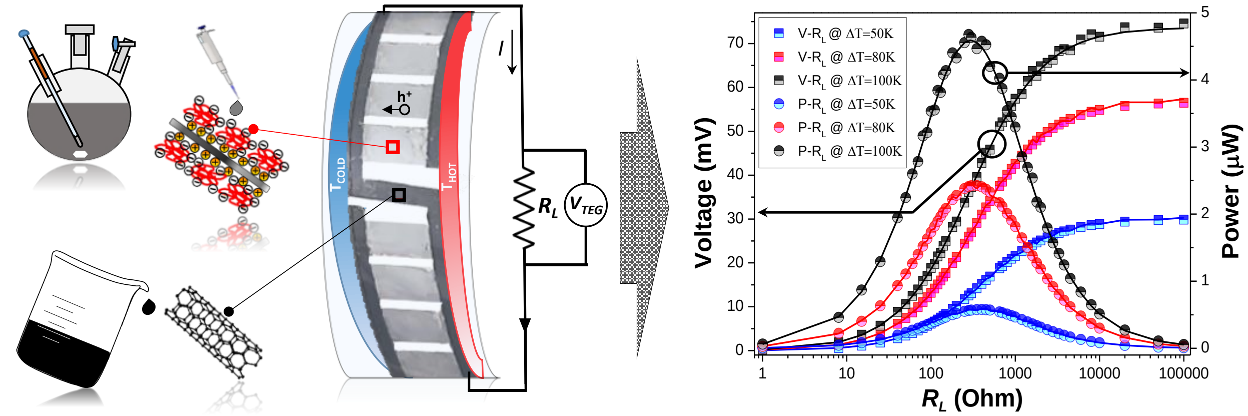

2.1.1 Introduction

The ubiquitous energy from waste heat provides a huge motivation for energy harvesting via the development of new and efficient thermoelectric (TE) power generating materials [1]. The ability of the TE material to generate voltage upon being exposed to a temperature difference is known as the "Seebeck effect". The TE material performance is evaluated by the dimensionless figure of merit *ZT*, determined as $ZT = (\sigma \cdot S^2) \cdot T/\kappa$, where σ presents the electrical conductivity, S the Seebeck coefficient, T the absolute temperature and κ the thermal conductivity. The power factor ($PF = \sigma \cdot S^2$) is also used as a TE performance indicator since it is directly related to the produced power. In order to achieve high TE performance, a combination of high σ and S with as low as possible κ is desirable [1–3].

Conventional high performance inorganic TE materials face some limitation issues corelated with high cost, brittleness and toxicity. In most bulk inorganic conventional thermoelectric materials, the increase of Seebeck coefficient (S) may result in the decrease of electrical conductivity (σ) and vice versa [3]. For inorganic materials, this antagonistic relation limits the degree to which improvements can be made to the power factor and as a result poses a fundamental challenge in improving *ZT* [4].

Inorganic and organic thermoelectric (TE) materials are within the focus of scientific interest during the last decade, due to their ability to directly convert the thermal energy to electricity. Organic materials, such as conductive polymers, are potential candidates due to their low thermal conductivity, which however is usually followed by poor thermoelectric performance [5–8].

The hybrid approach relates on the proper combination of organic and inorganic materials. As the organic part may pertain flexibility to the structure, the potential application range for efficient thermoelectric coatings is substantially enriched. Therefore, it is very often preferred by the research community [9,10]. Recent studies suggest that the improvement of the Seebeck coefficient of organic-based materials is feasible by adding inorganic nanomaterials with high Seebeck coefficient. Tellurium-based (Te-based) alloys, such as PbTe [4,11] have shown superior *ZT* values near room temperature as they combine high Seebeck voltage with low thermal conductivity. Nanocrystals have already been proved to offer substantially higher thermoelectric performance and further improvements are expected to arise from targeted architectural design of nanograins and their interfaces [12]. As is reported, it is possible to simultaneously increase the electrical conductance and thermopower at the organic–inorganic interface, mainly by tuning the scattering mechanisms [13]. Nanostructuring of various alloys may also lead to significant improvement in *ZT* values, mainly because it significantly reduces lattice thermal conductivity [3]. Low-dimensional materials, such as nanowires and nanorods, may possibly decouple electrical conductance and heat transport by suppressing phonon propagation because of their short mean free path [9,14]. As a result, the thermal conductivity of low-dimensional materials can be significantly lower than that of bulk without negatively affecting the electrical conductivity.

PEDOT:PSS is one of the most researched commercially used conjugated polymer due to its good electrical conductivity (σ) and environmental stability. Although its Seebeck coefficient (S) is relatively low compared to inorganic counterparts and its applications are limited to a lower temperature (T) range, it is relatively low-cost, lightweight, non-toxic and easily processable with inherently low thermal conductivity (κ) [15,16]. More specifically, nanocomposites made of PEDOT:PSS and tellurium nanowires exhibit a low out-of-plane thermal conductivity *i.e.* not more than 0.3 W/m · K, which is somewhat lower than the bulk thermal conductivity of tellurium, *i.e.* 2 W/m · K. The high interfacial area between tellurium nanowires and PEDOT:PSS may lead to phonon scattering, which reduces the thermal conductivity [17–20]. A characteristic example which is extensively studied in the recent years is the Te nanowires hybrid nanocomposite systems. For instance, See *et al.* have explored the use of tellurium nanowires as an inorganic filler material [9]. The in situ growth of nanowires was carried out in the presence of PEDOT:PSS, which resulted in stable aqueous dispersions. These could be used to drop-cast and spin-coat thin films with a tellurium content of ca. 85 %. Nanowires were coated by PEDOT:PSS, which enhanced their oxidation resistance in air and improved electrical contact. An in-plane Seebeck coefficient of +163 μV/K led to a power factor of 71 μW/m · K^2, which was higher than power factors obtained individually for neat PEDOT:PSS and tellurium nanowires respectively. This behavior could be described using a 3-component series model consisting of *i)* the polymer matrix, *ii)* the tellurium nanowire filler and *iii)* an interfacial layer. Carrier transport was found to occur predominantly within this PEDOT:PSS interfacial layer. The authors proposed a mechanism whereby the

PEDOT:PSS coating displayed a higher electrical conductivity because of a templating effect that impacts the nanostructure of the polymer complex or energy filtering due to scattering of low energy charge carriers [12].

Waste heat harvesting is also a major challenge both in transport and industry sectors. Furthermore, the increasing demand for self-powered micro-sensors in industry, has driven the focus to flexible power-conversion devices which in their turn are expected to dominate the micro-TEG fabrication market. Commercial TEGs are generally used in niche applications and require power in the range of 1 μW to 100 W [21,22].

Recently, many research groups focus on flexible TEG modules fabrication due to their great potential for new markets related to self-powered wearables and low energy consumption electronics [23,24]. Candidate heat sources include the human body, power stations, heating systems, motor vehicles *etc.*. As these sources may have arbitrary shapes, a flexible and efficient TEG module is necessary for practical applications. Based on real case scenarios, research on the application of flexible TEGs has also been performed for various sectors of structural materials large-scale thermal energy harvesting [25–27].

A prerequisite for the flexible TEG technology to be competitive is high efficiency when coupled with low-power consuming electronics. The incorporation of TEG powered wireless technologies is also particularly challenging. Whereas most wireless sensors are designed to last 15 years or even more, batteries limit this autonomy to a few years. At the same time, in industrial applications battery replacement is often difficult and costly primarily due downtime as well as access restrictions often encountered in chemical facilities, power plants (including nuclear), military facilities or secure data centers. Current intelligent sensors require only a few hundred microwatts or a few milliwatts to operate posing them within the achievable power range for TEGs. As should be noted at this stage, powering these devices from the TEG power output requires compliance to specifications posed by commercially available step-up boost converters [28,29]. As a result, micro generators producing a few microwatts are needed to power these micro-devices rendering them autonomous. In industrial environments heat sources are abundant *e.g.* hot fluid pipes, ovens, steam lines, motors, air conditioning, heating *etc.*. In these harsh environments, TEGs present an ideal solution for waste heat harvesting, particularly when combined with minimum maintenance and high efficiency. Very small TEGs (a few square millimeters) are a solution to power these sensors permanently [30,31].

This study reports the synthesis and formulation process of an efficient TE hybrid ink with tuned transport properties for coating applications with a view to the production of high efficiency flexible

TEGs. Te NWs were synthesized in aqueous solution medium and characterized. The water-dispersed nanoparticles were subsequently employed for various formulations via hybridization of the TE ink with different ratios of PEDOT:PSS, resulting in an efficient TE nanomaterial with a power factor of 102.42 μW/m · K^2 and *ZT* of 0.2. The Drude model validated theoretically the enhanced carrier filtering properties. Finally, an efficient flexible TEG device was fabricated a with ~4.5 μW electrical power output and a respective power density of 2.57 W/m^2 at Δ*T* of 100 K. To our knowledge it is the first time that a highly conductive SWCNT-based ink was successfully implemented and extensively tested for efficiency and durability for all device interconnections, replacing conventional Ag metallic ones.

2.1.2 Experimental section

2.1.2.1 Materials

Sodium tellurite (Na_2TeO_3, ~100 mesh, >99 % purity, L-Ascorbic acid (reagent grade with 99 % purity), cetyltrimethylammonium bromide (CTAB, ≥98 %, Sigma), Poly(3,4-ethylenedioxythiophene)-poly(styrenesulfonate) – PEDOT:PSS highly conductive grade (Orgacon™ ICP 1050 Agfa, 1.1 wt. % in H_2O) from Sigma Aldrich were employed for this study. Silver paste consisting of Ag flakes and a thermoplastic binder suitable for achieving highly conductive metallic contacts after drying at room temperature for 24 h was procured from Agar scientific (Germany). All chemicals were analytical grade and used as received without further purification. Double distilled water (d-H_2O) was used throughout all the different processes in this work.

2.1.2.2 Synthesis of Te NWs and TeNW@PEDOT:PSS hybrids

Prior to use, all glassware were cleaned with a 3:1 v/v acidic solution consisting of hydrochloric / nitric acid (36 % and 68 %, respectively) and then rinsed with copious d-H_2O. Te NWs were synthesized following a surfactant-assisted chemical reduction solvothermal protocol as previously reported in literature with several variations [32–34]. In brief, d-H_2O (200 mL) and 4.93 g L-ascorbic acid (155.9 mM) as reducing agent and 0.1 g CTAB (1.37 mM) as surfactant-capping-nucleation and shape promoting / structure-directing agent were added in a spherical bottom flask. Vigorous stirring for 1 h led to the production of a clear solution. Subsequently, 0.277 g Na_2TeO_3 (6.25 mM) were added and stirred for 30 min to allow the full dissociation of the Te NWs precursor. The obtained white suspension was heated in an oil bath at 90 °C and maintained at this temperature for 24 h so as to complete the reduction reaction. Afterwards, the solution was let to cool down naturally till room temperature. The resulting CTAB surface modified Te NWs were centrifuged at 9000 rpm for 1 h, the supernatant was removed and the precipitate was redispersed in 500 mL d-H_2O. Eventually, the Te NWs were collected as a filter cake (denoted as Te NWs "bucky-paper") using a vacuum filtration apparatus and a PVDF filter membrane (47 mm diameter and 0.4 μm pore size). The Te NWs bucky-paper was peeled-off from the support membrane and dried overnight under vacuum at 60 °C. It should be mentioned that the above protocol resulted into 0.168 ± 0.05 g of Te NWs, *i.e.*, a reaction yield of ~60.6 % from the Na_2TeO_3 (0.277 g) precursor.

Three types of Te NWs / PEDOT:PSS hybrids of an inorganic / organic core@shell structure were prepared employing an electrostatic interaction between the positively charged CTAB stabilized Te NWs and the negatively charged PEDOT:PSS micelle-based water suspension. More specifically, dried Te NWs were dispersed in 100 mL of d-H_2O using an ultrasonic bath for 10 min at a concentration of 25 mg/mL (H0). PEDOT:PSS was added dropwise at three different mass ratios in relation to the Te NWs solid content within the 100 ml dispersion (1:2, 1:1 and 2:1) and kept under stirring for 24 h. This resulted in three different TeNW@PEDOT:PSS formulations, hereafter referred to as H1: TeNW@PEDOT:PSS at 1:2 w/w (rich in PEDOT:PSS conductive organic phase), H2: TeNW@PEDOT:PSS at 1:1 w/w (equal amounts of Te NWs solid content and PEDOT:PSS solution) and H3: TeNW@PEDOT:PSS at 2:1 w/w (rich in Te NWs). The three different hybrid inks were used to fabricate thermoelectric films in order to select the optimal thermoelectric performance in terms of power factor (*PF*) to fabricate printed flexible thermoelectric generators.

Figure 19 illustrates the steps followed for the synthesis of TeNW@PEDOT:PSS hybrid inks and high quality films. The following processes are depicted in sequence: the water-based "green" solvothermal sol-gel reaction (**Figure 19a**), the cleaning process followed to acquire Te NWs in a bucky-paper form via vacuum filtration (**Figure 19b**), redispersion of Te NWs in d-H_2O at 25 mg/mL (**Figure 19c**, H0), the hybridization using PEDOT:PSS (**Figure 19d**) and the resulting H1, H2 and H3 thermoelectric inks (**Figure 19e** – note that images of inks were taken two weeks after preparation). The inks were subsequently casted on glass slides for electrical and thermoelectric studies (**Figure 19f**). Silver paste (Ag-paste) was employed to achieve electrical continuity for the thermoelectric measurements. Prior to film fabrication via drop-casting, the glass substrates were cleaned with a basic piranha solution consisting of NH_4OH / H_2O_2 / d-H_2O (1:1:1 in volume, respectively) for 2 h at 65 °C, while N_2 blowing was used for drying the substrates before ink deposition.

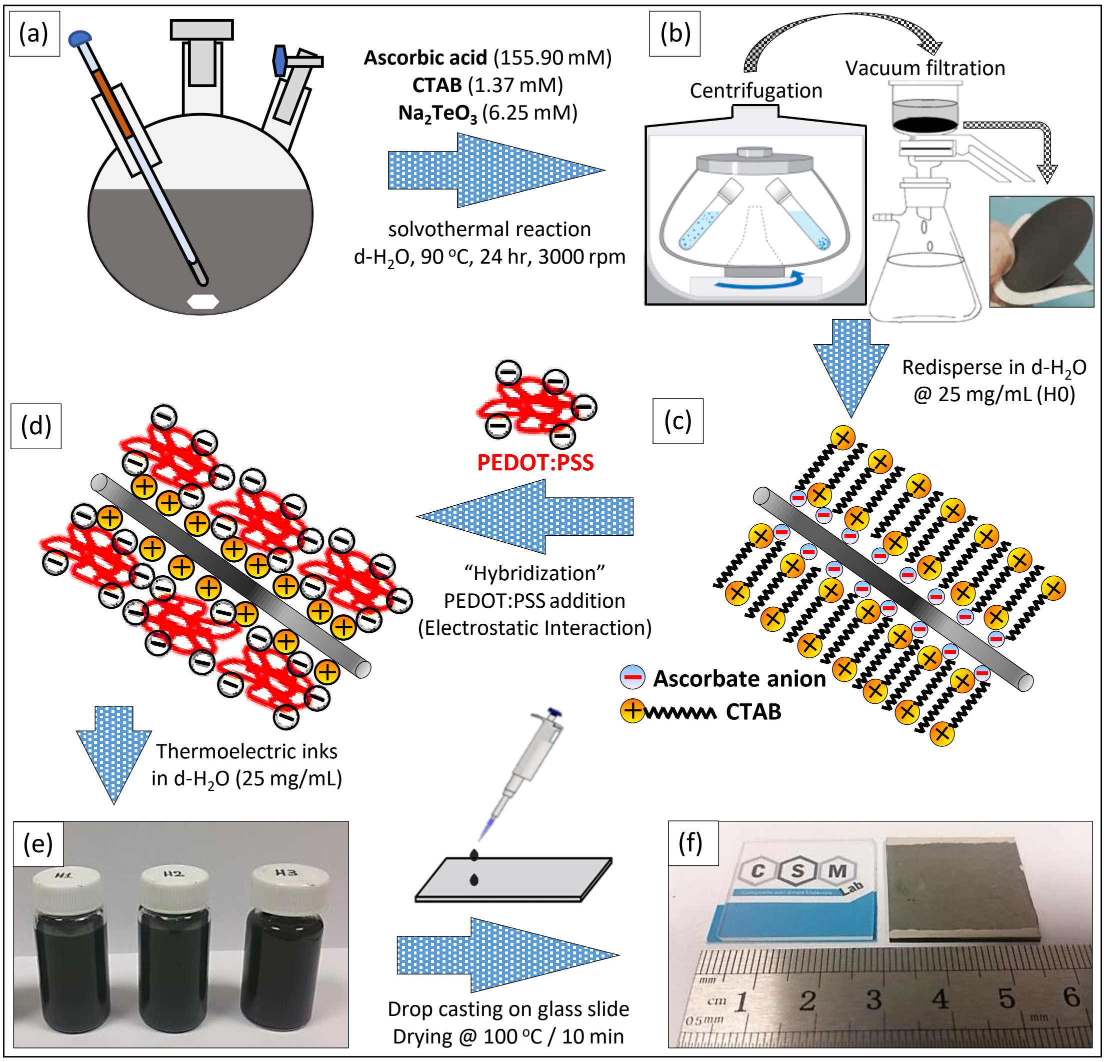

Figure 19. Illustration of the steps followed to synthesize TeNW@PEDOT:PSS hybrid inks and films, **(a)** the water-based "green" solvothermal sol-gel reaction, **(b)** the cleaning process to obtain Te NWs in a bucky-paper, **(c)** Te NWs in d-H_2O at 25 mg/mL (H0), **(d)** hybridization with PEDOT:PSS and **(e)** the obtained H1, H2 and H3 hybrid thermoelectric inks, **(f)** a representative high quality and uniform thermoelectric film deposited on a glass slide, utilized for the electric and thermoelectric investigations.

2.1.2.3 *Characterization techniques*

A Labram HR-Horiba scientific micro-Raman system was used in order to verify the crystallinity of Te NWs in the form of bucky-paper films. The 514.5 nm line of an Ar^+ ion laser operating at a laser power of 1 mW at the focal plane was employed for the Raman excitation. An optical microscope equipped with a 100× objective served both for the delivery of the excitation light and the collection of the back-scattering Raman activity. Raman activity was monitored in the range of 90-3500 cm^{-1}.

X-ray diffractometry (XRD) was performed with an X-Ray diffractometer (XRD Bruker D8 ADVANCE) in symmetric step-scan mode with $\Delta 2\theta = 0.05°$ in transmission mode. The diffractometer operated at 40 KV and 30 mA with Kα radiation ($\lambda = 1.5406$ Å), diffraction angle (θ, $10° < 2\theta < 80°$), and a step size of 5° at room temperature.

The electrical conductivity of H0, H1, H2 and H3 materials, as well as that of PEDOT:PSS in the form of bucky-paper films was determined by measuring the sheet resistance (R_s) at room temperature using a 4-point probe system (Ossila Ltd UK), taking into account the film thickness and the dimensions of rectangular-shaped cut samples. More analytically, films were fabricated via vacuum filtration with a predetermined amount of ink to yield a self-standing film of ~80 μm thickness which was cut into rectangular shaped samples. Resistivity was calculated as $R_s = \rho/t$ (ρ: resistivity, t: film thickness) and electrical conductivity as its reciprocal *i.e.,* $\sigma = 1/\rho$. The 4-point probe system used 4 equally-spaced, co-linear probes to the material (interelectrode probe distance / spacing: 1 mm) employed current from 10 nA to 150 mA, voltage from 100 μV to 10 V which allowed for the measurement of resistance ranging from 3 mOhm/□ to 10 MOhm/□. At least 4 measurements were performed on all samples.

The Seebeck coefficient of H0, H1, H2, H3 and PEDOT:PSS thermoelectric films was determined using a custom-made set-up. Samples were positioned so as their edges were in contact with two metal blocks so as to ensure thermal conduction. Silver conductive grease was deposited onto the area between the contact of the hot side metal block and the sample. To monitor the TE performance, indicative one block was kept at room temperature (~25 °C), while the other one was heated at 125 °C allowing the generation of a temperature gradient. The generated thermovoltage (ΔV) was measured by a digital multimeter-voltmeter (Agilent 34401A6½), while the temperature of the 2 blocks was controlled with K-type thermocouples so as to accurately determine temperature difference (ΔT). The Seebeck coefficient (S) was derived then from the ratio $\Delta V/\Delta T$.

Hall-effect measurements were performed at 0.55 T and 1 mA using the Ecopia HMS-3000 system, in order to determine the carrier concentration and mobility of H0, H1, H2 and H3 thermoelectric materials, as well as of PEDOT:PSS in the form of films with ~2 μm thickness fabricated by drop-casting (**Figure S1** in Supporting information).

Scanning electron microscopy (SEM) was performed in order to characterize the diameter, length, and morphology of the produced nanostructures using the Ultra Plus (Carl Zeiss Microscopy GmbH, Germany) under an accelerating voltage of 3 KV. Samples were prepared by drop casting 100 μL of H0 and H3 diluted dispersions on a 25 mm×10 mm glass slide substrate, followed by drying at 90 °C for 30 min in a fume cupboard. Focused Ion Beam (FIB) in NEON40 SEM (Carl Zeiss Microscopy GmbH, Germany) was used to determine the thickness of the thermoelements of the TEG. The region of interest was locally capped by ion beam deposited platinum. Milling was performed with a 30 KV Ga^+ ion beam, while the milling progress was controlled with the scanning electron microscope.

TEM studies and selected area electron diffraction (SAED) patterns of H0 and H3 Te NWs were performed with the Libra 200 transmission electron microscope (Carl Zeiss Microscopy GmbH, Germany) operating at 200 KV. Samples for TEM were prepared by dispensing 10 μL of each suspension on a Cu grid with a carbon support membrane.

2.1.2.4 Fabrication and characterization of a flexible TEG module

The highest *PF* formulated TE ink (H3) was employed to fabricate a flexible TEG module. A shadow-mask assisted wet-chemical deposition printing technique was followed. A planarized Polyethylene terephthalate (PET) foil was used as the TEG substrate and patterned vinyl foil (designed by CorelDRAW) as the deposition mask which determined the TEG geometry. In more detail, a vinyl-based mask with one-sided adhesive was implemented in order to be stabilized and also be easily and selectively removed by a mild heat treatment of the planarized PET substrate. The TEG device consisted of two serially interconnected TEG modules, each of which comprised of ten parallelly connected thermoelements. For each thermoelement, 55 μL of ink were deposited using a drop casting method utilizing a micropipette followed by drying on a hot plate at 100 °C for 10 min. Each time the same ink quantity was deposited onto the predefined thermoelement areas (mask-assisted wet chemical deposition / printing process) and the drying process was simultaneously occurred, resulting in the printed thermoelements. The resulting thermoelement had a rectangular shape of 20 mm×5 mm. Ag-paste based metal electrodes were deposited via the mask-assisted deposition method and a blade coating apparatus for the interconnection of the printed thermoelectric legs. The Ag-paste was annealed for 30 min at 120 °C on a hot plate to reduce as much as possible the contact resistance between the Ag electrodes with the device thermoelements and ensure optimum electrical conductivity for the Ag electrodes. The overall dimension of the fabricated “in-plane” TEG was 140 mm (length)×20 mm (width). As an alternative to Ag-metallic printed contacts of the TEG module, a water-based suspension containing 0.2 % (w/v) of single walled carbon nanotubes (SWCNT) by TUBALL™, OCSiAl with carbon purity >75 %, average nanotube length 1.5 µm and nanotube diameter ca. 3 nm was employed. The suspension was deposited using a blade coating apparatus in conjunction with the mask-assisted method, as previously described for the Ag-paste.

The voltage output V_{out} (also reported in the literature as open circuit voltage V_{OC} or voltage of the TEG V_{TEG}) of the H3-based TEGs was again measured using the Agilent voltmeter. The in-plane temperature difference has been generated across the TEG using an in-house manufactured stage comprising both a “hot” and a “cold” block with temperature control (**Figure S2a**). Device power output measurements were carried out using a custom device schematically (shown in Supporting information, **Figure S2b-c**).

The flexibility of the TEG devices was subjected to purposely designed bending tests of 1000 cycles by rolling them onto different round objects to evaluate their overall performance and the relative change of the electrical resistance was monitored. In more detail, the test was performed by multiple flexing of the TEG on the perimeter of a steel cylinder. 2-cylinder diameters were employed, *i.e.,* 130 mm and 70 mm corresponding to a bending radius of 65 mm and 35 mm, respectively. Finally, the TEG device with SWCNT-contact as the metallic junctions was exposed to a temperature gradient of ΔT = 100 K for a total duration of 5 h (equal to 18000 s) so as to assess its thermal stability over time evolution.

2.1.3 Results and Discussion

2.1.3.1 Raman and XRD analysis

Figure 20a depicts the Raman spectra of pure Te NWs (H0) in bucky-paper form **Figure 20b** represents the Raman spectra of H0, H1, H2, H3 drop-casted films on glass slide substrates. The vibrational modes of Te were identified in all the spectra at 119-120 cm^{-1} and 139 cm^{-1}. These bands can be attributed to the A_1 and the E_2 vibrational modes of Te NWs, respectively [35,36]. It should be noted that the E_1 vibrational mode of Te expected at ~85 cm^{-1} was barely visible with the employed spectrometer as the cutoff of the notch filter for the Rayleigh scattering was at ca. 80 cm^{-1}. Te NWs in bucky-paper form did not present any other prominent vibrational modes. However, the Te NWs in film form (H0), as well as the H1, H2, H3 hybrid films showed additional vibrations at ~176 cm^{-1} and 222 cm^{-1} that can be attributed to the Te-Te stretching vibrations and a second order vibration of Te NWs, respectively [37,38]. Additional vibrational modes were also observed for the TeNW@PEDOT:PSS H1, H2, H3 hybrid films between 1220 cm^{-1} and 1657 cm^{-1} attributed to the presence of the PEDOT. These vibrational modes are observed like a double shoulder and can only be fitted by a combination of Lorentzian and Gaussian bands. These bands can be attributed to the asymmetric C=C stretching vibrations, the symmetric (C=C)−O stretching and the C−C stretching of PEDOT [39]. The contribution of PSS is too weak to be observed in the spectra of the hybrid films [40].

Figure 20c presents the XRD patterns of Te NWs and TeNW@PEDOT:PSS hybrid films. The XRD spectra confirmed the presence of crystalline hexagonal Tellurium with three atoms per unit cell and cell constants a and c equal to 4.46 Å and 5.92 Å, respectively as all the encountered peaks could be indexed to each reference spectrum (No. 36-1452). As should be noted, the crystalline nature of Te NWs prevented the PEDOT:PSS polymer from becoming visible in the XRD patterns. The XRD patterns hereby reported were in good agreement with those reported in literature for Te NWs [32,37,41].

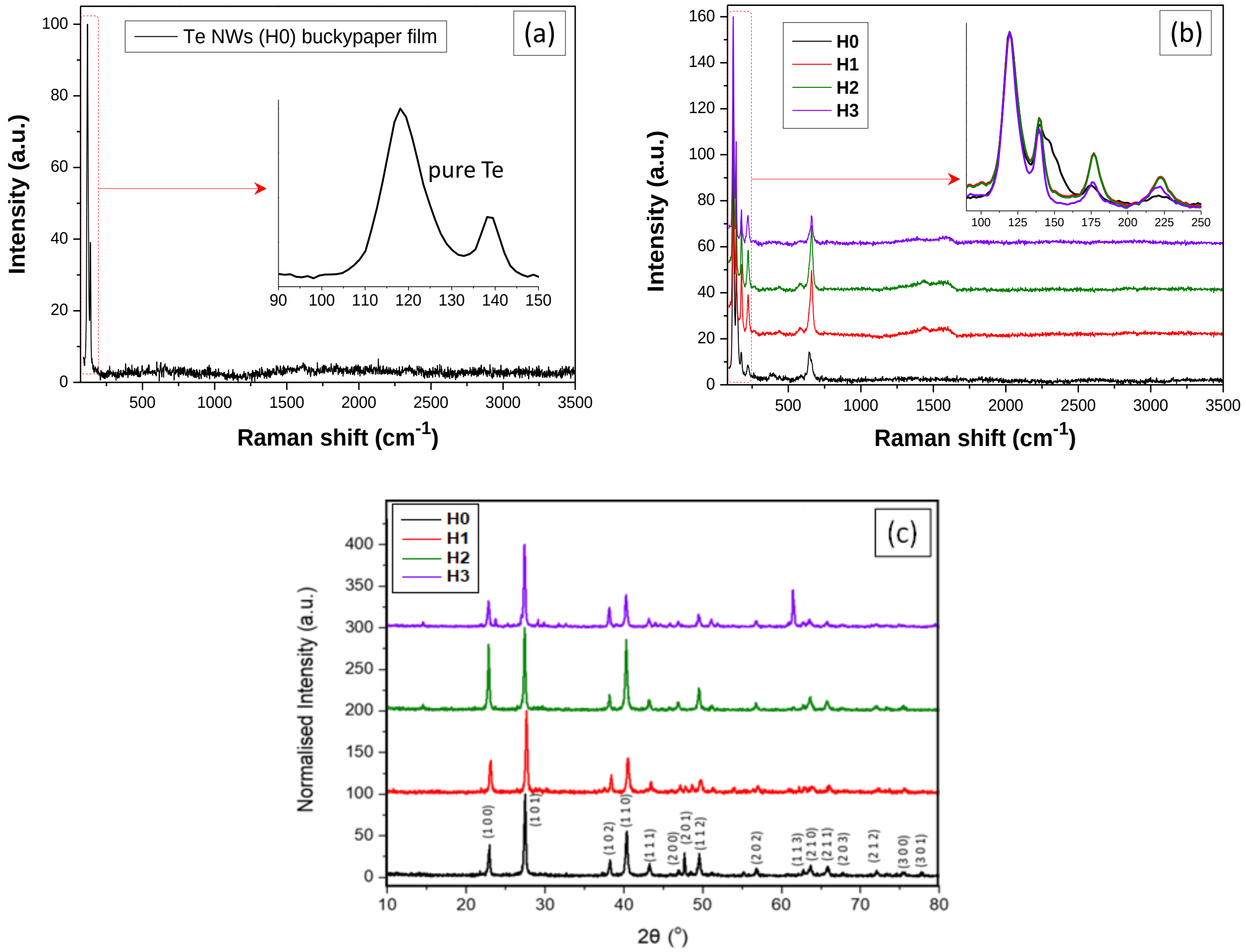

Figure 20. (a, b) Raman spectra of synthesized Te NWs (H0) in the form of bucky-paper film, as well as of H1, H2, H3 films, **(c)** X-Ray diffraction patterns of Te NWs (H0) and hybridized Te NWs with PEDOT:PSS (H1, H2, H3) films.

2.1.3.2 SEM and TEM investigation

Figure 21 shows the SEM images of bare Te NWs – H0 (**Figure 21a**) and Te NWs hybridized with PEDOT:PSS - H3 (**Figure 21b**), illustrating the nanowire microstructural characteristics. The Te NWs are quite monodispersed exhibiting diameters in the range of 50 nm with lengths varying from 1 to 2 μm on average. It can be deduced that the thermoelectrically generated carrier transport network is formed by the randomly distributed Te NWs in both cases. As can be observed, the addition of PEDOT:PSS led to the creation of NW bundles consisting of oriented adjacent Te NWs (dashed circled lines, insets within the SEM respective image), which could affect the film carrier transport properties. In addition, the hybrid TeNW@PEDOT:PSS film, as well as all hybrid formulations exhibited significant flexibility compared to the H0 Te NWs film, which appeared to be very brittle.

TEM analysis and selected area electron diffraction (SAED) patterns obtained from a single Te NW, namely H0 bare Te NWs (**Figure 21c-d**) and H3 PEDOT:PSS hybridized (**Figure 21e**) were performed in order to identify the nanowire crystal structure. The clear lattice fringes (**Figure 21d**) indicated that the nanowire is a structurally uniform and monocrystalline material. The interplanar spacing of ~5.9 Å corresponds to the distance between (001) lattice planes in hexagonal Te, as has also been reported in the literature [42]. Moreover, the PEDOT:PSS was visible as a thin layer of an amorphous material surrounding the Te NW with of ~5-10 nm thickness (**Figure 21e** - dashed red lines). The PEDOT:PSS shell was formed due to the electrostatic interactions between PEDOT:PSS with the positively charged CTAB stabilized Te NWs. This mechanism is schematically presented in **Figure 21d**. The polymer layer could serve as a protecting layer to passivate the surface of the nanocrystalline NWs. This layer may prevent oxidation during processing, fabrication, as well as operation under a thermal gradient in ambient conditions. Furthermore, an energy filtering effect beneficial for the enhancement of the thermoelectric film power factor may also be introduced by this polymer / nanocrystal interface, as will be discussed in the next paragraphs [43].

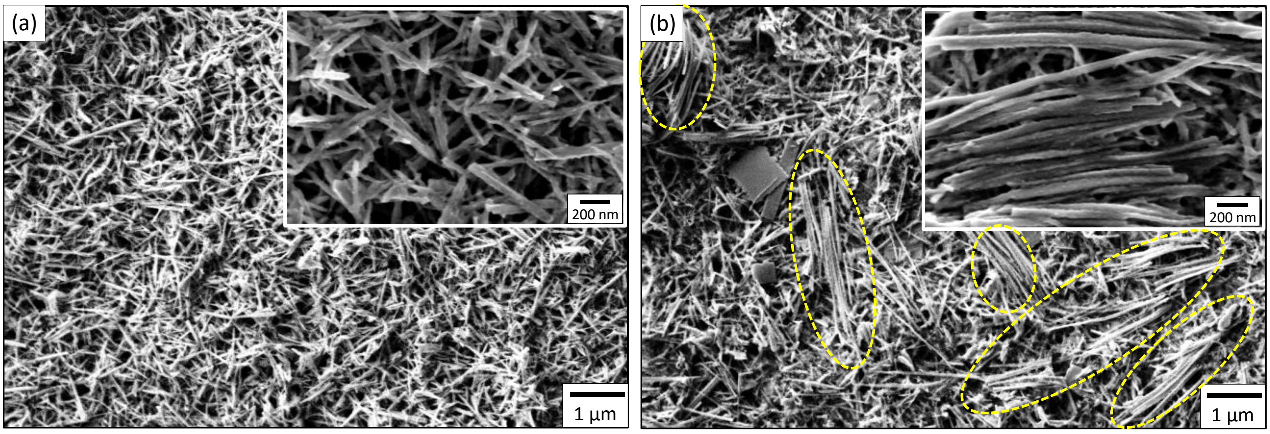

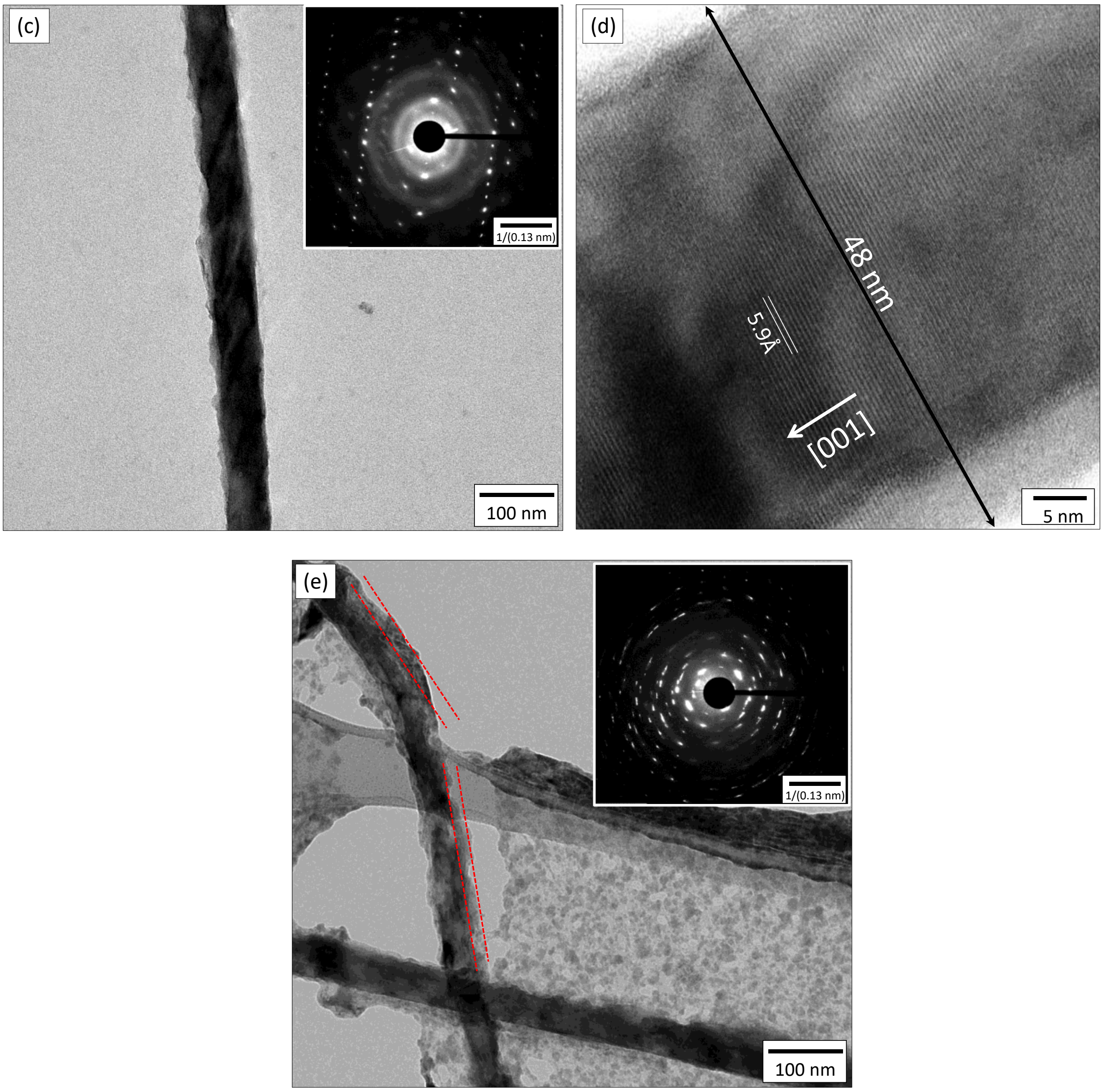

Figure 21. Scanning Electron Microscopy images of **(a)** the synthesized Te NWs – H0, and **(b)** Te NWs hybridized with PEDOT:PSS – H3 in the form of drop-casted films; Transmission Electron Microscopy images of the H0 **(c-d)** and H3 **(e)** systems (insets in **Figure 21c-e**) show the corresponding selected area electron diffraction pattern, while the red lines in **Figure 21e** depict the PEDOT:PSS shell).

2.1.3.3 TE performance and carrier transport characteristics of Te NWs and TeNW@PEDOT:PSS

The thermoelectric properties of H0, PEDOT:PSS, as well as of H1, H2 and H3 TeNW@PEDOT:PSS hybrid materials are shown in **Figure 22a**. The highly conductive grade PEDOT:PSS used in this work (Orgacon™ ICP 1050 Agfa, 1.1 wt. % in H_2O) exhibited an electrical conductivity of 2883 ± 2.1 S/m and a p-type thermoelectric character reflected by its positive measured Seebeck coefficient (S = +24.2 ± 0.8 μV/K). The PSS in the complex functioned as a counter ion for the cationic, conductive PEDOT and also allowed for the formation of a stable, easily processable dispersion of PEDOT:PSS polymer gel particle. PEDOT:PSS particles have excellent film forming properties and are easily processable for different coating techniques on a variety of substrates [15]. The addition of conducting polymers to the bare Te NWs reduced the contact resistance by bridging with conductive paths the nanograined Te NWs consisting films. The CTAB-stabilized Te NWs (H0) without PEDOT:PSS hybridization exhibited an electrical conductivity of 10.45 ± 0.5 S/m and an extremely high Seebeck coefficient (S = +484.3 ± 11.4 μV/K). This was attributed to the high crystalline quality of Te NWs, as was confirmed by both TEM and SAED. This is one of the highest values ever reported in literature among different wet-chemical protocols for the synthesis of Te nanowire and nanorod crystals [9,10]. More specifically, Park *et. al* [37] reported the synthesis of Te NWs with a Seebeck coefficient of S = +568 μV/K, whereas Choi *et. al.* [13] reported values of S = +487 μV/K and S = +559 μV/K, following two different protocols. As was observed, the electrical conductivity increased with the addition of PEDOT:PSS for all H1, H2 and H3 hybrid formulations. In **Figure 22b** representative *I-V* curves for H0, H1, H2 and H3 hybrid materials are shown. The enhanced electrical conductivity of the materials reflected the effect of hybridization. This effect was followed by a decrease in the Seebeck coefficient which however is a typical behavior of thermoelectric materials [3]. As the Seebeck coefficient is inversely proportional to the charge carrier concentration, which in its turn is directly proportional to the electrical conductivity, the increase of the electrical conductivity leads to the decrease in Seebeck coefficient.

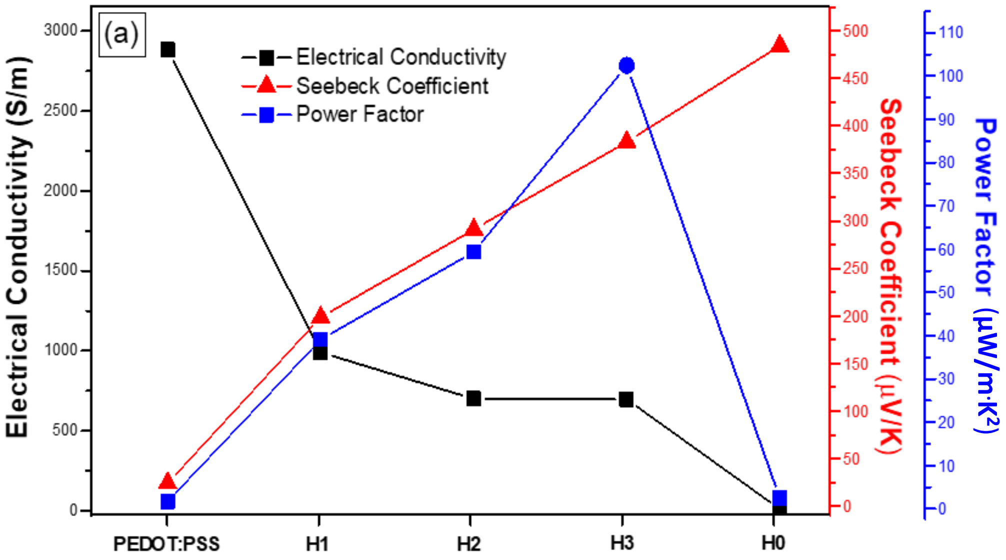

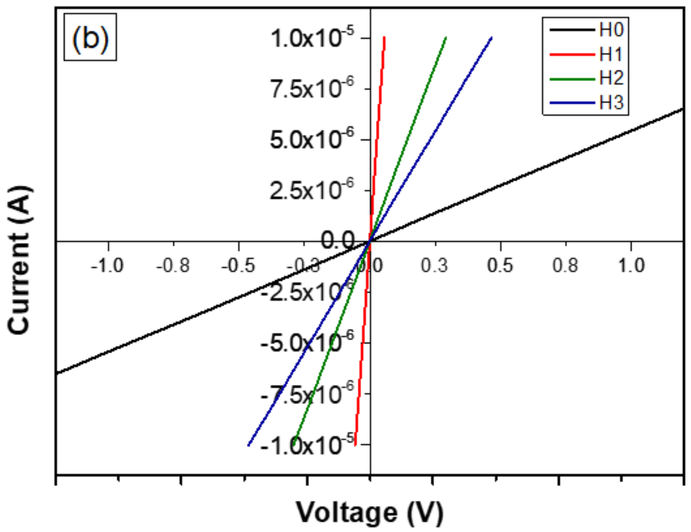

Figure 22. (a) In-plane thermoelectric properties: electrical conductivity, Seebeck coefficient and power factor, **(b)** *I-V* curves of H0, H1, H2 and H3 TeNW@PEDOT:PSS hybrid materials films.

Table 2 summarizes the transport parameters of H0, PEDOT:PSS, as well as H1, H2 and H3 hybrid materials. The H3 formulation showed the maximum power factor ($PF = \sigma \cdot S^2$), *i.e.*, 102.42 μW/m · K^2. The achieved *PF* was two orders of magnitude higher than the *PF* of both plain PEDOT:PSS and Te NWs. Based on literature findings Te NW-PEDOT:PSS nanocomposites possess an inherently low thermal conductivity at room temperature (RT) comparable with the polymer (~0.2 W/m · K) [12], while pure Te NWs thermal conductivity is ~0.15 W/m · K [44]. The calculated *ZT* values are 0.2 for H3 formulation and 0.006 for H0, respectively. Therefore, H3 was finally selected for the fabrication of the flexible TEGs. The optimal efficiency-η (Carnot efficiency) of thermal to electrical energy conversion for the H3 hybrid p-type TE material is 1.32 % at ΔT = 100 K, expressed by **Equation (1)** [30]:

$$\eta = \left(\frac{T_{\mathrm{H}} - T_{\mathrm{C}}}{T_{\mathrm{H}}}\right) \frac{\sqrt{1+ZT} - 1}{\sqrt{1+ZT} + (T_{\mathrm{C}}/T_{\mathrm{H}})} \quad \mathbf{(1)}$$

where T_{H} represents the temperature of the hot side and T_{C} is a steady temperature of a cold side.

Table 2. Summarized thermoelectric properties (Seebeck coefficient, power factor) at ΔT = 100 K and electrical, semiconductor carrier properties (electrical conductivity, carrier concentration, carrier mobility) for the different materials studied at room temperature (RT).

Sample	**Seebeck coefficient (S)** (μV/K)	**Electrical conductivity (σ)** (S/m)	**Power factor ($\sigma \cdot S^2$) (PF)** (μW/m · K^2)	**Carrier concentration (n)** (cm^{-3})	**Carrier mobility (μ)** (cm^2/V$_s$)
Single component materials					
PEDOT:PSS	+24.2 ± 0.8	2883 ± 2.1	1.69	7.89E+20	3.67E+02
TeNW (H0)	+484.3 ± 11.4	10.45 ± 0.5	2.45	8.41E+18	8.44E-01
Hybrid materials					
TeNW/PEDOT:PSS (H1)	+198.7 ± 4.6	990.8 ± 0.8	39.12	4.00E+19	1.01E-01
TeNW/PEDOT:PSS (H2)	+291.1 ± 4.2	700.3 ± 0.4	59.34	2.40E+19	1.64E-01
TeNW/PEDOT:PSS (H3)	+383.2 ± 4.4	697.5 ± 0.6	102.42	2.09E+19	1.72E-01

In order to further explain the origin of the drastic enhancement of *PF* for all H1, H2 and H3 hybrid materials the film transport characteristics have been investigated. Specifically, a plausible energy filtering mechanism at the PEDOT:PSS-Te NWs interfaces could be envisaged resulting into this power factor enhancement. Hall measurements were carried out to study the carrier concentration and mobility of Te NWs, PEDOT:PSS, as well as H1, H2 and H3 hybrid materials. These would reveal the link between the Seebeck coefficient and the electrical conductivity (**Table 2**). Pure Te NWs (H0) had low carrier concentration of 8.41×10^{18} cm^{-3} and mobility of 8.44×10^{-1} cm^2/V$_s$ which resulted to low electrical conductivity and high Seebeck coefficient. On the other hand, the H1 hybridized system of TeNW@PEDOT:PSS possessed higher carrier concentration of 4×10^{19} cm^{-3} followed by enhanced electrical conductivity and lower thermopower than pure Te NWs.

The synergistic effect which led to this *PF* enhancement may be attributed to an energy filtering mechanism at the Te NW-PEDOT:PSS interface. In the energy filtering effect, low-energy carriers are preferentially scattered by the potential barrier created at the Te NWs-PEDOT:PSS interface, whereas high-energy carriers readily cross the barrier [45]. Basically, high-energy carriers can transfer more heat than low-energy carriers resulting in higher Seebeck coefficient values [46]. In order to demonstrate the energy filtering at the Te NW-PEDOT:PSS interface, the scattering time and carrier mobility should be considered. The scattering time (defined as $\tau = \mu \cdot m^*/e$, where τ, μ and m^* are the scattering time, carrier mobility and effective mass of the carrier, respectively) was calculated from the measured carrier mobility. All the hybrid films showed lower scattering times

(5.74×10^{-17} s for H1, 9.33×10^{-17} s for H2 and 9.75×10^{-17} s for H3) compared to pure Te NWs (4.80×10^{-16} s). The same trend is followed for the measured carrier mobilities, indicating that more scattering events took place for the hybrid films. These decreased carrier mobilities and scattering times for the hybrid films could be regarded as an evidence for the energy filtering at the Te NWs-PEDOT:PSS interface.

The interrelationship between carrier concentration and Seebeck coefficient can be expressed by simple models for electron transport. The Drude model [3] was used to calculate the Seebeck coefficient for a quantitative interpretation of the thermoelectric data. The Seebeck coefficient, or thermopower is defined by **Equation (2)**:

$$\mathrm{S} = \frac{8\pi^2 K_B^2}{3eh^2} \cdot m^* \cdot \mathrm{T} \cdot (\frac{\pi}{3n})^{2/3} \quad \textbf{(2)}$$

where K_B, h, n, m^* and T is the Boltzmann constant, Plank constant, carrier concentration, effective mass of the carrier and absolute temperature, respectively. The thermopower arising from the Drude model (S_c) relates to the semiconductor carrier concentration without considering the potential effects from energy filtering. On the other hand, the measured thermopower (S_m) includes the enhancement from energy-dependent carrier scattering. As such, the ratio of these two parameters $[\left(\frac{S_m - S_c}{S_c}\right) \times 100\ (\%)]$ allows for the energy filtering effect to be quantified.

Table 3 shows the measured and calculated Seebeck coefficients for the pure TeNWs, PEDOT:PSS as well as H1, H2 and H3 TeNW@PEDOT:PSS hybrid films. The S_c and S_m values of the pure Te NWs were very similar indicating that no synergy took place. On the other hand, the S_m of the hybrid films were 16.4 % (H1), 21.3 % (H2) and 45.6 % (H3) higher than the respective S_c. The enhanced Seebeck coefficient for all hybrid films was a solid evidence for a synergistic energy filtering effect at the Te NWs-PEDOT:PSS interface.

Table 3. Measured and calculated thermopower of H0, PEDOT:PSS, as well as of H1, H2 and H3 TeNW@PEDOT:PSS hybrid films.

Sample	**Seebeck coefficient** (μV/K)		$\left(\frac{S_m - S_c}{S_c}\right) \times 100\ (\%)$
	Measured	**Calculated**	
Single component materials			
PEDOT:PSS	24.2	23.4	+3.51
Te NWs (H0)	484.3	482.7	+0.33
Hybrid materials			
TeNW/PEDOT:PSS (H1)	198.7	170.7	+16.4
TeNW/PEDOT:PSS (H2)	291.1	239.9	+21.3
TeNW/PEDOT:PSS (H3)	383.2	263.1	+45.6

2.1.3.4 Flexible TEG device performance and power output characteristics

Figure 23a illustrates the mask employed for the flexible TEG module fabrication following a mask-assisted dispensing printing method. Details about the TEG device / module fabrication could be found in the experimental part of this study. **Figure 23b** depicts the TEG device fabricated onto a flexible PET substrate with the corresponding dimensions represented by the ruler given as an inset. As aforementioned, the H3 hybrid thermoelectric p-type ink with the highest achieved power factor (PF = 102.42 μW/m · K^2) for the flexible TEG. The fabricated TEG device consists of 2 modules connected to each other in series, each one contains 10 individual thermocouples connected in parallel to reduce the total internal resistance R_{TEG} (**Figure 23a-b**). The Ag-paste metallic tracks that were used as the metallic junction for the thermoelement interconnection can also be seen. **Figure 23c** shows the SEM image after the FIB milling process performed onto a single H3 thermoelement in order to determine the TEG device film thickness, measured at ~3-4 μm. A nano porous structure can be observed throughout the whole thickness of the film, typical for randomly distributed one-dimensional (1D) nanowire consisting films.

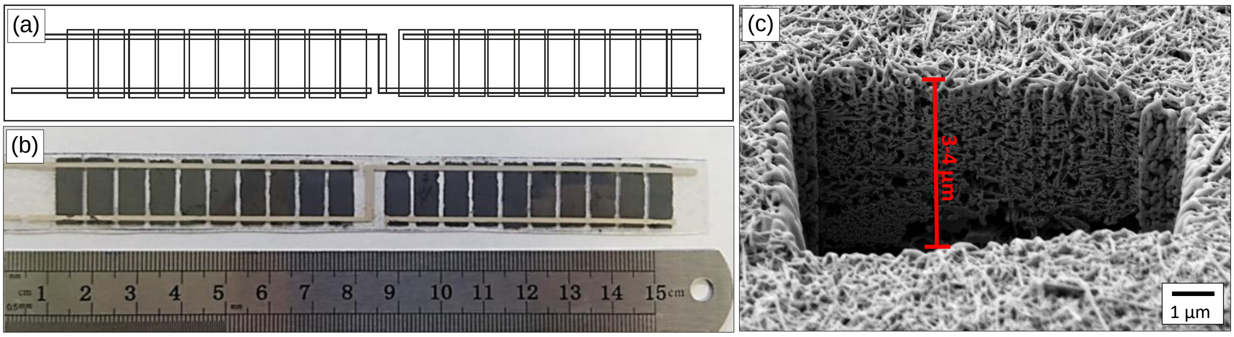

Figure 23. (a) Mask utilized to fabricate the TEG flexible module, **(b)** real TEG device onto a PET flexible substrate (utilizing the H3 hybrid ink) and **(c)** SEM image after the FIB milling process on a single thermoelement showing the printed film average thickness.

Figure 24 demonstrates two planar TEG devices in operation at ΔT = 80 K. The 2 devices with a voltage output (V_{out} or V_{TEG}) of 55.22 ± 1.1 mV (**Figure 24a**) and 56.53 ± 1.3 mV (**Figure 24b**), respectively, are fully identical *i.e.*, same geometry, thermocouple material and steps followed to fabricate the TEG device. The only difference is that Ag-paste used as the metallic junction for the thermoelement interconnection (**Figure 24a**), has been replaced with highly conductive and printable SWCNT (**Figure 24b**) with an electrical conductivity (σ) of ~8.2×10^5 S/m [47]. This was carried out in order to study and compare the device performance as well as the device flexibility. Considering the Seebeck coefficient of the H3 active thermoelectric material of the TEG device (+383.2 ± 4.4 µV/K), the maximum expected (theoretical) voltage output (V_{TEG} or V_{OC} or V_{OUT}) with the specific architecture fabricated in our study (**Figure 24a**) would be 61.15 mV at a ΔT = 80 K (the result of: $N \cdot S \cdot \Delta T$, where N is the number of the thermocouples). Interestingly enough, the experimental measurements of 55.22 ± 1.1 mV for the Ag-contact (**Figure 24a**) and 56.53 mV ± 1.3 mV for the SWCNT-contact (**Figure 24b**) TEG devices revealed lower V_{TEG} values as compared to the theoretical maximum one. The lower voltage output could be possibly attributed to geometrical points of the printed TEG devices where voltage losses may occur. For instance, such points could be the contacts between the H3 thermoelements with the Ag- and the SWCNT-metallic junctions, respectively.

Power output (P_{out}), otherwise defined as maximum output of electrical power (P_{max}) is of paramount importance for determining the TEG device performance. Therefore, the resistance of the TEGs (R_{TEG}) with Ag- and SWCNT-contacts was measured simultaneously with the voltage output (**Figure 24c**) during device testing at different ΔT (experiments up to ΔT = 100 K starting from ~25 °C). The P_{max} (with optimal impedance matching) for the TEG devices with Ag- and SWCNT-contacts was derived then from **Equation (3)** [26], and shown in **Figure 24d** as a function of ΔT.

$$P_{max} = \frac{\Delta V^2}{4R_0} \quad \textbf{(3)}$$

where ΔV is the thermoelectric power (TEP) or thermoelectric voltage potential or open circuit voltage (V_{oc}) equal to the device V_{TEG} experimentally measured, and R_0 is the internal electrical resistance of the TEG device (otherwise defined as R_{TEG}).

As it can be observed, both Ag- and SWCNT-contact consisting devices exhibit quite similar P_{max} characteristics over the different ΔT. Moreover, it is worth mentioning that the highest P_{out} produced at ΔT = 100 K in our study (~4.5 μW) is the highest value ever reported amongst other Te-based TEG devices [19,48,49]. Another interesting characteristic is that the R_{TEG} decreases in both cases with temperature, which is typical for semiconductor materials as the H3 hybrid TeNW@PEDOT:PSS in our devices [50]. Namely, the R_{TEG} at RT is 476.61 ± 16.4 Ohm for the Ag-contact and 545.15 ± 31.3 Ohm for the SWCNT-contact device, respectively (**Figure 24c**). The SWCNT-contact device shows slightly higher R_{TEG} at RT, due to the SWCNT lower conductivity at RT compared to the metallic Ag junctions, resulting thus in a slightly increased internal device resistance. However, the R_{TEG} at ΔT = 100 K is almost the same for both devices (**Figure 24c**). This is more precisely attributed to the fact that SWCNT conductivity increases with temperature as it has been previously demonstrated by Nakai *et. al.*, showing an extensive study of the temperature dependent electrical resistivity of semiconducting, mixed and metallic SWCNT films [51]. Therefore, the SWCNT internal resistance as contacts decreases with temperature, which results further in a total decrease of the device R_{TEG}. In **Figure 24c**, the V_{TEG} with respect to different applied ΔT can be also observed for the devices with Ag- and SWCNT-contacts, respectively. A linear dependence of the V_{TEG} with the increasing ΔT could be seen. This finding corroborates the linear dependence of the Seebeck coefficient with temperature, as well as the ohmic contacts achieved between the Ag and SWCNT metallic junctions with the H3 thermocouples in the fabricated TEG devices. The power density of the TEG module 2.57 W/m^2 at ΔT = 100 K was determined by dividing P_{max} with the total cross-sectional area of the device.

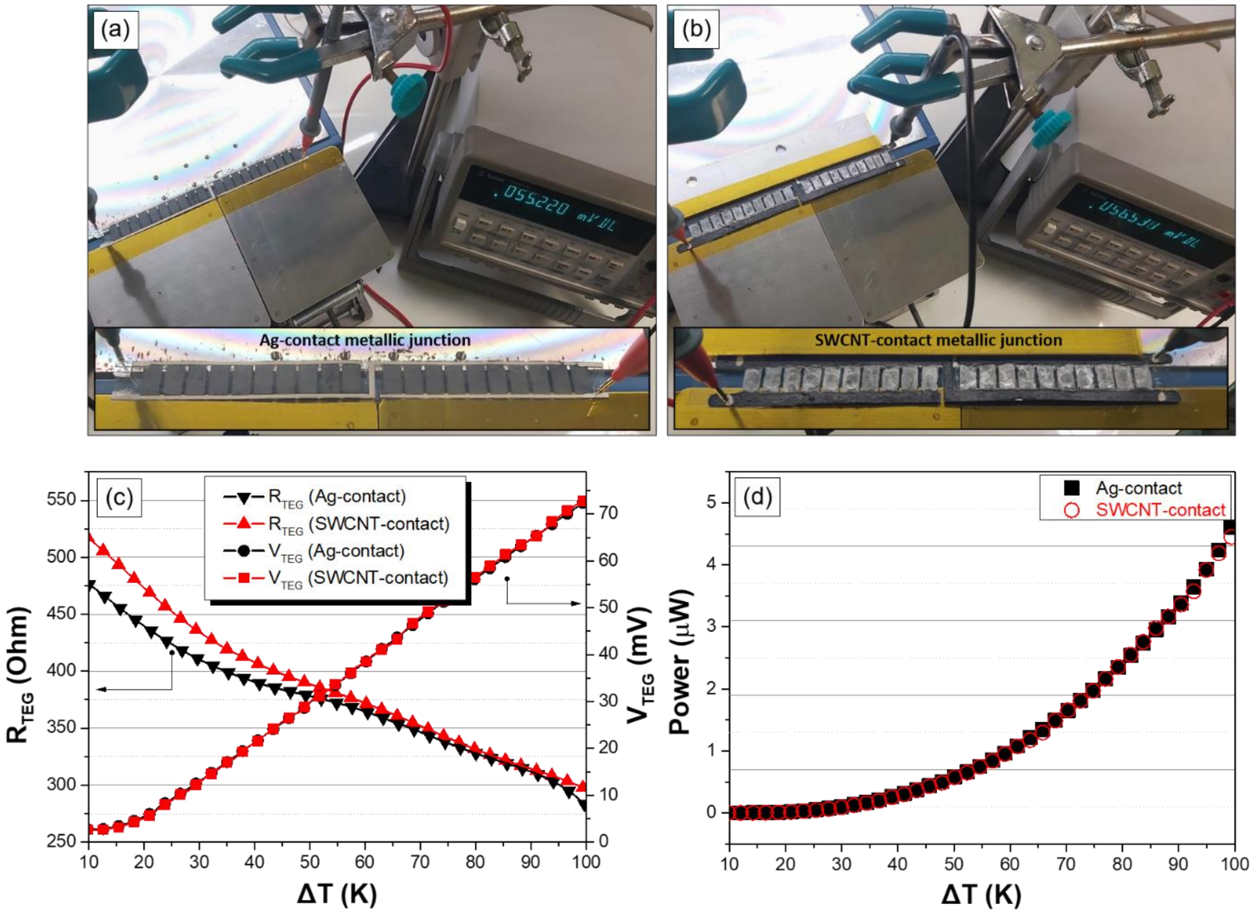

Figure 24. (a) Ag-contact and **(b)** SWCNT-contact consisting TEG devices in operation upon being exposed to an in-plane temperature gradient of ΔT = 80 K, **(c)** R_{TEG} and V_{TEG} of Ag- and SWCNT-contact consisting devices as a function of ΔT (experiments carried out up to ~125 °C generating a ΔT = 100 K, starting from ~25 °C), **(d)** P_{max} of the Ag- and SWCNT-contact consisting devices as a function of ΔT.

Practical use of the TEG devices requires power generation, which has been measured in our study using a homemade apparatus. Specifically, **Figure 25a** and **Figure 25d** show the equivalent circuit model of the TEG devices with Ag- and SWCNT-contacts, respectively, on the basis of which the power measurements have been carried out. **Figure 25b** shows the experimental output voltage-current (V-I) and that of output power-current (P-I) curves, while **Figure 25c** the output V-R_L and output P-R_L curves applying different external load resistances (R_L: R_{LOAD}) at three different in-plane applied ΔT (50, 80 and 100 K) for the TEG device with Ag-metallic contacts. Similarly, **Figure 25e** corresponds to the experimental V-I and P-I curves, while **Figure 25f** to the V-R_L and P-R_L curves of the TEG device with SWCNT-metallic contacts at 50, 80 and 100 K. The continuous lines in all curves have been derived from calculations of the following **Equation (4)**, giving the output power (P):

$$P = I^2 . R_L = \left(\frac{V_{OC}}{R_{in} + R_L}\right)^2 R_L \quad \textbf{(4)}$$

where I is the output current (defined also as I_L: current which passes through the load), R_{LOAD} or R_L is the load resistance, R_{in} is the internal resistance of the device (otherwise defined as R_{TEG}), and V_{oc} is the open circuit voltage (equal to the measured V_{TEG}) when the R_{LOAD} approaches infinity.

As can be observed in **Figure 25b-d**, the output voltage for the different R_{LOAD} was inversely proportional to the output current. The maximum power generation of 4.73 μW at $\Delta T = 100$ K (**Figure 25c**) was observed when R_{LOAD} matched the internal TEG resistance, *i.e.*, 281.9 Ohm. The same was observed for $\Delta T = 50$ K and $\Delta T = 80$ K, respectively, as well as for the SWCNT-contact TEG device at different ΔT (**Figure 25f**). The P_{max}, or the maximum electric power dissipated in the load resistor, was reached when the load resistance equaled the TEG device resistance (R_{TEG}). Moreover, at 281.9 Ohm as load resistance (**Figure 25c**), the thermoelectric power voltage V_{TEP} was 37.36 mV, compared to a V_{oc} of 73.11 mV at the same ΔT. Above 281.9 Ohm, V_{TEP} continued to increase as it approached the open circuit voltage (V_{TEG}), but P decreased as the load resistance increased. As $P = V_L^2/R_L$, V_{TEP} showed a parabolic behavior as expected.

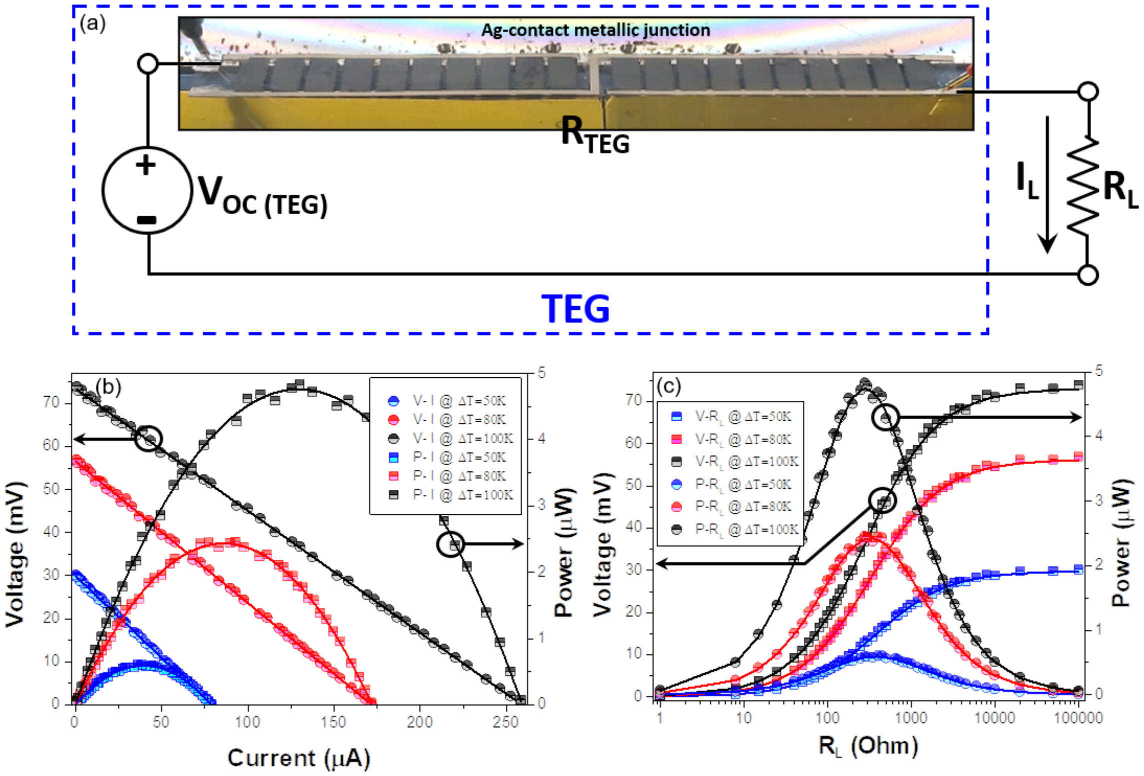

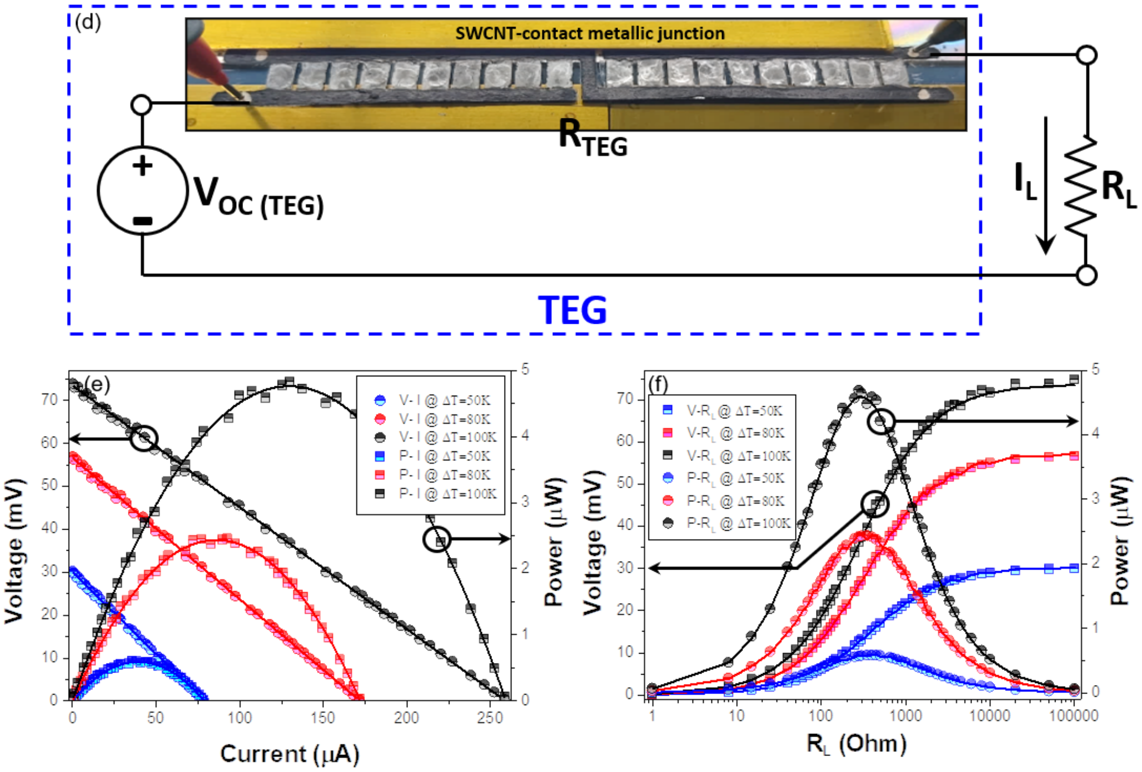

Figure 25. (a, d) Equivalent circuit of the TEG device with Ag- and SWCNT-contacts, respectively, **(b, e)** experimental output voltage-current (*V-I*) and output power-current (*P-I*) curves at 3 different in-plane applied Δ*T* (50, 80 and 100 K) for the TEG device with Ag- and SWCNT metallic contacts, respectively, **(c, f)** output $V\text{-}R_L$ and output $P\text{-}R_L$ curves at 3 different in-plane applied Δ*T* (50, 80 and 100 K) for the TEG device with Ag- and SWCNT metallic contacts, respectively.

2.1.3.5 TEG device flexibility performance

Figure 26a-b show the TEG device with Ag-contacts and **Figure 26c-d** depict the TEG device with SWCNT-contacts in flexed as well as in the free state tested under both 35 mm and 65 mm bending radii.

Figure 26e shows the ratio R/R_0 of the device electrical resistance as a function of the bending cycles, where $R_0 = R_{TEG}$ is the initial device resistance and *R* is the resistance of the device after *n* number of bending cycles at the specific bending radius. The R_{TEG} of the Ag-contact device increased by ca. 50 % after 1000 cycles at 65 mm bending radius. The phenomenon was considerably more pronounced for 35 mm of bending radius, even at the initial stages of the experiment, as after the first ten cycles *R* increased by a factor of 2.5. The rapid performance deterioration of R_{TEG} in the case of the Ag contacts would not allow its usage for practical harvesting applications when such bending strain conditions are necessary. The electrical contact loss between the Ag printed electrodes with the TEG device thermoelements during the bending test was the most probable reason for this performance deterioration. Notably, the Ag printed contacts did not seem to have undergone any visible fatigue damage *i.e.*, crack, discontinuity, *etc.* as the employed Ag-paste consisted of silver flakes in thermoplastic binder with good flexibility. Besides that, the micron-sized planar Ag flakes within the printed Ag-film / electrode could easily be detached from the Te NWs thermoelements, resulting in electrical contact loss with increasing bending cycles. According to literature experimental findings the electrical resistivity of bulk and nanograined Ag is temperature-dependent and increases with increasing temperature [52]. On the other hand, the TEG device with SWCNT-contacts exhibited an excellent flexibility performance. Namely, the device R_{TEG} remained unaltered for 1000 bending cycles at 65 mm bending radius, while it moderately increased (~33 %) after being tested at 35 mm bending radius for 1000 cycles. The SWCNT are both highly flexible as printed films / contacts, while their 1D geometry in conjunction with their very thin diameters (~3 nm) may favor their entanglement or "interlocking" with the Te NWs. This interlocking allows for increased flexibility while it prevents contact loss.

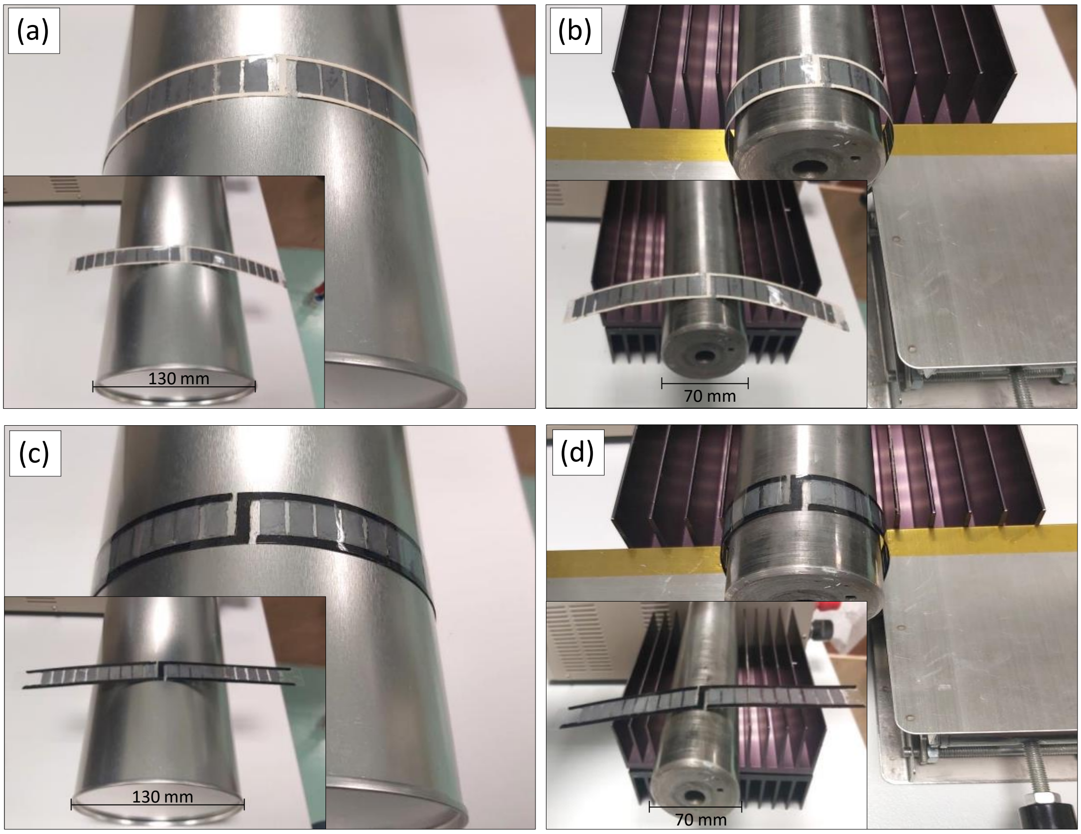

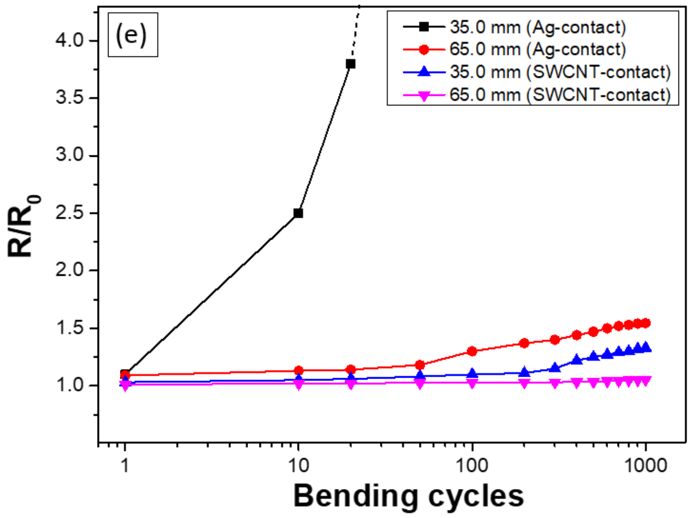

Figure 26. (a, b) TEG device with Ag-contacts in the bended, as well as in the released state tested at 35.0 and 65.0 mm bending radii. **(c, d)** TEG device with SWCNT-contacts in the bended as well as in the released state tested at 35.0 and 65.0 mm bending radii. **(e)** R/R_0 ratio of the device electrical resistance as a function of the bending cycles (R_0 = R_{TEG} is the initial device resistance and R is the resistance of the device after numbers of bending cycles at the specific bending radius).

2.1.3.6 TEG device stability over time

The device V_{TEG} and R_{TEG} with SWCNT-contacts were monitored over the total duration of the experiment (**Figure 27**). As was observed, the electrical characteristics remined constant within the experimental variation over the whole duration of the stability experiment. More specifically, both V_{TEG} and R_{TEG} presented remarkable stability for 5 h of device operation in air, without any sign of performance degradation underlying phenomena such as *i)* oxidation of the Te NWs H3 hybrid semiconductor active thermoelectric material, *ii)* moisture absorption of the SWCNT-based printed junctions, or *iii)* some possible metal-semiconductor contact loss due to the continuous ΔT exposure for an extended time period where thermal stresses could destroy the device interface resulting in a dramatic increase of the device R_{TEG}. In order to further enhance the performance stability of the TEG device, encapsulation strategies could be considered depending on the application environmental demands.

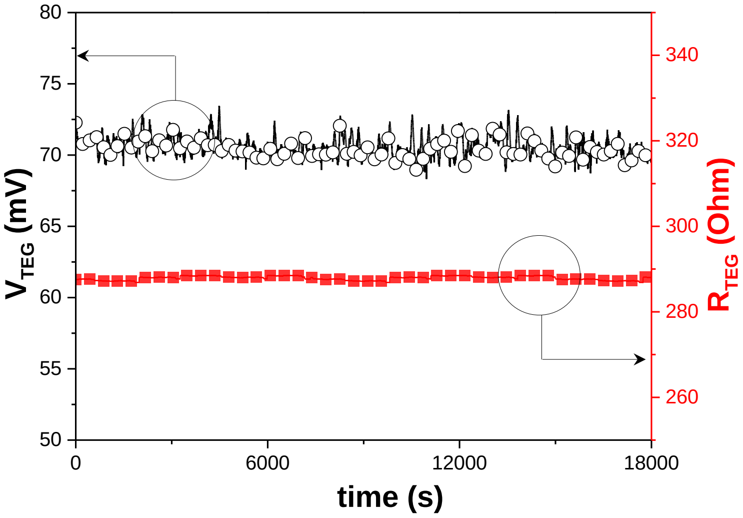

Figure 27. V_{TEG} and R_{TEG} of the TEG device with SWCNT-contact as the metallic junctions tested for its stability and performance over time upon being exposed to $\Delta T = 100$ K for 5 h (equal to 18000 s).

2.1.4 Conclusions

The tailoring of electron transport and thermal properties provides the potential for more efficient combinations of carrier mobility and phonon scattering phenomena in nanoscale organic / inorganic composites towards improved thermoelectric performance. As was demonstrated, a novel organic / inorganic hybrid may be an efficient strategy towards this goal. This hybridization combines the intrinsically low thermal conductivity of the polymer matrix and the introduced phonon-boundary scattering with the large thermal boundary resistance at the interface which synergistically hinder thermal transport. In this work, Te NWs were synthesized via a facile aqueous solvothermal reaction. The resulted nanocrystals were hybridized with commercially available PEDOT:PSS to form TE inks in various mass concentrations. The nanocomposite coatings exhibited superior film quality with enhanced thermoelectric performance. The hybrid TE ink with the highest power factor of 102.42 μW/m · K^2 was utilized for the fabrication of a flexible TEG. The TEG exhibited ~4.5 μW electrical power output at $\Delta T = 100$ K. The flexibility was substantially improved to an excellent level by the substitution of the Ag-junctions with printed SWCNT as metallic contacts. The fabricated TEG displayed remarkable device stability upon operation at $\Delta T = 100$ K for a total duration of 5 h in ambient atmosphere.

2.1.5 References

1. He J, Kanatzidis MG, Dravid VP. High performance bulk thermoelectrics via a panoscopic approach. *Mater Today* **2013**;16:166–76. https://doi.org/10.1016/j.mattod.2013.05.004.

2. Rowe DM. Thermoelectrics, an environmentally-friendly source of electrical power. *Renew Energy* **1999**;16:1251–6. https://doi.org/10.1016/s0960-1481(98)00512-6.

3. Snyder GJ, Toberer ES. 1. Complex thermoelectric materials. *Nat Mater* **2008**;7:105–14. https://doi.org/10.1038/nmat2090.

4. Han C, Tan G, Varghese T, Kanatzidis MG, Zhang Y. High Performance PbTe Thermoelectric Films by Screen Printing **2018**. https://doi.org/10.1021/acsenergylett.8b00041.

5. Russ B, Glaudell A, Urban JJ, Chabinyc ML, Segalman RA. Organic thermoelectric materials for energy harvesting and temperature control. *Nat Rev Mater* **2016**;1. https://doi.org/10.1038/natrevmats.2016.50.

6. Liebscher M, Petra P, Voit B, Heinrich G, Stamm M. Influence of a cyclic butylene terephthalate oligomer on the processability and thermoelectric properties of polycarbonate / MWCNT nanocomposites 2014;55:5381–8. https://doi.org/10.1016/j.polymer.**2014**.08.048.

7. Liebscher M, Gärtner T, Tzounis L, Mičušík M, Pötschke P, Stamm M, et al. Influence of the MWCNT surface functionalization on the thermoelectric properties of melt-mixed polycarbonate composites. *Compos Sci Technol* **2014**;101:133–8. https://doi.org/10.1016/j.compscitech.2014.07.009.

8. Tzounis L, Hegde M, Liebscher M, Dingemans T, Pötschke P, Paipetis AS, et al. All-aromatic SWCNT-Polyetherimide nanocomposites for thermal energy harvesting applications. *Compos Sci Technol* **2018**;156:158–65. https://doi.org/10.1016/J.COMPSCITECH.2017.12.030.

9. See KC, Feser JP, Chen CE, Majumdar A, Urban JJ, Segalman RA. Hybrids for Thermoelectrics **2010**:4664–7. https://doi.org/10.1021/nl102880k.

10. Yee SK, Coates NE, Majumdar A, Urban JJ, Segalman RA. Thermoelectric power factor optimization in PEDOT:PSS tellurium nanowire hybrid composites. *Phys Chem Chem Phys* **2013**;15:4024–32. https://doi.org/10.1039/c3cp44558e.

11. Xu B, Agne MT, Feng T, Chasapis TC, Ruan X, Zhou Y, et al. Nanocomposites from Solution-Synthesized PbTe-BiSbTe Nanoheterostructure with Unity Figure of Merit at Low-Medium Temperatures (500-600 K). *Adv Mater* **2017**;29. https://doi.org/10.1002/adma.201605140.

12. Zaia EW, Sahu A, Zhou P, Gordon MP, Forster JD, Aloni S, et al. Carrier Scattering at Alloy Nanointerfaces Enhances Power Factor in PEDOT:PSS Hybrid Thermoelectrics. *Nano Lett* **2016**;16:3352–9. https://doi.org/10.1021/acs.nanolett.6b01009.

13. Choi J, Lee JY, Lee SS, Park CR, Kim H. High-Performance Thermoelectric Paper Based on Double Carrier-Filtering Processes at Nanowire Heterojunctions. *Adv Energy Mater* **2016**;6. https://doi.org/10.1002/aenm.201502181.

14. Li G, Cui X, Tan C, Lin N. Solvothermal synthesis of polycrystalline tellurium nanoplates and their conversion into single crystalline nanorods. *RSC Adv* **2014**;4:954–8. https://doi.org/10.1039/c3ra41801d.

15. Mengistie DA, Chen CH, Boopathi KM, Pranoto FW, Li LJ, Chu CW. Enhanced thermoelectric performance of PEDOT:PSS flexible bulky papers by treatment with secondary dopants. *ACS Appl Mater Interfaces* **2015**;7:94–100. https://doi.org/10.1021/am507032e.

16. Wei Q, Mukaida M, Kirihara K, Naitoh Y, Ishida T. Polymer thermoelectric modules screen-printed on paper. *RSC Adv* **2014**;4:28802–6. https://doi.org/10.1039/c4ra04946b.

17. Ou C, Sangle AL, Datta A, Jing Q, Busolo T, Chalklen T, et al. Fully Printed Organic − Inorganic Nanocomposites for Flexible Thermoelectric Applications. *ACS Appl Mater Interfaces* **2018**;10:19580–7. https://doi.org/10.1021/acsami.8b01456.

18. We JH, Kim SJ, Cho BJ. Hybrid composite of screen-printed inorganic thermoelectric film and organic conducting polymer for flexible thermoelectric power generator. *Energy* **2014**;73:506–12. https://doi.org/10.1016/j.energy.2014.06.047.

19. Ni D, Song H, Chen Y, Cai K. Free-standing highly conducting PEDOT films for flexible thermoelectric generator **2019**;170:53–61. https://doi.org/10.1016/j.energy.2018.12.124.

20. Ryan JD, Mengistie DA, Gabrielsson R, Lund A, Mu C. Machine-Washable PEDOT : PSS Dyed Silk

Yarns for Electronic Textiles **2017**:0–5. https://doi.org/10.1021/acsami.7b00530.

21. Zappa W, Junginger M, Broek M Van Den, Cover CL. Is a 100 % renewable European power system feasible by 2050 ? *Appl. Energy* **2019**;234:1027–50. https://doi.org/10.1016/j.apenergy.2018.08.109.

22. Matiko JW, Grabham NJ, Beeby SP, Tudor MJ. Review of the application of energy harvesting in buildings. *Meas Sci Technol* **2014**;25. https://doi.org/10.1088/0957-0233/25/1/012002.

23. Madan D, Wang Z, Wright PK, Evans JW. Printed flexible thermoelectric generators for use on low levels of waste heat. *Appl Energy* **2015**;156:587–92. https://doi.org/10.1016/j.apenergy.2015.07.066.

24. Champier D, Favarel C, Bédécarrats JP, Kousksou T, Rozis JF. Prototype combined heater/thermoelectric power generator for remote applications. *J Electron Mater* **2013**;42:1888–99. https://doi.org/10.1007/s11664-012-2459-x.

25. Karalis G., Tsirka K., Tzounis L., Mytafides C., Koutsotolis L., Paipetis A.S., Epoxy/Glass Fiber Nanostructured p- and n-Type Thermoelectric Enabled Model Composite Interphases. *Appl. Sci.* **2020**, 10, 5352. https://doi.org/10.3390/app10155352.

26. Karalis G, Tzounis L, Lambrou E, Gergidis LN, Paipetis AS. A carbon fiber thermoelectric generator integrated as a lamina within an 8-ply laminate epoxy composite: Efficient thermal energy harvesting by advanced structural materials. *Appl Energy* **2019**;253. https://doi.org/10.1016/j.apenergy.2019.113512.

27. Tzounis L, Liebscher M, Fuge R, Leonhardt A, Mechtcherine V. P- and n-type thermoelectric cement composites with CVD grown p- and n-doped carbon nanotubes: Demonstration of a structural thermoelectric generator. *Energy Build* **2019**;191:151–63. https://doi.org/10.1016/j.enbuild.2019.03.027.

28. Weng PS, Tang HY, Ku PC, Lu LH. 50 mV-input batteryless boost converter for thermal energy harvesting. *IEEE J Solid-State Circuits* **2013**;48:1031–41. https://doi.org/10.1109/JSSC.2013.2237998.

29. Carlson EJ, Strunz K, Otis BP. A 20 mV input boost converter with efficient digital control for thermoelectric energy harvesting. *IEEE J Solid-State Circuits* **2010**;45:741–50. https://doi.org/10.1109/JSSC.2010.2042251.

30. Elefsiniotis A, Kokorakis N, Becker T, Schmid U. A thermoelectric-based energy harvesting module with extended operational temperature range for powering autonomous wireless sensor nodes in aircraft. *Sensors Actuators, A Phys* **2014**;206:159–64. https://doi.org/10.1016/j.sna.2013.11.036.

31. Samson D, Kluge M, Becker T, Schmid U. Wireless sensor node powered by aircraft specific thermoelectric energy harvesting. *Sensors Actuators, A Phys* **2011**;172:240–4. https://doi.org/10.1016/j.sna.2010.12.020.

32. Xi G, Liu Y, Wang X, Liu X, Peng Y, Qian Y. Large-Scale Synthesis, Growth Mechanism, and Photoluminescence of Ultrathin Te Nanowires. *Crystal Growth & Design*. **2006**;6:2567-70.

33. Choi J, Lee K, Park CR, Kim H. Enhanced thermopower in flexible tellurium nanowire films doped using single-walled carbon nanotubes with a rationally designed work function. *Carbon N Y* **2015**;94:577–84. https://doi.org/10.1016/j.carbon.2015.07.043.

34. Liang Z, Boland MJ, Butrouna K, Strachan DR, Graham KR. Increased power factors of organic-inorganic nanocomposite thermoelectric materials and the role of energy filtering. *J Mater Chem A* **2017**;5:15891–900. https://doi.org/10.1039/c7ta02307c.

35. Silva RR, Mejia HAG, Ribeiro SJL, Shrestha LK, Ariga K, Oliveira ON, et al. Facile synthesis of tellurium nanowires and study of their third-order nonlinear optical properties. *J Braz Chem Soc* **2017**;28:58–67. https://doi.org/10.5935/0103-5053.20160145.

36. Roy A, Amin KR, Tripathi S, Biswas S, Singh AK, Bid A, et al. Manipulation of Optoelectronic Properties and Band Structure Engineering of Ultrathin Te Nanowires by Chemical Adsorption. *ACS Appl Mater Interfaces* **2017**;9:19462–9. https://doi.org/10.1021/acsami.6b12064.

37. Park H, Son W, Lee SH, Kim S, Lee JJ, Cho W, et al. Aqueous chemical synthesis of tellurium

nanowires using a polymeric template for thermoelectric materials. *CrystEngComm* **2015**;17:1092–7. https://doi.org/10.1039/c4ce02222j.

38. Tverjanovich A, Cuisset A, Fontanari D, Bychkov E. Structure of Se–Te glasses by Raman spectroscopy and DFT modeling. *J Am Ceram Soc* **2018**;101:5188–97. https://doi.org/10.1111/jace.15758.

39. Garreau S, Duvail JL, Louarn G. Spectroelectrochemical studies of poly(3,4-ethylenedioxythiophene) in aqueous medium. *Synth Met* **2001**;125:325–9. https://doi.org/10.1016/S0379-6779(01)00397-6.

40. Farah AA, Rutledge SA, Schaarschmidt A, Lai R, Freedman JP, Helmy AS. Conductivity enhancement of poly(3,4-ethylenedioxythiophene)- poly(styrenesulfonate) films post-spincasting. J *Appl Phys* **2012**;112. https://doi.org/10.1063/1.4768265.

41. Liang F, Qian H. Synthesis of tellurium nanowires and their transport property. *Mater Chem Phys* **2009**;113:523–6. https://doi.org/10.1016/j.matchemphys.2008.07.101.

42. Ma J, Lian J, Duan X, Liu Z, Peng P, Liu X, et al. Growth of tellurium nanowire bundles from an ionic liquid precursor. *CrystEngComm* **2011**;13:2774–8. https://doi.org/10.1039/c0ce00978d.

43. Meng C, Liu C, Fan S. A promising approach to enhanced thermoelectric properties using carbon nanotube networks. *Adv Mater* **2010**;22:535–9. https://doi.org/10.1002/adma.200902221.

44. Song H, Cai K. Preparation and properties of PEDOT:PSS/Te nanorod composite films for flexible thermoelectric power generator. *Energy* **2017**;125:519–25. https://doi.org/10.1016/j.energy.2017.01.037.

45. Narducci D, Selezneva E, Cerofolini G, Frabboni S, Ottaviani G. Impact of energy filtering and carrier localization on the thermoelectric properties of granular semiconductors. *J Solid State Chem* **2012**;193:19–25. https://doi.org/10.1016/j.jssc.2012.03.032.

46. He M, Ge J, Lin Z, Feng X, Wang X, Lu H, et al. Thermopower enhancement in conducting polymer nanocomposites via carrier energy scattering at the organic-inorganic semiconductor interface. *Energy Environ Sci* **2012**;5:8351–8. https://doi.org/10.1039/c2ee21803h.

47. Tzounis L, Zappalorto M, Panozzo F, Tsirka K, Maragoni L, Paipetis AS, et al. Highly conductive ultra-sensitive SWCNT-coated glass fiber reinforcements for laminate composites structural health monitoring. *Compos Part B Eng* **2019**;169:37–44. https://doi.org/10.1016/j.compositesb.2019.03.070.

48. Song H, Cai K. Preparation and properties of PEDOT:PSS/Te nanorod composite films for flexible thermoelectric power generator. *Energy* **2017**;125:519–25. https://doi.org/10.1016/j.energy.2017.01.037.

49. Jin Bae E, Hun Kang Y, Jang KS, Yun Cho S. Enhancement of Thermoelectric Properties of PEDOT:PSS and Tellurium-PEDOT:PSS Hybrid Composites by Simple Chemical Treatment. *Sci Rep* **2016**;6:1–10. https://doi.org/10.1038/srep18805.

50. Morgan KA, Tang T, Zeimpekis I, Ravagli A, Craig C, Yao J, et al. High-throughput physical vapour deposition flexible thermoelectric generators. *Sci Rep* **2019**;9:1–9. https://doi.org/10.1038/s41598-019-41000-y.

51. Nakai Y, Honda K, Yanagi K, Kataura H, Kato T, Yamamoto T, et al. Giant Seebeck coefficient in semiconducting single-wall carbon nanotube film. *Appl Phys Express* **2014**;7. https://doi.org/10.7567/APEX.7.025103.

52. Cheng Z, Liu L, Xu S, Lu M, Wang X. Temperature dependence of electrical and thermal conduction in single silver nanowire. *Sci Rep* **2015**;5:1–12. https://doi.org/10.1038/srep10718.

2.2 Supporting information

In order to carry out Hall-effect measurements as a means to determine the carrier concentration and mobility of H0, H1, H2 and H3 thermoelectric materials, as well as that of PEDOT:PSS films of approx. 2 μm thickness were fabricated initially. Each ink was deposited via drop-casting using the same coating parameters and ink concentration on square-shaped glass substrates, while silver contacts were deposited at the substrate four corners in order to contact the samples and perform the Hall-effect experiments. **Figure S1** shows representatively the SEM image of the focused ion beam milled depth profile showing a micro-scale film thickness of approx. 2 μm utilized in the Hall-effect measurement calculations for the carrier concentration (n) (cm^{-3}) and carrier mobility (μ) (cm^2/V$_s$).

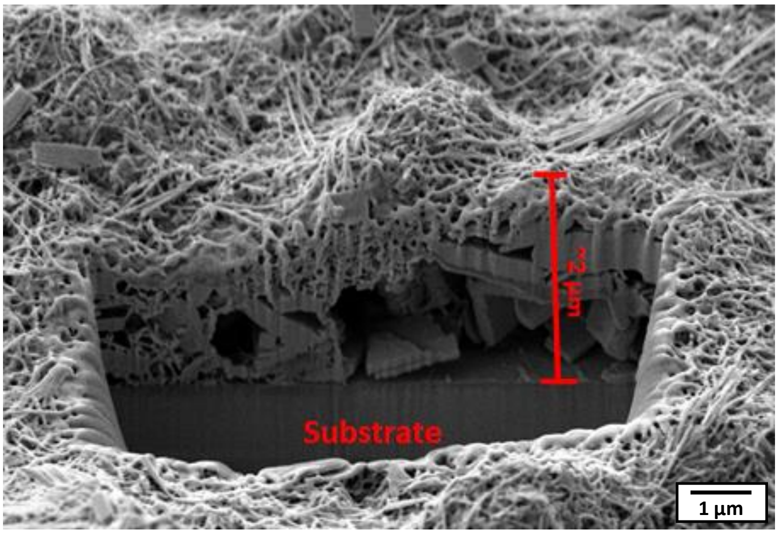

Figure S1. Representative SEM image of the focused ion beam milled depth profile showing a micro-scale film thickness of approx. 2 μm (representative for the films fabricated by drop-casting of H0, H1, H2 and H3 employing the same ink concentrations and used for the Hall-effect measurements).

Figure S2a shows the set-up used to generate the in-plane temperature difference across the TEG consisting of a "hot" and "cold" block thermal gradient stage. All the main components used in this custom-made set-up could be seen. Namely, the cold block sustained two metal plates / support sustained at room temperature, while the hot block temperature was controlled via a hot plate at specific temperature to create the ΔT. The temperature of the hot block was continuously measured with K-type thermocouples to determine the temperature difference, ΔT. For all measurements of V_L and I_L used to derive the P_{out} upon applying different load resistances (set-up shown in **Figure S2a-b-c**), the temperature difference at the TEG device has been measured using an IR-thermometer, while more details of the measurement are included in the experimental section of the main part of the manuscript.

A homemade power output experimental set-up has been used in this work shown in **Figure S2b-c**. In order to examine the TEG device power output characteristics at different temperature gradients (50 and 80 and 100 K) as a function of different in-series connected external load resistances (R_L). Below, it can be schematically seen the custom-built set-up with the TEG device connected the different load resistances, as well as the Amp meter and two voltage meters used, one before the Amp meter and one afterwards to check if the Amp meter internal resistance affects the voltage on the R_L by any potential voltage drop. No variations in voltage have been observed, while this testing has been performed just for the experimentalists own proof. This set-up gives the open circuit voltage (V_{oc} or V_{TEG}, otherwise defined), as well as the short circuit current (I_{sc}) upon the voltage meter and the Amp meter are connected, respectively while the jumper (red jumper shown in **Figure S2c**) is not connected in any of the load resistances. For the power output measurements, the jumper is placed over the various load resistances and then the voltage and Amp meter are used to measure the voltage and current (V_L, I_L) on the load resistance, allowing the calculation of the power output as $P_{out} = V_{L.} \cdot I_L$ upon applying different external specific load resistances.

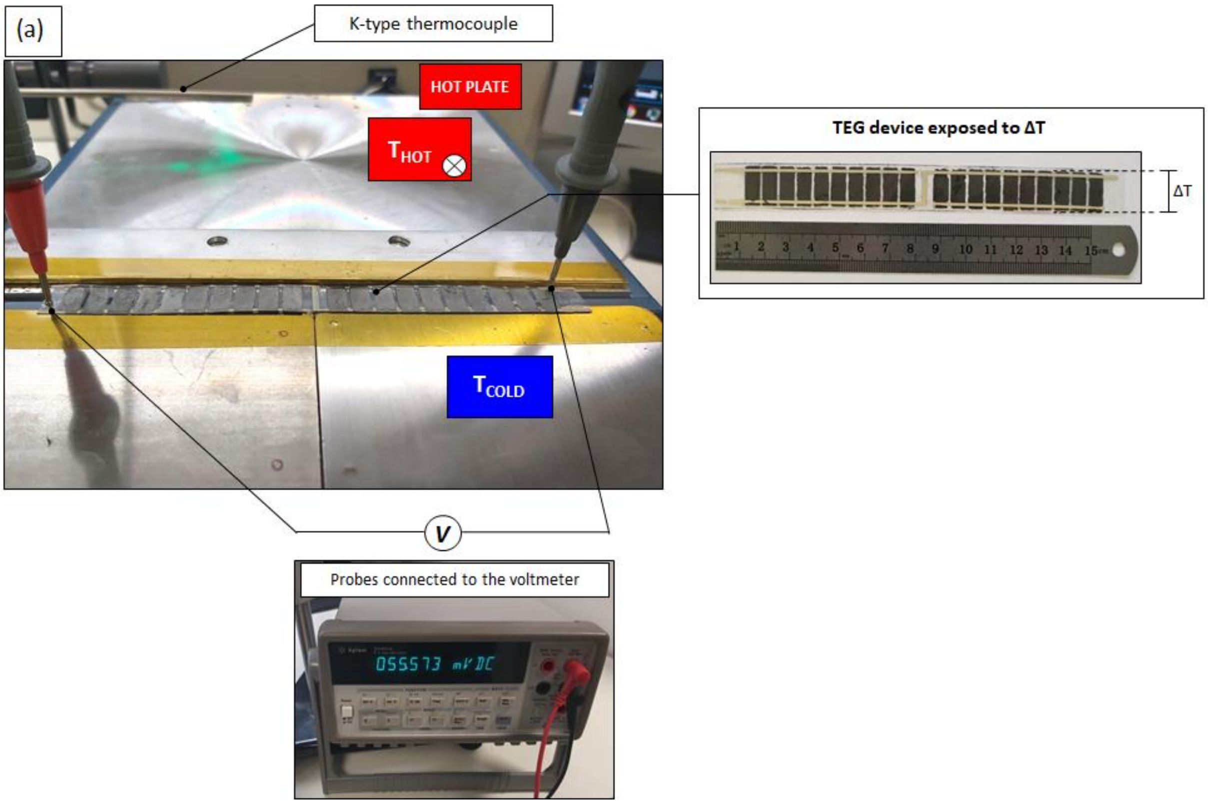

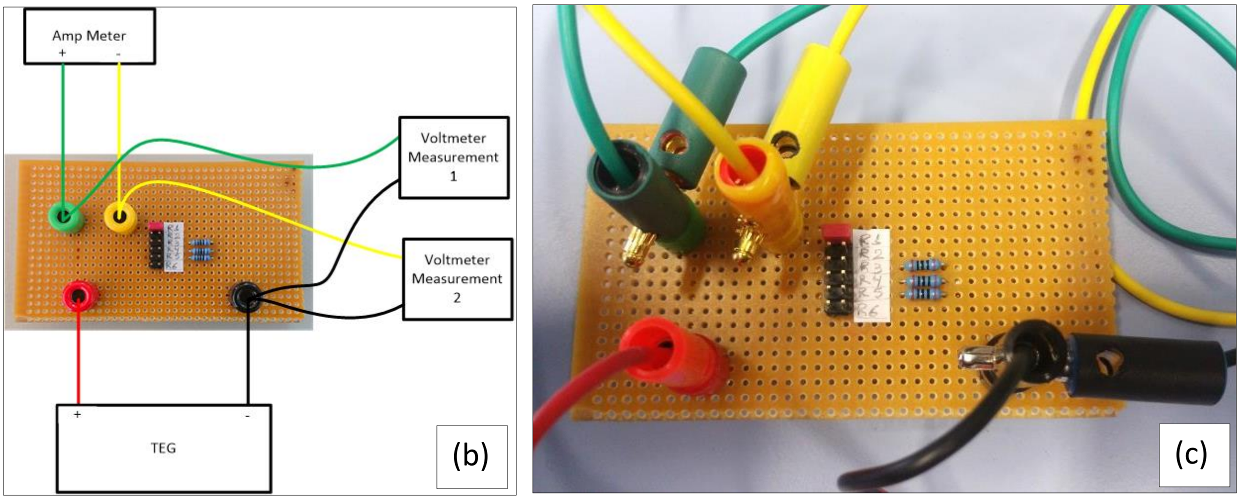

Figure S2. (a) Set-up used to generate the in-plane temperature difference across the TEG consisting of a “hot” and “cold” block thermal gradient stage, **(b, c)** homemade power output experimental set-up to examine the TEG device power output characteristics at different temperature gradients (50 and 80 and 100 K) as a function of different in-series connected external load resistances (R_L).

Chapter 3

Physicochemical and Micromechanical study of functional reinforcing fibers

---

Part of the results included in **Chapter 3** have been published at the *Key Engineering Materials* peer-reviewed scientific journal as part of the study "Hierarchical reinforcing fibers for energy harvesting applications - A strength study" and can be found under *https://doi.org/10.4028/www.scientific.net/KEM.827.252*. Additionally, part of the results has been published at the peer-reviewed scientific Journal of *Applied Sciences* under the title "Epoxy / glass fiber nanostructured p- and n-type thermoelectric-enabled model composite interphases" and can be found under *https://doi.org/10.3390/app10155352.*

3. Physicochemical and Micromechanical study of functional reinforcing fibers

3.1 Hierarchical reinforcing fibers for energy harvesting applications - A strength study

Abstract

This work is concerned with the study of the strength of nano-coated reinforcing fibers. In more detail, glass fibers (GFs) were coated with an efficient thermoelectric (TE) ink in order to create multifunctional reinforcing fibers for advanced composite structural applications. The main scope is to evaluate the fracture properties of the TE-enabled hierarchical GFs. The hybrid nanocrystal TE ink was synthesized via a solvothermal reaction and further fully characterized in coating form. The morphology and wetting properties of the TE ink deposition onto GFs were evaluated via SEM and contact angle (CA) measurements. Enhanced values by 19.4 % in tensile strength (TS) for the coated GFs compared to the reference are being reported, measured at single fiber level, resulting in an 8.9 % enhanced interfacial shear strength (IFSS).

Keywords**:** Hierarchical fibers; Energy harvesting; Micromechanical characterization; Fiber strength; Multifunctional model composites; Thermoelectric inks

Highlights**:**

- Hierarchical glass fibers with 19.4 % enhanced tensile strength
- Functional model composites with 8.9 % enhanced interfacial shear strength
- TE-enabled model composites with Seebeck coefficient of +76.5 μV/K

Graphical Abstract

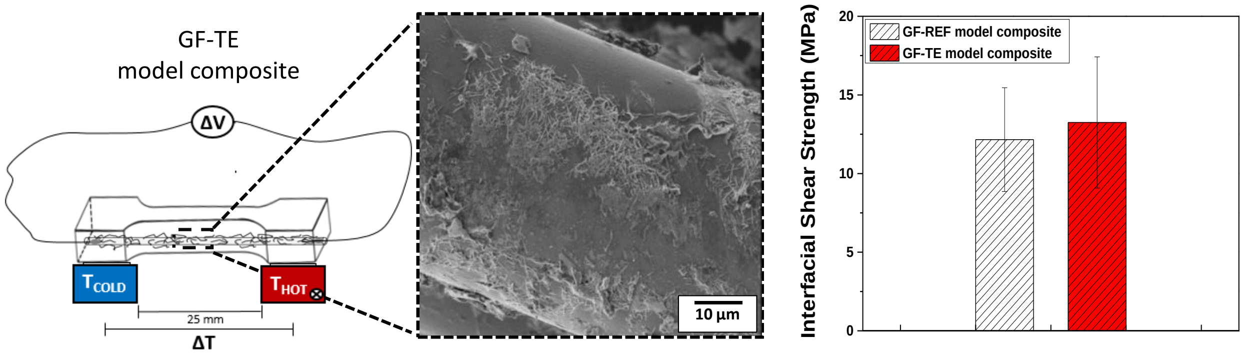

3.1.1 Introduction

Structural reinforced polymers constitute an extremely interesting field of research due to their potential for exploitation of various additional functionalities. Understanding of their mechanical behavior requires the study of the interfaces, the common physico-chemical areas between the distinct phases [1-3]. This fact is vitally important for the design of every kind of composite material, as the failure most times is determined from the interfacial properties. A biomimetic approach towards multiscale reinforcements with improved wettability, increased adhesion, more robust mechanical interlocking and enhanced interfacial stress transfer due to the emergence of additional energy dissipation mechanisms related to the introduction of nanophases such as carbon nanotubes (CNTs) [4-8]. The hierarchical approach has been widely investigated for the transformation of conventional reinforcing fibers to hierarchical structures with various functional capabilities such as energy harvesting [9-11].

The technologies that facilitate the conversion of heat to electricity (*e.g.,* thermoelectricity) are a good candidate for energy harvesting in the aforementioned applications. An electric current is created through the diffusion of charge carriers, either electrons or holes from the hot side of the material to the cold. Thermoelectric (TE) energy conversion is based on the Seebeck effect which permits the generation of electricity directly from a material upon subjecting it to a sufficient temperature gradient. The Seebeck coefficient (S) is the voltage rate of change $S = \Delta V/\Delta T$, where ΔV is the electric potential difference created by a temperature gradient ΔT. The dimensionless figure of merit (ZT) $ZT = (\sigma \cdot S^2) \cdot T/\kappa$, where κ is the thermal conductivity and T is the absolute temperature, is also used to define the thermoelectric efficiency. Consequently, it can be realized that the combination of high electrical conductivity and Seebeck coefficient, coupled with low thermal conductivity leads to an optimum TE efficiency [12, 13]. Research on the TE performance of organic materials can be classified into 4 different synthesis strategies. These strategies involve the study of nanocomposites including various combinations of materials *i)* conducting polymers / inorganic materials, *ii)* conducting polymers / graphitic nanostructures, *iii)* insulating polymers / inorganic materials and *iv)* insulating polymers / graphitic nanostructures. A key factor for higher TE efficiency is the use of low-bandgap semiconducting nanowires, nanorods and nanocrystals which are characterized by a reduced thermal conductivity [14-18].

In this study, the mechanical properties (strength and strain to fracture) of glass fibers (GFs) coated with TE nanoparticles were examined in comparison to the reference uncoated GFs. More specifically, an efficient hybrid nanoparticle-based TE ink was synthesized in order to create chemically stable and homogenous functional hierarchical coatings onto the reinforcing GFs. The

GF tensile strength (TS) of the TE-coated GFs was evaluated via single fiber tensile tests according to ASTM C1557-14 [19]. The single GF TS values are critical for the calculation of the interfacial shear strength (IFSS) via the single fiber fragmentation test (SFFT). The TE functionality was evaluated at model composite level.

3.1.2 Experimental section

3.1.2.1 Materials

Glass fibers (GFs) 1062 Multi-End Roving (NEG) were employed for this study with a tensile strength of 2300-2400 MPa and tensile modulus of 72 GPa, specifically designed for use with epoxy resin systems in applications that require high mechanical strength and corrosion resistance such as filament wound pipe. Also, the filament diameter was 13.3 ± 0.6 μm as stated by the manufacturer's technical data specification. The thermoset matrix employed for the fabrication of the model composites was the two component MY-750 / HY-951 epoxy system (Huntsman, MY-750: unmodified liquid epoxy resin, and HY-951: triethylene tetramine curing agent), which exhibits a tensile strength of 75-90 MPa along with an elongation at a break of 3-4 % and a modulus of 3.5-4.0 GPa. Sodium tellurite (Na_2TeO_3, ~100 mesh, >99 % purity, ascorbic acid (reagent grade with 99 % purity), Poly(3,4-ethylenedioxythiophene)-poly (styrenesulfonate) – PEDOT:PSS highly conductive grade (Orgacon™ ICP 1050 Agfa, 1.1 wt % in H_2O) from Sigma Aldrich were utilized for this study. RS Pro silver (Ag) loaded epoxy conductive paste was used for the creation of adhesive ohmic contacts. All chemicals were analytical grade and used as received without further purification. Distilled water (d-H_2O) was used throughout all the different processes in this work. All chemical reagents were used as received.

3.1.2.2 Synthesis and development of TE ink

In a reaction three-necked round flask 4.93 g ascorbic acid was dissolved in 200 mL of distilled water followed by addition of 2.5 mL PEDOT:PSS. After the homogenization of the solution, 0.277 g Na_2TeO_3 were added to the vigorously stirred mixture. The mixture was then raised to 90 °C for 20 h and then left to cool down to room temperature. The cleaning process consisted of centrifugation at 9000 rpm for 1 h and removal the crude reaction mixture, by pouring off the PEDOT:PSS rich supernatant. The final product was collected with vacuum assisted filtration through a PVDF membrane filter (pore size 45 μm). Finally, the produced nanoparticle-based powder was re-dispersed in distilled water in the proper ratio (~20 mg/mL) and then was drop-casted into films for measurements.

3.1.2.3 *Production of TE-enabled hierarchical GFs and model composites*

TE ink depositions were performed on GF pre-stretched yarns with simple deposition-drop casting at a 30^{o} angle on a heated substrate contributing to the drying process. Then, single GFs (reference and TE-coated) and GF tows (coated) were impregnated with epoxy resin in dog-bone molds for the manufacturing of model composite single fiber fragmentation test (SFFT) specimens and specimens for the TE measurements, respectively.

3.1.3 Results and Discussion

3.1.3.1 *TE ink-coating characterization*

The water-soluble nanoparticle-based ink was produced in order to coat the reinforcing GFs. These coatings were physico-chemically characterized initially in film forms and then as coatings onto GFs for the production of the hierarchical structures. The Raman (Labram HR-Horiba) spectra and the XRD (Bruker D8 ADVANCE) analysis indicated the presence of both highly crystallized Te particles as well as the crystalline PEDOT:PSS polymer via the appearance of well-defined peaks vibrational modes and diffraction patterns [20, 21], respectively (**Figure 28b-c**).

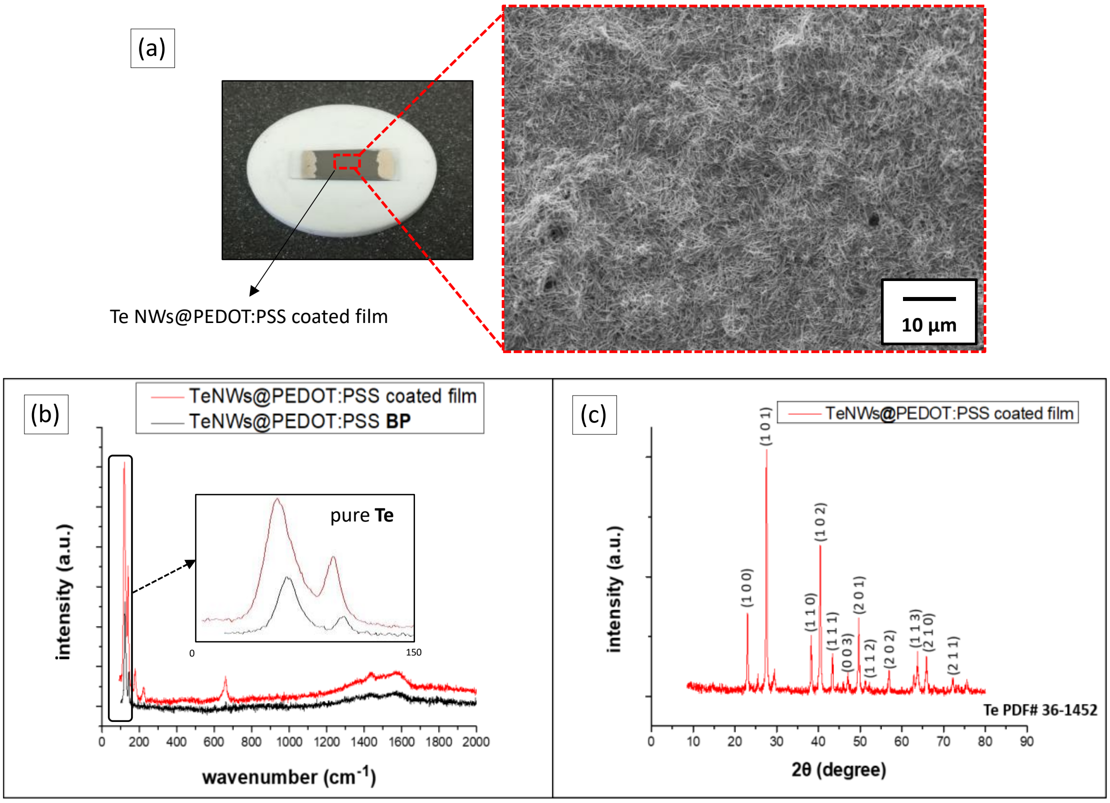

Figure 28. (a) SEM image, **(b)** Raman spectroscopy and **(c)** XRD measurements for the produced TE hybrid ink on film form.

3.1.3.2 Measurements of TE-enabled hierarchical GFs and model composites

Tests were carried out to assess the wetting capability of the TE ink when deposited on the GFs by contact angle measurements. Moreover, SEM (JEOL JSM 6510 LV) was used for the TE hierarchical structure inspection. Finally, TE measurements (in-house manufactured set-up was used to measure the Seebeck voltage) were carried out for evaluating the GF-TE model composite Seebeck coefficient ($S = +76.5 \pm 0.5$ μV/K), as presented in **Figure 29**.

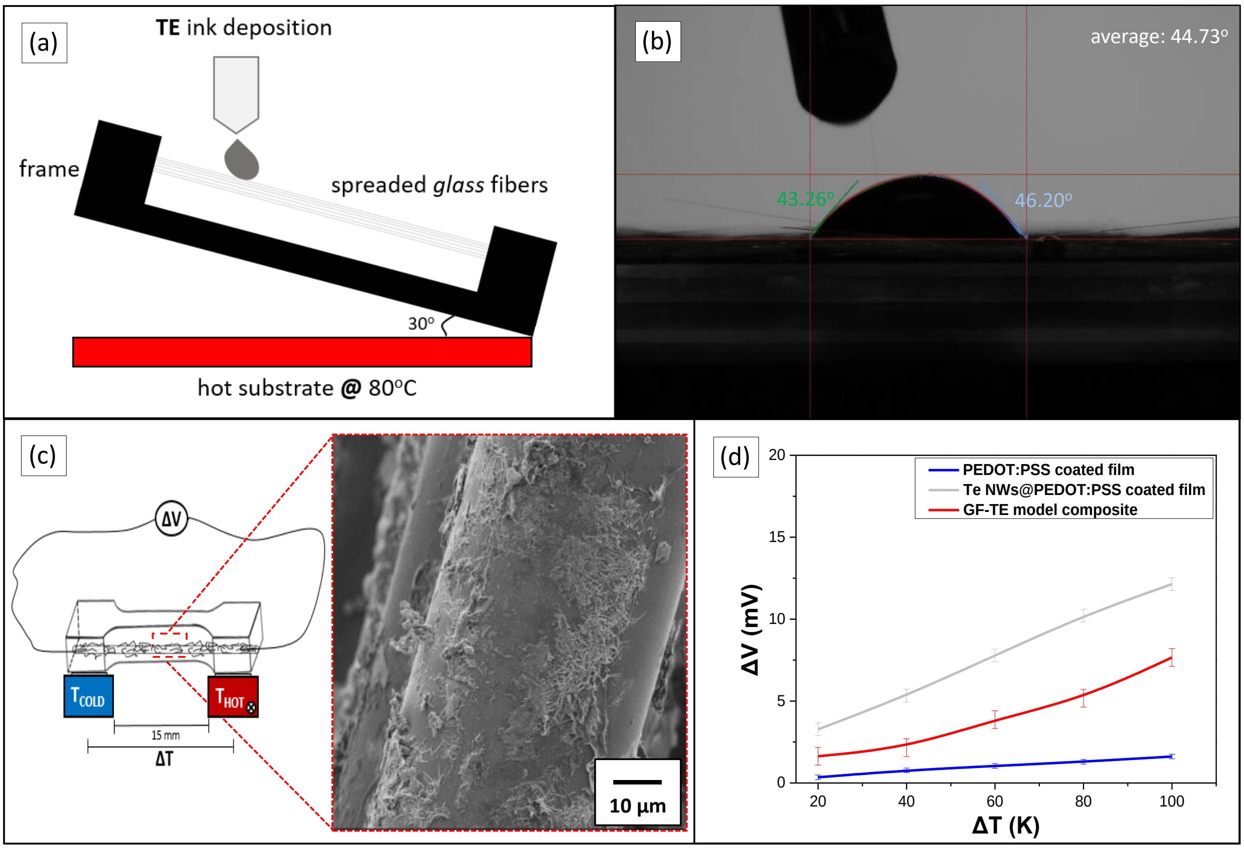

Figure 29. (a) schematic of the TE-enabled GFs fabrication process, **(b)** contact angle measurements for the TE ink wetting properties onto GFs, **(c)** SEM morphology evaluation of the coated GFs and **(d)** Seebeck voltage for the produced hierarchical structure as model composite.

3.1.3.3 TE-coated GF tensile strength and interfacial shear strength evaluation

The number of filaments tested from each category was about 30 for 25 mm length, but cases which exhibited slippage or nonlinearity were excluded, and thus 15 GFs the studied length are presented. Additionally, the Weibull shape, *m*, and scale parameters were calculated for all the tested GFs by considering the following statistical analysis [22]. If a GF filament is regarded as a single chain of units with length L_0, which fail at stresses equal to σ_{fu}, then the cumulative probability of failure for the entire chain is given by the Weibull distribution from **Equation 1**:

$$P=1-\exp[-L(\sigma/\sigma_0)^{m}] \quad \textbf{(1)}$$

where σ is the applied stress, σ_0 is a scale parameter, and m is the dimensionless Weibull modulus. **Equation 1** can also be written in linear form as:

$\ln(-1(1-P))-\ln(L)=m\ln(\sigma)-m\ln(\sigma_0)$ **(2)**

Thus, if the ln(-ln(1-P)) is plotted against ln(σ), then the Weibull modulus can be calculated from the slope of the curve while the scale parameter can be estimated from the value of the intercept through **Equation 3**:

$\sigma_0=\exp^{-\text{intercept}/m}$ **(3)**

plots of the hierarchical GFs and the reference were plotted using the **Equation 4:**

$\ln\ln(1/1-P)=m\ln\sigma-m\ln\sigma_0$ **(4)**

The probability of failure was calculated in this study by the maximum likelihood estimator which is given by the **Equation 5**:

$P=\sigma-0.5/n$ **(5)**

where σ is the failure stress of each GF and n is the number of tested samples.

The diameters of the TE-coated GFs were determined via optical microscopy to be equal to 16.80 ± 1.72 μm, value which is being used for the GF strength calculations.

The TE-coated GFs with the TE nanoparticles resulted in a 19.4 % enhancement of their strength, as can be seen in **Table 4**. On the other hand, they were presented much more brittle than the reference GFs, being able to undertake almost half of the strain until fracture.

Table 4. Micromechanical properties for the examined single GFs.

specimen	Strength (MPa)	Strain (%)	Weibull shape, m	Weibull scale, σ	R^2
reference GFs	2465.71 ± 1019.50	0.021 ± 0.006	2.47597	2798.31	0.96
TE-coated GFs	2943.52 ± 603.49	0.012 ± 0.007	5.44334	3190.63	0.98

Furthermore, a statistical analysis using the Weibull distribution was performed for both the reference and the TE modified GF populations and the results are presented in **Figure 30**. The linear regression indicated that the tested GF populations can be effectively described by a two parameter Weibull distribution (R^2: 0.96 and 0.98, respectively). The coating procedure led to notable enhancement of both the Weibull shape and scale parameters (**Table 4)**, indicating limited scattering in the fracture stress data and less weak filaments for the TE-coated GFs in comparison to the reference GFs. Concerning the TS (σ_{fu}) of the uncoated GFs (reference), the exported values were in a good agreement with the manufacturer's specifications.

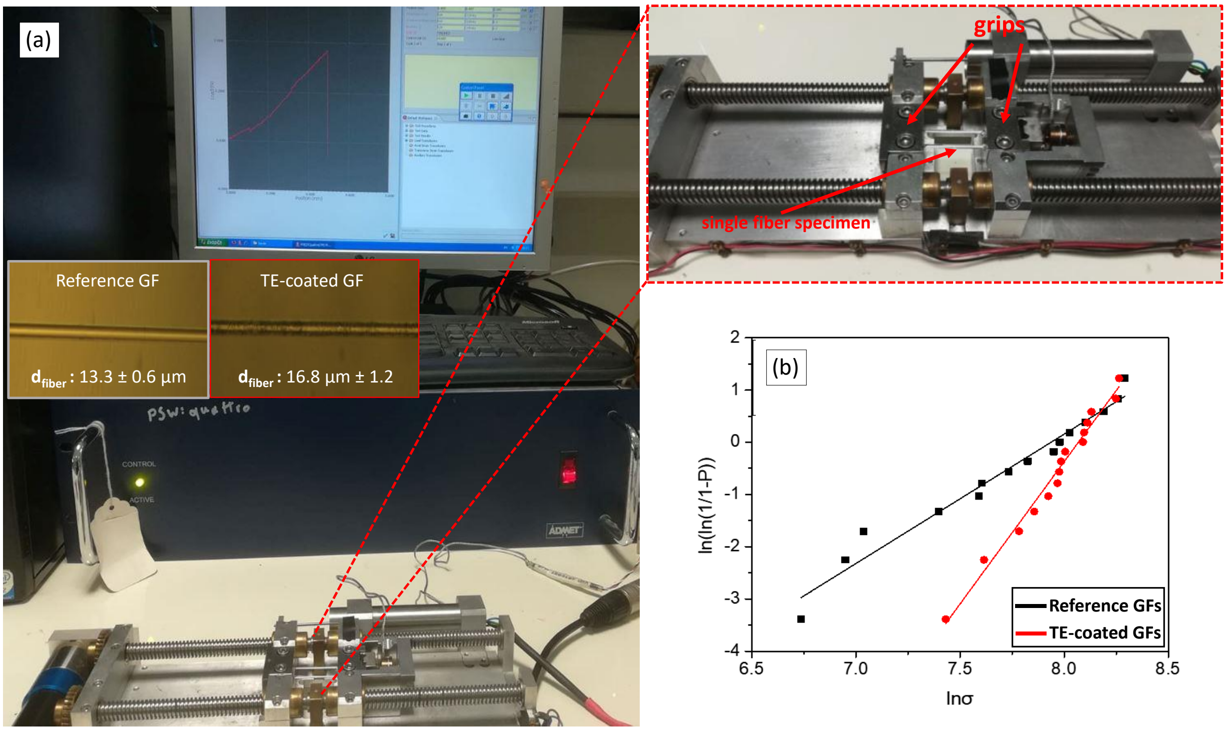

Figure 30. (a) the custom-made experimental set-up used for the single GF-tensile tests (inset: optical microscope images of both examined single GFs), **(b)** Weibull analysis distribution for the tested GFs.

Subsequently, SFFT reveal an 8.9 % enhancement of IFSS for the resulted functional nanostructured interphases compared to the reference ones, resulting in from 6 successfully tested specimens for each category. **Figure 31** summarizes the both the SFFT testing procedure, as well as the respective polarized optical (record of single fiber fragments) and SEM microscopy images (fractography for the evaluation of failure process). The σ_{IFSS} was determined using the **Equation 6**: $\tau_{rz} = \sigma_{fu}/2 \cdot (d_f/l_c)$ **(6)** [2], where l_c is the critical length (4/3 l_f, l_f: average fragment length), as shown in **Figure 31g**.

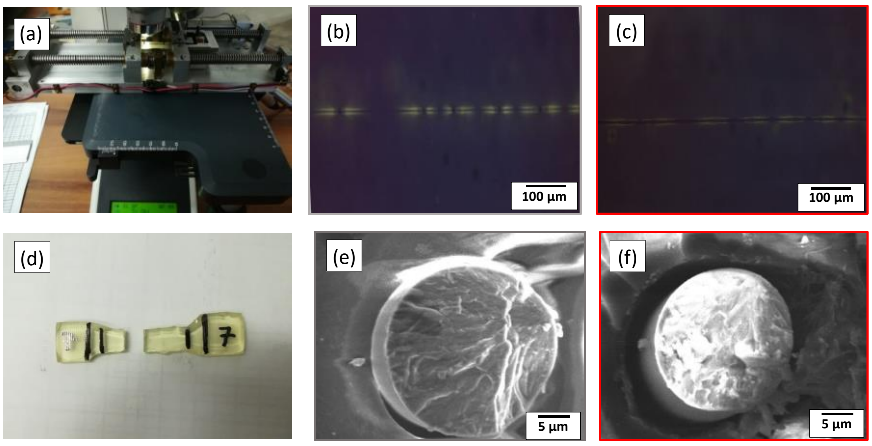

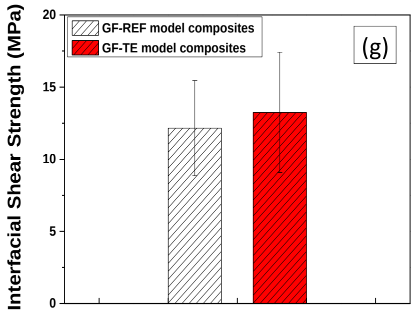

Figure 31. (a) the experimental configuration for SFFT, **(b, c)** polarized optical microscopy images for the GF-REF and the GF-TE model composite specimens, respectively, **(d)** tested SFFT specimen and the corresponding **(e, f)** SEM fractography images for the GF-REF and the GF-TE model composite specimens, respectively, **(g)** comparative IFSS graph.

3.1.4 Conclusions

Efficient TE-coated GF hierarchical reinforcements were produced during this study by initially developing TE inks using a wet chemical process and then coating the GF's surfaces. The synthesized TeNWs@PEDOT:PSS hybrid was characterised via XRD and Raman measurements to verify the successful synthesis. Then, the TE response of the produced GF-TE model composites was evaluated by subjecting the material to a temperature difference of 100 K, exhibiting a Seebeck coefficient of +76.5 ± 0.5 μV/K. Finally, the effects of the TE coating process on the mechanical properties of single GFs were assessed via single fiber tensile tests and Weibull analysis. The TE-coated GFs presented an enhanced by 19.4 % TS in comparison to the reference GFs. The evaluated GF strength utilized for evaluating the interface of the TE-coated GFs with the epoxy resin matrix via SFFT, resulting an enhanced by 8.9 % IFSS with respect to the reference ones.

3.1.5 References

1. Jin, S.Y.; Young, R.J.; Eichhorn, S.J. Controlling and mapping interfacial stress transfer in fragmented hybrid carbon fibre-carbon nanotube composites. *Compos. Sci. Technol.* **2014**, *100*, 121–127, doi:10.1016/j.compscitech.2014.05.034.
2. Paipetis, A., Galiotis, C., Liu, Y. C. and Nairn, J. Stress Transfer from the Matrix to the Fibre in a Fragmentation Test: Raman Experiments and Analytical Modeling, *Journal of Composite Materials* **1999**, 33(4), p.377.
3. Tsirka, K.; Karalis, G.; Paipetis, A.S. Raman Strain Sensing and Interfacial Stress Transfer of Hierarchical CNT-Coated Carbon Fibers. *J. Mater. Eng. Perform.* **2018**, *27*, 5095–5101, doi:10.1007/s11665-018-3532-2.
4. Wu, G.; Ma, L.; Liu, L.; Wang, Y.; Xie, F.; Zhong, Z.; Zhao, M.; Jiang, B.; Huang, Y. Interfacially reinforced methylphenylsilicone resin composites by chemically grafting multiwall carbon nanotubes onto carbon fibers. *Compos. Part B Eng.* **2015**, *82*, 50–58, doi:10.1016/j.compositesb.2015.08.012.
5. An, Q.; Rider, A.N.; Thostenson, E.T. Electrophoretic deposition of carbon nanotubes onto carbon-fiber fabric for production of carbon/epoxy composites with improved mechanical properties. *Carbon*

N. Y. **2012**, *50*, 4130–4143, doi:10.1016/j.carbon.2012.04.061.

6. Moaseri, E.; Karimi, M.; Maghrebi, M.; Baniadam, M. Two-fold enhancement in tensile strength of carbon nanotube-carbon fiber hybrid epoxy composites through combination of electrophoretic deposition and alternating electric field. *Int. J. Solids Struct.* **2014**, *51*, 774–785, doi:10.1016/j.ijsolstr.2013.11.007.
7. Mei, H.; Zhang, S.; Chen, H.; Zhou, H.; Zhai, X.; Cheng, L. Interfacial modification and enhancement of toughening mechanisms in epoxy composites with CNTs grafted on carbon fibers. *Compos. Sci. Technol.* **2016**, *134*, 89–95, doi:10.1016/j.compscitech.2016.08.010.
8. Moaseri, E.; Karimi, M.; Baniadam, M.; Maghrebi, M. Enhancement in mechanical properties of multi-walled carbon nanotube–carbon fiber hybrid epoxy composite: effect of electrostatic repulsion. *Appl. Phys. A Mater. Sci. Process.* **2016**, *122*, 1–8, doi:10.1007/s00339-016-9600-2.
9. González, C.; Vilatela, J.J.; Molina-Aldareguía, J.M.; Lopes, C.S.; LLorca, J. Structural composites for multifunctional applications: Current challenges and future trends. *Prog. Mater. Sci.* **2017**, *89*, 194–251, doi:10.1016/j.pmatsci.2017.04.005.
10. Liang, D.; Yang, H.; Finefrock, S.W.; Wu, Y. Flexible Nanocrystal-Coated Glass Fibers for High-Performance Thermoelectric Energy Harvesting. **2012**, 8–13.
11. Tzounis L, Liebscher M, Tzounis A, Petinakis E, Paipetis AS, Mäder E, et al. CNT-grafted glass fibers as a smart tool for epoxy cure monitoring, UV-sensing and thermal energy harvesting in model composites. *RSC Adv*. 2016;6(60):55514–25. DOI=C6RA09800B
12. Snyder, G.J.; Toberer, E.S. 1. Complex thermoelectric materials. *Nat Mater* **2008**, *7*, 105–114, doi:10.1038/nmat2090.
13. Vineis, C.J.; Shakouri, A.; Majumdar, A.; Kanatzidis, M.G. Nanostructured thermoelectrics: Big efficiency gains from small features. *Adv. Mater.* **2010**, *22*, 3970–3980, doi:10.1002/adma.201000839.
14. Yu, C.; Choi, K.; Yin, L.; Grunlan, J.C. Correction to Light-Weight Flexible Carbon Nanotube Based Organic Composites with Large Thermoelectric Power Factors. *ACS Nano* **2013**, *7*, 9506–9506, doi:10.1021/nn404924h.
15. Nonoguchi, Y.; Ohashi, K.; Kanazawa, R.; Ashiba, K.; Hata, K.; Nakagawa, T.; Adachi, C.; Tanase, T.; Kawai, T. Systematic conversion of single walled carbon nanotubes into n-type thermoelectric materials by molecular dopants. *Sci. Rep.* **2013**, *3*, 1–7, doi:10.1038/srep03344.
16. See, K.C.; Feser, J.P.; Chen, C.E.; Majumdar, A.; Urban, J.J.; Segalman, R.A. Water-processable polymer-nanocrystal hybrids for thermoelectrics. *Nano Lett.* **2010**, *10*, 4664–4667, doi:10.1021/nl102880k.
17. Meng, Q.; Cai, K.; Du, Y.; Chen, L. Preparation and thermoelectric properties of SWCNT/PEDOT:PSS coated tellurium nanorod composite films. *J. Alloys Compd.* **2019**, *778*, 163–169, doi:10.1016/j.jallcom.2018.10.381.
18. Zaia, E.W.; Sahu, A.; Zhou, P.; Gordon, M.P.; Forster, J.D.; Aloni, S.; Liu, Y.S.; Guo, J.; Urban, J.J. Carrier Scattering at Alloy Nanointerfaces Enhances Power Factor in PEDOT:PSS Hybrid Thermoelectrics. *Nano Lett.* **2016**, *16*, 3352–3359, doi:10.1021/acs.nanolett.6b01009.
19. ASTM C 1557, Standard Test Method for Tensile Strength and Young's Modulus of Fibers, Astm. **2014** 1–10. doi:10.1520/C1557-14.2.
20. Li, G.; Cui, X.; Tan, C.; Lin, N. Solvothermal synthesis of polycrystalline tellurium nanoplates and

their conversion into single crystalline nanorods. *RSC Adv.* **2014**, *4*, 954–958, doi:10.1039/c3ra41801d.

21. Song, H.; Cai, K. Preparation and properties of PEDOT:PSS/Te nanorod composite films for flexible thermoelectric power generator. *Energy* **2017**, *125*, 519–525, doi:10.1016/j.energy.2017.01.037.

22. van der Zwaag, S. Concept of filament strength and the Weibull modulus. *J. Test. Eval.* **1989**, *17*, 292–298, doi:10.1520/jte11131j.

3.2 Epoxy / glass fiber nanostructured p- and n-type thermoelectric-enabled model composite interphases

Abstract

This experimental study is associated with the modification of glass fibers (GFs) with efficient, organic, functional, thermoelectrically-enabled coatings. The thermoelectric (TE) behavior of the coated GF tows with either inherent p-type semiconductor single wall carbon nanotubes (SWCNT) or the n-type molecular doped SWCNT were examined within epoxy resin matrix in detail. The corresponding morphological, thermogravimetric, spectroscopic, and thermoelectric measurements were assessed in order to characterize the produced functional interphases. For the p-type model composites, the Seebeck coefficient was +16.2 μV/K which corresponds to a power factor (*PF*) of 0.02 $\mu W/m \cdot K^2$ and for the n-type −28.4 μV/K which corresponds to power factor of 0.12 $\mu W/m \cdot K^2$. The p–n junction between the model composites allowed for the fabrication of a single pair thermoelectric element generator (TEG) demonstrator. Furthermore, the stress transfer at the interphase of the coated GFs was studied by tow pull-out tests. The reference GF tows presented the highest interfacial shear stress (IFSS) of 42.8 MPa in comparison to the p- and n-type SWCNT coated GF model composites that exhibited reduced IFSS values by 10.1 % and 28.1 %, respectively.

Keywords: Seebeck effect; Model composites; SWCNT; Organic thermoelectrics; Functional interphases; Thermal energy harvesting

Highlights:

- p-type TE-enabled GF / epoxy nanostructured interphases
- n-type TE-enabled GF / epoxy nanostructured interphases

Graphical Abstract

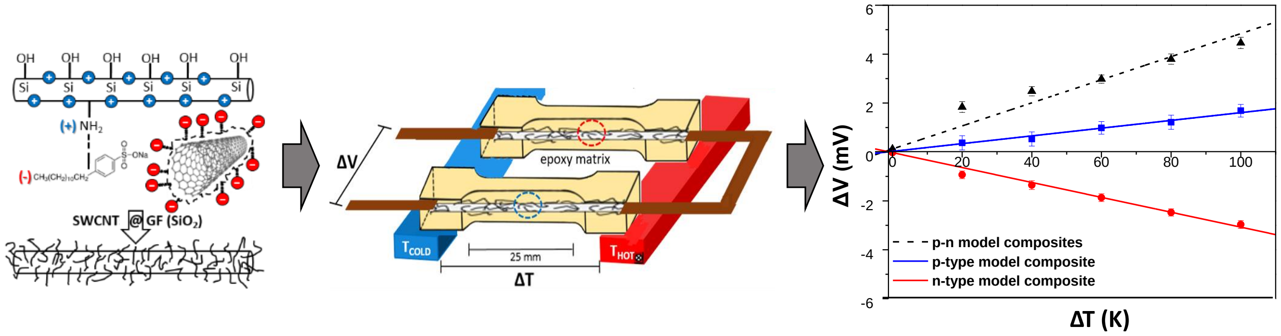

3.2.1 Introduction

During the last decades, the growing demand for the utilization of lightweight, high-performance structural composite materials has rapidly increased in various commercial sectors, such as the aerospace and automotive industries. Fiber reinforced polymers constitute an extremely interesting field of research due to their potential for the exploitation of additional functionalities. Tailoring or "architecting" the material in relation to both its structural and non-structural services is an inherent ability of advanced composites and is rapidly emerging technology for their next generation. Understanding their mechanical behavior requires the study of the interface, the common physicochemical areas between the distinct phases (reinforcing and matrix materials) [1,2]. This is a prerequisite for the design of a composite material, as its behavior is most of the times governed by its interfacial properties [3].

The approach of blending nano-scaled reinforcements into the matrix of micro-scale reinforced systems, with a view to enhancing both the matrix dominated properties as well as imparting multifunctionality, has been extensively studied in the last decade. Additional functionalities include both capabilities that relate to structural integrity, such as wear resistance, morphing, or self-healing, as well as non-structural ones, such as inherent structural health monitoring, sensing and actuation, power harvesting, and power storage [4–7].

In an alternative approach, the nanomaterials are deposited directly onto the surface of reinforcing fibers, such as carbon, aramid, and glass fibers (GFs), and this has triggered a new class of functional materials, where the nanoscale functional reinforcement is following the architecture of the microscale reinforcement. This leads to a biomimetic 'hierarchical' approach towards multiscale reinforcements with improved wettability, increased adhesion, robust interlocking mechanisms, and enhanced interfacial stress transfer related to the introduction of nanophases such as carbon nanotubes (CNTs) [8–12]. The resultant hierarchical interphases except for the modified mechanical properties also transfuse extra functionalities [13–17].

Du and co-workers presented a synergistic strategy by taking advantage of polyetherimide (PEI) and ZIF-67 to enhance the interfacial strength of carbon fiber (CF) reinforced polyetheretherketone (PEEK) composites via a facile route. After modification, the tensile strength of single CFs showed no deterioration and the interfacial shear strength (IFSS) of the as-prepared modified CF / PEEK model composites revealed an increase of 40.5 % [18]. De Luca *et al.* [19] developed nanostructured ordered "brick-and-mortar" interphases using layer by layer deposition of PDDA / $(PSS / LDH)_{25}$ solution onto the surface of hydroxylated GFs. The resulting anisotropic morphology caused strain hardening phenomena to the produced nanostructured interphases and thus reduced the local stress concentrations arising from fiber breaks and increased the extent of stable fiber slippage. Pozegic *et al.* presented a scalable method for growing CNTs during either the CF fabrication or the CF surface treatment stage, that could potentially further minimize their damage and offer a suitable replacement for the CF polymer sizing. Moreover, improvements in electrical conductivity in all three directions with significant enhancement in the surface (300 %), thickness (450 %) and volume (230 %) were observed. Additionally, the thermal conductivity was improved by 107 % in the through-thickness direction [20]. Another study documented the strongly orthotropic electrical properties of composite materials comprised of hierarchical GFs coated with single-walled carbon nanotubes (SWCNT). The exceptional damage-sensing capability of the SWCNT hierarchical composites was predicted by simulations and validated experimentally [21].

CNTs dispersed-inks deposition onto fibrous substrates are capable of to convert insulating reinforcing fibers to semi-conductive reinforcements for composites with modified IFSS and secondary additional properties. The resulting composite materials can be used for a wide range of applications, such as electrostatic charge dissipation, damage sensing, and energy harvesting. Gao *et al.* reported on the strain, humidity and temperature sensing ability of hierarchical GFs, coated with commercial oxidized CNTs by electrical measurements [22]. Tzounis *et al.* systematically examined the thermoelectric response of reinforcing fibers coated with CNTs [23], thermoelectric materials based on engineered polymer nanocomposites, and/or polymer / fiber composites [14,24], appropriate for large-scale structural applications with thermal energy harvesting capabilities.

It is common knowledge that energy loss is inevitable during the operation of an engine resulting in a fuel efficiency less than 50 %. Most of the wasted energy is in the form of heat. For typical diesel engines, tests from as early as 2009 showed that, the heat lost by the exhaust was approximately a quarter of the energy produced by the utilized fuel [25]. Thermoelectric energy harvesting and pyroelectric energy harvesting exploitation, relying on the temperature change over distance and time, respectively. The aforementioned technologies constitute the two most common thermal energy harvesting methods. Thermoelectric (TE) conversion is a promising technique to recover temperature waste heat as electricity. In general, heat coming from temperature fluctuation in the environment can be reclaimed as electricity on account of the well-known ‘Seebeck effect’. TE materials exhibit the Seebeck effect, in which charge carriers move in response to temperature gradients. The Seebeck coefficient is directly related to the density of states, whereas the electrical conductivity can be limited by electronic and morphological defects. Charge carriers diffuse across the temperature gradient (ΔT), creating an accumulation of charge and thus a potential difference, ΔV. The magnitude of this effect is described by the Seebeck coefficient (S) and is simply the voltage difference divided by the applied thermal gradient $S = \Delta V/\Delta T$. The Seebeck coefficient is further used for the calculation of the power factor *($PF = \sigma \cdot S^2$)*, a well-established quantity for comparing the TE performance of different TE materials. Finally, the overall TE efficiency for specific temperature range applications of a material is classified by the dimensionless thermoelectric figure of merit, ZT ($ZT = (\sigma \cdot S^2) \cdot T/\kappa$), where σ is the electrical conductivity, S is the Seebeck coefficient, κ is the thermal conductivity and T is the corresponding temperature.

An efficient thermoelectric material presents a high value of ZT, combining high electrical and poor thermal conductor characteristics. The three thermoelectric parameters σ, S and κ are correlated with the intrinsic carrier concentration of the material [26–29]. Thermoelectric energy harvesting is a conventional technique for converting wasted thermal energy into the electrical power by means of thermoelectric element generators (TEGs). A typical TEG device consists of p–n junctions properly interconnected electrically in series and thermally in parallel. When a temperature gradient is established between the hot and the cold side, free electrons and holes are able to move towards specific directions and generate a potential difference proportional to the temperature difference between the p-type and n-type semiconductors. Compared to the traditional TEG devices, high performance flexible TEGs that exploit the nanotechnology advancements are being extensively reported [17,30].

In this study, hierarchical glass fiber tows coated with p-type and n-type SWCNT as well as reference tows were evaluated in terms of their thermal stability and physicochemical relevance with the epoxy resin. The thermoelectric response of the produced p- and n-type epoxy model composites have been assessed for a single pair TEG fabrication. The tow pull-out test was used to determine the quality of interfacial bonding between the epoxy matrix and the nanocoated glass fibers. Fracture morphologies of the pulled-out tows obtained via optical microscopy revealed a cohesive type of failure in all cases, as the epoxy material remained attached on the surface of the tows after the pull-out process.

3.2.2 Experimental section

3.2.2.1 Materials

The 1062 Multi-End Roving (NEG) GFs were employed for this study with a tensile strength of 2300–2400 MPa and tensile modulus of 72 GPa, specifically designed for use with epoxy resin systems in applications that require high mechanical strength and corrosion resistance such as filament wound pipes. The filament diameter is 13.3 ± 0.6 μm as stated by the manufacturer.

SWCNT in powder form were provided by OCSiAl (TUBALL, carbon content: >85 wt. %, outer mean diameter of SWCNT 1.8 ± 0.4 nm, length of SWCNT >5 μm, metal impurities <15 wt. %).

SDBS (sodium dodecylbenzenesulfonate – M_w = 348.48 g/mol), PEI (Poly(ethyleneimine)) solution ~50 % in H_2O (M_r = 600000–1000000) were purchased from Sigma Aldrich. All chemical reagents were used as received. RS Pro silver (Ag) loaded epoxy conductive paste was utilized for the adhesive ohmic contacts. A commercial low viscosity liquid epoxy resin system was employed, consisting of EPIKOTE Resin 828LVEL (100.0 parts by weight) EPIKURE™, Curing Agent 866 (83.0 parts by weight), and EPIKURE™ Catalyst 101 (1.5 parts by weight). The curing cycle and post-curing included heating at 90 °C for 90 min and at 130 °C for 180 min, respectively.

3.2.2.2 Dispersion and deposition of the TE p- and n-type SWCNT inks onto GF tows

The SWCNT powder was dispersed using the UP400S manufactured by Hielscher Ultrasonics tip-ultrasonic probe processor for 45 min at 10 a Watt amplitude to deliver the wave directly into the aqueous solvent. For the p-type TE ink, 2 mg/mL SWCNT and 5 mg/mL of SDBS were utilized in order to produce a suspension with a proper critical micelle concentration (CMC) and achieve a stable dispersion. Accordingly, for the n-type TE ink, 2 mg/mL SWCNT and 2 mg/mL of SDBS coupled with 5 mg/mL of poly(ethyleneimine) were used. The notation "p-type and n-type" refers to the type of the charge carriers induced in the two different formulations of the CNTs and does not imply any type of substitutional doping of the CNTs.

Then, the p- and n-type TE inks were used for coating of the GF tows via a simple blade coating process. In more detail, 100 mm long single GF tows were cut from the reel, stabilized, and coated towards the creation of homogeneous continuous TE efficient p-type and n-type films onto the GFs. After the coating process, the tows were left to dry on a hot plate at 90 °C for 30 min.

3.2.2.3 Manufacturing of model composites for thermoelectrical characterization

Model composites were prepared and characterized for the study of the effect of the epoxy resin system addition on the thermoelectric response of the coated glass fibers. The coated single GF tows were placed flat onto a pre-cleaned silicon dog-bone shaped mold and secured in place on both sides with an adhesive tape. Then, two thin copper (Cu) foil electrodes were adjusted tightly on each side of the functional single tows and glued with silver paste on the tow to ensure proper ohmic contacts. Upon drying of the contacts, a well-mixed and degassed epoxy resin / hardener / catalyst mixture was casted in the mold, which impregnated thoroughly the whole GF tow. The system was cured and post-cured following the aforementioned protocol. At least 5 model composites for each category were fabricated and the mean experimental values with the corresponding standard deviations are presented. The electrical properties and the thermoelectric response of the model composites were measured with the set up that is displayed in **Figure 32**.

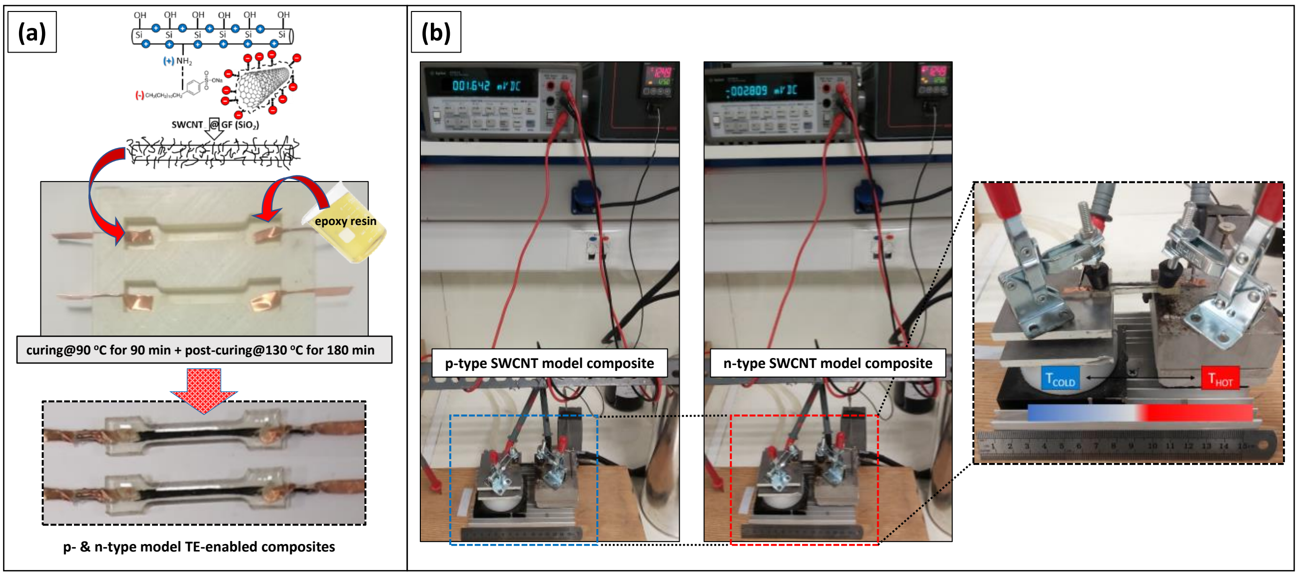

Figure 32. Manufacturing process of the TEG-enabled model composites (**a**) silicon mold utilized for the preparation of dog-bone shaped specimens with Cu electrodes placed at both sides ready for the epoxy resin casting and (**b**) demonstration of the TE-enabled p- and n-type model composites exposed to temperature gradient.

3.2.2.4 Preparation of model composite specimens for micromechanical tests

Tests for the interfacial shear strength calculations were performed on single GF tows using a pull-out configuration. These tests were performed in order to evaluate the effects of the nanostructured coatings on the interfacial mechanical properties between the hierarchical fibers and the epoxy resin system.

For the selected manufacturing process, both uncoated and nanocoated GF tows with a length of 100 mm were pre-impregnated with a thin layer of epoxy resin at 3/4 of their length, using a micro-pipette and were semi-cured until the resin was viscous enough so as not to leak from the impregnated tow.

These epoxy resin semi-cured tows were lowered into the aluminum molds by using purposely made fixture is presented in **Figure 33b**. The fixture was designed so as to hold the pre-impregnated tows aligned during the thermal treatment of the resin. Then, 20 g of the resin / hardener / catalyst system were poured into each of the aluminum molds. Particular attention was paid in order to avoid buckling of the tows and simultaneously maintain the impregnated embedded length in the range of 1–2 mm. Finally, the specimens were cured and post cured according to the recommended curing cycles.

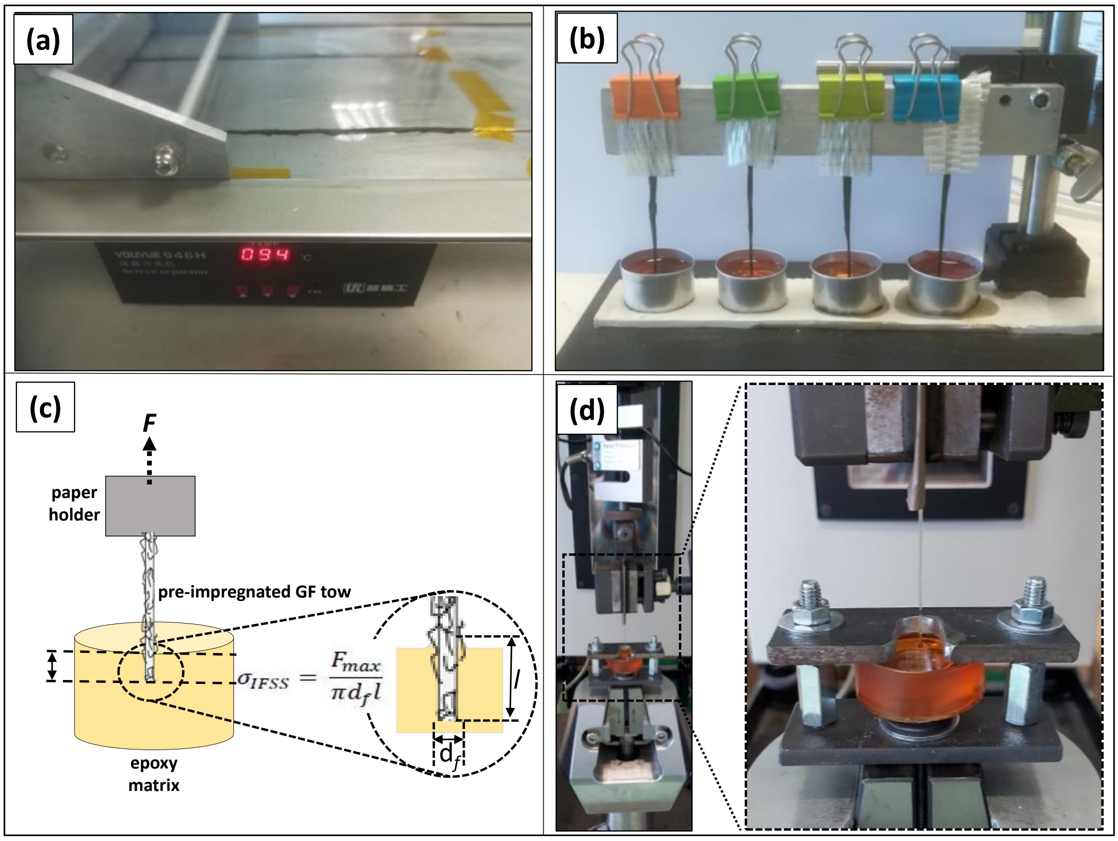

Figure 33. (a) A custom-made blade coating unit for the tows modifications, **(b)** impregnation of the tows within the epoxy resin mold utilizing the in-house built apparatus for the preparation of the pull-out test specimens, **(c)** schematic of a pull-out test specimen and **(d)** photo during the pull-out testing.

The tow pull-out experiments were conducted at room temperature using the Universal Testing Machine by JINAN TESTING EQUIPMENT IE CORPORATION with a 2 KN Load cell. A two-piece metal jig held the epoxy resin mold while the top part was clamped using the appropriate jaw faces. A constant cross-head speed of 5 mm/min was employed for tensile loading to induce the pull-out shear force at the tow / resin interphase. Tests were considered successful when the GF tow was completely pulled out from the polymer matrix. The applied load (F) and the corresponding displacement were recorded and the interfacial shear stress (σ_{IFSS}) was calculated using the equation $\sigma_{IFSS} = F_{\max}/\pi \cdot d_f \cdot l$, where $F_{\max}$ is the maximum load prior to the fracture of the GF tow, d_f is the diameter-width of the tow, and l is the embedded length, including the meniscus, as determined by optical microscopy.

The apparent interfacial shear strength of the functional GF tows and the epoxy resin matrix was calculated and compared with reference uncoated GF tow model composites. The mean values of shear strength presented correspond to the average of 8 successful pull-out experiments for each type of specimens. Finally, the surface morphology of the pulled-out fiber tows from all categories was studied using an optical stereoscope at low magnification.

3.2.2.5 Characterization techniques

Contact angle measurements were acquired via a commercial automated contact angle goniometer system manufactured by Ossila Ltd.

The morphology of the hierarchical GFs, as well as the reference GFs were evaluated via SEM using the JEOL JSM 6510 LV SEM/Oxford Instruments with an operating voltage of 3.5 KV.

Thermogravimetric measurements were carried out in the STA 449C analyzer Netzsch-Gerätebau GmbH, Germany. The experimental procedure included a dynamic step from 25 to 1000 °C with a heating rate of 10 °C/min at ambient conditions to examine the reference and the nanocoated GFs mass loss.

The Labram HR-Horiba scientific micro-Raman system was used. The 514.5 nm line of an Ar + ion laser operating at a power of 1.5 mW at the focal plane was employed for the Raman excitation. An optical microscope equipped with a 50× long working distance objective served both for delivering the excitation light and collecting the back-scattered Raman light. Raman spectra in the range of 90–3500 cm^{-1} were collected.

In order to determine the basic electrical characteristics, p- and n-type bucky paper films were prepared by overnight vacuum filtering of the respective SWCNT dispersions and 4-probe sheet resistance measurements were conducted (**Table 5**). A typical 4-probe technique (4-Point Probe commercial system manufactured by Ossila Ltd.) was used to calculate the electrical conductivity based on the following formula: $\sigma = 1/R \cdot L/A \cdot (\ln2/\pi)$, where R is the measured 4-probe sheet resistance, L is the length, and A is the cross section of each sample. It should be mentioned that the employed 4-point probe system with 4 equally-spaced, co-linear probes to the material (interelectrode probe distance / spacing: 1 mm) is capable of delivering currents between 10 nA and 150 mA, and can measure voltages from as low as 100 μV up to 10 V, which results in a sheet resistance measurement range of 3 mOhm/□ to 10 MOhm/□. The values reported are mean values of at least 4 measurements performed on different samples.

The DC measurements were conducted with a standard 2-probe method using the Agilent 34401A multimeter with 6½ digits resolution. Model composites were placed and measured at 25 mm electrode-electrode distance at room temperature and 25 % relative humidity (RH).

The voltage output of the model composites was determined using a custom-made setup. The samples were mounted on 2 metal blocks, which enabled the generation of a temperature difference. For all measurements, the one aluminum block (T_C) was kept at room temperature (~24 °C) via mild water circulation, while the other one (T_H) was heated until 125 °C via calibrated temperature-controlled resistors, allowing for the generation of a temperature gradients. The generated thermovoltage (Δ*V*) was measured across the electrodes by a multimeter-voltmeter. The temperature of the two blocks was measured with an IR-thermometer (OMEGA OS-VIR50 Dual Laser Video IR Video Thermometer) to verify the temperature difference (Δ*T*), and the Seebeck coefficient (S) was derived from the ratio Δ*V*/Δ*T*.

3.2.3 Results and Discussion

In this study, organic materials were evaluated as emerging candidates for thermoelectric power generation. Chemical doping was employed for tuning the semiconductive nature of the graphitic material from p-type to n-type. In the literature, the terms p-type and n-type are frequently used to describe which apparent carrier mobility is in larger percentage in a material, rather than the position of the Fermi level [29]. Organic semiconductors can be ambipolar and in some cases the hole and electron mobilities are comparable, but one type of carrier prevails owing to the reactivity of the preferred dopant material to stably tune the initial material [31–33]. Contact angle (CA) measurements and scanning electron microscopy (SEM) were employed in order to assess the specific morphological characteristics of the produced nanocoated GFs, while their thermal stability was investigated via thermal gravimetric analysis (TGA). Raman spectroscopy (RS) was used to evaluate the quality of and distribution of the SWCNT deposited on the surface of the GFs under temperature gradients. Finally, the p–n nanostructured interphases were estimated via thermoelectric measurements and micromechanical studies.

3.2.3.1 Morphological measurements of the coated GFs

Representative contact angle images for each case are represented in **Figure 34**. Contact angle is a major surface property in terms of assessing the solid liquid interphase. In this study, the static contact angles of the SWCNT inks onto the GFs as a measure of the surface wetting properties of the coated GFs.

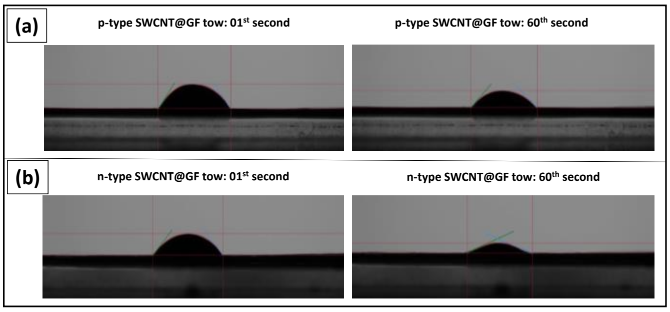

Figure 34. Static contact angle images measured by a goniometer's software for **(a)** p-type SWCNT dispersion droplet in contact with GF tow and **(b)** n-type SWCNT dispersion droplet in contact with GF tow.

The good wetting of the glass fiber tows by both the p- and n-type SWCNT ink droplets is indicative of the inherent hydrophilic behavior of the GFs, which promotes the forming of a uniform SWCNT film on the GFs and is a measure of the level of adhesion. In **Figure 34**, images are shown for each case, captured just after the drop was suspended onto the surface of the GFs and also 60 s later to evaluate the progression of the wetting. For the GFs coated with p-type SWCNT the average contact angle was found to be ca. 56.47° and for the n-type 52.39°.

The coated GFs morphologies were also studied using SEM in order to determine the homogeneity of the coatings and illustrate the specific characteristics of the nanostructuring onto the microscale reinforcing phase. **Figure 35a-b** illustrates the hierarchical morphology of the coated GFs with homogeneously distributed SWCNT covering the fiber surfaces for the p- and n-type SWCNT coated GFs, respectively, at two different magnifications.

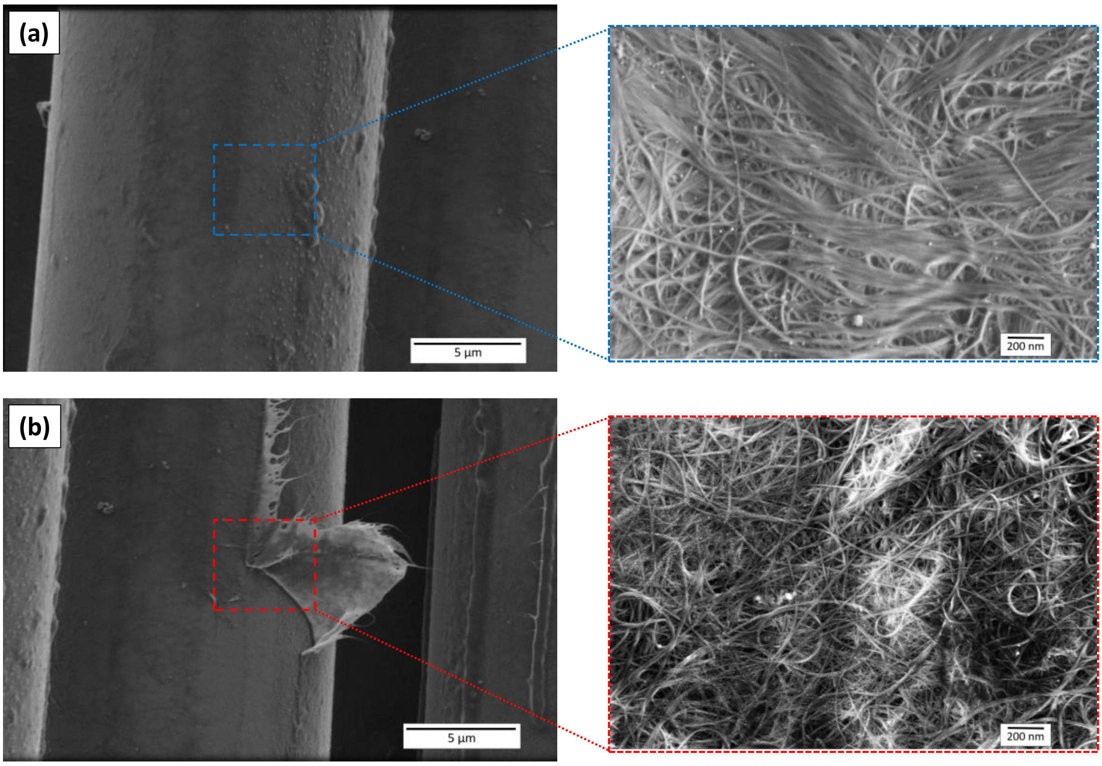

Figure 35. SEM images depicted surface morphology characteristics at different magnifications of **(a)** p-type SWCNT coated GF tow and **(b)** n-type SWCNT coated GF tow.

As was observed in the SEM study (**Figure 35**), both the p- and n-type SWCNT films formed on the GFs are satisfactorily uniform and dense exhibiting an interconnected network of SWCNT which fully cover the surface. Some SWCNT agglomerates are barely visible. The observed SWCNT–SWCNT junctions are impart the high values of electrical conductivity to the films, which alter the inherently dielectric behavior of the GF tows.

3.2.3.2 Thermogravimetric analysis of the TE-enabled GFs

In order to assess the thermal stability of the produced functional hierarchical structures, dynamic thermogravimetric scans were performed from 25 to 1000 °C. Thermogravimetric analysis under air atmosphere is very sensitive to the increase of the surface area which promotes the oxidation of the examined material. High thermal stability of these hierarchical structures is critical for the thermoelectric applications that involve high operational temperatures. **Figure 36** illustrates the TGA graph of the uncoated and the nanocoated GF tows.

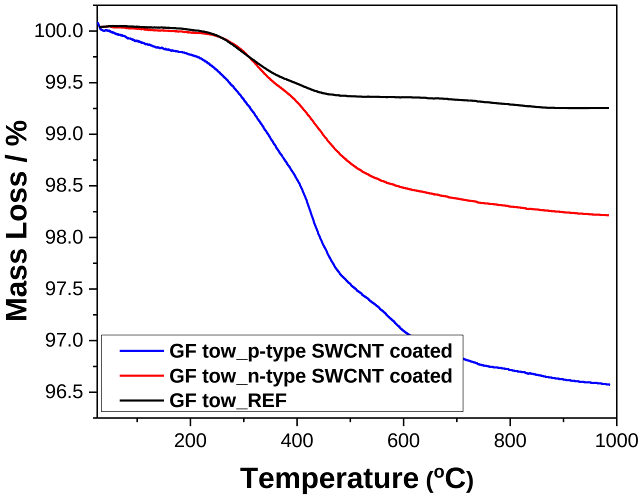

Figure 36. Thermogravimetric measurements of uncoated GFs, coated GFs with p-type and n-type SWCNT, respectively.

Thermogravimetric analysis was used in order to characterize the thermal stability of the SWCNT coated GFs in comparison to the reference GFs.

As depicted in **Figure 36**, a minor mass loss in the order of almost 0.05 % was observed for the reference GFs as well as for the n-type SWCNT coated GFs above 100 °C and up to 241.5 and 213.2 °C, respectively. The p-type SWCNT coated GFs depicted a similar behavior at that temperature range losing, however a slightly higher amount of its mass, namely 0.28 % up to 175.3 °C. This mass loss is attributed to the evaporation of residual moisture for all the samples and is observed to be increased in the p-type SWCNT coated GFs due to the increased amount of carboxy moieties. At higher temperatures, between about 241.5 and 539.2 °C the reference GFs lost 0.7 % of their mass due to the combustion of the silane type sizing [38–40]. Then, the mass of the E-glass fibers remained almost constant without considerable weight loss up to 1000 °C.

The thermal degradation of the p-type and the n-type molecular doped SWCNT is a multistage process due to the existence of the various functional groups that are absorbed on their surface or are interacting with it. The functional chemical groups as moieties that SWCNT contain are in general decomposed during the second temperature range that spans from roughly 200 to 500 °C. In more detail, the p-type SWCNT exhibited the typical decomposition behavior of pristine SWCNT that are inherently p-doped by a small amount of adsorbed oxygen containing groups. The oxygen-based moieties promote the electron withdrawing process from the CNT electron-rich back-bone, effectively introducing holes as main charge carriers (p-doping). The p-type SWCNT coated GFs lost ca. 1 % of their mass up to 373 °C that can be attributed to smaller in size oxygen containing functional groups like hydroxy and ether moieties. Another 1.35 % mass loss was observed up to 531 °C that can be due to larger oxygen containing moieties like carboxyl and ester moieties [41]. The initial mass loss of SDBS molecules is owing to burning with the presence of oxygen (330–450 °C) and the burning of the SDBS continued to occur above 800 °C [42]. Overall, due to the fact that the SDBS concentration is lower (2 mg/mL) in the n-type SWCNT coatings, this may also explain the loose of less weight compared to the p-type SWCNT coatings (5 mg/mL). The observed loss amount is in agreement with the percentage of SDBS and CNTs that were used for the preparation of the inks. Additionally, any amorphous carbon that might be present into the SWCNT coating would also be combusted at this temperature range. A further 0.7 % mass loss occurred up to 756 °C that can be attributed to the combustion of the SWCNT. Then, the mass of the underlying GFs remained almost stable up to 1000 °C with only a further 0.18 % mass loss that can be attributed to some possible remaining percentage of catalyst particles from the production process of the CNTs [43].

A slightly different behavior was presented by the n-type SWCNT coated GFs. The decomposition of the nitrogen containing moieties that are included in the PEI molecules, which are entangled in between the CNT network, was responsible for the 0.53 % mass loss from 213 up to 368 °C. A further 1 % mass loss was observed up to 626 °C that is attributed the total decomposition of the SWCNT. Afterwards the mass of the underlying GFs remained almost stable up to 1000 °C, with only a small amount equal to a further 0.24 % being decomposed up to 1000 °C maybe on account of some possible remaining percentage of catalyst particles due to the production process of the CNTs [43].

3.2.3.3 Spectroscopic measurements of the TE-enabled GFs

The Raman spectra of the p-type SWCNT coated GF and the n-type SWCNT coated GF were acquired at ambient conditions (room temperature–RT), as well as at temperature gradients of 50 and 100 K by performing measurements at 75 and 125 °C, respectively.

The respective results are presented in **Figure 37**. A linear baseline was subtracted from the spectra of the p-type and the n-type SWCNT coated GFs.

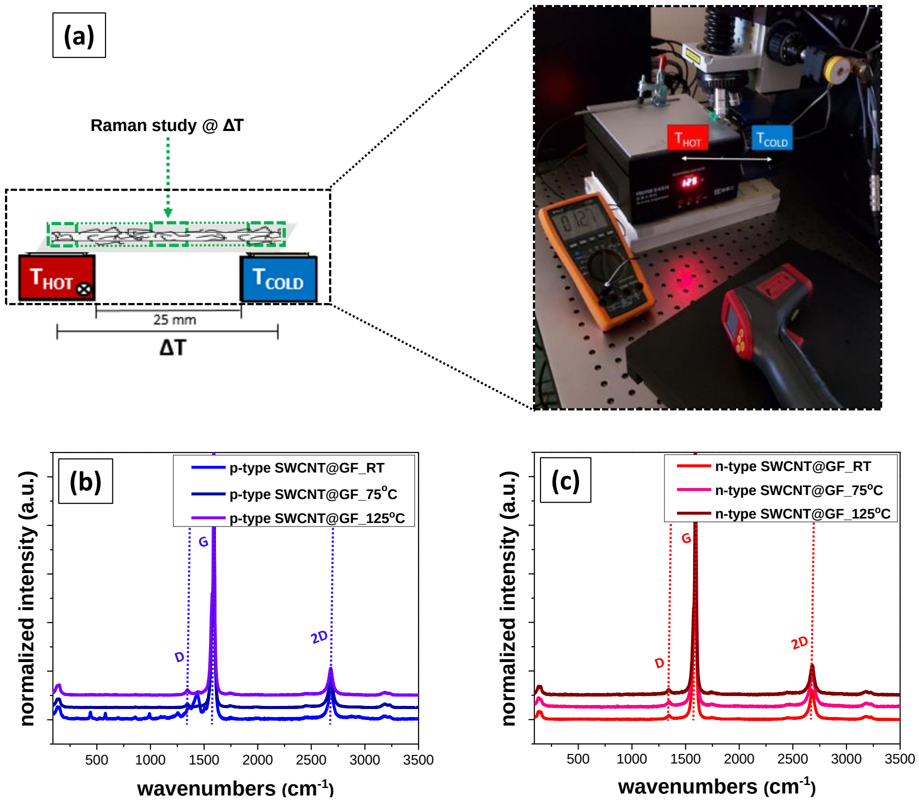

Figure 37. (**a**) Experimental set-up used to study the Raman spectra of p-type SWCNT coated GFs and n-type SWCNT coated GFs at room temperature, as well as at Δ*T* of 50 and 100 K and **(b, c)** Raman spectra of the p-type and n-type SWCNT coated GFs at ambient and at temperature gradients of 50 and 100 K, respectively.

The p-type and the n-type SWCNT coatings onto the GFs possess all the expected vibrational modes commonly encountered in graphitic materials. More specifically, the most prominent band of the spectrum of SWCNT was the graphitic or G band with E_{2g} symmetry located at about 1590 cm^{-1}. The radial breathing mode, which is a unique phonon mode of SWCNT was also observed at the 120 cm^{-1} to 140 cm^{-1} regions. Another disorder-induced band appearing in the first order spectrum of the SWCNT is the D band, at about 1340 cm^{-1}. The D band is caused by either amorphous carbon or sp^3 carbon atoms at defect sites on the CNT sidewalls [44]. Furthermore, the 2D peak dominated the second order spectrum of the SWCNT coatings. This band was located at about 2685 cm^{-1}. This overtone results from a double resonance process and is a symmetry allowed band which requires two phonons to be completed [45,46].

As can be seen in **Figure 37b-c** no changes were observed in the Raman spectra of both the p-type and the n-type SWCNT coatings onto the GFs when they were subjected to temperature gradients of 50 and 100 K, apart from minor positive frequency shifts of all vibrational modes which were attributed to the increased temperature. This result indicates that the hierarchical GFs which are coated with the organic SWCNT inks of both p-type and n-type TE behavior are chemically and structurally stable.

3.2.3.4 TE response of the model composites

In **Table 5** the TE properties of both p-type and n-type bucky paper films are presented. The conductivity and the TE response introduced from the coating can be attributed to the nanoparticle-based networks deposited onto the fiber surfaces creating the electron transport pathways. In fact, the electrical conductivity and the Seebeck coefficient values can be explained more precisely if we consider the existence of a continuous self-assembled layer with thickness (t) onto the fiber surface with electrical conductivity (σ) stemming from the electrostatic interactions [34].

More analytically, when the anionic surfactant (SDBS) is added to distilled water it tends to ionize and give a negative charge to the created micelles which include the dispersed de-aggregated SWCNT. Conversely, the positively charged free silanol particles from the GFs surface interact with the ambient oxygen groups result in non-covalent bonding of the CNTs [35]. The resistivity (ρ) of an epoxy coated GF tow along the longitudinal direction is given by the formula: $\rho = \mathrm{A} \cdot R/\mathrm{L}$ (A: circular cross section area). Executing this equation, the coated GF tows with SWCNT (p- and n-type) consist of a highly conductive continuous network and could be assumed approximately as a tubular-like geometry resistor ($V = \pi \cdot \mathrm{r}^2 \cdot \mathrm{L}$) with electrical conductivity of $\sigma = (4 \cdot \mathrm{L})/\pi \cdot d^2 \cdot R$ [23]. The average diameter (d = r/2, r: radius) was ~1654 μm for p-type GF tows within the epoxy resin and ~1600 μm for the n-type GF tows within the epoxy resin, measured via a calibrated optical microscope. The electrical resistance (R) was measured along the length (L) via a two-probe method. It should be mentioned that the nanoparticle-based layers for both p-type and n-type SWCNT coatings onto GFs possess lower electrical conductivity values in comparison to the aggregated and highly dense structure of the corresponding bucky paper films form, as presented in **Table 5**. Furthermore, the bulk thermoelectric properties of both p- and n-type bucky paper films were studied. The positive measured values of the Seebeck coefficient correspond to the p-type semi-conducting behavior and the negative to the n-type, respectively.

Table 5. Electric and TE values of both p-type and n-type bucky paper films.

TE Material	**Electrical Conductivity (σ) (S/m)**	**Seebeck Coefficient (S) (μV/K)**	**Power Factor ($\sigma \cdot S^2$) (μW/m · K^2)**
SWCNT@SDBS (2 mg/mL & 5 mg/mL)	$1.05 \times 10^5 \pm 0.05$	+23 ± 1	55.5
SWCNT@SDBS (2 mg/mL & 2 mg/mL)_PEI (5 mg/mL)	$1.4 \times 10^5 \pm 0.08$	−31 ± 1.5	134.5

The hierarchical GF tows model composites were evaluated in terms of their TE response as presented in **Figure 38**.

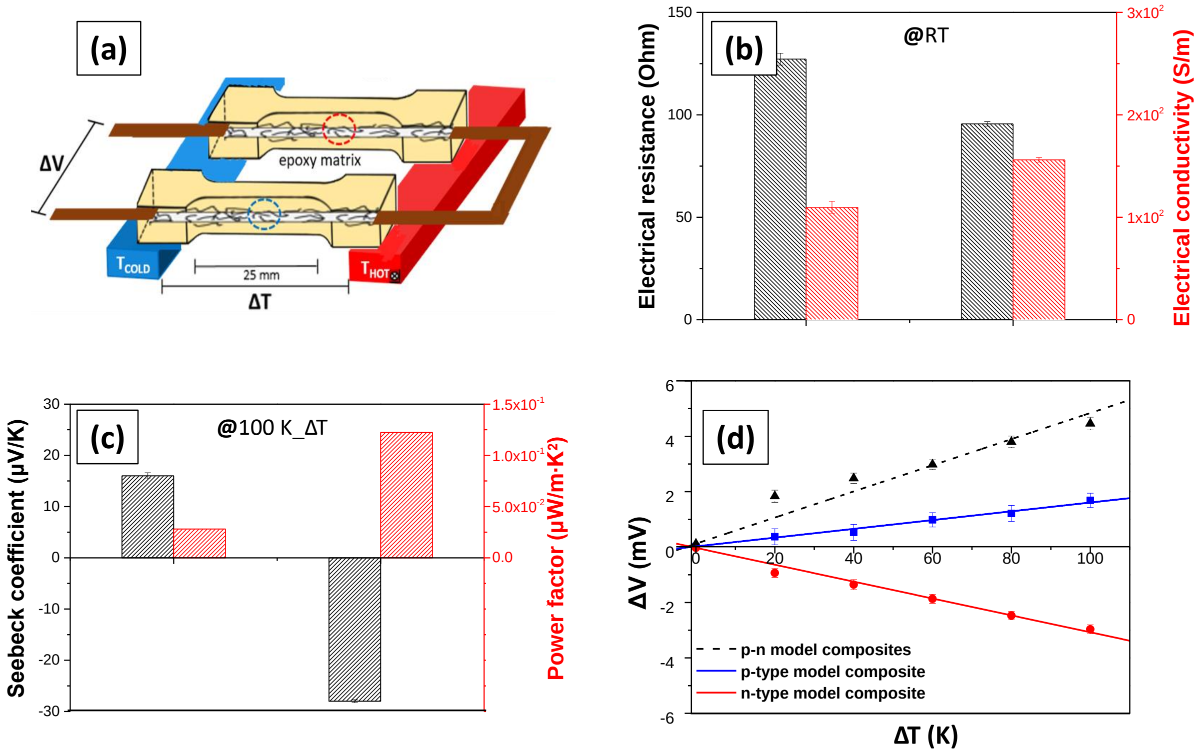

Figure 38. (a) schematic illustration of a p-n junction between the model composites created by interconnecting in series the p-type and the n-type model composites by a Cu foil at the hot side (125 °C), while at the cold side (~24 °C) the Cu electrodes were attached with the multimeter for a 2-probe measurement, graphs of **(b)** electrical resistance-electrical conductivity, **(c)** Seebeck coefficient-*PF* and **(d)** Δ*V* *vs*. Δ*T* curves for the coated p- and n-type TE model composites.

The electrical resistance as well as the electrical conductivity of the prepared model composites are presented in **Figure 38b**. The p-type SWCNT coated GF model composites exhibited electrical resistance of 127.2 ± 2.9 Ohm, which corresponds to electrical conductivity of 109.7 ± 5.8 S/m, while for the n-type SWCNT coated GF model composites showed very similar values *i.e.*, 95.6 ± 1.1 Ohm and 156.1 ± 2.3 S/m, respectively. The high electrical conductivity of the coated GFs is a key parameter for thermoelectric performance, since it can facilitate the flow of the thermally induced charge carriers upon being exposed to a temperature difference. Additionally, as aforementioned, low thermal conductivity is also desirable for the sustainability of the thermoelectric effect. In the case of the SWCNT interphase, it may also be postulated that the infusion of the thermally insulating epoxy molecules reduces thermal conductivity, thus further enhancing thermoelectric performance. More analytically, this mechanism creates a barrier at the SWCNT junctions and prevents the direct physical contact between them resulting in reduced thermal energy transport [23,29].

The Seebeck coefficient (S = Δ*V*/Δ*T*) was derived from the slope of Δ*V* *vs*. Δ*T* curves by linear fitting. **Figure 38c** shows the Seebeck coefficients of the p and the n-type model composites. For the p-type model composite, the Seebeck coefficient was found to be +16.2 ± 6 μV/K corresponding to a power factor of 0.02 μW/m · K^2 and for the n-type −28.4 ± 4 μV/K corresponding to a power factor of 0.12 μW/m · K^2.

As was observed, the p-type SWCNT coated GF model composites exhibited slightly lower values of Seebeck coefficient compared to the corresponding bucky papers. This can be attributed to the high nitrogen amount of the hardener within the epoxy system, acting as a n-dopant [32]. On the other hand, for the n-type SWCNT coated GF model composites the Seebeck coefficient values remain almost identical.

Figure 38d depicts the generated thermovoltage upon exposure to various values of ΔT, for both p and n-type SWCNT coated GF model composites. More specifically, the TE voltage of the in-series electrical and the in parallel thermal connection between the p-type and the n-type model composites creating a p–n junction are being displayed. As can be observed, within the studied temperature range, the generated voltage increased linearly with increasing temperature, $R^2>0.98$ for all cases. The measured voltage output was 4.46 ± 0.3 mV with a device resistance of 235.5 ± 2.5 Ohm at 100 K ΔT. The maximum output of the p–n model composites TEG device was calculated 0.02 μW at a temperature difference of 100 K, according to the following equation $P_{max} = \Delta V^2/4 \cdot R_{TEG}$ [24]. The derived maximum output power density of the device (p–n model composites pair) was 0.016 μW/cm^2.

Overall, the relatively high values of the electrical resistance were directly related to the area of the evaluated coated GF tows. It is expected that by increasing the area of the thermoelement (in this case the single coated GF tow), the electrical conductivity could be significantly increased while the Seebeck coefficient would not be affected as it is an inherent material property and is independent of the geometry of the evaluated specimen. To further elaborate on this statement, when the cross-sectional area of the coated substrate is increased, by increasing the thickness of the CNT coating on the GF substrate, its electrical resistance is reduced. Generally, the electrical resistivity of the CNTs films decreases as the thickness of the coatings is being increased. The property of the electrical resistivity highly depends on carrier concentration and carrier mobility, while the electrical resistance depends on the resistor shape geometry and the specific material. Electrical resistivity is an intrinsic property of a conductive film which is directly proportional to the total resistance R, an extrinsic quantity that depends on the length and cross-sectional area of the corresponding film. Larger cross section areas present lower values of electrical resistance. In the case of SWCNT, changes within the conductive network due to thickness optimization are able to positively impact the electrical conductivity. Both cases are true until the bulk resistance value is reached, thereby no further increments in electrical conductivity can be achieved. There also exists an optimal area that produces the highest possible thermoelectric values, as it is able to host the highest possible electron flow / current under a fixed ΔT. Therefore, since the Seebeck coefficient is a material property, the power factor of the coated GFs can be optimized by combining the most appropriate substrate dimensions and coating thickness. This is of the utmost importance for the exploitation of the nanomaterial coated reinforcements as thermoelectric elements in composite structures.

3.2.3.5 Study of the nanostructured interfacial mechanical properties

Apart from the thermoelectric functionality, the interfacial shear strength of the hierarchical GFs was also measured by tow pull-out tests and compared to the interfacial properties of the reference uncoated GF tows. While the influence of the CNTs on the interfacial bonding of the GF with epoxy resin is usually determined by measuring the interfacial shear strength through single fiber fragmentation [2] or pull-out tests [36,37], the pull out test configuration was deemed as more appropriate for this study and was used to quantify the quality of interfacial bonding between the epoxy matrix and the nanocoated GFs which were used in this study.

Figure 39a shows the results of apparent interfacial shear strength (σ_{IFSS}) measurements, which is indicative of the stress transfer efficiency of the interphase. As can be observed, the uncoated GF tows (REF GF) exhibited the highest interfacial shear strength, *i.e.*, 42.8 ± 0.9 MPa. Comparatively, the p-type SWCNT coated GF model composites exhibited lower interfacial shear strength values at 38.5 ± 1.5 MPa, that is a 10.1 % decrease in comparison to the uncoated GFs. For the n-type SWCNT coated GF model composites the interfacial shear strength was about 30.8 ± 3.4 MPa, which corresponds to a 28.1 % reduction compared to the uncoated GF tows.

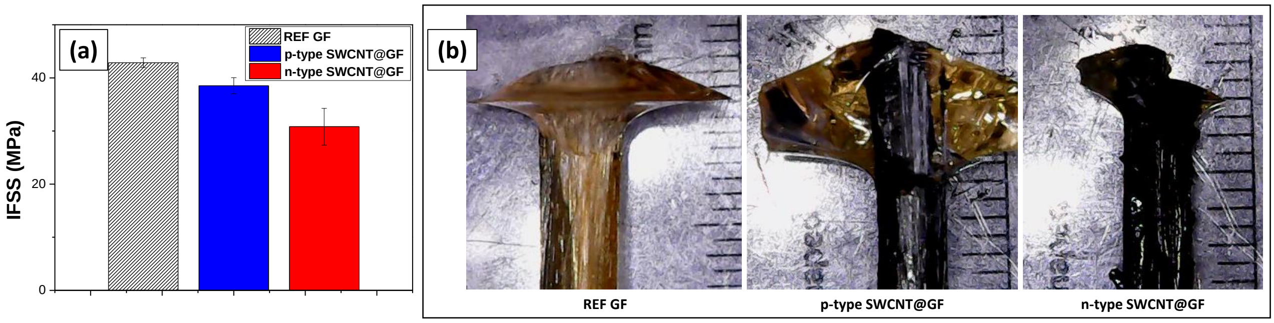

Figure 39. (a) Interfacial shear strength values for the p-type and the n-type TE model composites compared to the reference one, **(b)** fractography images for the respective three examined categories.

Optical stereoscopic images indicate the failure modes of the model composites after the pull-out testing. Representative fractographic images of the pulled-out tows are shown in **Figure 39b**.

Tow pull-out testing as opposed to single fiber pull-out testing was the preferred methodology for assessing the stress transfer between the nanocoated tow and the matrix, as it resulted in a more realistic measurement of the interfacial shear strength. Moreover, it was possible to effectively reduce the errors associated with the handling of single fiber filaments, which typically requires extremely careful manipulation due to their small size and brittle nature [47,48]. Several trials were performed with different specimen designs in order to consider all the different aspects that are involved in the particular test. Since the tow-pull out process is not a standard test [49,50], preliminary tests were performed to optimize parameters such as the embedded length and the resin pre-impregnation process before insertion in the matrix.

Fracture morphologies of the pulled-out tows obtained via optical microscopy reveal a cohesive type of failure in all cases, since epoxy material remained on the tow surface after the pull-out process. In general, the GF tow was covered by a cone of resin and as such it was detached from the matrix. In the case of the n-type tows, a mixed type of failure mode was observed, whereby fiber / matrix-to-matrix failure was also present. The fiber-to-matrix failure, whereby the GF tow was completely detached from the resin, was not observed in any of the tested specimens. As should be noted, the persistent presence of cohesive failure within the matrix suggests that measured values were an underestimate of the true IFSS. This was also suggested during the process of experimental optimization where it was observed that small embedded length and low values of pull-out force correlated more with fiber to matrix failure than cohesive failure.

In conclusion, it can be assumed that the presence of surfactant for the dispersions of both SWCNT inks affected negatively the IFSS when a commercial epoxy resin was used as a matrix. Further studies could be performed oriented to optimize the coating process and simultaneously assess the effect of the surfactant existence on the interfacial shear strength [51,52]. As is well known, a strong interface provides efficient stress transfer but promotes brittle failure, whereas a weaker may promote energy dissipation and thus improve toughness. Balancing these conflicting requirements by engineering composite interphases to improve optimal strength and toughness values remains a great challenge.

3.2.4 Conclusions

The scope of this research study was to introduce and evaluate functional interphases between modified GFs with p- and n-type SWCNT model epoxy composites. Efforts were devoted to the morphological inspection as well as the evaluation of the structural changes that might be caused by the functional nanocoated GFs in the presence of temperature gradients. The thermal stability of the nanocoated GF tows was investigated through thermogravimetric analysis. Additionally, the chemical and structural stability of the TE nanoparticle-coated GF tows were studied by Raman measurements at elevated temperatures. The Raman spectra of p-type SWCNT coated GFs and n-type SWCNT coated GFs were acquired at ambient conditions, as well as at temperature differences of 50 and 100 K by performing measurements at 75 °C and 125 °C. The results indicated that both the p-type and n-type TE-enabled GF tows are chemically and structurally stable. The effect of the integration of the modified nanocoated GFs into a conventional epoxy resin was evaluated. The TE performance of the functional GF tows was only slightly affected by the resin encapsulation. Both p- and n-type SWCNT model composites exhibited a combination of high electrical conductivity and Seebeck coefficient. N-type model composites exhibited higher electrical conductivity compared to the corresponding p-type, due to their higher intrinsic electrical properties, as measured on SWCNT bucky paper films. Moreover, the n-type model composites exhibited excellent behavior as thermoelectric materials with remarkably high values of Seebeck coefficient very close to the properties of the bulk SWCNT material. An epoxy-based TEG model composite was manufactured to demonstrate the potential application of the technology in a TE generator, using a pair of alternating p- and n-type junctions interconnected in series via a metallic junction. The interfacial shear strength for both p- and n-type TE-enabled model composites was assessed by tow pull-out tests. The presence of SDBS as surfactant for the dispersion of the SWCNT affected negatively the IFSS when epoxy resin was used as a matrix leading to a slight reduction of the IFSS values for both systems comparatively to the reference one. Finally, the fractographic study of the tested samples revealed that the matrix-to-matrix failure was more dominant than fiber / matrix-to-matrix failure, indicating strong interfacial adhesion. Further optimization of the thermoelectric performance which involves the increase of both the electrical conductivity and the Seebeck coefficient could be as achieved via doping of SWCNT, use of different types of SWCNT and creating efficient p–n heterojunctions for the fabrication of TEG module devices. The generation of thermoelectricity using structural engineering materials that are routinely exposed to high temperatures will represent a breakthrough in multifunctional materials, rendering them an attractive technology for aerospace and automobile applications.

3.2.5 References

1. Jin, S.; Young, R.J.; Eichhorn, S.J. Controlling and mapping interfacial stress transfer in fragmented hybrid carbon fibre – carbon nanotube composites. *Compos. Sci. Technol.* **2014**, *100*, 121–127, doi:10.1016/j.compscitech.2014.05.034.
2. Paipetis, A., Galiotis, C., Liu, Y. C. and Nairn, J. Stress Transfer from the Matrix to the Fibre in a Fragmentation Test: Raman Experiments and Analytical Modeling. **1999**, 377.

3. Jin, S.; Young, R.J.; Eichhorn, S.J. Hybrid carbon fibre – carbon nanotube composite interfaces. *Compos. Sci. Technol.* **2014**, *95*, 114–120, doi:10.1016/j.compscitech.2014.02.015.

4. Wicks, S.S.; Wang, W.; Williams, M.R.; Wardle, B.L. Multi-scale interlaminar fracture mechanisms in woven composite laminates reinforced with aligned carbon nanotubes. *Compos. Sci. Technol.* **2014**, *100*, 128–135, doi:10.1016/j.compscitech.2014.06.003.

5. Bekas, D.G.; Paipetis, A.S. Damage monitoring in nanoenhanced composites using impedance spectroscopy. *Compos. Sci. Technol.* **2016**, *134*, 96–105, doi:10.1016/j.compscitech.2016.08.013.

6. Orfanidis, S.; Papavassiliou, G.; Paipetis, A.S. Microcapsule-based self-healing materials: Healing efficiency and toughness reduction vs. capsule size. *Compos. Part B* **2019**, doi:10.1016/j.compositesb.2019.04.030.

7. Foteinidis, G.; Tsirka, K.; Tzounis, L.; Baltzis, D.; Paipetis, A.S. The role of synergies of MWCNTs and Carbon Black in the enhancement of the electrical and mechanical response of modified epoxy resins. *Appl. Sci.* **2019**, *9*, doi:10.3390/app9183757.

8. Wu, G.; Ma, L.; Liu, L.; Wang, Y.; Xie, F.; Zhong, Z.; Zhao, M.; Jiang, B.; Huang, Y. Interfacially reinforced methylphenylsilicone resin composites by chemically grafting multiwall carbon nanotubes onto carbon fibers. *Compos. Part B Eng.* **2015**, *82*, 50–58, doi:10.1016/j.compositesb.2015.08.012.

9. An, Q.; Rider, A.N.; Thostenson, E.T. Electrophoretic deposition of carbon nanotubes onto carbon-fiber fabric for production of carbon/epoxy composites with improved mechanical properties. *Carbon N. Y.* **2012**, *50*, 4130–4143, doi:10.1016/j.carbon.2012.04.061.

10. Mei, H.; Zhang, S.; Chen, H.; Zhou, H.; Zhai, X.; Cheng, L. Interfacial modification and enhancement of toughening mechanisms in epoxy composites with CNTs grafted on carbon fibers. *Compos. Sci. Technol.* **2016**, *134*, 89–95, doi:10.1016/j.compscitech.2016.08.010.

11. Moaseri, E.; Karimi, M.; Baniadam, M.; Maghrebi, M. Enhancement in mechanical properties of multi-walled carbon nanotube–carbon fiber hybrid epoxy composite: effect of electrostatic repulsion. *Appl. Phys. A Mater. Sci. Process.* **2016**, *122*, 1–8, doi:10.1007/s00339-016-9600-2.

12. Tsirka, K.; Foteinidis, G.; Dimos, K.; Tzounis, L.; Gournis, D.; Paipetis, A.S. Production of hierarchical all graphitic structures: A systematic study. *J. Colloid Interface Sci.* **2017**, *487*, 444–457, doi:10.1016/j.jcis.2016.10.075.

13. Muæoz, B.E.; Dalton, A.B.; Collins, S.; Kozlov, M.; Razal, J.; Coleman, J.N.; Kim, B.G.; Ebron, V.H.; Selvidge, M.; Ferraris, J.P.; et al. Multifunctional Carbon Nanotube Composite Fibers. **2004**, 801–804, doi:10.1002/adem.200400092.

14. Tzounis, L.; Liebscher, M.; Mäder, E.; Pötschke, P.; Stamm, M.; Logothetidis, S. Thermal energy harvesting for large-scale applications using MWCNT-grafted glass fibers and polycarbonate-MWCNT nanocomposites. **2015**, *138*, 138–148, doi:10.1063/1.4908594.

15. Malakooti, M.H.; Patterson, B.A.; Hwang, H.S.; Sodano, H.A. ZnO nanowire interfaces for high strength multifunctional composites with embedded energy harvesting. *Energy Environ. Sci.* **2016**, *9*, 634–643, doi:10.1039/c5ee03181h.

16. Karalis, G.; Mytafides, C.; Polymerou, A.; Tsirka, K.; Tzounis, L.; Gergidis, L.; Paipetis, A.S. Hierarchical Reinforcing Fibers for Energy Harvesting Applications - A Strength Study. *Key Engineering Materials* **2020**;827 :252–7, doi:10.4028/www.scientific.net/KEM.827.252.

17. Liang, D.; Yang, H.; Finefrock, S.W.; Wu, Y. Flexible Nanocrystal-Coated Glass Fibers for High-Performance Thermoelectric Energy Harvesting. **2012**, 8–13.

18. Liu, H.; Zhao, Y.; Li, N.; Zhao, X.; Han, X.; Li, S.; Lu, W.; Wang, K.; Du, S. Enhanced interfacial strength of carbon fiber/PEEK composites using a facile approach via PEI&ZIF-67 synergistic modification. *J. Mater. Res. Technol.* **2019**, *8*, 6289–6300, doi:10.1016/j.jmrt.2019.10.022.

19. Luca, F. De; Sernicola, G.; Sha, M.S.P.; Bismarck, A. " Brick-and-Mortar " Nanostructured Interphase for Glass-Fiber- Reinforced Polymer Composites. **2018**, doi:10.1021/acsami.7b16136.

20. Pozegic, T.R.; Anguita, J. V; Hamerton, I.; Jayawardena, K.D.G.I.; Chen, J.; Stolojan, V. Multi-

Functional Carbon Fibre Composites using Carbon Nanotubes as an Alternative to Polymer Sizing. *Nat. Publ. Gr.* **2016**, 1–11, doi:10.1038/srep37334.

21. Tzounis, L.; Zappalorto, M.; Panozzo, F.; Tsirka, K.; Maragoni, L.; Paipetis, A.S.; Quaresimin, M. Highly conductive ultra-sensitive SWCNT-coated glass fiber reinforcements for laminate composites structural health monitoring. *Compos. Part B Eng.* **2019**, *169*, 37–44, doi:10.1016/j.compositesb.2019.03.070.

22. Gao, S.L.; Zhuang, R.C.; Zhang, J.; Liu, J.W.; Mäder, E. Class fibers with carbon nanotube networks as multifunctional sensors. *Adv. Funct. Mater.* **2010**, *20*, 1885–1893, doi:10.1002/adfm.201000283.

23. Tzounis, L.; Liebscher, M.; Tzounis, A.; Petinakis, E.; Paipetis, A.S.; Mäder, E.; Stamm, M. CNT-grafted glass fibers as a smart tool for epoxy cure monitoring, UV-sensing and thermal energy harvesting in model composites. *RSC Adv.* **2016**, *6*, 55514–55525, doi:10.1039/C6RA09800B.

24. Karalis, G.; Tzounis, L.; Lambrou, E.; Gergidis, L.N.; Paipetis, A.S. A carbon fiber thermoelectric generator integrated as a lamina within an 8-ply laminate epoxy composite: Efficient thermal energy harvesting by advanced structural materials. *Appl. Energy* **2019**, *253*, doi:10.1016/j.apenergy.2019.113512.

25. Petsagkourakis, I.; Tybrandt, K.; Crispin, X.; Ohkubo, I.; Mori, T. Thermoelectric materials and applications for energy harvesting power generation. *Sci. Technol. Adv. Mater.* **2018**, *19*, 836–862, doi:10.1080/14686996.2018.1530938.

26. Snyder, G.J.; Toberer, E.S. 1. Complex thermoelectric materials. *Nat Mater* **2008**, *7*, 105–114, doi:10.1038/nmat2090.

27. Minnich, A.J.; Dresselhaus, M.S.; Ren, Z.F.; Chen, G. Bulk nanostructured thermoelectric materials : current research and future prospects. **2009**, 466–479, doi:10.1039/b822664b.

28. Vineis, C.J.; Shakouri, A.; Majumdar, A.; Kanatzidis, M.G. Nanostructured thermoelectrics: Big efficiency gains from small features. *Adv. Mater.* **2010**, *22*, 3970–3980, doi:10.1002/adma.201000839.

29. Yu, C.; Choi, K.; Yin, L.; Grunlan, J.C. Correction to Light-Weight Flexible Carbon Nanotube Based Organic Composites with Large Thermoelectric Power Factors. *ACS Nano* **2013**, *7*, 9506–9506, doi:10.1021/nn404924h.

30. Kim, S.J.; We, J.H.; Cho, B.J. A wearable thermoelectric generator fabricated on a glass fabric. *Energy Environ. Sci.* **2014**, *7*, 1959–1965, doi:10.1039/c4ee00242c.

31. Tzounis, L.; Hegde, M.; Liebscher, M.; Dingemans, T.; Pötschke, P.; Paipetis, A.S.; Zafeiropoulos, N.E.; Stamm, M. All-aromatic SWCNT-Polyetherimide nanocomposites for thermal energy harvesting applications. *Compos. Sci. Technol.* **2018**, *156*, 158–165, doi:10.1016/J.COMPSCITECH.2017.12.030.

32. Nonoguchi, Y.; Ohashi, K.; Kanazawa, R.; Ashiba, K.; Hata, K.; Nakagawa, T.; Adachi, C.; Tanase, T.; Kawai, T. Systematic conversion of single walled carbon nanotubes into n-type thermoelectric materials by molecular dopants. *Sci. Rep.* **2013**, *3*, 1–7, doi:10.1038/srep03344.

33. Luo, J.; Cerretti, G.; Krause, B.; Zhang, L.; Otto, T.; Jenschke, W.; Ullrich, M.; Tremel, W.; Voit, B.; Pötschke, P. Polypropylene-based melt mixed composites with singlewalled carbon nanotubes for thermoelectric applications: Switching from p-type to n-type by the addition of polyethylene glycol. *Polym.* **2017**, *108*, 513–520, doi:10.1016/j.polymer.2016.12.019.

34. Stamm, M.; Kirsten, M.; Simon, F.; Ma, E. The interphase microstructure and electrical properties of glass fibers covalently and non-covalently bonded with multiwall carbon nanotubes. **2014**, *3*, doi:10.1016/j.carbon.2014.02.069.

35. Zhang, J.; Zhuang, R.; Liu, J.; Ma, E.; Heinrich, G.; Gao, S. Functional interphases with multi-walled carbon nanotubes in glass fibre / epoxy composites. **2010**, *8*, doi:10.1016/j.carbon.2010.03.001.

36. Zhou, J.; Li, Y.; Li, N.; Hao, X.; Liu, C. Interfacial shear strength of microwave processed carbon fiber/epoxy composites characterized by an improved fiber-bundle pull-out test. *Compos. Sci.*

Technol. **2016**, *133*, 173–183, doi:10.1016/j.compscitech.2016.07.033.

37. Padmanabhan, K. Modelling considerations for fibre tow/epoxy matrix interfacial pullout tests. *J. Inst. Eng. Mech. Eng. Div.* **2010**, *91*, 30–33.
38. Kessler, E.; Gadow, R.; Straub, J. Basalt , glass and carbon fibers and their fiber reinforced polymer composites under thermal and mechanical load. **2016**, *3*, 1561–1576, doi:10.3934/matersci.2016.4.1561.
39. Garay, C.; Heck, V.; Zattera, A.J.; Souza, J.A.; Amico, S.C. Influence of calcium carbonate on RTM and RTM light processing and properties of molded composites. **2011**, doi:10.1177/0731684411416033.
40. Rahman, A.S.; Rangari, V.; Jeelani, S. Thermal and Mechanical Properties of Woven Glass Fiber Reinforced Epoxy Composites with Carbon Nanotubes. **2015**, 54–61.
41. Wepasnick, K.A.; Smith, B.A.; Bitter, J.L.; Howard Fairbrother, D. Chemical and structural characterization of carbon nanotube surfaces. *Anal. Bioanal. Chem.* **2010**, *396*, 1003–1014, doi:10.1007/s00216-009-3332-5.
42. King, S.G.; McCafferty, L.; Stolojan, V.; Silva, S.R.P. Highly aligned arrays of super resilient carbon nanotubes by steam purification. *Carbon N. Y.* **2015**, *84*, 130–137, doi:10.1016/j.carbon.2014.11.061.
43. Tzounis, L.; Liebscher, M.; Fuge, R.; Leonhardt, A.; Mechtcherine, V. P- and n-type thermoelectric cement composites with CVD grown p- and n-doped carbon nanotubes: Demonstration of a structural thermoelectric generator. *Energy Build.* **2019**, *191*, 151–163, doi:10.1016/j.enbuild.2019.03.027.
44. Dresselhaus, M.S.; Dresselhaus, G.; Saito, R.; Jorio, A. Raman spectroscopy of carbon nanotubes. *Phys. Rep.* **2005**, *409*, 47–99, doi:10.1016/j.physrep.2004.10.006.
45. Ferrari, A., Robertson, J. Interpretation of Raman spectra of disordered and amorphous carbon. *Phys. Rev.* **2000**, *B 61*, 14095, doi:10.1007/BF02543692.
46. Tsirka, K.; Karalis, G.; Paipetis, A.S. Raman Strain Sensing and Interfacial Stress Transfer of Hierarchical CNT-Coated Carbon Fibers. *J. Mater. Eng. Perform.* **2018**, *27*, doi:10.1007/s11665-018-3532-2.
47. Mulvihill, D.M.; Smerdova, O.; Sutcliffe, M.P.F. Friction of carbon fibre tows. *Compos. Part A Appl. Sci. Manuf.* **2017**, *93*, 185–198, doi:10.1016/j.compositesa.2016.08.034.
48. Mottershead, B.; Eichhorn, S.J. SCIENCE AND Deformation micromechanics of model regenerated cellulose fibre-epoxy / polyester composites. **2007**, *67*, 2150–2159, doi:10.1016/j.compscitech.2006.11.003.
49. D 4018 Standard Test Methods Standard Test Methods for properties of continuos filament carbon and graphite fiber tows. *Annu. B. ASTM Stand.* **2011**, *i*, 1–7, doi:10.1520/D4018-11.2.
50. Chen, J.; Zhao, Y.; Li, Y.; Yang, Z.; Cheng, M. Effects of Different Testing Conditions on Tensile. **2015**, 19–24.
51. De Greef, N.; Gorbatikh, L.; Godara, A.; Mezzo, L.; Lomov, S. V.; Verpoest, I. The effect of carbon nanotubes on the damage development in carbon fiber/epoxy composites. *Carbon N. Y.* **2011**, *49*, 4650–4664, doi:10.1016/j.carbon.2011.06.047.
52. Sui, G. Improved interfacial properties of carbon fiber composites by building stress transition layer with carbon nanotubes. **2018**, 2510–2519, doi:10.1002/adv.21926.

Chapter 4

In-plane TEG-enabled Fiber Reinforced Polymer composites

Part of the results included in **Chapter 4** have been published at *Applied Materials & Interfaces* peer-reviewed scientific journal as part of the study "Advanced glass fiber polymer composite laminate operating as a thermoelectric generator: A structural device for micropower generation and potential large-scale thermal energy harvesting" and can be found under *https://doi.org/10.1021/acsami.1c04527*.

4. In-plane TEG-enabled Fiber Reinforced Polymer composites

4.1 Advanced glass fiber polymer composite laminate operating as a thermoelectric generator: A structural device for micropower generation and potential large-scale thermal energy harvesting

Abstract

This study demonstrates for the first time a structural glass fiber reinforced polymer (GFRP) composite laminate with efficient thermal energy harvesting properties as a thermoelectric generator (TEG). This TEG laminate was fabricated by stacking unidirectional glass fiber (GF) laminae coated with p- and n-type single wall carbon nanotubes (SWCNT) inks via a blade coating technique. According to their thermoelectric (TE) response, the p- and n-type GF-SWCNT fabrics exhibited a Seebeck coefficient of +23 μV/K and -29 μV/K with 60 $\mu W/m \cdot K^2$ and 118 $\mu W/m \cdot K^2$ power factor values, respectively. The in-series p-n interconnection of the TE-enabled GF-SWCNT fabrics and their subsequent impregnation with epoxy resin effectively generated an electrical power output of 2.2 μW directly from a 16-ply GFRP TEG laminate exposed to a temperature difference (ΔT) of 100 K. The structural integrity of the multifunctional GFRP was tested by 3-point bending coupled with on-line monitoring of the steady state TE current (I_{sc}) at a ΔT of 80 K. I_{sc} was found to closely follow all transitions and discontinuities related to structural damage in the stress / strain curve, showing thus its potential to serve the functions of power generation and damage monitoring.

***Keywords*:** Seebeck effect; Organic thermoelectrics; Large-scale thermal energy harvesting; In-plane thermal gradient; Multi-functional composites; Advanced glass fiber reinforced polymer (GFRP) composites; Structural TEG-laminate

Highlights:

- p-type GF-SWCNT fabric with 60 $\mu W/m \cdot K^2$
- n-type GF-SWCNT fabric with 118 $\mu W/m \cdot K^2$
- TEG-laminate with 2.2 μW electrical power output & 0.1 W/m^2 power density
- power generation & damage monitoring

Graphical Abstract

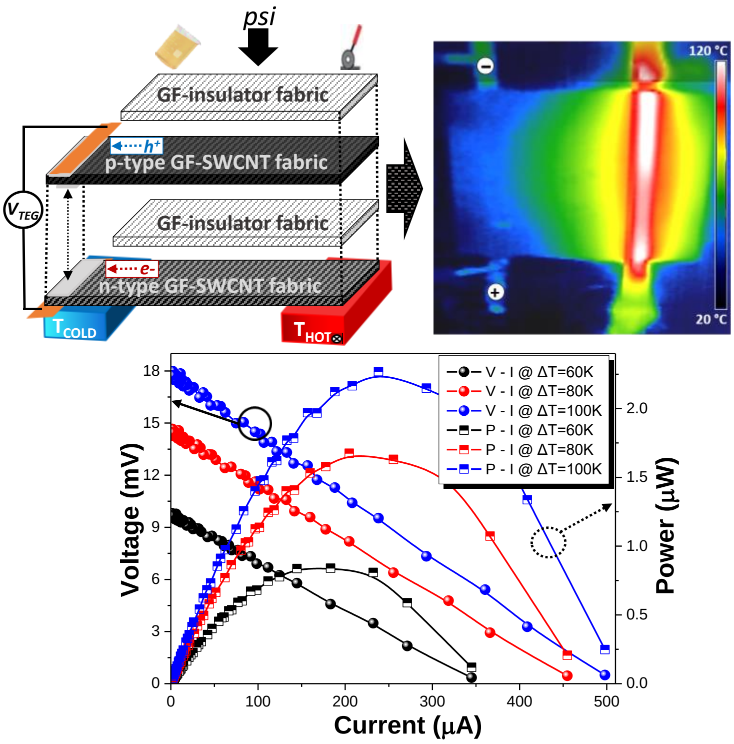

4.1.1 Introduction

Waste heat management and recovery of the thermal energy are a big challenge in the transport, energy and most other industrial sectors as human activity inadvertently involves production of waste heat. Micro power-conversion devices in particular are attracting increasing attention owing to the increasing needs of self-powered driven low-energy consumption electronics for IoT (Internet of Things) applications [1,2]. For this reason, there is a persistent need in the market for micro generators which will render artefacts of any size and purpose autonomous in terms operational power. Since heat sources are abundant in the man-made environment *e.g.* hot fluid pipes, ovens, steam lines, motors, air conditioning, heating, etc., thermoelectric generators (TEGs) are ideal candidates for this challenge [3–5].

TEGs are solid-state devices that directly convert thermal energy into electrical energy. The operating principle for a TEG is based on the Seebeck effect, where a thermoelectric (TE) material generates a voltage under the application of a temperature difference. The magnitude of the generated voltage is proportional to the applied temperature difference and the constant of proportionality is the Seebeck coefficient. The TE material performance is evaluated using the dimensionless figure of merit ZT, determined as $ZT = (\sigma \cdot S^2) \cdot T/\kappa$, where σ represents the electrical conductivity, S the Seebeck coefficient, T the absolute temperature and κ the thermal conductivity. The power factor ($PF = \sigma \cdot S^2$) is also used as a TE performance indicator, since it is directly related to the produced power attributed to the “Seebeck effect”. Consequently, to attain high TE performance, a synergy of high σ and S with minimum κ is sought [6,7]. The most widely used TE materials are based on inorganic semiconductors and in a best-case scenario, the generated voltage from a single TE leg does not exceed 500 μV/K. To effectively increase the generated voltage, TEGs are fabricated by connecting p- and n-type legs electrically in series and thermally in parallel [8,9].

Recent advances in organic based TE materials show promising results for their application as a sustainable alternative to conventional inorganic materials [10,11]. In addition, solution-processed organic semiconductors have recently emerged as viable replacements to traditional inorganic semiconductors, especially for flexible devices, due to their light weight and their potential for low-cost continuous fabrication processes.

Chemical doping of graphitic materials such as carbon nanotubes (CNTs) relies on the addition or removal of holes or electrons by the specific molecular dopant. In this way, an effective and stable tuning of carrier mobility can be achieved. SWCNT doping strategies have been extensively studied to optimize both the final p- and n-type thermoelectric properties [12,13]. For instance, the ion conducting polymer polyethyleneimine (PEI) has been employed to modify CNTs which are inherently of p-type to produce thermoelectric nanocomposites with n-type nitrogen doped CNTs [14–16]. The intrinsically p-type CNTs were treated with salt/crown elements or amino groups in order to further enhance the p-type behaviour or the n-type behaviour of the resulting nanocomposites [17,18]. Kim *et al.* reported a production of thermoelectric fibers prepared via simple wet-spinning of single walled carbon nanotube (SWCNT) / poly(vinylidene fluoride) (PVDF) pastes with power factors for the p- and n-type SWCNT / PVDF composite fibers of 378 and 289 $\mu W/m \cdot K^2$ respectively [19].

Numerous research studies report that tailored nanostructuring combining conjugated or dielectric polymer phases may enhance phonon scattering effect and impede carrier scattering phenomena [20]. These TE nanocomposite manufacturing approach facilitates the attainment of low thermal conductivity values without reducing the electrical conductivity and the Seebeck coefficient, resulting thus in *PF*s [21]. Semiconductive polymers such as PEDOT:PSS have a relatively low thermal conductivity (κ: ~0.1–1 $W/m \cdot K$), while their electrical conductivity can be as high as σ ~100000 S/m. This unique combination of properties makes this class of material an ideal candidate for TE applications [22]. Additionally, in comparison to their inorganic rigid counterparts, most polymers have the major advantages of being flexible, moldable and printable [23].

Caroll *et al.* [24] reported a solid-state multiple element TEG module for the conversion of thermal energy to electrical based on MWCNT / PVDF composite thin films. The TE voltage generated by these layers was the sum of contributions from each layer, resulting in increased power output. Ishida and co-workers proposed a proof-of-concept study of organic thermoelectric modules fabricated by thermal lamination at low temperature using the benchmark p-type material poly(3,4 ethylenedioxythiophene) / poly(styrenesulfonate) (PEDOT:PSS). The fabricated 1.54 cm^2 device produced a power output of 37 mW at a ΔT of 50 K corresponding to a power density of 24 mW/cm^2 [25].

Considerable research effort is also devoted to conversion of non-conductive fibers such as glass fibers (GFs) to thermoelectric fibers. TE-enabled GFs may perform both as thermal insulators and also recover waste heat by producing electricity. Most importantly, by applying functional aqueous solutions of TE nanocrystals as a coating on the otherwise TE inactive reinforcing GFs, they are transformed to thermoelectric-enabled materials [26–31]. By optimizing manufacturing protocols to include TE coatings on GFs employed for advanced composites, large-scale production of TE harvesting devices may be realized. For instance, a TE textile was prepared via applying SWCNT / PANI composites on polyester using ultrasonic induction. A *PF* of ~0.28 $\mu W/m \cdot K^2$ was achieved when the initial aniline concentration was 1.83 mM, corresponding to a more than two orders of magnitude increase when compared to textiles coated with pure PANI. When two pieces of the TE textiles were serially assembled, the module could generate a TE voltage output of 3.82 mV, producing a power output of 48 nW at a temperature difference of 75 K [32].

Multifunctional fiber reinforced polymer composites have also been reported to attain functionalities related to energy generation, energy storage and energy harvesting [33–35]. Recently, the development of structural supercapacitors and batteries has been reviewed. So far, most works focus on using conductive carbon fibers (CF) as the active material and a solid polymer electrolyte as structural matrix. Senokos *et al.* presented a method to produce structural composites capable of energy storage by integrating CNT fiber veils and an ionic liquid-based polymer electrolyte as thin sandwich structures between carbon fiber reinforcing plies. The resulting structure acted simultaneously as a structural composite and an electric double-layer capacitor with flexural modulus of 60 GPa and flexural strength of 153 MPa, combined with 88 mF/g specific capacitance and very high power (30 W/kg) and energy (37.5 mWh/kg) densities [36].

The current study introduces for the first time the manufacturing of a structural TEG-enabled glass fiber reinforced polymer (GFRP) composite which exhibits high electrical power output of 2.2 μW when exposed in 100 K ΔT in an in-plane configuration. Finally, the mechanical properties of the multifunctional laminate composite were examined under static and dynamic mechanical testing coupled with on line structural health monitoring (SHM) based on the TE functionality of the structural TEG.

4.1.2 Experimental section

4.1.2.1 Materials

SWCNT powder provided from OCSiAl (TUBALL, carbon content: >85 wt. %, CNTs: ≥75 wt. %, outer mean diameter of SWCNT 1.8 ± 0.4 nm, length of SWCNT >5 μm, metal impurities <15 wt. %). SDBS (sodium dodecylbenzenesulfonate - M_w = 348.48 g/mol), Poly(ethyleneimine) solution ~50 % in H_2O-PEI (M_r = 600000-1000000) were purchased from Sigma Aldrich. The PEDOT:PSS conductive polymer screen-printing ink (Orgacon™ EL-P5015 with 2.5-5.5 % wt. solid content) was provided by Agfa.

Silver (Ag) paint was received from Agar scientific. Distilled water (DI water) and Isopropyl alcohol (IPA) of ≥98 % purity has been used throughout all the different processes in this research work.

A unidirectional (UD) glass fabric (GF) (320 g/m^2) of 0.26 mm single ply thickness was used. The LY-5052 DGEBA-based epoxy resin and amine-based hardener by Huntsman Advanced Materials Inc. was utilized as the composite matrix (resin to hardener weight ratio 100:38 w/w) with $T_g \approx 131$ ^oC. Curing was conducted under 3 MPa pressure using a hydraulic press at room temperature (RT) for 24 h and the post-curing at 100 ^oC for 4 h.

4.1.2.2 Fabrication and optimization of the p- & n-type GF-SWCNT fabrics

Pristine SWCNT (2 mg/mL) were dispersed using the ultrasonic probe UP400S by Hielscher at low amplitude and power of 10 Watt for 45 min. Various amounts of SDBS anionic surfactant were employed to produce SWCNT dispersions with p- and n-type TE behaviour. The initial dispersion (SWCNTs:SDBS - 1:2.5) for the production of the p-type TE ink that contained 2 mg/mL of the SWCNTs dispersed in water with the assistance of 5 mg/mL SDBS. For the p-type TE ink preparation, a PEDOT:PSS solution was prepared by diluting a 35 % by weight of the conductive polymer paste in 1:1 (DI water:IPA) via gentle stirring for 1 h. Then, the prepared PEDOT:PSS solution was added at a 2:1 ratio (SWCNT initial dispersion to PEDOT:PSS solution) and left for 1 h stirring, resulting in the final p-type TE ink. For the production of the n-type TE ink SWCNT (2 mg/mL) were dispersed assisted with SDBS (2 mg/mL) with the presence of PEI (5 mg/mL). As shown in **Figure 40a**, the produced p- and n-type SWCNT TE inks were deposited onto GF fabrics via blade coating which resulted to homogeneous and continuous TE films, both of p- and n-type. The optimization process correlates with the dry film thickness reduction onto the GF substrates without eliminating the desirable electrical properties. Electrical resistivity is an intrinsic property of a conductive film which is directly proportional to the total resistance R, an extrinsic quantity that depends on the length and cross-sectional area of the corresponding film. Larger cross section areas present lower values of electrical resistance. In the case of SWCNT, changes within the conductive network due to thickness optimization are able to positively impact the electrical conductivity. Both cases are valid until the bulk electrical resistance value is reached, thereby no further increments in electrical conductivity can be achieved (**Figure 40b**). Therefore, since the Seebeck coefficient is a material property [6], the *PF* of the coated GFs can be optimized by combining the most appropriate substrate dimensions and coating thickness. This is of utmost importance for the exploitation of the nanomaterial coated reinforcements as thermoelectric elements in composite structures. For the blade coating process, the distance between the heated GF substrate and the blade was fixed at 200 μm. The same quantity of each TE ink was deposited on both sides via blade coating. In order to fully evaporate the residual aqueous solvent, the drying process was carried out at 90 ^{o}C for 60 min on a hot-plate. The optimized dry film thicknesses (t) of the produced p- and n-type GF-SWCNT TE-enabled fabrics were ~12.9 μm and ~13.7 μm, respectively. These values were calculated indirectly, using electrical measurements according to $\sigma = 1/R_S \cdot t$ [37], where σ is the bulk electrical conductivity measured on "bucky paper" film forms derived from vacuum-assisted filtrations with a PVDF filter membrane (47 mm diameter and 0.45 μm pore size). R_S is the measured sheet resistance of the produced films onto the p- and n-type GF-SWCNT fabrics corresponding to 0.68 Ohm/□ and 0.52 Ohm/□, respectively.

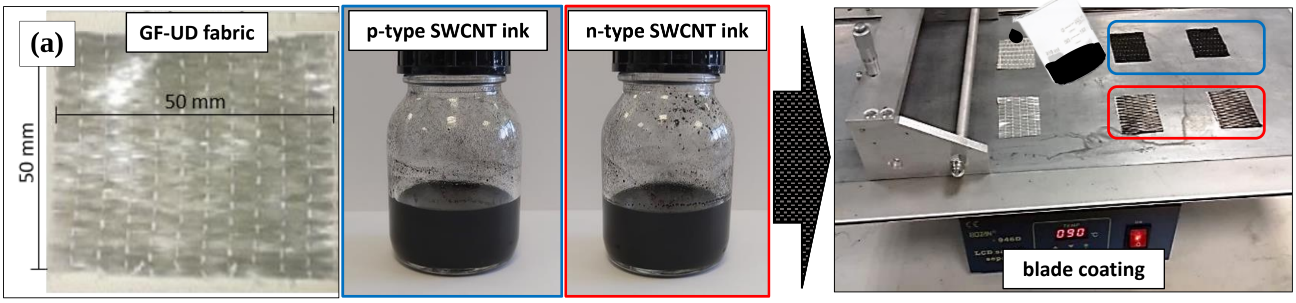

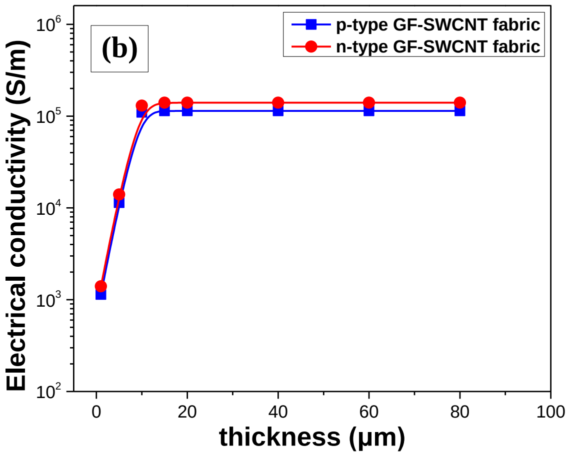

Figure 40. (a) Fabrication process of the p- and n-type GF-SWCNT fabrics, **(b)** graph presenting the electrical conductivity of both p- and n-type GF-SWCNT fabrics as a function of the coating thickness.

4.1.2.3 Lamination of the GFRP structural TEG device

The formation of a p-n heterojunction between the respective TE-enabled laminae is needed to manufacture a TE-enabled laminate. In this case, the heterojunction always involves 2 dissimilar materials, *i.e.*, a GF lamina coated with p-type SWCNT and a GF lamina coated with n-type SWCNT. The 2 functional laminae are electrically connected to form an interlaminar interface, resulting in a p-n TE junction. As aforementioned, the p- and n-type coated laminae are obtained by the modification of the glass fibers with acceptor and donor properties, respectively. An advantage of using the interlaminar interface as the TE junctions is that the fibrous laminae in different directions *e.g.*, perpendicular to one another give a multi-dimensional array of interconnected TE legs. Every TE junction was a well-defined region between the epoxy resin and the coated p-n GF laminae interlaminar interface. For this purpose, the TE junctions were formed by allowing two dissimilar TE-enabled laminae to overlap partially. The overlapping regions served as the p-n TE junctions, while the remaining regions served both as the TE legs, as well as the reinforcing phase (**Figure 41**). A plain GF lamina was employed as an insulator in between all pairs of functional laminae, covering all interlaminar area apart from the heterojunction.

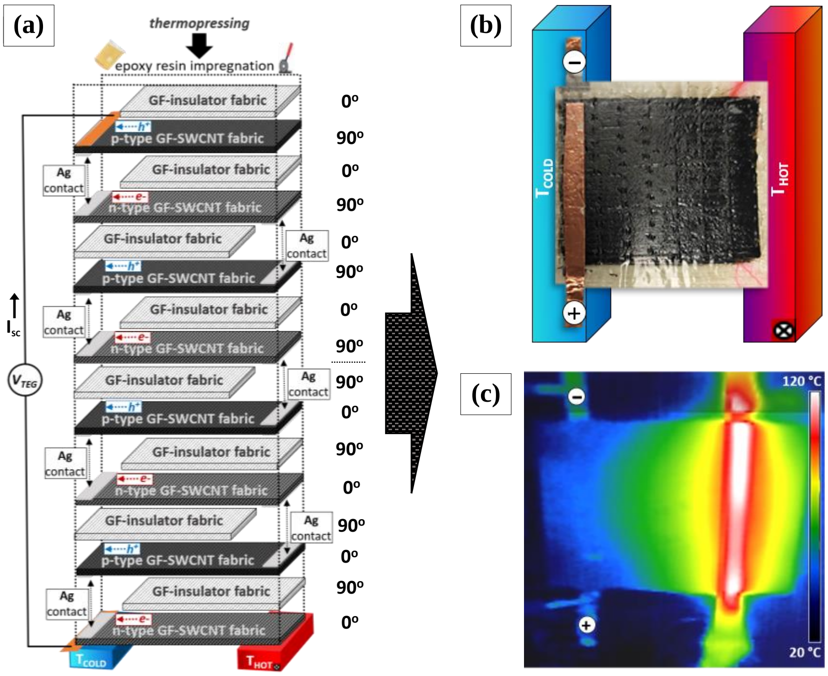

Figure 41. **(a)** Schematic depiction of the lamination process for the in-plane structural TEG device fabrication, **(b)** top-view illustration of the 16-ply $[0/90]_{4s}$ TEG-enabled GFRP laminate and **(c)** corresponding IR-T image with an in-plane ΔT of 100 K.

A functional TEG structural laminate consisting of 16 reinforcing plies with a cross-ply balance symmetric alternating lamination $[0/90]_{4s}$ was manufactured, as schematically illustrated in **Figure 41a**. 4 p-type GF-SWCNT fabrics, 4 n-type GF-SWCNT fabrics and 8 GF fabrics acting as the insulating layers were used. As electrical and thermal continuity is of primary importance to minimise contact resistance, Ag paint was chosen for the interface of the heterojunction. Ag paint has high electrical and thermal conductivity, low sintering temperature and good physicochemical stability over a large operating temperature range. Metallic contact stripes were accurately deposited onto the coated p- and n-type GF fabrics. 2 copper (Cu) foil electrodes were utilized as the external contacts of the device. Finally, all GF fabrics were impregnated with epoxy resin and laminated by hand lay-up. The laminate was cured and post cured according to the manufacturer's datasheet.

4.1.2.4 Structural integrity evaluation coupled with on-line SHM

The structural TEG device was evaluated as a possible novel sensitive self-sensing indicator for on-line structural health monitoring of the laminate, based on the inherent TE functionality. 2 metal alloy wire joule heaters attached on one edge and on both the top and the bottom surface of the TEG-enabled laminate. For the thermal activation of the metallic-alloy based heaters, 2 independent power supplies (Xantrex XPH 18-10 DC) were utilized. The power supplies maintained steady ΔT

of 80 K the left and right side of the TEG-enabled laminate throughout a quasi-static 3-point bending mechanical test. The generated TE short circuit current (I_{sc}) change profile was continuously monitored together with the load application. Thermal imaging was employed to ascertain the stability of ΔT.

4.1.2.5 Characterization techniques

The viscosity of the p-type and the n-type ink was characterized via the NDJ-9S digital rotary viscometer.

The FEI NanoSem 200 (FEI, Eindhoven / Netherlands) Scanning Electron Microscope (SEM) at an operational voltage of 5 KV was used to study the morphology of the nanographitic structures.

The Labram HR- by Horiba Scientific Raman system was used to identify the existing phases. The 514.5 nm line of an Ar^+ ion laser operating at a laser power of 1.5 mW at the focal plane was employed for the Raman excitation. An optical microscope equipped with a 100× objective served both for delivering the excitation light and collecting the back-scattered Raman activity. All Raman spectra were collected in the range of 100-3500 cm^{-1}. The spectral A linear baseline subtraction and subsequent normalization in relation to the peak with the maximum intensity was performed to all acquired spectra.

Contact angle measurements were acquired via a commercial automated contact angle goniometer system manufactured by Ossila Ltd.

4-probe sheet resistance measurements were conducted to determine the basic electrical characteristics of the produced films. The 4-point probe commercial system by Ossila Ltd was used to measure the 4-probe sheet resistance R_s and calculate electrical conductivity as $\sigma = 1/R_s \cdot L/A \cdot (\ln 2/\pi)$ where, L is the length, and A is the cross section of each sample. The reported values are mean values from at least 4 measurements performed on different samples.

The Seebeck voltage was determined using a custom setup, by thermally coupling one edge of the laminate on a controlled temperature aluminum block and the other on an aluminum block at room temperature. The temperature of the hot and the cold blocks was continuously monitored with a K-type thermocouple and an IR-thermometer (OMEGA OS-VIR50 Dual Laser Video IR Video Thermometer) respectively, to determine the temperature difference (ΔT). The electrical and thermoelectrical measurements were carried out using a digital multimeter (Agilent 34401,A6½) with a standard 2-probe method. The generated voltage difference ΔV was recorded for different values of ΔT. The Seebeck coefficient was determined from the slope of the temperature difference versus output voltage curve. Thermal images were captured via Seek Thermal UWAAA Compact PRO Imaging Camera IR Infrared Imager with a temperature working range of -40 to 330 °C.

3-point bending quasi-static tests were performed using the 100 KN Universal Testing Machine by Jinan Testing Equipment IE Corporation, according to the ASTM D 790-03. Five reference specimens (without TEG functionality) and 5 TEG-enabled specimens were tested. $[0/90]_{2s}$ TEG-enabled GFRP laminates and plain $[0/90]_{2s}$ GFRP laminates were manufactured as reference. More specifically, the laminated structures were cut into flat rectangular specimens 50 mm long, 13 mm wide with a bending length equal to 34 mm. The thickness of the reference specimens was ca. 2.1 mm while that of the TEG laminate specimens was ca. 2.4 mm. The difference in the thickness of the respective laminated structures is due to the p- and n-type SWCNT coatings onto the GF fabrics from both top and bottom sides, which lead to an individual increase of each reinforcing layer thickness. A loading speed of 1 mm/min was used for the tests.

The Netzsch thermal analyser (DMA 242 cell) Dynamic Mechanical Analysis (DMA) was employed to study the dynamic properties of the reference and TEG-enabled systems. The 3-point bending mode operating at 1 Hz with 3 °C/min heating rate from 30 to 200 °C was used. 3 specimens from each configuration were tested. The dimensions of the specimens were 50×10×(2.1 or 2.4) mm^3.

Prior to testing, all specimens cut from the laminates were dried in a vacuum-oven at 40 °C overnight. All tests took place in ambient conditions (temperature: 22 °C ± 3 °C, humidity 50 % ± 10 %).

4.1.3 Results and discussion

For the exploitation of the exceptional properties of the SWCNT, it is critically important to accomplish a stable dispersion, de-agglomerated to the highest possible degree. In most cases, the handling of aqueous CNTs solutions remains complicated due to the physicochemical tendency of the CNTs to be entangled. The suitable processing of the dispersion can lead to sufficient de-agglomeration of the SWCNT, thus unlocking their beneficial properties. The produced p- and n-type SWCNT dispersions (TE inks) were evaluated according to their rheological behaviour, morphological characteristics, spectroscopically and in terms of wetting by epoxy resin. All the previous techniques are prerequisites to study and interpret the potential for printing TE-enabled coatings onto fibrous reinforcing substrates for manufacturing of multifunctional composite laminates.

4.1.3.1 Physicochemical characterization of the p- and n-type GF-SWCNT fabrics

The functional inks were also selected based on the acceptable rheological behaviour for blade coating technique in order to create the desirable dry film thicknesses with the appropriate electrical values onto the fibrous substrates. Accordingly, viscosity measurements were carried out in order to assess that both the resulting p- and n-type TE inks were capable of the aforementioned printing technique. More precisely, for the p-type TE ink viscosity was found to be 202.5 mPa · s and for the n-type TE ink was slightly higher at 244.5 mPa · s at room temperature conditions.

The resulting p- and n-type SWCNT coating morphologies onto the GF fabrics were investigated via SEM. **Figure 42a-b** illustrates the morphology of the coated GFs with homogeneously distributed SWCNT covering the surface of the fibrous substrates.

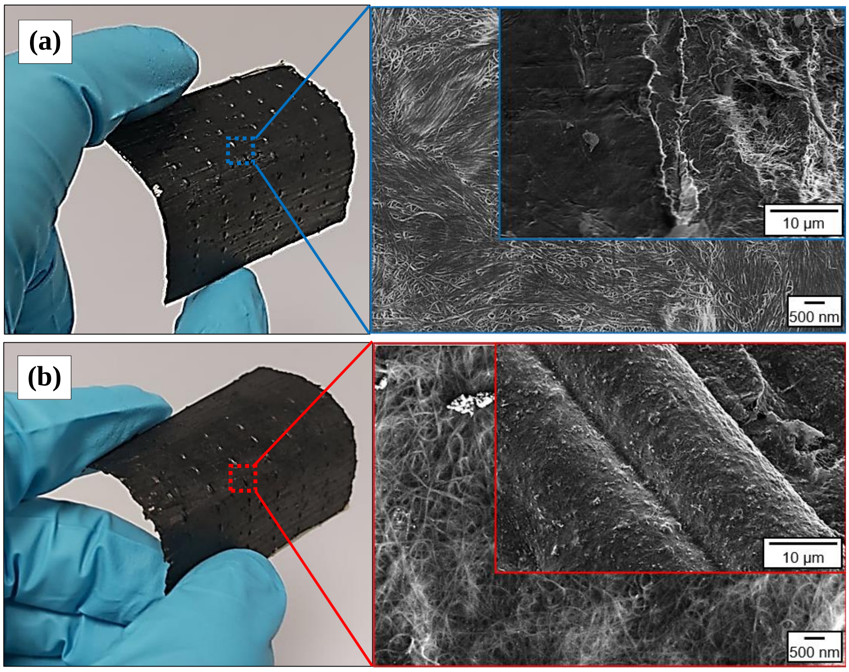

Figure 42. SEM images of the **(a)** coated p-type GF-SWCNT and **(b)** coated n-type GF-SWCNT TE-enabled fabrics at different magnifications.

In more detail, it can be observed that the existence of PEDOT:PSS within the p-type SWCNT coated film induced a tendency to create a more oriented CNTs network due to electrostatic interactions. On the contrary, the n-type SWCNT bundles disclose a more randomly distributed CNTs network. Both images reveal a quite uniform and thick coating with a dense interconnected network of SWCNT, succeeding a continuous film onto the GF fabric. No visible aggregates were observed at the lower magnification images as well as at the different high-magnified SEM images. This fact indicates the high-quality dispersion of the functional inks and the adhesion properties with the fibrous substrate.

The Raman spectra of the p-type and n-type SWCNT were evaluated both in “bucky paper” films form and coated onto GF fabrics to evaluate the presence of each of the constituents that were used in the two dispersions. Raman spectroscopy has been widely used for studying SWCNT as their spectra present prominent features that are easily identified.

Following the steps of the preparation process of the SWCNT dispersions, **Figure 43** depicts the Raman spectra of the SWCNT “bucky paper” film derived from the initial SWCNT:SDBS (1:2.5) dispersion (black curve), the PEDOT:PSS solution (blue curve) that was added to the initial SWCNT dispersion, the resulting p-type SWCNT TE ink in “bucky paper” film form (green curve) and the latter ink coated on a GF fabric (p-type GF-SWCNT fabric – dark green curve). Moreover, are depicted the Raman spectra of the n-type SWCNT “bucky paper” film (purple curve) and the same ink coated on a GF fabric (n-type GF-SWCNT fabric - red curve).

Inset plots were also included in all the spectrum to ease the observation of the very low intensity peaks. The position of each vibrational mode was evaluated by a fitting procedure. The fitted spectra are presented in Supporting Information (**Figure S3 and Figure S4**).

The acquired SWCNT spectra presented all the expected vibrational modes commonly encountered in graphitic materials [38]. In more detail, the most pronounced vibrational mode, that was located at about 1570 cm^{-1}, was the graphitic or G band with E_{2g} symmetry. The radial breathing mode, that is a unique feature of SWCNT was also observed at about 130 cm^{-1} to 150 cm^{-1}. Some minor defects (sp^3 carbon atoms) were also present in the SWCNT film, as demonstrated by the D vibrational mode which is a disorder-induced band that appeared at about 1345 cm^{-1}. Furthermore, the 2D vibrational mode dominated the second order spectrum of the SWCNT coatings. This band was located at about 2680 cm^{-1}.

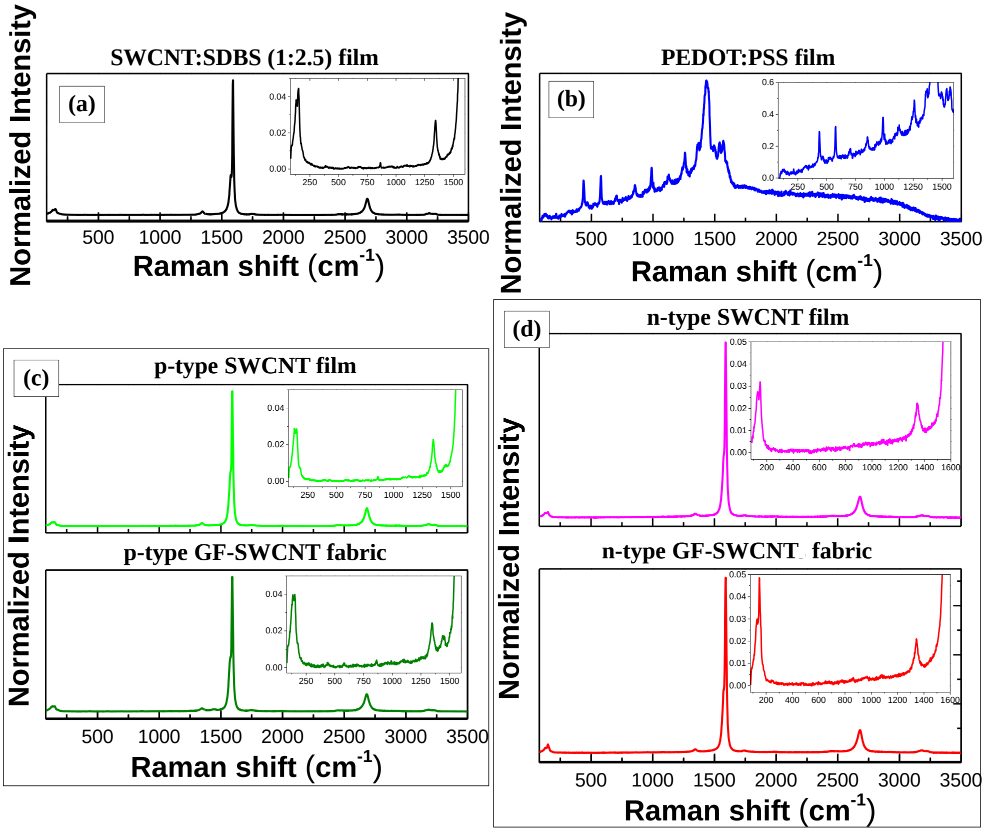

Figure 43. Raman spectra of **(a)** the initial SWCNT dispersion as film**, (b)** the PEDOT:PSS film**, (c)** the p-type SWCNT film and the corresponding p-type GF-SWCNT fabric, **(d)** the n-type SWCNT film and the respective n-type GF-SWCNT fabric.

The initial dispersion (SWCNT:SDBS - 1:2.5 film) for the production of the p-type TE ink that contained 2 mg/mL of the SWCNT dispersed in water with the assistance of 5 mg/mL SDBS is represented in the **Figure 43a**. Then, the PEDOT:PSS solution (**Figure 43b**)**,** PEDOT:PSS film) was added in the previous dispersion to achieve the final p-type TE ink at a 2:1 ratio of SWCNT to PEDOT:PSS. In general, the intensity of the raw spectrum of the PEDOT:PSS film was much lower than the intensity of the SWCNT' raw spectra. The most pronounced contribution of the PEDOT:PSS solution into final p-type TE ink was a band located at ~1433 cm^{-1} in the spectrum of PEDOT:PSS film that can be attributed to the symmetric $C_\alpha=C_\beta$ (-O) stretching of PEDOT polymer structure [39]. The position of this vibrational mode was evident at the p-type TE ink in "bucky paper" film form and was even more pronounced when the ink was used as a coating on the GF fabric, as can be seen in the inset plots of the (1455 cm^{-1}) and green curves (1446 cm^{-1}), respectively (**Figure 43c**).

Also, for the production of the n-type TE ink SWCNT (2 mg/mL) were dispersed assisted with SDBS (2 mg/mL) with the presence of PEI (5 mg/mL). The addition of PEI during the dispersion process did not produce any new vibrational modes in the Raman spectra of the n-type SWCNT as a "bucky paper" film nor when applied as a coating onto GFs in **Figure 43d**.

Static contact angle measurements were utilized as a sensitive tool for evaluating the interaction of the surface of the SWCNT coated GF fabrics with the epoxy resin, which was employed for the laminate fabrication. The wetting of the pristine and both p-, n-type coated GF substrates by the resin system could indicate the inherent hydrophilic behaviour of the glass fibers, which is apparently a satisfying indicator to achieve a good adhesion and interfacial compatibility. From the contact angle experiments, the nature and the expected compatibility of TE-enabled GF laminae coated with p-type SWCNT, as well as the n-type SWCNT coated GFs were elucidated. Typical results are represented in **Figure 44** showing the relative contact angle measurements. The images on the left side for each case were captured the first moment that the suspended epoxy resin drop landed onto the surface of the fabric, while the images on the right side were acquired 60 seconds later.

Considering the instantaneous contact angle, the pristine GF substrate exhibited hydrophobic behaviour and really poor wetting from the epoxy resin droplet (95.13^o) in comparison to the p-type and the n-type SWCNT coated GF substrates that exhibited limited wetting (47.24^o) and a hydrophilic behaviour with good wetting (80.53^o), respectively. However, the porosity of the fibrous substrates facilitated their wetting by the epoxy resin droplet with time. As can be seen in the inset images of **Figure 44** all the fabrics were successfully wetted by the epoxy resin in one minute after their contact. In more detail, the pristine GF fabric, the p-type and n-type SWCNT coated GF substrates presented similar average contact angles at this stage, namely 26.93^o. Comparatively, the p-type SWCNT coated GF showed a contact angle of around 28.38^o, 28.38^o and 27.01^o, respectively. Taking also into account the pressure that is typically applied for the manufacturing of the composite laminates, no impregnation problems are expected to be met due to the existence of the coatings onto the fibrous laminae.

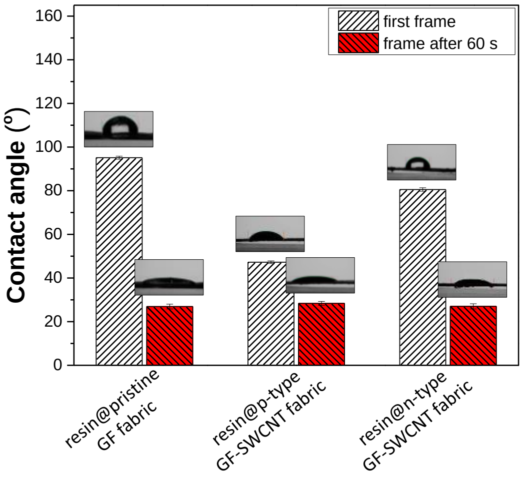

Figure 44. Average static contact angle measurements for each GF system (insets: images of a resin droplet in contact with the GF substrate, processed by a goniometer's software).

4.1.3.2 TE performance of the p- and n-type GF-SWCNT fabrics

To produce sufficient micro-power, any TE material needs to be combined into a module containing many alternating p-type and n-type TE legs that are connected electrically in series and thermally in parallel. This arrangement of TE elements is being utilized because it allows the direct contribution of each TE leg to the total TE voltage, while being subjected to the same maximum available Δ*T*. This device architecture results in the highest attainable TE power for a given number of TE legs, when exposed to the available temperature difference. In this study, the p- and n-type GF-SWCNT fabrics acted as the efficient TE legs.

Grunlan *et al.* reported enhanced *PF* values from CNTs blended with PEDOT:PSS composites stemming from decorated particles of PEDOT:PSS onto the surface of CNTs, creating extra electrical junctions between the CNTs conductive networks. On the other hand, the thermal transport remained comparable to typical polymeric materials due to the dissimilar bonding between CNTs and PEDOT:PSS [40,41]. Towards this approach, it becomes feasible to achieve higher electrical conductivity values without negatively affecting the TE efficiency, as also observed in this study in comparison to a previous work [31]. Moreover, the thermal conductivity was shown to be maintained as low as those of a heat insulating polymer [42,43]. Particularly, the p- or n-type molecular doped SWCNT-based nanocomposites reveal thermal conductivity values in the range of ~0.15-0.25 W/m · K at room temperature (RT) [40].

Initially, the bulk TE properties of both films were studied. The relevant results are presented on **Table 6.** The positive values of the Seebeck coefficient indicate the p-type semi-conducting behaviour and the negative values indicate n-type measured at Δ*T* of 100 K. Moreover, the electrical conductivity measurements have been carried out at RT as shown in Supporting Information (**Figure S5**).

Table 6. TE properties of the p-type and n-type films on “bucky paper” form.

TE film	**Electrical conductivity** (**σ**) (S/m)	**Seebeck coefficient** **(S)** (μV/K)	**Power factor** **($\sigma \cdot S^2$)** (μW/m · K^2)
p-type SWCNT	$1.14\text{x}10^5 \pm 225$	+26 ± 1.2	77
n-type SWCNT	$1.4\text{x}10^5 \pm 447$	-31 ± 1.5	135

The calculated *ZT* values are 0.12 for the p-type SWCNT films and 0.36 for the n-type SWCNT films. Consequently, the thermal to electrical energy conversion efficiency (Carnot efficiency - η) of the p- and the n-type SWCNT TE material is 0.83 % and 2.17 % at Δ*T* = 100 K, respectively.

The aforementioned values are determined by the following equation [6]: $\eta = (T_H\text{-}T_C)/T_H \cdot \surd(1+ZT)\text{-}1/\surd 1+ZT+(T_C/T_H)$, where T_H represents the temperature of the hot side and T_C is a steady temperature of a cold side.

The TE performance for the produced p- and n-type GF-SWCNT fabrics was examined as a function of temperature. The respective values of the electrical conductivity, Seebeck coefficient and *PF* are illustrated in **Figure 45**.

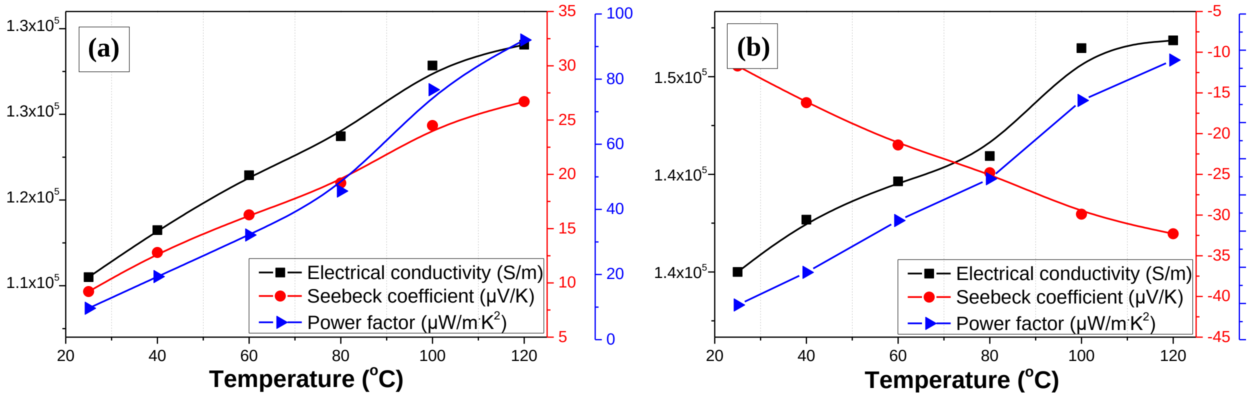

Figure 45. TE performance of **(a)** p-type GF-SWCNT fabrics and **(b)** n-type GF-SWCNT fabrics at a wide range of temperatures.

Regarding their TE response, the p- and n-type GF-SWCNT fabrics exhibited a Seebeck coefficient of +23 ± 1.3 μV/K corresponding to 60 $\mu W/m \cdot K^2$ and -29 ± 1.6 μV/K corresponding to 118 $\mu W/m \cdot K^2$ *PF* values, respectively. The aforementioned thermoelectric characteristics are strictly comparable with the corresponding bulk thermoelectric values of both p- and n-type films, as were measured in “bucky paper” form.

Overall, the TE properties of both type TE functional coated GF fabrics presented remarkable long-term stability while functioning at various temperature gradients exposed in ambient conditions, before the impregnation with the epoxy resin.

These fully organic, water-processable and flexible nanocomposite films possess many advantages for large-scale production of printed thermoelectric devices onto various types of substrates.

4.1.3.3 *Power output characteristics of the TEG-enabled GFRP laminate*

Two key points are critical for the TEG device fabrication using the lamination approach with the epoxy resin polymer matrix. The first is the existence of the necessary insulating GF laminae to avoid the direct contact between the p-type and n-type coated GF laminae. From the device design perspective, all the TE legs should be connected electrically in series and thermally in parallel. The second important point for fabricating a working device is to implement the proper localized ohmic interconnections between the p- and n-type TE-enabled laminae.

To evaluate the power output characteristics of the fabricated TEG-enabled GFRP laminates, the exact temperature difference of both sides of the structural device must be known. In order to improve the measurement reliability, the hot side temperature was ramped up, while the cold side temperature was kept constant at room temperature.

Figure 46 demonstrates the 16-ply (50×50 mm^2) with a thickness of 4.4 mm structural TEG laminate thermoelectric performance, when being subjected to an in-plane temperature difference of 100 K. **Table 7** includes the basic calculated power output characteristics.

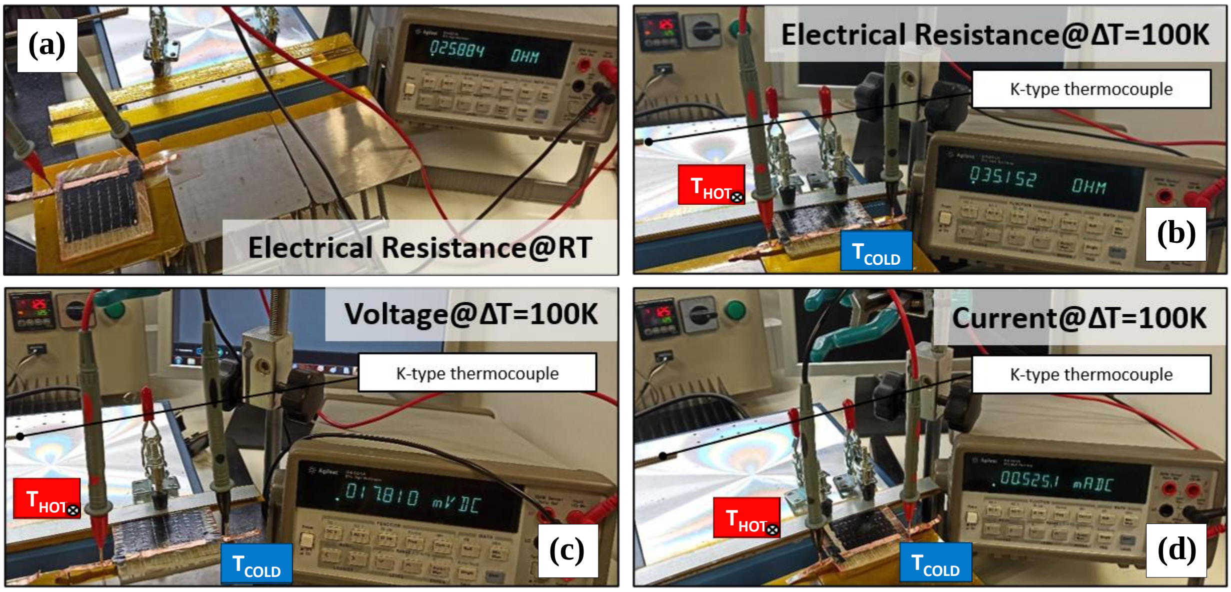

Figure 46. Demonstration of the TEG device **(a)** internal resistance (R_{TEG}) at room temperature, **(b)** internal resistance (R_{TEG}) at ΔT of 100 K and TE performance **(c)** voltage (V_{TEG}), **(d)** current (I_{sc}) during exposure to ΔT of 100 K.

Table 7. Power output characteristics for the GFRP TEG laminate.

T (K)	R_{TEG} (Ohm)	V_{TEG} (mV)	I_{SC} (μA)	P_{max} (μW)	Power density (W/m^2)
RT	25.8 ± 0.5	-	-	-	-
ΔT=100	35.1 ± 1.5	17.8 ± 1.1	525.1 ± 21.1	2.2	0.1

The maximum electrical power output (P_{max}) of the structural laminate TEG was calculated according to the following equation [34]: $P_{max} = (N \cdot S \cdot \Delta T)^2/4 \cdot R_{TEG} = \Delta V^2/4 \cdot R_{TEG}$, where N is the number of the TE legs, S the Seebeck coefficient and ΔT is the temperature difference. For the TEG laminate with dimensions of 50×50 mm^2 and 4 p-n TE junctions appeared an internal resistance

(R_{TEG}) of 35.1 ± 1.5 Ohm, generated V_{TEG} (V_{oc}: open circuit voltage) of 17.8 ± 1.1 mV, a short circuit current (I_{sc}) of 525.1 ± 21.1 μA, resulting in a calculated P_{max} of 2.2 μW with a corresponding power density of 0.1 W/m^2 at ΔT of 100 K. The total mass of the demonstrated GFRP TEG laminate was ~28.5 g and ca. 20 % increased compared to a corresponding plain GFRP laminate. Consequently, the gravimetric power density (estimated by dividing the achieved P_{max} at a ΔT of 100 K with the total mass of the structural device) of the 8 p- / n- thermoelements was 7.72×10^{-5} mW/g. According to previous literature findings, Kim *et al.* [44] developed p- and n-type CNT-based fabric-like lightweight thermoelectric device consisting of 144 p- / n- thermoelement pairs with a maximum power output of 1.8 μW at a temperature gradient of 32 K. Recently, an all-carbon SWCNT-based flexible TEG with 116 p- / n- thermoelement pairs was reported, able to succeed a maximum power density of 1.79 W/m^2 with a gravimetric power density of 0.65 mW/g at ΔT of 50 K [45].

The power output characteristics of the structural TEG device were examined at different temperature gradients of 60, 80 and 100 K, as a function of different applied external load resistances (R_{LOAD}) connected in series. The maximum power generation of 2.2 μW at ΔT = 100 K, was observed when the load resistance matched the internal TEG resistance of 35.1 Ohm. **Figure 47a** depicts the TE current-voltage-power experimental values of the 16-ply TEG GFRP laminate, while **Figure 47b** presents the TE voltage-power curves as a function of the applied external load resistances. The structural TEG device power output characteristics have been evaluated using a custom-built fully automated electronic system as shown in Supporting Information (**Figure S6**).

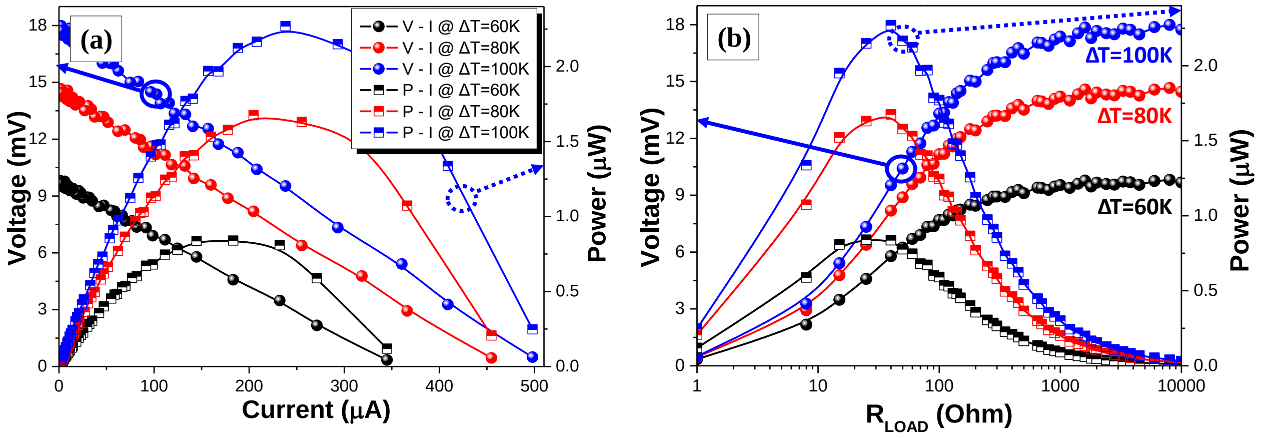

Figure 47. (a) TE characteristics of the 16-ply structural TEG-enabled GFRP laminate and **(b)** TE voltage and power at different load resistances- R_{LOAD} for various ΔT.

If higher voltage output is required, the number of connected in-series TEG-enabled GFRP composites could be increased resulting in an improved voltage output. As an illustration, the electrically in parallel connection of 2 TEG-enabled GFRP laminates was able to produce a V_{TEG} of

17 ± 1.4 mV, a I_{sc} of 1049.5 ± 42.4 μA and a P_{max} of 2.6 μW at ΔT of 100 K as presented in **Figure 48** and **Table 8**.

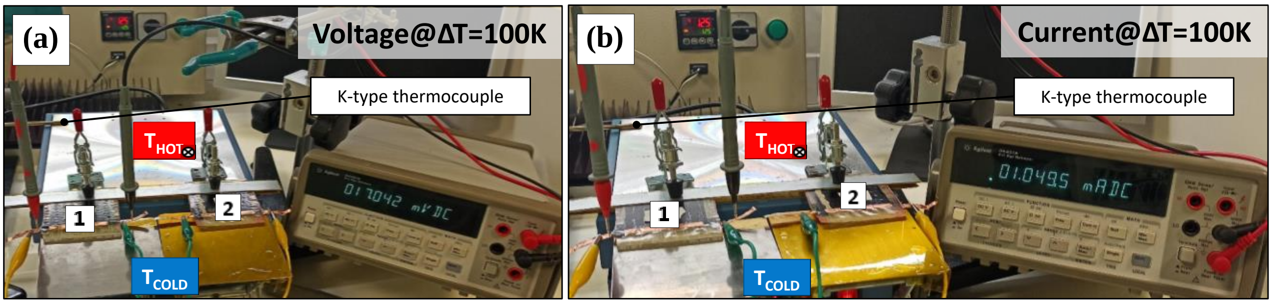

Figure 48. Demonstration of the power output characteristics **(a)** TE voltage (V_{TEG}), **(b)** TE current (I_{sc}) of 2 structural TEG-enabled GFRPs electrically connected in parallel exposed to a temperature gradient of 100 K.

Table 8. Power output characteristics for electrically in parallel connection of 2 similar TEG-enabled GFRP laminates.

T (K)	R_{TEG} (Ohm)	V_{TEG} (mV)	I_{SC} (μA)	P_{max} (μW)
RT	26.1 ± 0.7	-	-	-
ΔT=100	27.8 ± 1.7	17.0 ± 1.4	1049.5 ± 42.4	2.6

This approach enables the fabrication of high-performance, large-area organic TE devices via a continuous fabrication process such as roll-to-roll technique. Further improvements to the total power output could potentially be made through further optimization of the TE film efficiency of the single TE leg. This could be achieved by improving the Seebeck coefficient through chemical treatments of the nanotubes [21], or decreasing further the thermal conductivity by introducing phonon scattering defects along the nanotubes [11,14].

4.1.3.4 TEG-laminate under mechanical stress coupled with on-line SHM

A widely used in-situ strategy of monitoring the structural integrity of FRP composites *e.g.*, carbon fiber reinforced is the method of measuring the electrical resistance change (ERCM). The structural integrity of the structure is being directly monitored through the conductive nature of carbon fibers, which promotes their functionality of acting as self-sensing materials, without using any additional sensors [46]. To improve the sensitivity of ERCM, the integration of conductive materials (CNTs, carbon black, or even a combination of both) into the polymer matrix has been reported in various studies [47–52]. The addition of conductive phases into the matrix of the composite material not only enhances the electrical properties of the matrix but may also improve the mechanical properties of the final composite leading to a multifunctional "smart" composite. Thostenson and

Chou [53] studied the change of electrical resistance of GFRPs during tensile loading, where multi-walled carbon nanotubes (MWCNT) were introduced in their parent phase. Initially, a linear increase in the electrical resistance with respect to the load was observed. Subsequently, as the load increased further, a further increase in the electrical resistance was observed. Based on the previous principles, within this study the TE generated I_{sc} fingerprint during applied stress has been correlated with possible fracture mechanisms and damage of the TEG-enabled laminate.

Figure 49c depicts a graph indicating a 5.94 % TE short-circuit current (I_{sc}) relative change at ~2.1 % of the applied strain for a 16-ply $[0/90]_{4s}$ GFRP TEG-enabled laminate tested under quasi-static mechanical loads within a 3-point bending configuration. More specific, there been distinguished four areas. In first, there is no significant change in normalized TE I_{sc}, resulting in that the material has not developed permanent damage at this stage (elastic area). Then (area 2), a gradual drop of normalized TE I_{sc} is observed. There is also a change in the slope of the deformation curve which can be observed roughly in the middle of stage 2, which indicates a reduction of the flexibility and possibly mark the beginning of permanent damage growth inside the composite. Afterwards (area 3), the TE I_{sc} stabilizes and immediately after (area 4) follows one monotonous decrease which continues until the final failure of the composite. This decrease is correlated with the development of permanent defects within the material and thus its structural degradation.

All in all, a relatively sensitive self-powered piezoresistive indicator for the structural integrity of the multifunctional laminate composite was noticed. In more detail, the generated I_{sc} due to the thermoelectric effect during loading is a responsive dynamic fingerprint of the open circuit voltage (V_{TEG}) or V_{OC} and the internal electrical resistance (R_{TEG}) of the structural TEG device. Authors indicate that the monitoring of internal properties such $\Delta I_{sc}/I_{sc0}$ based on the energy harvesting non-structural functionalities of the composites could establish a roadmap for energy autonomous structural health monitoring of advanced composites.

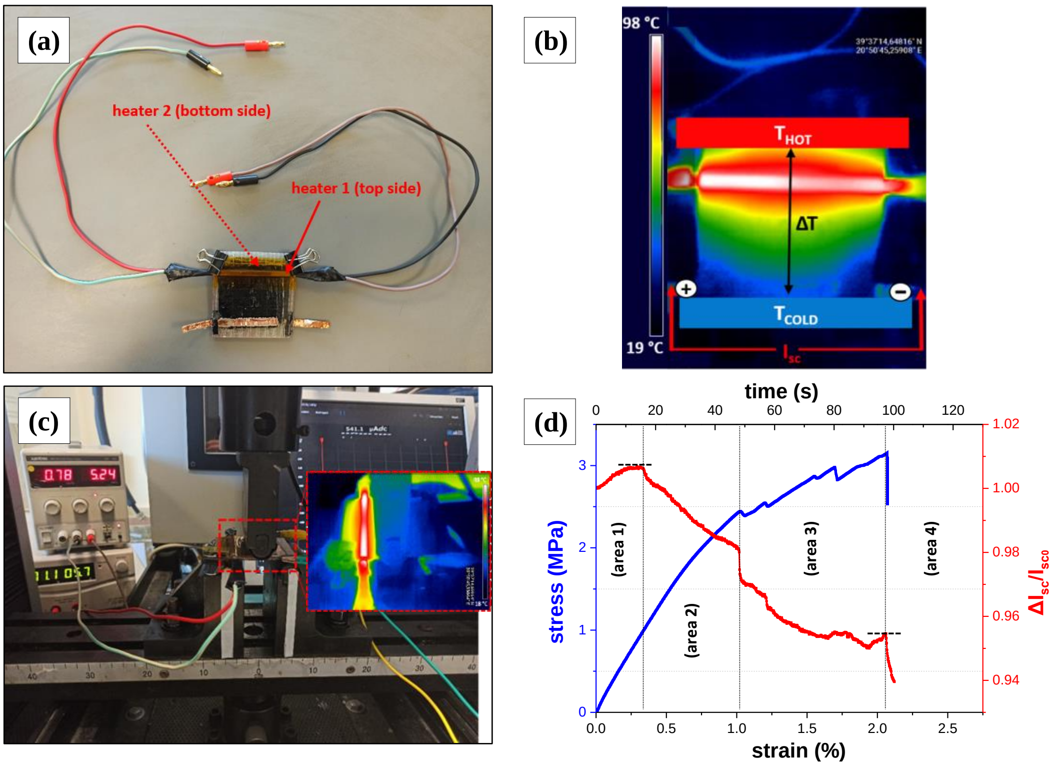

Figure 49. (a) photo of a 16-ply GFRP TEG-enabled laminate with surface mounted metallic-alloy based electrothermal resistive heaters on both same up and down sides, **(b)** top-view IR-T image at ΔT of 80 K, **(c)** set-up illustration of quasi-static mechanical test coupled with electric and thermal monitoring measurements and **(d)** graph of the thermo-electromechanical testing results.

4.1.3.5 Mechanical performance evaluation of the multifunctional laminate

The results obtained from the quasi-static 3-point bending tests are presented in **Figure 50a-b**. As shown in the stress-strain diagram, a reduced mechanical response of the TEG-enabled laminate specimens is being perceived. However, a 28.8 % increase of the maximum load of the TEG laminate specimens and a 12.4 % increase of the displacement compared to the reference laminate until the failure was recognized. Moreover, the bending strength of the TEG-enabled laminate specimens was decreased by 33.4 % and the flexural modulus by 34.7 % in contrast with the reference GFRP laminate specimens. The higher force values, combined with lower strength values are a consequence of the increased thickness of the TEG-enabled laminate specimens. So, as the elastic resistance to bending is proportional to the thickness of the specimen squared, the developing stress is inversely proportional to this size. In addition, as can be seen from the fracture images, the TEG-enabled laminate specimens showed a different type of failure than the reference specimens. Specifically, the reference specimens failed mainly due to bending, while the TEG-enabled specimens displayed several delaminations at their edges. This fact is due to the combination of increasing the thickness / bending ratio of the specimens, which makes its behaviour against bending more prone to shear failure. Also, the existence of the surfactant SDBS in both p-and n-type TE coatings onto the GF laminae may degrade the adhesion of the matrix to the coated fibers and reduces the interfacial affinity, causing the specimens to fail in this type of fracture against bending.

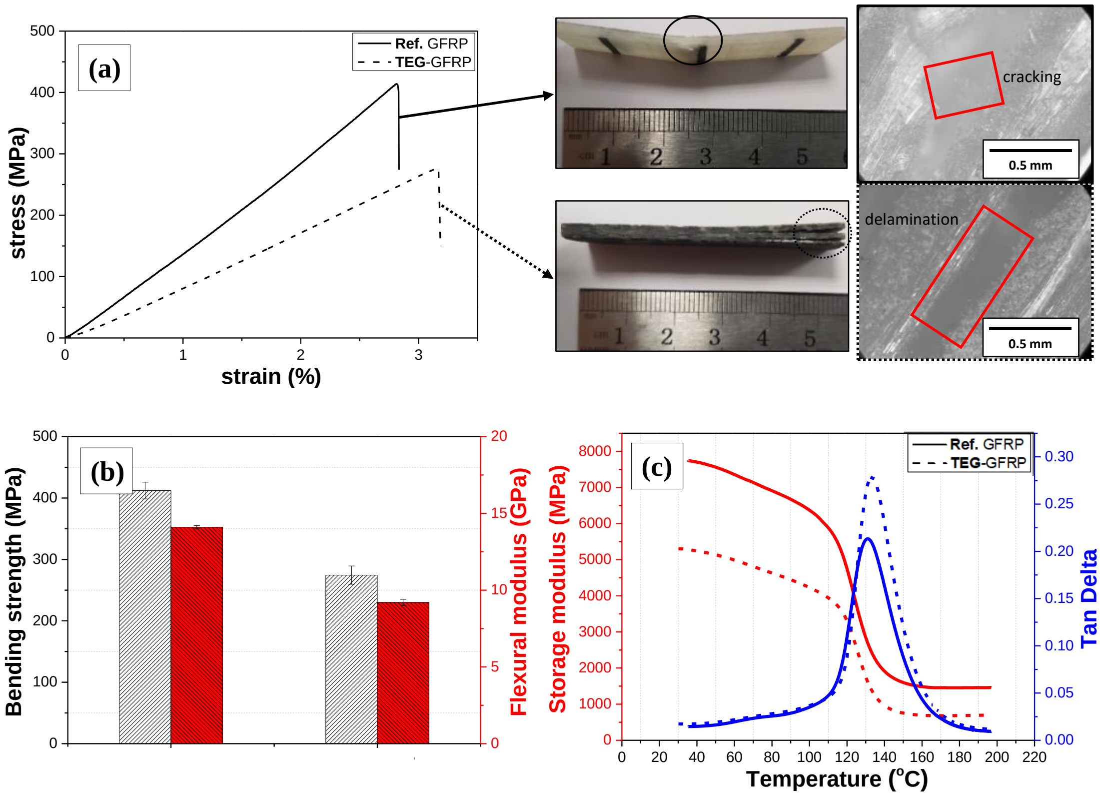

Figure 50. Reference specimens and TEG-enabled specimens: **(a)** Stress-strain curves, optical and microscopic images of the failed specimens, **(b)** Bending strength and flexural modulus and **(c)** Dynamic Mechanical Analysis.

Dynamic Mechanical Analysis (DMA) tests were conducted according to ASTM D7028-07 [54], which is designed for determining the glass transition temperature (T_g) of continuous fiber reinforced polymer composites. The T_g value from DMA is frequently used to define the temperature range of composite materials usage, as well as an indicator for quality control of the production.

The results obtained from the 3-point bending dynamic stress tests are presented in **Figure 50c**. A 31.5 % degradation of the storage modulus for the TEG-enabled laminate (TEG-GFRP) compared to reference specimens (Ref. GFRP) was calculated from the comparison plot. Furthermore, a shift of the Tan Delta at higher temperatures was observed, which corresponds to an increase of the glass transition temperature about 3 °C. The interaction of the integrated CNTs within the epoxy matrix tends to increase some degrees of Celsius the T_g of the epoxy resin system, possibly due to a reduction of epoxy chains mobility around the them, as reported in the literature [55]. Tan Delta describes the damping of the measure of elasticity of the composite system, *i.e.*, the quantification of the internal energy storage, which can no longer be recovered. In general, higher Tan Delta ratio values are correlated with a behaviour of a fluid with high viscosity Newtonian character, whereas lower values denote a more viscoelastic behaviour under applied stresses. Therefore, it could be assumed that the formation of a continuous dense SWCNT network is associated with increased stiffness of the TEG-enabled laminate specimens. Accordingly, the relocation of the Tan Delta values could rely on this possible effect [56,57].

Overall, the knockdown effect of the mechanical properties which was declared for both quasi-static and dynamic testing was attributed to the altered geometrical parameters of the TEG-enabled GFRP laminate. In addition, the incorporation of the SWCNT based TE coatings for the fabrication of the p- and n-type GF functional laminae could be further optimized via more sophisticated manufacturing techniques.

4.1.4 Conclusions

The scope of this work was the demonstration of a 16-ply TEG-enabled GFRP composite laminate with a proper in-series interconnected assembly of TE efficient p- and n-type SWCNT coated GF fabrics. Both experimental and numerical analysis were employed for the determination of the maximum power of 2.2 μW at a temperature gradient of 100 K. If higher power levels are required, potential approaches for connecting more laminate TEGs electrically in series and/or in parallel are easily achievable.

Eventually, the TEG-enabled GFRP was examined from the mechanical perspective both dynamically and statically coupled with TE performance monitoring. As a consequence, the sensitivity for potential on-line SHM was evaluated by exploiting the inherent electrical energy generation from the composite structure, when exposed to a standard temperature gradient during mechanical testing.

Since these functional GF laminae possess the prospect to be low cost, light and easily processable, they consist a promising realistic application in various sectors for efficient energy harvesting. In contrast to conventional structural composites, GFRP TEG-laminates may enable large-scale thermal energy harvesting, because of the potential large areas where temperature differences exist naturally or artificially.

The generation of electrical power from energy harvesting sources, such as thermal energy directly from advanced composites constitutes a novelty in multifunctional materials rendering them attractive for zero energy consumption constructions. The extensive demand of powering low-energy consuming electronics from energy harvesting solutions leads to the constant refinement of the requirements for such applications. These energy harvesting systems need to be able to acquire low-grade energy in order to increase the energy conversion characteristics and efficiency oriented to provide fully energy autonomous solutions in a wide application range. This fact leads to a constantly evolving development cycle in the relative markets, as companies constantly provide new solutions with diverse characteristics to cover the entire energy harvesting application spectrum.

4.1.5 References

1. Petsagkourakis, I.; Tybrandt, K.; Crispin, X.; Ohkubo, I.; Mori, T. Thermoelectric materials and applications for energy harvesting power generation. *Sci. Technol. Adv. Mater.* **2018**, *19*, 836–862, doi:10.1080/14686996.2018.1530938.
2. Matiko, J.W.; Grabham, N.J.; Beeby, S.P.; Tudor, M.J. Review of the application of energy harvesting in buildings. *Meas. Sci. Technol.* **2014**, *25*, doi:10.1088/0957-0233/25/1/012002.
3. Rowe, D.M. Thermoelectrics, an environmentally-friendly source of electrical power. *Renew. Energy* **1999**, *16*, 1251–1256, doi:10.1016/s0960-1481(98)00512-6.
4. von Lukowicz, M.; Abbe, E.; Schmiel, T.; Tajmar, M. Thermoelectric Generators on Satellites—An Approach for Waste Heat Recovery in Space. *Energies* **2016**, *9*, 541, doi:10.3390/en9070541.
5. Zappa, W.; Junginger, M.; Broek, M. Van Den; Cover, C.L. Is a 100 % renewable European power system feasible by 2050 ? *Appl. Energy* **2019**, *233–234*, 1027–1050, doi:10.1016/j.apenergy.2018.08.109.
6. He, J.; Kanatzidis, M.G.; Dravid, V.P. High performance bulk thermoelectrics via a panoscopic approach. *Mater. Today* **2013**, *16*, 166–176, doi:10.1016/j.mattod.2013.05.004.
7. Snyder, G.J.; Toberer, E.S. 1. Complex thermoelectric materials. *Nat Mater* **2008**, *7*, 105–114, doi:10.1038/nmat2090.
8. Han, C.; Tan, G.; Varghese, T.; Kanatzidis, M.G.; Zhang, Y. High Performance PbTe Thermoelectric Films by Screen Printing. **2018**, doi:10.1021/acsenergylett.8b00041.
9. Vineis, C.J.; Shakouri, A.; Majumdar, A.; Kanatzidis, M.G. Nanostructured thermoelectrics: Big efficiency gains from small features. *Adv. Mater.* **2010**, *22*, 3970–3980, doi:10.1002/adma.201000839.
10. Russ, B.; Glaudell, A.; Urban, J.J.; Chabinyc, M.L.; Segalman, R.A. Organic thermoelectric materials for energy harvesting and temperature control. *Nat. Rev. Mater.* **2016**, *1*, doi:10.1038/natrevmats.2016.50.
11. Macleod, B.A.; Stanton, N.J.; Gould, I.E.; Wesenberg, D.; Ihly, R.; Owczarczyk, Z.R.; Hurst, K.E.; Fewox, C.S.; Folmar, C.N.; Hughes, H.; et al. Environmental Science nanotube thin films. **2017**, 2168–2179, doi:10.1039/c7ee01130j.
12. Tambasov, I.A.; Voronin, A.S.; Evsevskaya, N.P.; Volochaev, M.N.; Fadeev, Y. V; Simunin, M.M.; Aleksandrovsky, A.S.; Smolyarova, T.E.; Abelian, S.R.; Tambasova, E. V; et al. Physica E : Low-dimensional Systems and Nanostructures Thermoelectric properties of low-cost transparent single wall carbon nanotube thin films obtained by vacuum filtration. *Phys. E Low-dimensional Syst. Nanostructures* **2019**, *114*, 113619, doi:10.1016/j.physe.2019.113619.
13. Liebscher, M.; Gärtner, T.; Tzounis, L.; Mičušík, M.; Pötschke, P.; Stamm, M.; Heinrich, G.; Voit, B. Influence of the MWCNT surface functionalization on the thermoelectric properties of melt-mixed polycarbonate composites. *Compos. Sci. Technol.* **2014**, *101*, 133–138, doi:10.1016/j.compscitech.2014.07.009.

14. Nonoguchi, Y.; Ohashi, K.; Kanazawa, R.; Ashiba, K.; Hata, K.; Nakagawa, T.; Adachi, C.; Tanase, T.; Kawai, T. Systematic conversion of single walled carbon nanotubes into n-type thermoelectric materials by molecular dopants. *Sci. Rep.* **2013**, *3*, 1–7, doi:10.1038/srep03344.

15. Luo, J.; Cerretti, G.; Krause, B.; Zhang, L.; Otto, T.; Jenschke, W.; Ullrich, M.; Tremel, W.; Voit, B.; Pötschke, P. Polypropylene-based melt mixed composites with singlewalled carbon nanotubes for thermoelectric applications: Switching from p-type to n-type by the addition of polyethylene glycol. *Polym.* **2017**, *108*, 513–520, doi:10.1016/j.polymer.2016.12.019.

16. Tzounis, L.; Hegde, M.; Liebscher, M.; Dingemans, T.; Pötschke, P.; Paipetis, A.S.; Zafeiropoulos, N.E.; Stamm, M. All-aromatic SWCNT-Polyetherimide nanocomposites for thermal energy harvesting applications. *Compos. Sci. Technol.* **2018**, *156*, 158–165, doi:10.1016/J.COMPSCITECH.2017.12.030.

17. Kim, J.; Bae, E.J.; Kang, Y.H.; Lee, C.; Cho, S.Y. Elastic thermoelectric sponge for pressure-induced enhancement of power generation. *Nano Energy* **2020**, *74*, doi:10.1016/j.nanoen.2020.104824.

18. Cheng, X.; Wang, X.; Chen, G. A convenient and highly tunable way to n-type carbon nanotube thermoelectric composite film using common alkylammonium cationic surfactant. *J. Mater. Chem. A* **2018**, *6*, 19030–19037, doi:10.1039/c8ta07746k.

19. Kim, J.; Mo, J.; Kang, Y.H.; Cho, S.Y.; Jang, K. Thermoelectric fibers from well-dispersed carbon nanotube/poly(vinyliedene fluoride) pastes for fiber-based thermoelectric generators. *Nanoscale* **2018**, *10*, 19766–19773, doi:10.1039/c8nr06415f.

20. See, K.C.; Feser, J.P.; Chen, C.E.; Majumdar, A.; Urban, J.J.; Segalman, R.A. Hybrids for Thermoelectrics. **2010**, 4664–4667, doi:10.1021/nl102880k.

21. Mengistie, D.A.; Chen, C.H.; Boopathi, K.M.; Pranoto, F.W.; Li, L.J.; Chu, C.W. Enhanced thermoelectric performance of PEDOT:PSS flexible bulky papers by treatment with secondary dopants. *ACS Appl. Mater. Interfaces* **2015**, *7*, 94–100, doi:10.1021/am507032e.

22. Wei, Q.; Mukaida, M.; Kirihara, K.; Naitoh, Y.; Ishida, T. Polymer thermoelectric modules screen-printed on paper. *RSC Adv.* **2014**, *4*, 28802–28806, doi:10.1039/c4ra04946b.

23. Ni, D.; Song, H.; Chen, Y.; Cai, K. Free-standing highly conducting PEDOT fi lms for flexible thermoelectric generator. **2019**, *170*, 53–61, doi:10.1016/j.energy.2018.12.124.

24. Hewitt, C.A.; Kaiser, A.B.; Roth, S.; Craps, M.; Czerw, R.; Carroll, D.L. Multilayered Carbon Nanotube/Polymer Composite Based Thermoelectric Fabrics. **2012**, 10–13.

25. Mukaida, M.; Wei, Q.; Ishida, T. Polymer thermoelectric devices prepared by thermal lamination. **2017**, *225*, 64–69.

26. Choi, J.; Jung, Y.; Yang, S.J.; Oh, J.Y.; Oh, J.; Jo, K.; Son, J.G.; Moon, S.E.; Park, C.R.; Kim, H. Flexible and Robust Thermoelectric Generators Based on All-Carbon Nanotube Yarn without Metal Electrodes. *ACS Nano* **2017**, *11*, 7608–7614, doi:10.1021/acsnano.7b01771.

27. Liang, D.; Yang, H.; Finefrock, S.W.; Wu, Y. Flexible Nanocrystal-Coated Glass Fibers for High-Performance Thermoelectric Energy Harvesting. **2012**, 8–13.

28. Tzounis, L.; Gravalidis, C.; Vassiliadou, S.; Logothetidis, S. Fiber yarns/CNT hierarchical structures as thermoelectric generators. *Mater. Today Proc.* **2017**, *4*, 7070–7075, doi:10.1016/j.matpr.2017.07.040.

29. Ryan, J.D.; Mengistie, D.A.; Gabrielsson, R.; Lund, A.; Mu, C. Machine-Washable PEDOT : PSS Dyed Silk Yarns for Electronic Textiles. **2017**, 0–5, doi:10.1021/acsami.7b00530.

30. Karalis, G.; Mytafides, C.; Polymerou, A.; Tsirka, K.; Tzounis, L.; Gergidis, L.; Paipetis, A.S. Hierarchical Reinforcing Fibers for Energy Harvesting Applications - A Strength Study. *Key Engineering Materials* **2020**;827 :252–7, doi:10.4028/www.scientific.net/KEM.827.252..

31. Karalis, G.; Tsirka, K.; Tzounis, L.; Mytafides, C.; Koutsotolis, L.; Paipetis, A.S.. Epoxy/Glass Fiber Nanostructured p- and n-Type Thermoelectric Enabled Model Composite Interphases. *Appl. Sci.* **2020**, 10, 5352, doi:10.3390/app10155352.

32. Peng Li, Yang Guo, Jiuke Mu, Hongzhi Wang, Qinghong Zhang, Y.L.S.-W.C.N.P.T.T. with G.I.S. prepared by U.I. *RSC Advances*. **2016**, doi:10.1039/C6RA16532J.

33. Tzounis, L.; Liebscher, M.; Tzounis, A.; Petinakis, E.; Paipetis, A.S.; Mäder, E.; Stamm, M. CNT-grafted glass fibers as a smart tool for epoxy cure monitoring, UV-sensing and thermal energy harvesting in model composites. *RSC Adv.* **2016**, *6*, 55514–55525, doi:10.1039/C6RA09800B.

34. Karalis, G.; Tzounis, L.; Lambrou, E.; Gergidis, L.N.; Paipetis, A.S. A carbon fiber thermoelectric generator integrated as a lamina within an 8-ply laminate epoxy composite: Efficient thermal energy harvesting by advanced structural materials. *Appl. Energy* **2019**, *253*, doi:10.1016/j.apenergy.2019.113512.

35. Carlson, T.; Ordéus, D.; Wysocki, M.; Asp, L.E. Structural capacitor materials made from carbon fibre epoxy composites. **2010**, *70*, 1135–1140, doi:10.1016/j.compscitech.2010.02.028.

36. Senokos, E.; Ou, Y.; Torres, J.J.; Sket, F.; González, C.; Marcilla, R.; Vilatela, J.J. Energy storage in structural composites by introducing CNT fiber / polymer electrolyte interleaves. **2018**, 1–10, doi:10.1038/s41598-018-21829-5.

37. Zhang, D.; Ryu, K.; Liu, X.; Polikarpov, E.; Ly, J.; Tompson, M.E.; Zhou, C. Transparent, conductive, and flexible carbon nanotube films and their application in organic light-emitting diodes. *Nano Lett.* **2006**, *6*, 1880–1886, doi:10.1021/nl0608543.

38. Tsirka, K.; Karalis, G.; Paipetis, A.S. Raman Strain Sensing and Interfacial Stress Transfer of Hierarchical CNT-Coated Carbon Fibers. *J. Mater. Eng. Perform.* **2018**, *27*, doi:10.1007/s11665-018-3532-2.

39. Farah, A.A.; Rutledge, S.A.; Schaarschmidt, A.; Lai, R.; Freedman, J.P.; Helmy, A.S. Conductivity enhancement of poly(3,4-ethylenedioxythiophene)- poly(styrenesulfonate) films post-spincasting. *J. Appl. Phys.* **2012**, *112*, doi:10.1063/1.4768265.

40. Blackburn, J.L.; Ferguson, A.J.; Cho, C.; Grunlan, J.C. Carbon-Nanotube-Based Thermoelectric Materials and Devices. **2018**, *1704386*, 1–35, doi:10.1002/adma.201704386.

41. Moriarty, G.P.; Wheeler, J.N.; Yu, C.; Grunlan, J.C. Increasing the thermoelectric power factor of polymer composites using a semiconducting stabilizer for carbon nanotubes. *Carbon N. Y.* **2012**, *50*, 885–895, doi:10.1016/j.carbon.2011.09.050.

42. Yu, C.; Choi, K.; Yin, L.; Grunlan, J.C. Correction to Light-Weight Flexible Carbon Nanotube Based Organic Composites with Large Thermoelectric Power Factors. *ACS Nano* **2013**, *7*, 9506–9506, doi:10.1021/nn404924h.

43. Cho, C.; Wallace, K.L.; Tzeng, P.; Hsu, J.H.; Yu, C.; Grunlan, J.C. Outstanding Low Temperature Thermoelectric Power Factor from Completely Organic Thin Films Enabled by Multidimensional Conjugated Nanomaterials. *Adv. Energy Mater.* **2016**, *6*, 1–8, doi:10.1002/aenm.201502168.

44. Kim, S.L.; Choi, K.; Tazebay, A.; Yu, C. Flexible power fabrics made of carbon nanotubes for harvesting thermoelectricity. *ACS Nano* **2014**, *8*, 2377–2386, doi:10.1021/nn405893t.

45. Mytafides, C.K.; Tzounis, L.; Karalis, G.; Formanek, P.; Paipetis, A.S. High-Power All-Carbon Fully Printed and Wearable SWCNT-Based Organic Thermoelectric Generator. *ACS Appl. Mater. Interfaces* **2021**, *13*, 11151–11165, doi:10.1021/acsami.1c00414.

46. Chung, D.D.L. Self-monitoring structural materials. *Mater. Sci. Eng. R Reports* **1998**, *22*, 57–78, doi:10.1016/S0927-796X(97)00021-1.

47. Bekas, D.G.; Paipetis, A.S. Damage monitoring in nanoenhanced composites using impedance spectroscopy. *Compos. Sci. Technol.* **2016**, *134*, 96–105, doi:10.1016/j.compscitech.2016.08.013.

48. Foteinidis, G.; Tsirka, K.; Tzounis, L.; Baltzis, D.; Paipetis, A.S. The role of synergies of MWCNTs and Carbon Black in the enhancement of the electrical and mechanical response of modified epoxy resins. *Appl. Sci.* **2019**, *9*, doi:10.3390/app9183757.

49. Grammatikos, S.A.; Paipetis, A.S. On the electrical properties of multi scale reinforced composites for damage accumulation monitoring. *Compos. Part B Eng.* **2012**, *43*, 2687–2696,

doi:10.1016/j.compositesb.2012.01.077.

50. Todoroki, A.; Tanaka, M.; Shimamura, Y. Electrical resistance change method for monitoring delaminations of CFRP laminates: Effect of spacing between electrodes. *Compos. Sci. Technol.* **2005**, *65*, 37–46, doi:10.1016/j.compscitech.2004.05.018.

51. Kostopoulos, V.; Vavouliotis, A.; Karapappas, P.; Tsotra, P.; Paipetis, A. Damage monitoring of carbon fiber reinforced laminates using resistance measurements. Improving sensitivity using carbon nanotube doped epoxy matrix system. *J. Intell. Mater. Syst. Struct.* **2009**, *20*, 1025–1034, doi:10.1177/1045389X08099993.

52. Carraro, P.A.; Zappalorto, M.; Quaresimin, M. Health monitoring of cross-ply laminates: Modelling the correlation between damage evolution and electrical resistance change. *Compos. Part A Appl. Sci. Manuf.* **2016**, *82*, 151–158, doi:10.1016/j.compositesa.2015.12.001.

53. Thostenson, E.T.; Chou, T.W. Carbon nanotube networks: Sensing of distributed strain and damage for life prediction and self healing. *Adv. Mater.* **2006**, *18*, 2837–2841, doi:10.1002/adma.200600977.

54. Materials, C.; By, T.; Mechanical, D.; Analyzers, M. Standard Test Method for Glass Transition Temperature (DMA Tg) of Polymer Matrix Composites by Dynamic Mechanical Analysis (DMA) 1. **2015**, *i*, 1–13, doi:10.1520/D7028-07E01R15.2.

55. Loos, M.R.; Coelho, L.A.F.; Pezzin, S.H.; Amico, S.C. Effect of carbon nanotubes addition on the mechanical and thermal properties of epoxy matrices. *Mater. Res.* **2008**, *11*, 347–352, doi:10.1590/S1516-14392008000300019.

56. Gkikas, G.; Douka, D.D.; Barkoula, N.M.; Paipetis, A.S. Nano-enhanced composite materials under thermal shock and environmental degradation: A durability study. *Compos. Part B Eng.* **2015**, *70*, 206–214, doi:10.1016/j.compositesb.2014.11.008.

57. Baltzis, D.; Bekas, D.G.; Tzachristas, G.; Parlamas, A.; Karabela, M.; Zafeiropoulos, N.E.; Paipetis, A.S. Multi-scaled carbon reinforcements in ternary epoxy composite materials : Dispersion and electrical impedance study. *Compos. Sci. Technol.* **2017**, *153*, 7–17, doi:10.1016/j.compscitech.2017.09.035.

4.2 Supporting information

Following the steps of the preparation process of the initial SWCNT dispersion, **Figure S3** depicts the fitted Raman spectra of the SWCNT:SDBS (1:2.5) “bucky paper” film, the PEDOT:PSS solution that was added to the initial SWCNT dispersion (in film form), the resulting p-type TE ink in film form and the latter ink coated on a GF fabric.

In relation to the Raman spectrum of the PEDOT:PSS solution as a film, the fitting was performed in the 80–1600 cm^{-1} region where it presented all of its Raman activity. The intensity of its most pronounced vibrational mode is not equal to 1 as a linear ascending baseline was subtracted after the normalization process to facilitate the fitting process. The subtraction of this baseline caused a redshift of the position of the vibrational modes of PEDOT:PSS film by up to 10 cm^{-1} from their initial position. However, this did not affect the interpretation of the spectra and the conclusions that were drawn, as the peaks of interest did not overlap with the SWCNT vibrational modes.

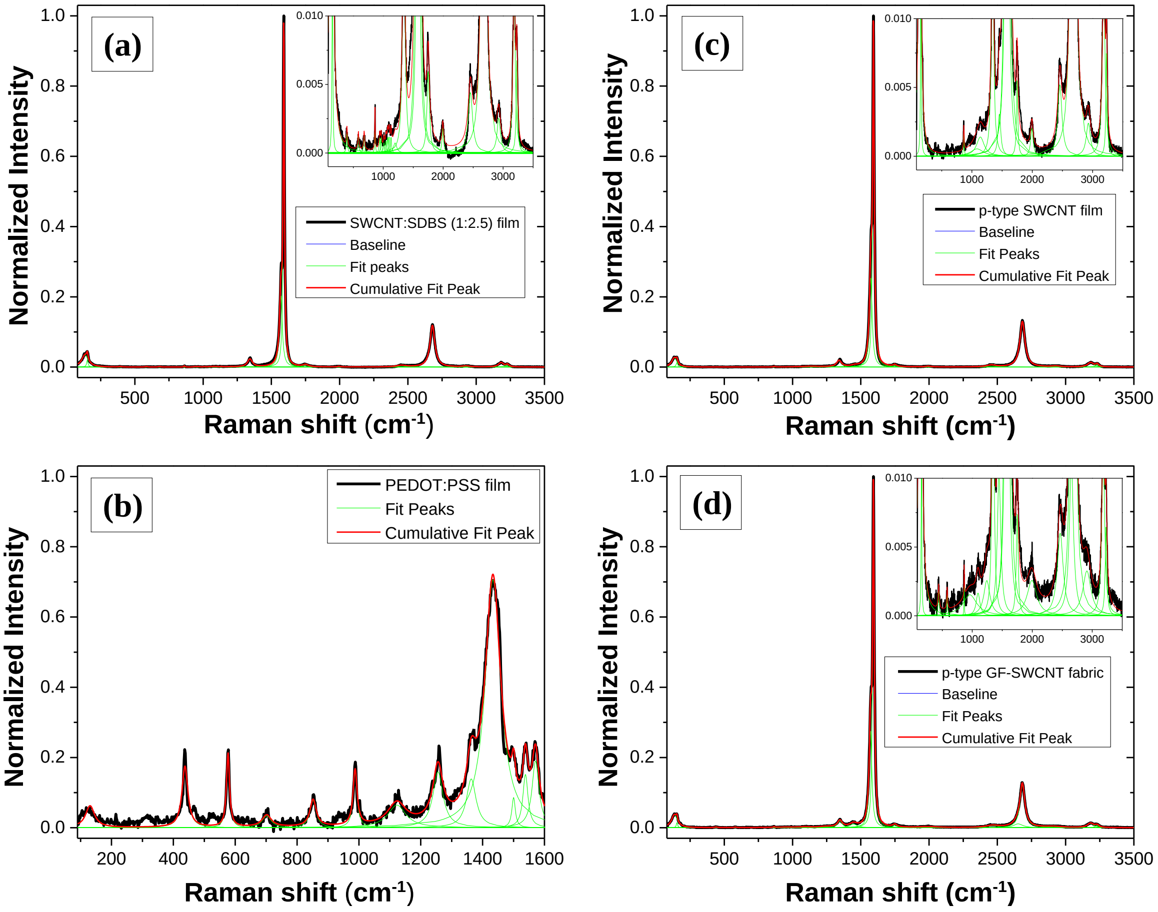

Figure S3. Fitted Raman spectra of **(a)** the initial SWCNT “bucky paper” film, **(b)** the PEDOT:PSS solution as a film, **(c)** the p-type TE ink as a film and **(d)** the p-type ink coated on GF fabric.

Figure S4 depicts the fitted Raman spectra of the n-type SWCNT “bucky paper” film and the same TE ink coated on a GF fabric.

The fitting was performed with Lorentzian peaks and a linear baseline. All the spectra were normalized to the peak with the highest intensity prior to fitting.

In each plot the Raman spectrum is represented by the black curve, the fitted peaks by green curves, the baseline by a blue curve and the cumulative fitted spectrum by a red curve. Inset plots were also included in all the SWCNT graphs to allow for the presentation of the fitting process of the very low intensity peaks.

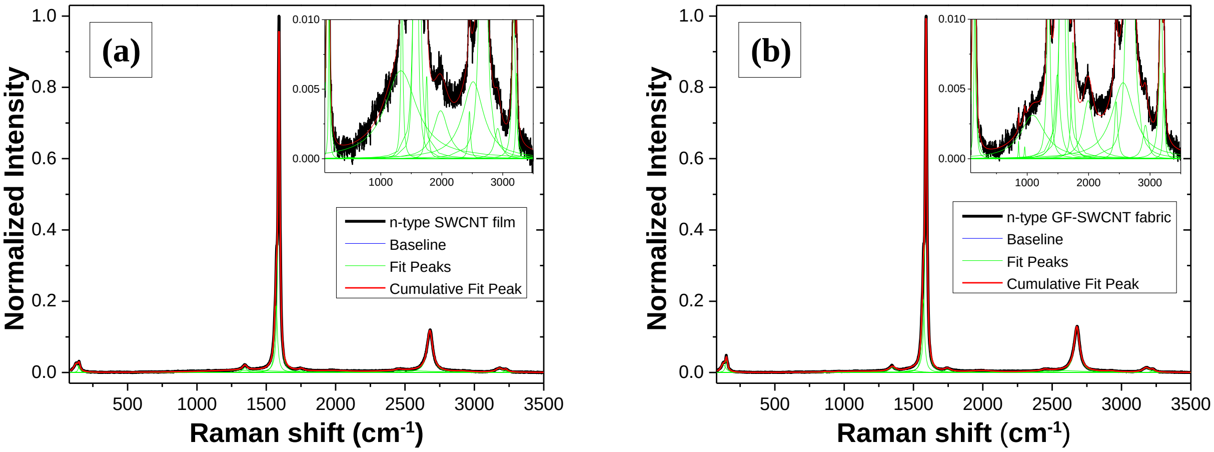

Figure S4. Fitted Raman spectrum of **(a)** the n-type SWCNT “bucky paper” film and **(b)** the n-type ink coated on GF fabric.

Figure S5 illustrates the production vacuum-assisted filtration process for the p- and n-type SWCNT “bucky paper” films, which were typically ~80 μm in thickness, mean value extracted from 10 measurements for each sample via a digital caliper. Then, the resulting films were employed for the 4-probe sheet resistance measurements in order to determine the respective values of the electrical conductivities and the Seebeck coefficient measurements in order to calculate the TE power factor.

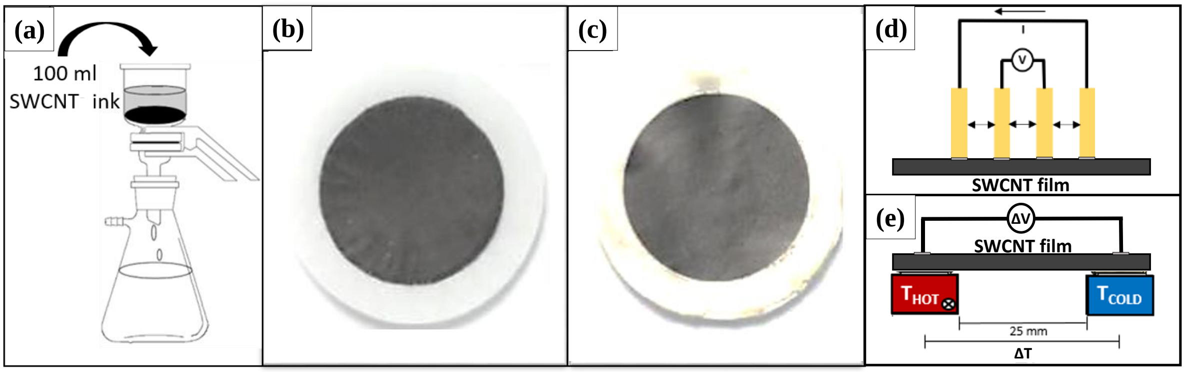

Figure S5. (a) Schematic illustration of the vacuum-assisted filtration apparatus utilized for the SWCNT “bucky paper” films production and photos of the respective **(b)** p-type SWCNT film, **(c)** n-type SWCNT film for **(d)** the 4-probe sheet resistance measurements and **(e)** the Seebeck coefficient measurements.

Figure S6 shows the set-up used to generate the in-plane temperature difference across the structural TEG consisting of a "hot" and "cold" aluminum block thermal gradient stage. All the main components used in this homemade set-up could be seen. Namely, the cold block sustained at room temperature, while the hot block temperature was controlled via a hot plate at specific temperature to create the ΔT. The temperature of the hot block was continuously measured with a K-type thermocouple to determine the exact temperature difference, ΔT. Additionally, the temperature difference at the TEG device had been checked frequently using an IR-thermometer.

Additionally, in **Figure S6** can be seen the custom-built fully automated based on a LabVIEW-PC interface electronic system with a range of applied external load resistances from 1 Ohm to 10000 Ohm with discretion capability down to 1 Ohm for the TEG device characterization.

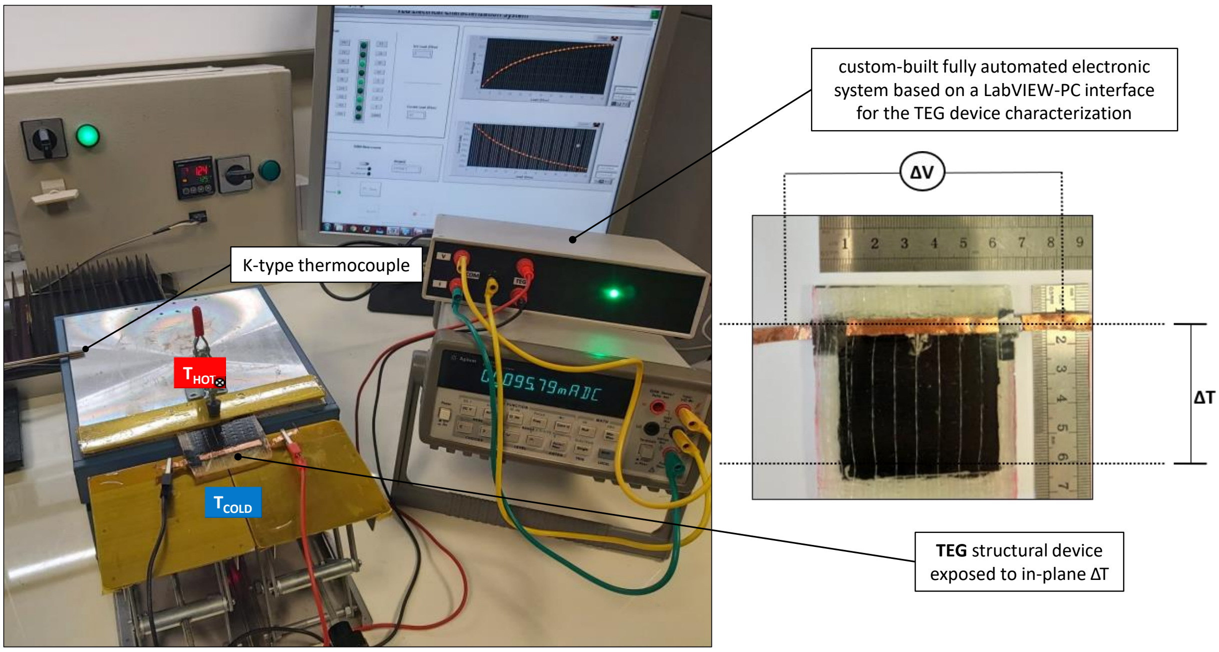

Figure S6. Set-up used to generate the in-plane temperature difference across the structural TEG consisting of a "hot" and "cold" Al block thermal gradient stage and custom-built electronic system for the experimental power output measurements to examine the structural TEG device power output characteristics at different temperature gradients (60, 80 and 100 K) as a function of different in-series connected external load resistances (R_{LOAD}).

4.3 Appendix / Practical application of thermal energy harvesting by FRP composites

4.3.1 TEG-enabled FRP demonstrator for thermal energy harvesting and power utilization

For the manufacturing of the 8-ply multi TEG-enabled GFRP composite laminate, multiple p-n TE junctions were printed onto GF fabrics following a TEG pattern. The 4 functional TEG patterned GF reinforcing fabrics where properly combined with 4 plain insulating uncoated GF fabrics and were integrated within GFRP structure, as illustrated in **Figure 51**. In this way, more electrically in series and thermally in parallel interconnected thermoelements (TE junctions) contributed to the overall TE power, in order to achieve a sufficient power for practical energy harvesting applications. The final design and fabrication were carried out taking into account the energy requirements of the available electronic circuit (ALD-EH4295 / *Micropower Step up Low Voltage Booster Module. 2012, No. 408, 1-5*) for the conversion of the generated power into usable energy.

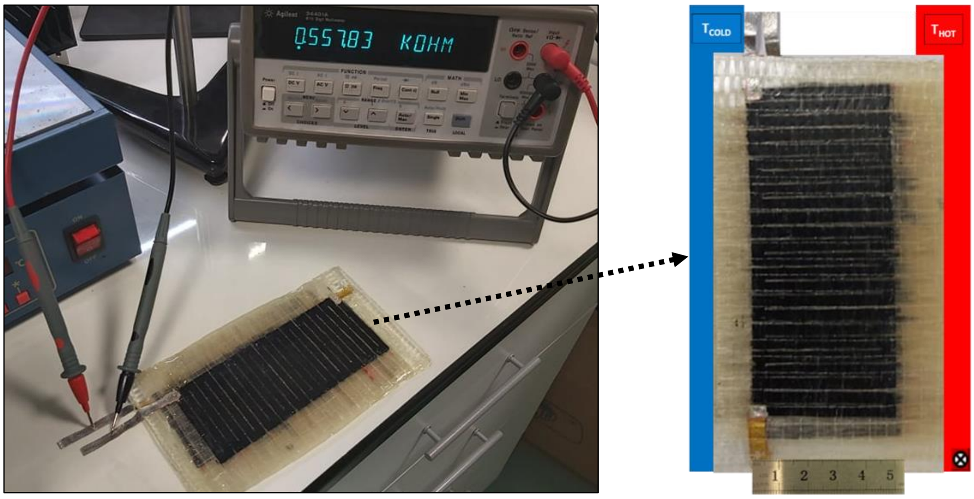

Figure 51. Demonstration of the manufactured multi TEG-enabled GFRP composite laminate.

In more detail, for the fabrication of individual 12 p-n TE junctions / printed TEG patterned onto GF fabrics the depicted in **Figure 52** procedure was followed. The deposition of the p- and n-type SWCNT-based TE inks was performed using a pipette-assisted method utilizing a self-adhesive vinyl foil mask with a predetermined TEG pattern geometry (designed by CorelDRAW). Simultaneously, the drying process was occurred via a hot plate for the aqueous solvent removal in order to create the TE films onto the GF substrates. Finally, the vinyl mask was removed allowing the uniform printing of the TEG device. Ag paste was applied in specific points for the creation of the device's Ohmic contacts.

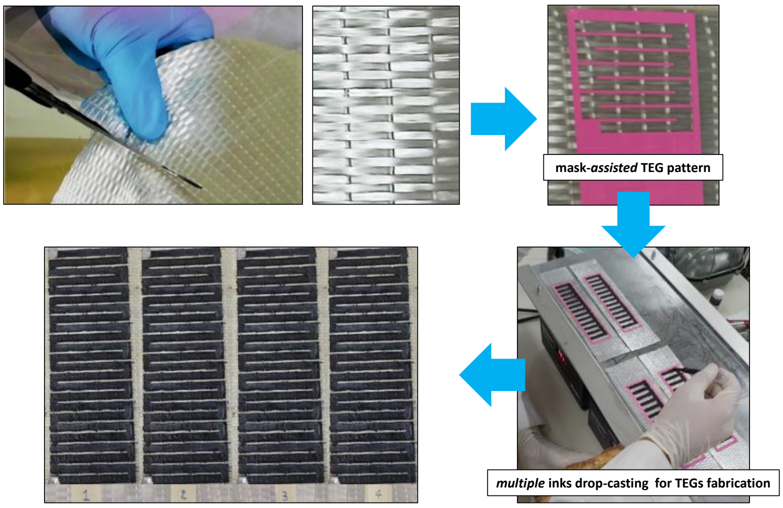

Figure 52. Preparation and printing stages resulting in TEG devices onto GF fabrics.

Figure 53 depicts the TE measurements for resulted printed TEGs onto the GF fibrous substrates before the epoxy resin impregnation step. For TE measurements, the temperature difference was achieved using a proportionally adapted measuring stage consisting of a controlled heating Al plate and an Al plate at RT. The temperature of the hot and cold plate for the creation and time-dependent sustainment of the applied ΔT was continuously controlled with K-type thermocouples and an IR thermometer (OMEGA OS-VIR50 Dual Laser Video IR Video thermometer). The DC electrical and TE values were acquired with the Agilent 34401A6½ digital bench multimeter using the standard 2-probe method.

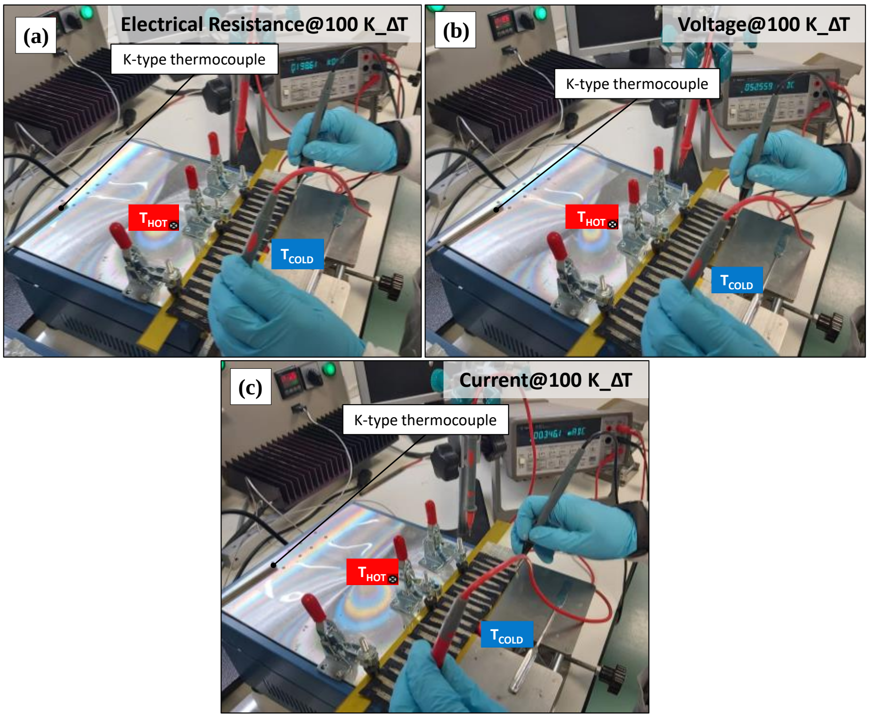

Figure 53. TE characteristics **(a)** R_{TEG}: ~200 Ohm, **(b)** V_{TEG}: ~50 mV and **(c)** I_{sc}: ~350 μA upon exposure to a ΔT of 100 K) for the printed TEGs.

Figure 54 presents the manufacturing of the multi TEG-enabled GFRP composite laminate for the demonstration of practical thermal energy harvesting by advanced structural materials. Therefore, for the multiple TEGs lamination, 4 individual printed TEGs onto GFs and 4 insulating GFs were purposely impregnated with the epoxy resin (matrix) system via hand lay-up in cross-ply configuration, as shown in **Figure 54**. Then, the multi TEG-enabled GFRP lamination with the appropriate metallic spacer was placed in a hydraulic press and pressured at 3 MPa for 24 h (RT) and for 4 h (100 ^{o}C) for the polymerization process, according to the manufacturer's recommended instructions.

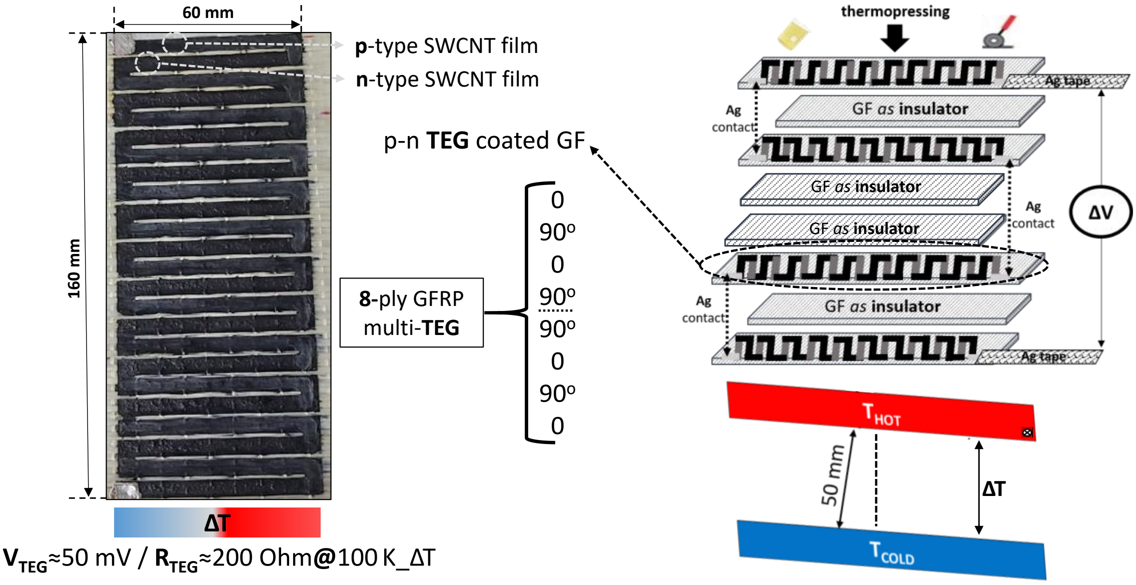

Figure 54. Schematic representation of the multi TEG-enabled GFRP composite laminate manufacturing process.

Figure 55a-b shows the optical and the corresponding thermal image of the multi TEG-enabled GFRP composite laminate during continuous operation in applied thermal field (ΔT of 75 K) Indicatively, it was observed that upon continuous operation the produced TE power remained constant (**Figure 55c**), as long as the temperature difference does not present any fluctuations. For the 8-ply multifunctional structure with the total 48 p-n TE junctions, the respective TEG values exhibited R_{TEG} = 732.4 Ohm, V_{TEG} = 183.1 mV and I_{sc} = 329.9 μA corresponding to a P_{max} of 11.4 μW at ΔT of 75 K.

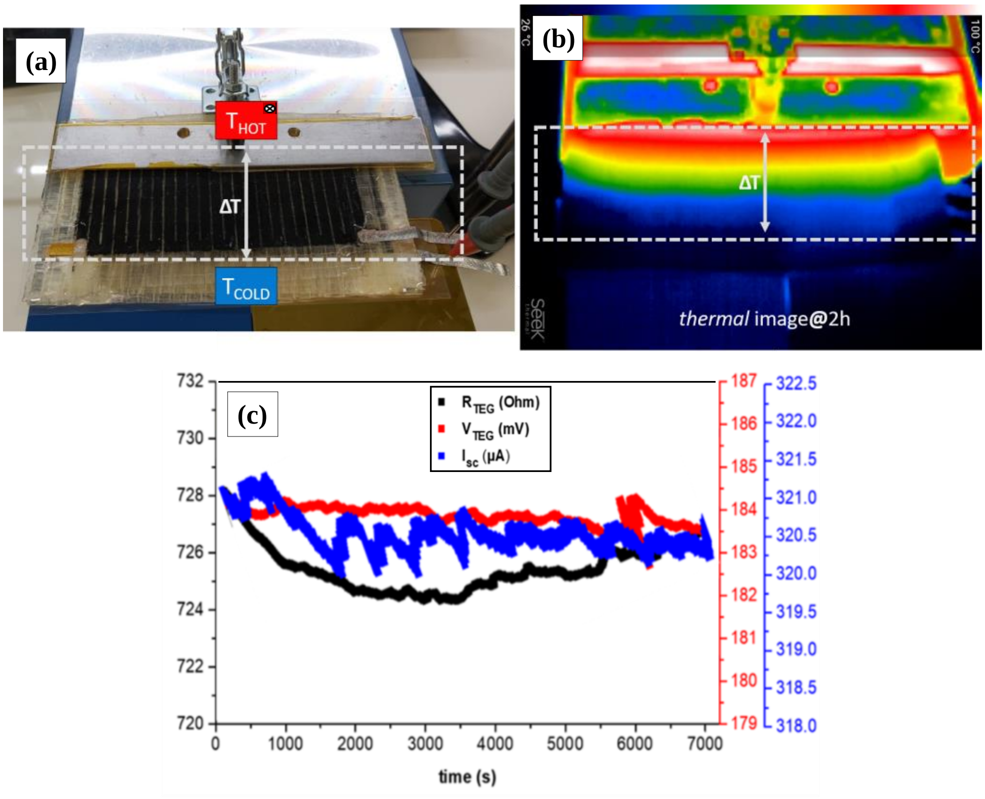

Figure 55. (a) Visual, **(b)** thermal and **(c)** electrical - TE monitoring of the multi TEG-enabled GFRP composite laminate performance upon exposure to a Δ*T* of 75 K for 2 h.

The power output characteristics of the 8-ply multi TEG-enabled GFRP composite laminate were tested at different temperature differences of 55, 75 and 100 K, as a function of different applied external load resistors connected in series (R_{LOAD}). The maximum power output of 13.3 μW at Δ*T* of 100 K, was observed when the load resistance matches with the internal resistance of ~750 Ohm. **Figure 56a** a illustrates the experimental voltage-current-power curves and **Figure 56b** shows the voltage-power curves as a function of the applied external load resistors.

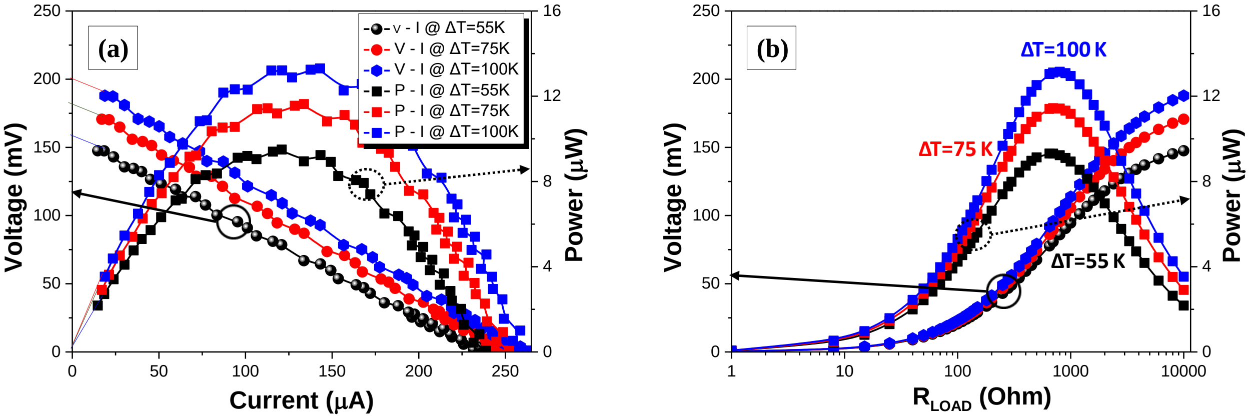

Figure 56. Experimental curves **(a)** TE voltage-current-power at 3 different Δ*T* and **(b)** TE voltage-power at different applied R_{LOAD}.

Figure 57a demonstrates the TE measurements of the 8-ply multi TEG-enabled GFRP composite laminate connected with the electronic circuit (ALD-EH4295) for the management (storing) and exploitation (powering) of the generated TE power. It is observed that within a time of 28 min under exposure to a Δ*T* of 75 K the green LED of the electronic circuit is able to light-up, as the harvested thermal energy exceeded the critical limit of 3.6-3.8 V (**Figure 57b**).

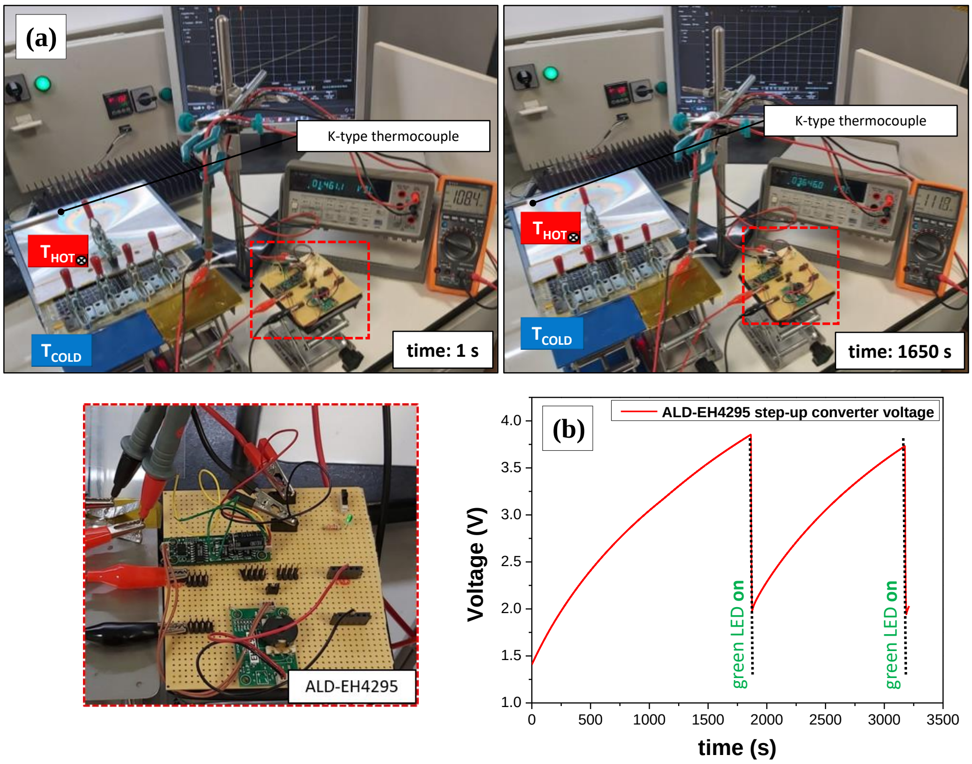

Figure 57. (a) Demonstration and **(b)** evaluation of practical thermal energy harvesting and power utilization by multifunctional FRP composites interfaced with a DC step-up boost converter electronic circuit.

4.3.2 TEG-enabled GFRP demonstrator as potential IR and UV radiation sensor

In order to evaluate the response of the 8-ply multi TEG-enabled GFRP composite laminate upon exposure to infrared and ultraviolet radiation, the relevant measurements were performed using the appropriate instrumentation. The satisfactory sensitivity and response of the multifunctional FRP structure to the aforementioned environmental stimuli could enable it to be used as a sensor to detect changes in specific environmental conditions. The measured sensitivity for each form of radiation applied to the active surface of multifunctional FRP structure was analyzed and characterized accordingly.

Figure 58a shows the set-up for evaluating the functionality of IR radiation sensor for the 8-ply TEG-enabled GFRP structure. The FLIR A6750 MWIR thermal camera was used, with a resolution of 640×512 pixels and a frame rate of 60 Hz. In combination, 2×1000 W IR lamps were used as heat sources, activated either manually or by the Tektronix AFG3052C signal generator for the pulse thermography method. The ramp pulse lasted for 5 s and the peak-to-peak voltage was 9 V. The distance between the multifunctional FRP laminate and the array of lamps, as well as the distance between the laminate and the camera was 1 m.

In particular, **Figure 58b** presents the response of the 8-ply multifunctional FRP laminate upon the application of both IR pulsed and continuous radiation with the corresponding thermal images (**Figure 58c**) during heating and cooling cycles. For both cases, an immediate TE response was observed during the infrared radiation time period with an almost instantaneous increase of the produced TE voltage, *e.g.*, from. 0.8 mV to 50 mV in 30 s of continuous application, while an expected direct drop of the generated TE voltage was occurred when the IR lamps were switched off.

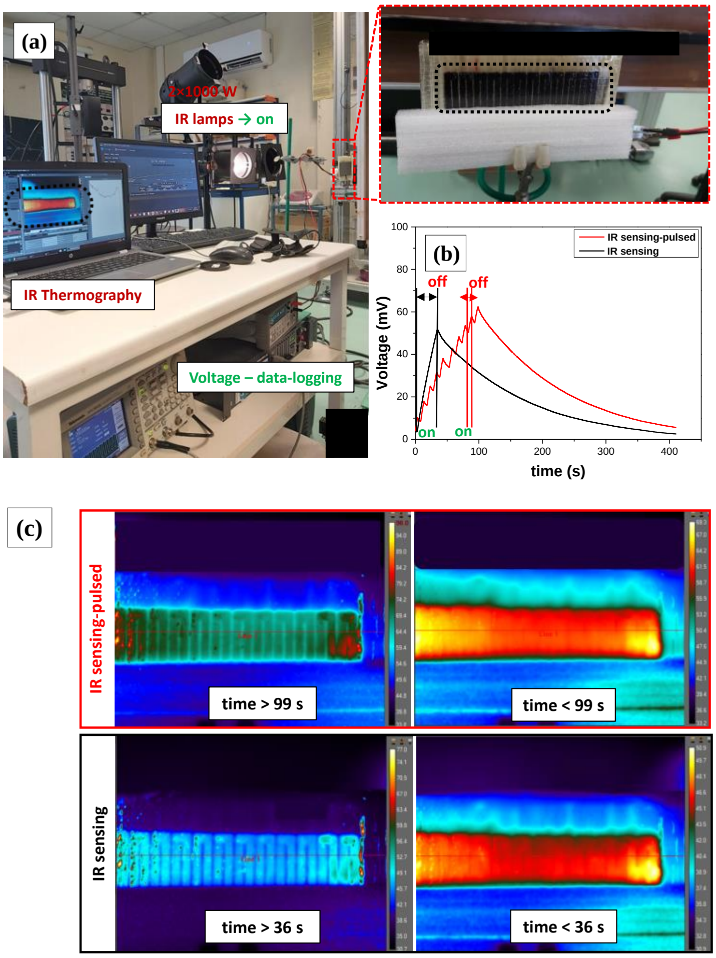

Figure 58. (a) IR radiation sensing set-up for evaluating the multifunctional FRP laminate performance, **(b)** data-logged TE response upon specific application of pulsed and continuous IR radiation, **(c)** thermal imaging captures of the TEG-enabled laminate for both pulsed and continuous IR during heating and cooling.

Figure 59a shows the set-up utilized for the UV sensing evaluation by the 8-ply TEG-enabled laminate. An array of 4×15 W UV-C lamps in a darkroom was employed as UV radiation source for the measurements of the possible UV sensor functionality. The Fluke 179 portable digital multimeter was also used. Additionally, a programmable measuring system (Keithley 2001 sourcemeter) was used for the supply of constant V_{bias} and recording of the corresponding produced light current values during the period of exposure of the structure to ultraviolet radiation.

The ability of an advanced FRP structure to detect UV radiation could be used to monitor the physicochemical state of the polymeric matrix. The degradation of polymer chains and formed crosslinks is related to the time of exposure of the material to UV radiation. Thus, the provision of continuous and high photoconductivity due to the efficient exchange of electron-hole carriers that takes place on the surface of certain materials with semiconductor characteristics could effectively detect either UV radiation or visible light, depending on the energy bandgap of the selected semiconductor.

Upon exposure of the multifunctional FRP structure to UV radiation, the measured response did not show sufficient sensitivity to further study its potential as a radiation sensor. **Figure 59a** depicts the 2 snapshots of TE measurements (~0.8 mV) before and after the application of UV radiation (~2.7 mV). The observed slight relative change of the TE voltage for the specific time period of exposure of the laminate's surface cannot be correlated with sensing capabilities arising from the proposed p-n TEG architecture. Moreover, **Figure 59b** presents the response of the TEG-enabled FRP laminate during the application of a constant V_{bias} of 0.05 V upon the activation and de-activation of the UV lamps and the record of the produced current (I_{UV}) divided by the dark current (I_D) against time. The observed slow response as a UV sensor is due to the creation of minimally excited carriers due to UV radiation and a slight increase in surface temperature.

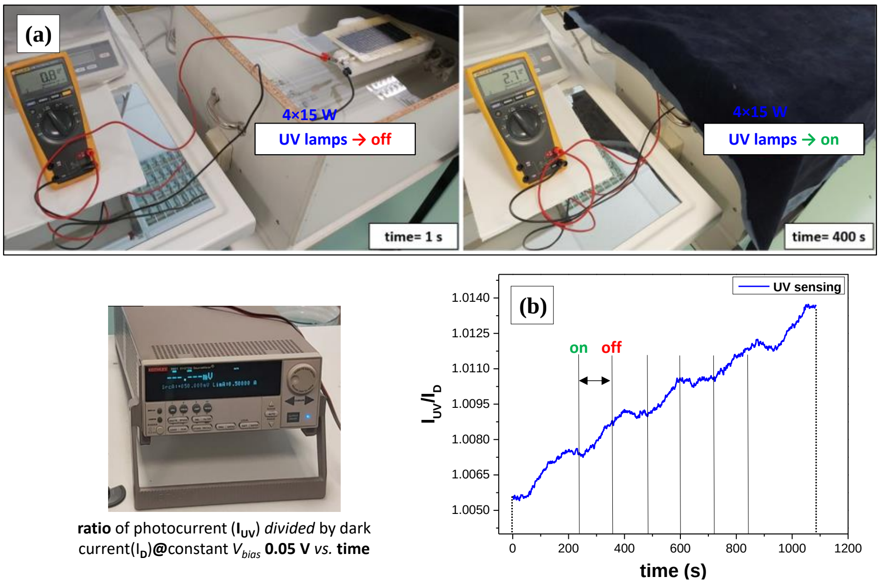

ratio of photocurrent (I_{UV}) *divided* by dark current(I_D)@constant V_{bias} **0.05 V** *vs.* **time**

Figure 59. (a) UV radiation sensing set-up for evaluating the multifunctional FRP laminate performance and **(b)** data-logged TE response upon specific application of UV radiation.

Chapter 5

Through-thickness TEG-enabled Fiber Reinforced Polymer composites

Part of the results included in **Chapter 5** have been published at the *Materials* peer-reviewed scientific journal as part of the study "An approach towards the realization of a through-thickness glass fiber / epoxy thermoelectric generator" and can be found under *https://doi.org/10.3390/ma14092173*. Additionally, part of the results has been submitted at the peer-reviewed scientific Journal of *Composites Science and Technology* under the title "Carbon fiber / epoxy composite laminates as through-thickness thermoelectric generators".

5. Through-thickness TEG-enabled Fiber Reinforced Polymer composites

5.1 An approach towards the realization of a through-thickness glass fiber / epoxy thermoelectric generator

Abstract

The present study demonstrates, for the first time, the ability of a 10-ply glass fiber-reinforced polymer (GFRP) composite laminate to operate as a structural through-thickness thermoelectric generator (TEG). For this purpose, inorganic tellurium nanowires (Te NWs) were mixed with single wall carbon nanotubes (SWCNT) in a wet chemical approach, capable of resulting in a flexible p-type thermoelectric (TE) material with a power factor (*PF*) value of 58.88 μW/m · K^2. This material was used to prepare an aqueous thermoelectric ink, which was then deposited onto a glass fiber (GF) substrate via a simple dip-coating process. The coated GF ply was laminated as top lamina with uncoated GF plies underneath to manufacture a thermoelectric composite capable of generating 54.22 nW power output at a through-thickness temperature difference (ΔT) of 100 K. The mechanical properties of the proposed through-thickness TE laminate were tested and compared with those of the plain laminates. A minor reduction of approximately 11.5 % was displayed in both the flexural modulus and strength after the integration of the TE ply. Spectroscopic and morphological analyses were also employed to characterize the obtained TE nanomaterials and the respective coated GF ply.

Keywords: Glass fiber-reinforced polymer composite; Multifunctional structural laminate; Thermal energy harvesting; Through-thickness thermal gradient; Thermoelectric generator (TEG)

Highlights:

- TE-enabled GF functional ply with 58.88 μW/m · K^2
- through-thickness TEG GFRP laminate device with 54.22 nW power output
- through-thickness TEG GFRP laminate device with 0.02 W/m^2 power density
- multifunctional GFRP laminate without elimination of structural properties

Graphical Abstract

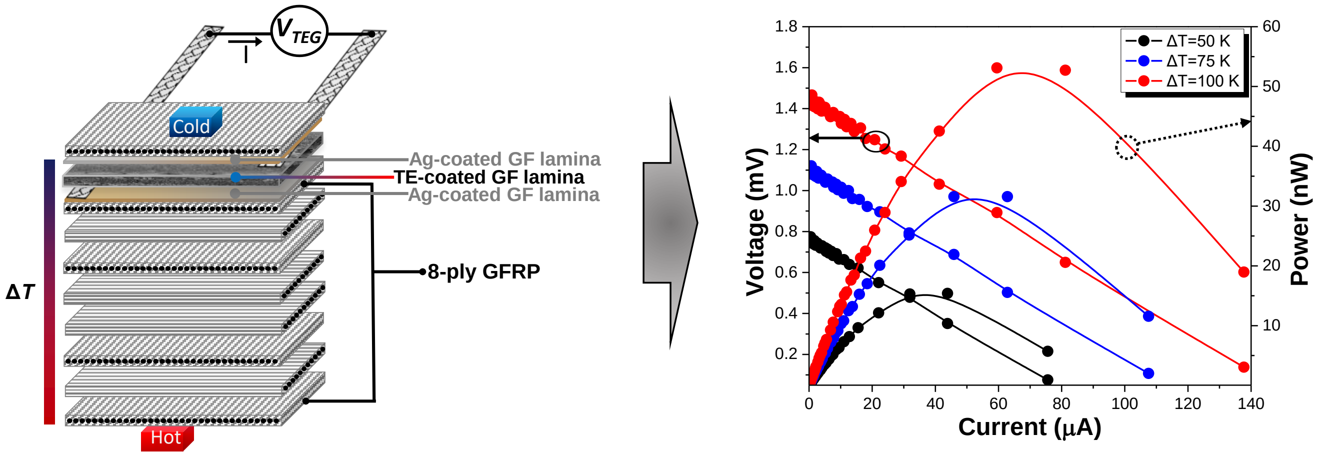

5.1.1 Introduction

Nowadays, there is a continuously increasing rate of global energy consumption. Although efforts have been made toward the exploitation of renewable or alternative energy sources, their use is still limited [1]. Moreover, eco-friendly solutions are required not only in terms of the source of energy but also in the way the power is supplied. For example, low power-consuming electronics such as wireless sensor networks typically use batteries as a power source. The limited lifetime of batteries results in increased total costs associated with their replacement in remote areas [2,3]. Next to that, high amounts of energy losses, often in the form of heat, could be partially recovered as power by proper energy conversion methodologies [4]. A promising way toward eco-friendly and autonomous structures is, thus, to broadly embed self-powered energy harvesting solutions, such as solar cells, vibration-based or thermal energy harvesters in structural materials [5–9]. This could be extremely relevant for boilers and steam piping systems, especially in large industrial and power plants, which show high amounts of wasted heat [10]. As a consequence, a reduction of operating and control costs could be achieved, also contributing to the new global requirements for CO_2 emissions reduction [11].

The basic principle behind thermal energy harvesting is the thermoelectric effect (*i.e.*, the Seebeck effect). It is well known that when a thermoelectric (TE) material is exposed to a temperature difference (ΔT), it spontaneously generates a potential difference (ΔV) due to the motion of free electrons (n-type semi-conductor material) or holes (p-type) toward specific directions. The magnitude of the Seebeck effect is expressed by the Seebeck coefficient (S), which is employed for the estimation of the power factor (*PF*) (see **Equations 1** and **2**). This quantity is used for the direct comparison of various materials' TE efficiency. The overall TE performance is classified by the dimensionless figure of merit (*ZT)* (see **Equation 3**).

$$S = \frac{\Delta V}{\Delta T} \tag{1}$$

where:

S = the Seebeck coefficient in μV/K

ΔV = the generated TE voltage in mV

ΔT = the externally applied temperature difference in K

$$PF = \sigma . S^2 \tag{2}$$

where:

PF = the power factor in $\mu W/m \cdot K^2$

σ = the electrical conductivity in S/m

$$ZT = \frac{\sigma . S^2 . \mathrm{T}}{\kappa} \tag{3}$$

where:

ZT = dimensionless figure of merit

T = the absolute temperature

κ = thermal conductivity in $W/m \cdot K$

Depending on their intrinsic carrier mobility and concentration, efficient TE materials present high values of ZT, combining high electrical and low thermal conductivity (κ) [12,13]. Traditional TE materials typically consist of low bandgap semiconductors, *e.g.*, Te, Bi_2Te_3, PbTe, etc. [14,15]. Recently, hybrid or organic nanostructured materials have been suggested as auspicious candidates for TE applications [16,17]. The scientific community is highly interested in blends of conductive polymers with inorganic thermoelectric crystals, bulk and 1D superlattice nanostructures, etc., due to their ability to tune the carrier transport via, *i.e.*, energy filtering mechanisms, inherent low thermal conductivity, tailored electrical conductivity, facile processing, relatively moderate large-scale production cost and superior flexibility properties [18–20].

Large-scale TE energy harvesting and conversion to sustainable electrical power is realized by TE generators (TEGs) devices. A common TEG device comprises single-type, or p- / n-type thermoelements interconnected electrically in series and thermally in parallel. Advancements in flexible and wearables TEGs have been recently reported, presenting desired power output values for practical applications [21–25]. Scientific works related to bulk or structural TEGs targeting different application areas have also been published [26–28]. Special interest has been concentrated on polymer nanocomposites [29–31], and fiber-reinforced polymer (FRP) composites [32,33] since such materials are widely used in aerospace, automotive, renewable energy, *etc*. applications. FRPs offer the potential for flexible design and novel manufacturing approaches with significantly improved specific properties, such as high strength to weight ratio [34,35]. Additionally, a variety of secondary functionalities can be introduced, transforming these materials into smart and multifunctional structures. This can be realized via the integration of dispersed nanomaterials in a polymer matrix or through hierarchical coatings deposited onto the reinforcing phases, such as glass and carbon fibers. Functionalities may include increased interfacial adhesion strength [36], increased interlaminar shear strength [37,38], non-destructive structural diagnostics [39,40], self-healing perspectives [41], energy storage capabilities [42], lightning-strike protection [43] and energy harvesting solutions [28].

More specifically, in the area of structural polymer composites, research has focused on the targeted enhancement of FRP's TE properties through the introduction of nanomaterials [44]. Previous studies on in-plane and through-thickness TE properties of FRP laminates mainly focused on the polymer matrix-interfaces modification with nano or micro-scale fillers [45]. For instance, Han *et al.* reported increased Seebeck coefficient values from +8 to +163 μV/K by brushing a mixture of tellurium and bismuth microparticles onto carbon fiber prepregs of a polymer matrix-based structural composite [46].

Based on the above, the existing literature findings are limited to the bulk through-thickness interface modifications, mainly with inorganic microparticles, to achieve enhanced TE response at the laminate level. Instead of modifying the matrix and/or the interface of a structural composite, the main goal of the current work is to develop, for the first time, an approach that involves the integration of a proper architecture acting as a through-thickness structural TEG device in a composite laminate. To achieve this goal, an inorganic-organic nanomaterial based on tellurium nanowires (Te NWs) with surfactant-dispersed single wall carbon nanotubes (SWCNT) added during growth is deployed. The nanostructured TE material is produced following a surfactant-assisted chemical reduction reaction based on previously well-established synthetic routes [47–49] with a few variations. The rationale behind this selection is to obtain enhanced performance through the combination of the TE properties of the two nanomaterials and flexibility at a film level via the use of highly durable SWCNT. By redispersing the synthesized nanomaterials, an aqueous TE ink is prepared and used to coat a glass fiber (GF) unidirectional (UD) fabric via a simple dip-coating and oven-drying process. Eventually, the coated ply is purposely laminated to manufacture a 10-ply GF reinforced polymer (GFRP) laminate. The structure of the obtained nanomaterials is characterized using Raman spectroscopy (RS) and X-Ray diffraction (XRD) analyses. Successful GF coating is confirmed via scanning electron microscopy (SEM). The TE performance of the nanomaterials and TEG laminates is also assessed. Finally, the effect of the TE ply integration on the mechanical performance of the obtained laminates is investigated under flexural loading. The obtained results reveal that it is possible to modify a conventional thin laminate with inorganic-organic nanomaterials on a ply level to enable efficient through-thickness thermal energy harvesting capabilities without eliminating the structural integrity of the obtained structure. Thus, the current paper deals with the demonstration of the ability of FRPs to act, by design, as through-thickness TEGs, with the aim to harvest thermal energy during the operational lifetime in the presence of temperature gradients.

5.1.2 Experimental section

5.1.2.1 Materials

For the preparation of the TE nanomaterials, ascorbic acid (AA) with 99 % purity, sodium dodecylbenzenesulfonate (SDBS, M_w = 348.48 g/mol), and sodium tellurite (Na_2TeO_3) ~100 mesh with >99 % purity were purchased from Sigma Aldrich. SWCNT dispersion (TUBALL, INK H_2O 0.2 %) was acquired by OCSiAl. All chemicals were analytical grade and used as received without any further purification procedure. Distilled (DI) water was used throughout this research. PVDF membrane (pore size 45 μm) was purchased from Merck and used for the preparation of Te-based buckypapers.

For the manufacturing of the GFRP laminates, unidirectional (UD) glass fabric 320 g/m^2 with a single-ply thickness of 0.26 mm from Fibermax was used. The epoxy resin system Araldite LY 5052 / Aradur 5052 was purchased from Huntsman and was used as the matrix of the composite. To facilitate the fabrication of the TEG device, silver (Ag) paste (ORGACON^{TM} Nanosilver Screen Printing Ink SI-P2000) was received from Agfa, while Ag foil tape (thickness of 0.055 mm) with conductive adhesive was acquired by 3M™.

5.1.2.2 Synthesis of TE nanomaterial and ink preparation

The whole process, from the synthesis of the TE material to the formation of the TE ink is illustrated in **Figure 60**. Initially, Te NWs were synthesized according to the following procedure: 4.93 g AA was dissolved in 200 mL of DI water in a reaction flask followed by the addition of 0.10 g SDBS. SDBS has been introduced due to its high dispersion efficiency that results in the prevention of agglomeration phenomena [50,51]. After the homogenization of the solution, 0.28 g Na_2TeO_3 was added to the vigorously stirred mixture. For the synthesis of the inorganic-organic TE nanomaterial, 2.5 mL of the SWCNT commercial ink was added to the previous mixture. Consequently, the mixture was raised up to 90 °C for 20 h and then left to cool down. The cleaning procedure included centrifugation at 8000 rpm for 30 min and removal of the sediment by dilution with DI water and pouring off repeatedly the SDBS rich supernatant side products and the residual reagents. The final precipitated material was redispersed and via a vacuum filtration process through a PVDF membrane filter (0.45 µm filter pore size) collected in the form of buckypaper while being kept finally for drying at 80 °C overnight. Finally, the buckypaper was redispersed in DI water (40 mg/mL) via bath-sonication for 30 min, resulting in a homogenous dispersion, hereafter denoted as TE ink. For comparison reasons, a buckypaper film was developed based on Te NWs before the in-situ growth in the presence of SWCNT and used as reference material.

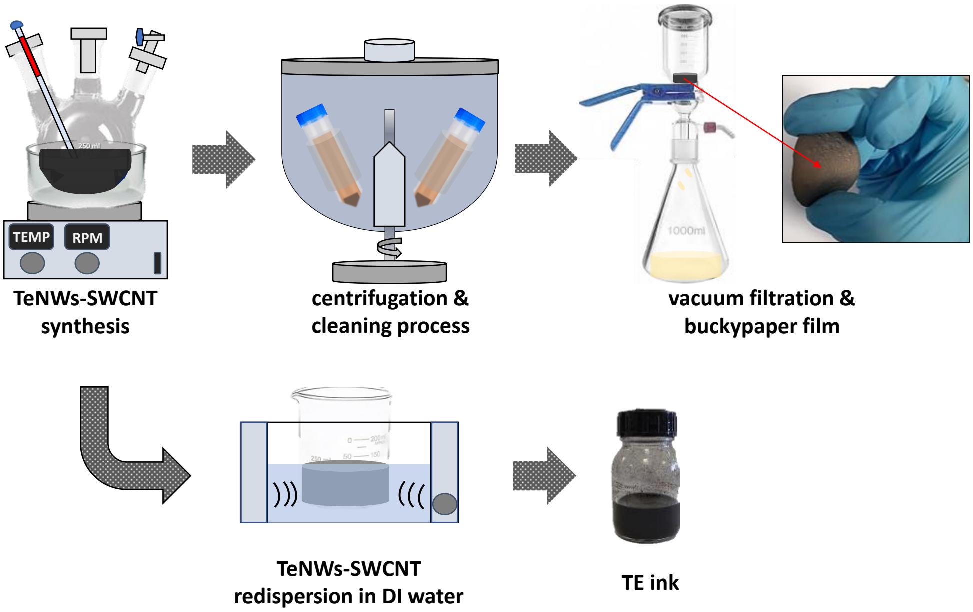

Figure 60. The steps followed for the synthesis of the inorganic-organic TE material and respective ink including: the solvothermal reaction step, the centrifugation and cleaning procedure with DI water, the vacuum filtration and buckypaper preparation procedure, the re-dispersion process, and the final TE ink.

5.1.2.3 *Manufacturing of the GFRP laminate with the through-thickness TEG functionality*

The fabrication of a single thermoelement TEG required firstly the integration of highly conductive electrode-like plies that will function as the interconnection between the internal TEG structure and the external electrodes. To do so, two GF plies were one-sided blade-coated with Ag paste, as shown schematically in **Figure 61a**. Then, the Ag-coated GF laminae were transferred in a ventilated oven and cured for 10 min at 150 °C. Afterward, Ag tape stripe was adapted to each Ag-coated GF lamina using a conductive adhesive to create the external electrodes. The next step was the incorporation of the TE functional ply into the laminate, as depicted in **Figure 61b**. This was achieved employing a facile dip-coating process, where the GF ply was immersed into the TE ink and subsequently dried overnight at 80 °C. For the manufacturing of the 10-ply GFRP TEG (50×50 mm^2), the TE-coated GF ply was sandwiched between the Ag-coated GF plies to create the top layer of the composite, while seven unmodified GF plies were added below the internal Ag-coated

GF ply, following a cross-ply lamination (see **Figure 61c**). A plain 10-ply GFRP laminate was also developed for comparison. Both the TEG GFRP laminate, as well as the reference plain GFRP laminate, were manufactured by hand lay-up epoxy resin impregnation and thermopressing. According to the specifications of the thermoset system, the resin to hardener weight ratio was set at 100:38 w/w. Curing was conducted for 24 h at room temperature (RT) under 3 MPa pressure using a hydraulic press, and the post-curing was performed at 100 °C for 4 h. Based on the technical datasheet of the manufacturer, the T_g of the resin system, after this curing cycle, is in the range of 120 to 134 °C. Attention was paid to avoid any direct contact between the two Ag-coated GF laminae. This was ensured through the strict alignment of the functional GF ply during the fabrication of the TEG device. The manufactured GFRP TEG is presented in **Figure 61d**.

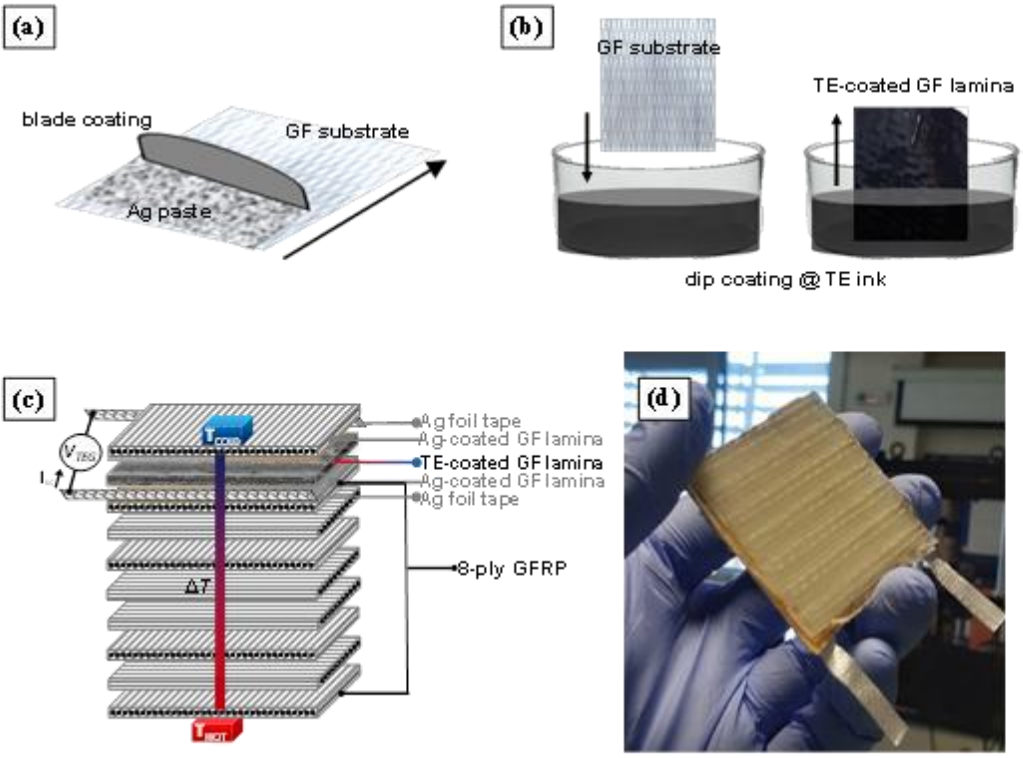

Figure 61. Schematic illustration of (**a**) blade coating for silver paste deposition onto the GF ply for the production of highly conductive electrode-like plies, (**b**) dip-coating of the GF ply within the TE ink to produce the coated functional ply, (**c**) the detailed lamination of the multifunctional GFRP and (**d**) photo of the manufactured through-thickness TEG GFRP laminate.

5.1.2.4 Characterization techniques

The structure of the synthesized inorganic-organic TE nanomaterial was characterized via Raman spectroscopy and XRD. Both Raman and XRD spectra were obtained from the TE buckypaper films. The spectroscopic measurements were carried out with a Labram HR (Horiba, Japan) scientific micro-Raman system. The 514.5 nm line of an Ar+ ion laser operating at a power of 1.5 mW at the focal plane was employed for the Raman excitation. An optical microscope equipped with a 50× long working distance objective served both for delivering the excitation light and collecting the back-scattered Raman light. Raman spectra in the range of 90–3500 cm^{-1} were collected. XRD analysis was performed with a D8 ADVANCE system (Bruker, USA) in symmetric step-scan mode with $2\theta = 0.05°$ in transmission mode. The diffractometer operated at 40 KV and 30 mA with Kα radiation ($\lambda = 1.5406$ Å), diffraction angle (θ, $10° < 2\theta < 80°$), and a step size of 5° at room temperature. The morphology investigation of the coated GF ply was performed using JSM 6510 LV SEM/Oxford Instruments (JEOL, Japan) with an operating voltage of 3.5 KV.

The electrical resistivity values of the produced buckypaper films were obtained using a typical 4-probe sheet resistance commercial system (Ossila Ltd, UK). The generated TE voltage (ΔV) of the produced buckypaper films (in-plane) and the TEG laminate (through-thickness) was measured with a 34401A multimeter (Agilent, USA). As illustrated in **Figure 61c**, the voltage was measured using the metallic connectors-electrodes (Ag-coated GF laminae) located in the 8th and 10th plies of the TEG laminate. Thus, the through-thickness TE voltage output measurements were defined in the transverse direction of the device based on a ~0.27 mm interelectrode distance (thickness of the TE ply). A custom-made set-up consisting of 2 metal blocks was developed for the generation of a temperature gradient (see **Figure 62**). For all measurements, one block was kept at room temperature (~25 °C) via water circulation, while the other was heated at higher temperatures via calibrated temperature-controlled resistors, allowing the generation of a ΔT. Three different levels of the thermal gradient were applied (*i.e.*, ΔT of 50, 75, and 100 K), which result in temperatures below or close to the T_g of the TEG laminates to avoid any substantial degradation in the structural integrity upon heating. The temperature of the 2 blocks was constantly measured with K-type thermocouples. **Figure 62** demonstrates the generated short-circuit current at ΔT of 100 K. Note that optical inspection for the TEG GFRP laminates indicated the absence of obvious evidence for any kind of degradation after several testing hours of continuous operation at the enforced maximum temperature gradient of 100 K.

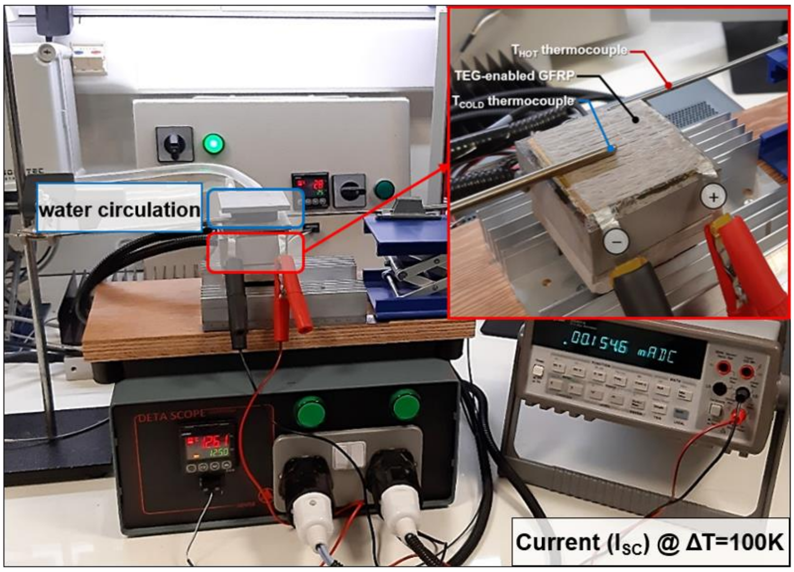

Figure 62. Demonstration of the through-thickness TEG GFRP performance during exposure to ΔT = 100 K.

This enables the calculation of S, *PF*, and *ZT* according to **Equations (1) – (3)**. Consequently, the thermal to electrical energy conversion efficiency (Carnot efficiency-η) can be determined by

$$\eta = \left(\frac{T_H - T_C}{T_H}\right)\frac{\sqrt{1+Z\bar{\bar{T}}}-1}{\sqrt{1+Z\bar{\bar{T}}}+(T_C/T_H)} \qquad \textbf{(4)}$$

Equation (4) [52]:

where:

T_H = the temperature of the hot side in K

T_C = the temperature of the cold side in K

$\bar{T}$ = the average temperature between the hot and the cold side in K

Based on the above measurements, it is also possible to calculate the maximum TE power output of the TEG GFRP laminate according to the following **Equation (5)** [28]:

$$P_{max} = \frac{{V_{TEG}}^2}{4.R_{TEG}} \qquad \textbf{(5)}$$

where:

P_{max} = maximum power output in nW

V_{TEG} = the TE open-circuit voltage in mV

R_{TEG} = internal electrical resistance of the TEG in Ohm

Oriented to a TEG device characterization for practical applications, power output measurements as a function of the externally applied load resistances (R_{LOAD}) were carried out. Thus, the through-thickness TEG GFRP device power output characteristics have been evaluated using a custom-built fully automated electronic system based on a LabVIEW-PC interface with a range of applied external loads from 1 to 10000 Ohm with discretion capability down to 1 Ohm. Apart from the experimental power output values, it is possible to obtain calculated ones using **Equation (6)** [52]:

$$P = I^2 \, . \mathrm{R_{LOAD}} = \left(\frac{V_{TEG}}{R_{TEG} + \mathrm{R_{LOAD}}}\right)^2 . \mathrm{R_{LOAD}} \qquad \textbf{(6)}$$

where:
P = the output power in nW
I = the output current that passes through the load in μA.

All tests were performed at ambient conditions (1 atm, T_C ~25 °C, relative humidity: 40 ± 5 % RH).

Finally, the mechanical performance of the unmodified and TEG GFRP laminates was evaluated under flexural loading according to ASTM D 790-03 standard [53] using a 100 KN Universal Testing Machine (JINAN TESTING EQUIPMENT IE CORPORATION, Jinan, China). 5 rectangular specimens (50×10×~2.6 mm^3) were tested for each type of laminate at a deformation rate of 1 mm/min. All specimens were conditioned in an oven at 40 °C overnight prior to testing.

5.1.3 Results and Discussion

5.1.3.1 Characterization of the inorganic-organic nanomaterial and the coated GF fabric

Raman and XRD spectra were obtained from the developed buckypaper films to verify the presence of hybrid Te NWs-SWCNT inorganic-organic thermoelectric material. As illustrated in **Figure 63a**, the existence of Te NWs is identified through the Raman peaks at 118.1 cm^{-1} and 138.2 cm^{-1}. Furthermore, the peak at ca. 120 cm^{-1} is attributed to the Te content and the A$_1$ vibrational mode response of Te NWs [54]. SWCNT are also visible via the D (1337 cm^{-1}), G (1588 cm^{-1}), and 2D (2666 cm^{-1}) peaks. A characteristic peak at ca. 1588 cm^{-1} is related to the vibration of sp^2-bonded and in-plane stretching E$_{2g}$ mode of carbon atoms of the SWCNT. Raman spectra of SWCNT located this characteristic peat at ca. 1590 cm^{-1} [30]. As discussed previously, the slight shift of the peak position of the G-band can be attributed to the interaction between the Te NWs with SWCNT, leading to a decreased conjugation [47]. A relatively lower peak at ca. 1337 cm^{-1} is correlated with sp^3 hybridization [55].

Moreover, as illustrated in **Figure 63b**, the XRD pattern of the inorganic-organic buckypaper film is in agreement with the Te reference spectrum (36–1452, black inset bars) [49]. Thus, the XRD spectra confirmed the crystal hexagonal structure of tellurium with three atoms per unit cell and cell constants equal to 4.46 Å for a and 5.92 Å for c [56].

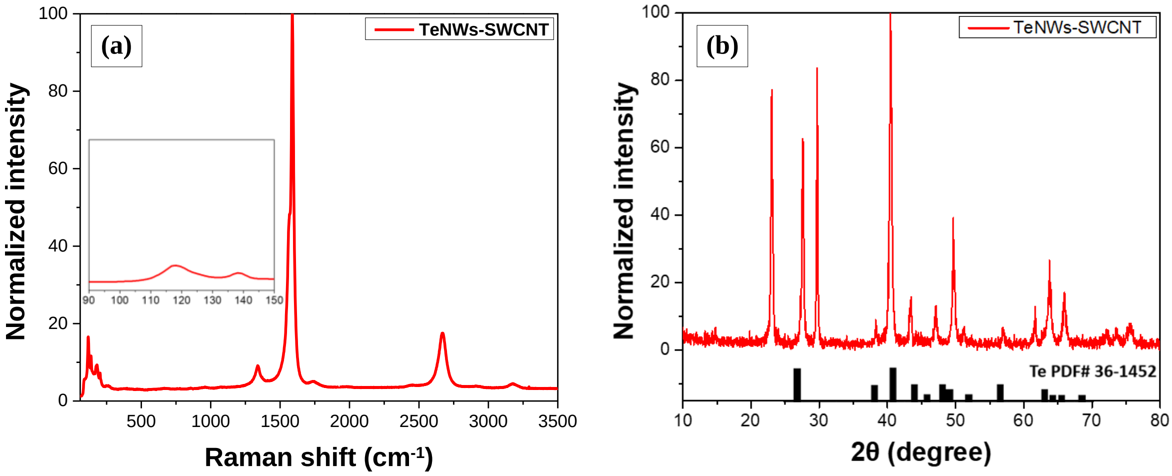

Figure 63. (**a**) Raman spectrum and (**b**) X-Ray diffraction pattern of the Te NWs-SWCNT buckypaper film.

For comparison purposes, the in-plane TE properties of the reference inorganic and the developed inorganic-organic buckypaper film are included in **Table 9**. The reported mean TE values are referred to five measurements of different buckypaper films for each case. The positive values of the Seebeck coefficient indicate the p-type semiconducting behavior for both materials. Furthermore, as observed in **Table 9**, the Te NWs-based film presented a relatively high Seebeck coefficient of approximately +302 μV/K combined with a low electrical conductivity of 8.4 S/m, which corresponds to a *PF* of 0.77 $\mu W/m \cdot K^2$. At the same time, the inorganic-organic film presented a Seebeck coefficient of approximately +80 μV/K combined with an electrical conductivity of 9200 S/m, resulting in a two order of magnitude higher *PF* of 58.88 $\mu W/m \cdot K^2$, compared to the inorganic TE film. Since κ values were not experimentally, the calculation of the *ZT* values was obtained using respective values from other studies [48] (see **Table 9**). We believe that this is a good approximation since similar synthetic routes were followed for the manufacturing of the Te NWs and Te NWs-SWCNT as those presented in [48]. It should also be noted that an average value of *ZT* was obtained since the actual temperature was approximated with the externally applied ΔT. As observed, the energy conversion efficiency for the reference system is as low as 0.008 %. On the contrary, the combination of the Te NWs with SWCNT resulted in approximately 74 times higher efficiency of the obtained TE nanomaterials. Based on the above, it can be concluded that the addition of the highly conductive SWCNT within the Te NWs was beneficial for the overall TE performance of the developed films. This can be attributed to bridging phenomena that create conductive paths between the 2 nanomaterials, resulting in a reduction of the contact resistance without eliminating the overall TE performance [57-59]. Moreover, the extremely brittle nature of Te NWs buckypaper films renders this material unsuitable for further processing and practical applications. Therefore, the inorganic-organic nanomaterial was employed for TE ink production.

Table 9. TE values of the inorganic and inorganic-organic buckypaper films at ΔT of 100 K.

TE Material	σ	**S**	***PF***	**κ**	***ZT***	η
	S/m	**μV/K**	**μW/m·K^2**	**W/(m·K)**	**-**	**%**
TeNWs	8.4 ± 0.6	+302 ± 8	0.77	0.28	0.001	0.008
TeNWs-SWCNT	9200 ± 5	+80 ± 4	58.88	0.26	0.080	0.590

Images of the TE-coated GF fabric at different magnifications are presented in **Figure 64**. Based on these images, satisfying adhesion properties between the TE coating and the fibrous substrate is elucidated by the continuously distributed nanostructures onto the surface of the GFs. Consequently, the created through-thickness uniform coating introduces multiple interconnected TE paths due to GF fabric porosity and voids between the stitched GF tows, as observed in **Figure 64a-b**. Subsequently, the highest magnification image (**Figure 64c**) reveals a dense network of high aspect ratio typical 1D nanostructures with a diameter of a few nm, which correspond to the Te NWs-SWCNT hybrid system. The absence of any aggregates implies the preparation of a high-quality TE ink and the application of an efficient coating process. This is expected to result in superior bulk TE properties of the coated GF fabric.

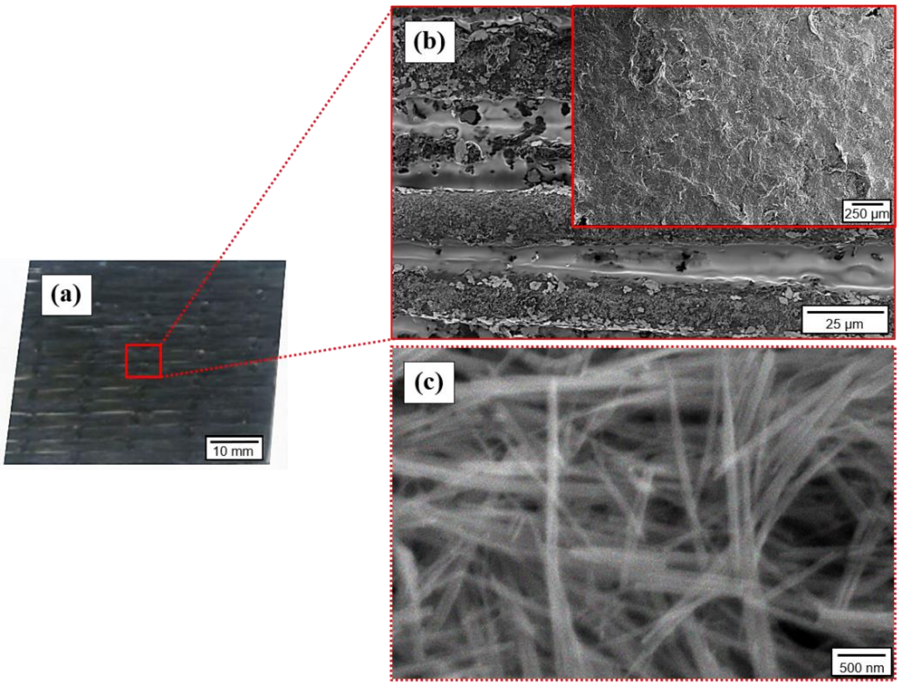

Figure 64. (**a**) Image of the TE-coated GF and (**b**, **c**) SEM images at different magnifications.

5.1.3.2 Characterization of the TEG GFRP laminate

Table 10 presents the experimentally measured TE values and the calculated maximum TE power output of the TEG GFRP laminate at different thermal gradients. The average output values correspond to TE measurements, which arose from four manufactured TEG GFRP laminates. At this point, it is worth mentioning that the measured through-thickness internal electrical resistance (R_{TEG}) value of the laminate system prior to the impregnation of the epoxy resin was as low as ~3 Ohm at RT. Subsequently, after the hardening of the epoxy matrix, the composite laminates' R_{TEG} value was slightly increased at 8.3 Ohm. This increase could be mainly ascribed to possible interactions between the epoxy resin, the thin coating of the TE GF lamina, and the Ag-coated GF laminae. Thus, the internal TEG interconnection marginally affected the electrical characteristics of the manufactured laminates.

Table 10. TE measurements of the through-thickness TEG GFRP laminate at various ΔT.

ΔT (K)	R_{TEG} (Ohm)	V_{TEG} (mV)	I_{SC} (μA)	P_{max} (nW)
0	8.30 ± 0.10	-	-	-
50	9.15 ± 0.15	0.76 ± 0.13	82.67 ± 0.18	15.78
75	9.33 ± 0.24	1.10 ± 0.17	119.84 ± 0.24	32.42
100	9.56 ± 0.32	1.44 ± 0.22	154.60 ± 0.38	54.22

As observed in **Table 10**, the manufactured through-thickness TEG GFRP laminate can harvest thermal energy upon exposure to a temperature gradient and under enforced cooling to sustain the design desired ΔT. In the case where there is no enforced cooling, the power output of the TEG appears to be insufficient. For instance, a ΔT of 50 K generates a sufficient open-circuit voltage (Seebeck voltage) of 0.76 mV, which increases with a further increase of the ΔT. Inevitably, a short-circuit current of 82.67 μA and a power output of 15.78 nW could be achieved at a temperature difference of 50 K that can be easily attained between a car engine in operation and the outside air that surrounds the car during its movement [60,61]. The maximum power output of 54.22 nW of the through-thickness TEG GFRP laminate, derived at ΔT = 100 K, corresponds to a power density of 0.02 W/m^2. The power density value was calculated by dividing the maximum TE power output with the cross-sectional active area of the coated GF ply.

Figure 65a-b shows the power output characteristics for the TEG GFRP laminate. In more detail, the multifunctional GFRP laminate exhibits an open-circuit voltage (V_{TEG}) of 1.44 mV and short-circuit current (I_{sc}) of 154.6 μA at ΔT of 100 K with an internal resistance (R_{TEG}) of 9.56 Ohm.

Figure 65a depicts the measured TE performance in various Δ*T*. Specifically, output voltage-current (*V*-*I*), output power-current (*P*-*I*) curves. **Figure 65b** depicts the output voltage-external load (V-R_{LOAD}) and output power-external load (P-R_{LOAD}) curves with the application of different external load resistances. The continuous lines in all cases have been derived from calculations, while the dots correspond to the experimental values that were acquired through the specially designed custom-built measuring unit. A maximum power generation of 54.22 nW at a through-thickness Δ*T* of 100 K is dissipated at the applied external electrically in-series connected R_{LOAD}. As it was noticed, when the external load is compatible with the R_{TEG} experimental value of 9.53 Ohm, the maximum output power is matched with the external load resistance of ca. 9.5 Ohm, which is equal to the R_{TEG} value. As expected, the output voltage for the different R_{LOAD} was inversely proportional to the output current, presenting a typical parabolic behavior.

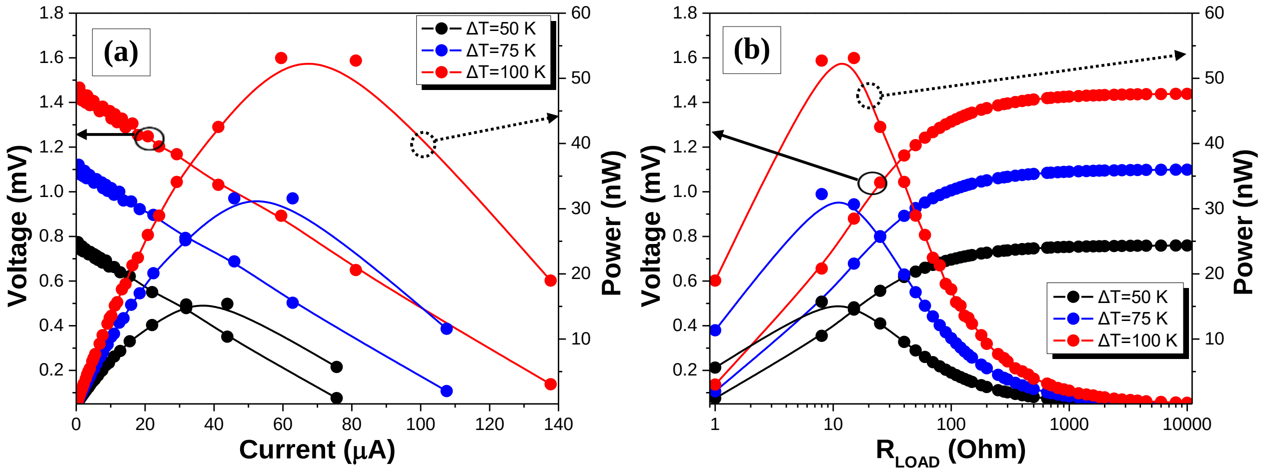

Figure 65. (**a**, **b**) Power output characteristics for Δ*T* of 50, 75 and 100 K.

Conventional bulk or micro-scale through-thickness TEG designs during application suffer from thermal gradient equilibrium during time evolution, especially in the case where the heat dissipation is spontaneous, without being sustained artificially [21,59]. For comparison purposes, it is important to mention that the in-plane TE output of the inorganic-organic buckypaper was 8 ± 0.12 mV, at 25 mm for an applied Δ*T* of 100 K. The respective through-thickness TE voltage of the TEG laminate was 1.44 mV, as stated in **Table 10**. Thus, the TEG laminate shows a lower through-thickness voltage by ~82 % compared to the voltage obtained from the in-plane measurement of the buckypaper. This could be attributed mainly to the extremely compact interelectrode distance ~0.27 mm in the case of the TEG laminate. Partially, the thermal insulating character of the GFRP laminate could also negatively affect the internal Δ*T* distribution, resulting in lower power output values in relation to the expected ones. Additionally, it is worth noting that the abovementioned values are the result of a single thermoelement. Indicative, Inayat *et al.* succeeded a TE power output of 112 nW for a Δ*T* of ~20 K resulting from a 4-thermoelement inorganic nanomaterial-based through-thickness TEG prototype window glass [62]. Similarly, Lu *et al.* developed a fabric-based through-thickness TEG prototype consisting of 12 inorganic nanostructured thermoelements that were able to achieve a TE power output of ca. 15 nW at a Δ*T* of ~30 K [63].

Based on the above, it is obvious that the developed laminate has the potential for significant thermal energy harvesting. This can be further optimized after the fabrication of in-series or in-parallel interconnected modules of thermoelements to increase the total TE power generation. It is therefore demonstrated that the exploitation of through-thickness TEG GFRP composite laminates could realize effective thermal energy harvesting power by structural components.

The mechanical performance of the multifunctional GFRP laminate was evaluated under flexural loading and compared with the plain reference laminate. Based on representative stress-strain curves of the tested specimens, it can be observed that the functional laminate behaves similarly with the reference GFRP, as shown in **Figure 66a**. The stress-strain curve of the TEG laminate lies slightly below one of the reference materials. The stress-strain curves of all tested specimens were assessed to calculate the average flexural modulus and strength before and after the GFRP modification. Based on the results presented in **Figure 66b**, the flexural strength was 371.70 ± 23.43 MPa, and the flexural modulus was 11.41 ± 1.5 GPa for the multifunctional GFRP, while the respective values for the plain GFRP were 420.04 ± 24.47 MPa and 12.89 ± 1.6 GPa. Thus, it can be concluded that the integration of the functional GF ply and the Ag-coated plies resulted in a minor alteration of the response of the functional laminate and a respective reduction of ~11.5 % in both the strength and the modulus.

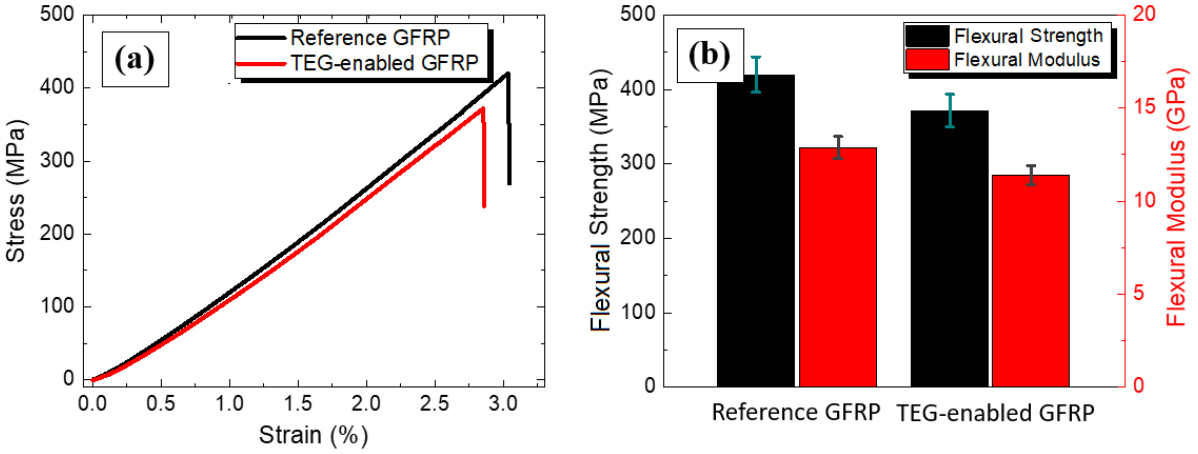

Figure 66. Comparison plots for the reference GFRP and the through-thickness TEG GFRP specimens (**a**) representative stress-strain curves and (**b**) average flexural strength and modulus.

The obtained mechanical results disclose relatively equivalent structures according to the flexural strength and the modulus. The requirement of both metallic and TE functional coatings onto specific GF plies contributes to the slightly decreased mechanical properties. However, the laminates maintained to a great extent their advanced properties and can still be used as structural composites.

5.1.4 Conclusions

The scope of this research was to introduce through-thickness thermal energy harvesting capabilities to conventional GFRP composite laminates without eliminating their structural integrity. For this reason, an efficient, flexible p-type inorganic-organic TE nanomaterial was synthesized and further processed to produce aqueous TE ink for dip-coating purposes creating hierarchically coated GF UD reinforcement fabrics. The resulting coated functional GF ply was employed for the first time to manufacture a through-thickness TEG-enabled GFRP laminate, which exhibited a power output of 54.22 nW from a single thermoelement upon exposure to a through-thickness ΔT of 100 K. Regarding the mechanical performance, the multifunctional structure displayed slightly decreased values ca. 11.5 % of bending strength and flexural modulus with respect to the reference GFRP laminates.

Future developments in flexible, chemically stable, and environmental-friendly TE materials with enhanced ZT values in the range of ~1 at reasonable temperature gradients could dramatically improve the power output characteristics at the material level, oriented to prospect practical applications. Thus, the fabrication at the device level of multiple in-series and/or in-parallel interconnected modules of thermoelements could further stimulate the total generated TE power from composite structures. Thermal energy harvesting and conversion by structural materials with promising power output in the range of several microwatts is sufficient to power up external step-up low power-consuming converters for the energy storage, leading to exploitable energy management and use toward the activation of low-power electronics such as wireless sensor networks, *etc*.. Based on the above, power generation by structural engineering materials designed to be routinely exposed to temperature gradient could emerge as an attractive technology for the realization of large-scale thermal energy harvesting applications in various industrial sectors.

5.1.5 References

1. Martín-González, M.; Caballero-Calero, O.; Díaz-Chao, P. Nanoengineering thermoelectrics for 21st century: Energy harvesting and other trends in the field. *Renew. Sustain. Energy Rev.* **2013**, *24*, 288–305, doi:10.1016/j.rser.2013.03.008.
2. Ball, A.D.; Gu, F.; Cattley, R.; Wang, X.; Tang, X. Energy harvesting technologies for achieving self-powered wireless sensor networks in machine condition monitoring: A review. *Sensors (Switzerland)* **2018**, *18*, 4113, doi:10.3390/s18124113.
3. Dilhac, J.M.; Monthéard, R.; Bafleur, M.; Boitier, V.; Durand-Estèbe, P.; Tounsi, P. Implementation of thermoelectric generators in airliners for powering battery-free wireless sensor networks. *J. Electron. Mater.* **2014**, *43*, 2444–2451, doi:10.1007/s11664-014-3150-1.
4. Zoui, M.A.; Bentouba, S.; Stocholm, J.G.; Bourouis, M. A review on thermoelectric generators: Progress and applications. *Energies* **2020**, *13*, 3606, doi:10.3390/en13143606.
5. Kraemer, D.; Poudel, B.; Feng, H.P.; Caylor, J.C.; Yu, B.; Yan, X.; Ma, Y.; Wang, X.; Wang, D.; Muto, A.; McEnaney, K.; Chiesa, M.; Ren, Z.; Chen, G. High-performance flat-panel solar thermoelectric generators with high thermal concentration. *Nat. Mater.* **2011**, *10*, 532–538, doi:10.1038/nmat3013.
6. Lee, J.J.; Yoo, D.; Park, C.; Choi, H.H.; Kim, J.H. All organic-based solar cell and thermoelectric generator hybrid device system using highly conductive PEDOT:PSS film as organic thermoelectric generator. *Sol. Energy* **2016**, *134*, 479–483, doi:10.1016/j.solener.2016.05.006.
7. Lee, D.; Kim, I.; Kim, D. Hybrid tribo-thermoelectric generator for effectively harvesting thermal energy activated by the shape memory alloy. *Nano Energy* **2021**, *82*, 105696, doi:10.1016/j.nanoen.2020.105696.
8. Boudouris, B.W. Engineering optoelectronically active macromolecules for polymer-based photovoltaic and thermoelectric devices. *Curr. Opin. Chem. Eng.* **2013**, *2*, 294–301, doi:10.1016/j.coche.2013.07.002.
9. Zi, Y.; Wang, Z.L. Nanogenerators: An emerging technology towards nanoenergy. *APL Mater.* **2017**, *5*, 074103, doi:10.1063/1.4977208.
10. Liu, L. Feasibility of large-scale power plants based on thermoelectric effects. *New J. Phys.* **2014**, *16*, 123019, doi:10.1088/1367-2630/16/12/123019.
11. Zappa, W.; Junginger, M.; Broek, M. Van Den; Cover, C.L. Is a 100 % renewable European power system feasible by 2050 ? *Appl. Energy* **2019**, *233–234*, 1027–1050, doi:10.1016/j.apenergy.2018.08.109.
12. Vineis, C.J.; Shakouri, A.; Majumdar, A.; Kanatzidis, M.G. Nanostructured thermoelectrics: Big efficiency gains from small features. *Adv. Mater.* **2010**, *22*, 3970–3980, doi:10.1002/adma.201000839.
13. Cho, C.; Wallace, K.L.; Tzeng, P.; Hsu, J.H.; Yu, C.; Grunlan, J.C. Outstanding Low Temperature Thermoelectric Power Factor from Completely Organic Thin Films Enabled by Multidimensional Conjugated Nanomaterials. *Adv. Energy Mater.* **2016**, *6*, 1–8, doi:10.1002/aenm.201502168.
14. Snyder, G.J.; Toberer, E.S. 1. Complex thermoelectric materials. *Nat Mater* **2008**, *7*, 105–114, doi:10.1038/nmat2090.
15. Madan, D.; Wang, Z.; Chen, A.; Juang, R.C.; Keist, J.; Wright, P.K.; Evans, J.W. Enhanced performance of dispenser printed MA n-type Bi2Te 3 composite thermoelectric generators. *ACS Appl. Mater. Interfaces* **2012**, *4*, 6117–6124, doi:10.1021/am301759a.
16. Cao, Z.; Koukharenko, E.; Tudor, M.J.; Torah, R.N.; Beeby, S.P. Flexible screen printed thermoelectric generator with enhanced processes and materials. *Sensors Actuators, A Phys.* **2016**, *238*, 196–206, doi:10.1016/j.sna.2015.12.016.
17. Shah, K.W.; Wang, S.X.; Soo, D.X.Y.; Xu, J. One-dimensional nanostructure engineering of conducting polymers for thermoelectric applications. *Appl. Sci.* **2019**, *9*, 1422, doi:10.3390/app9071422.

18. Dörling, B.; Ryan, J.D.; Craddock, J.D.; Sorrentino, A.; El Basaty, A.; Gomez, A.; Garriga, M.; Pereiro, E.; Anthony, J.E.; Weisenberger, M.C.; Goñi, A.R.; Müller, C.; Campoy-Quiles, M. Photoinduced p- to n-type Switching in Thermoelectric Polymer-Carbon Nanotube Composites. *Adv. Mater.* **2016**, *28*, 2782–2789, doi:10.1002/adma.201505521.
19. Wei, Q.; Mukaida, M.; Kirihara, K.; Naitoh, Y.; Ishida, T. Recent progress on PEDOT-based thermoelectric materials. *Materials.* **2015**, *8*, 732–750, doi:10.3390/ma8020732.
20. Kandemir, A.; Ozden, A.; Cagin, T.; Sevik, C. Thermal conductivity engineering of bulk and one-dimensional Si-Ge nanoarchitectures. *Sci. Technol. Adv. Mater.* **2017**, *18*, 187–196, doi:10.1080/14686996.2017.1288065.
21. Chen, W.Y.; Shi, X.L.; Zou, J.; Chen, Z.G. Wearable fiber-based thermoelectrics from materials to applications. *Nano Energy*. **2021**, *81*, 105684, doi:10.1016/j.nanoen.2020.105684.
22. Allison, L.K.; Andrew, T.L. A Wearable All-Fabric Thermoelectric Generator. *Adv. Mater. Technol.* **2019**, *4*, 1–7, doi:10.1002/admt.201800615.
23. Jung, K.K.; Jung, Y.; Choi, C.J.; Lee, J.M.; Ko, J.S. Flexible thermoelectric generator with polydimethyl siloxane in thermoelectric material and substrate. *Curr. Appl. Phys.* **2016**, *16*, 1442–1448, doi:10.1016/j.cap.2016.08.010.
24. K. Mytafides, C.; Tzounis, L.; Karalis, G.; Formanek, P.; S. Paipetis, A. High-Power All-Carbon Fully Printed and Wearable SWCNT-Based Organic Thermoelectric Generator. *ACS Appl. Mater. & Interfaces.* **2021**, *13*, 11151–11165, doi:10.1021/acsami.1c00414.
25. Kim, S.J.; We, J.H.; Cho, B.J. A wearable thermoelectric generator fabricated on a glass fabric. *Energy Environ. Sci.* **2014**, *7*, 1959–1965, doi:10.1039/c4ee00242c.
26. Wei, J.; Nie, Z.; He, G.; Hao, L.; Zhao, L.; Zhang, Q. Energy harvesting from solar irradiation in cities using the thermoelectric behavior of carbon fiber reinforced cement composites. *RSC Adv.* **2014**, *4*, 48128–48134, doi:10.1039/c4ra07864k.
27. Tzounis, L.; Liebscher, M.; Fuge, R.; Leonhardt, A.; Mechtcherine, V. P- and n-type thermoelectric cement composites with CVD grown p- and n-doped carbon nanotubes: Demonstration of a structural thermoelectric generator. *Energy Build.* **2019**, *191*, 151–163, doi:10.1016/j.enbuild.2019.03.027.
28. Karalis, G.; Tzounis, L.; Lambrou, E.; Gergidis, L.N.; Paipetis, A.S. A carbon fiber thermoelectric generator integrated as a lamina within an 8-ply laminate epoxy composite: Efficient thermal energy harvesting by advanced structural materials. *Appl. Energy* **2019**, *253*, 113512, doi:10.1016/j.apenergy.2019.113512.
29. Blackburn, J.L.; Ferguson, A.J.; Cho, C.; Grunlan, J.C. Carbon-Nanotube-Based Thermoelectric Materials and Devices. *Adv. Mater.* **2018**, *30*, 1–35, doi:10.1002/adma.201704386.
30. Kroon, R.; Mengistie, D.A.; Kiefer, D.; Hynynen, J.; Ryan, J.D.; Yu, L.; Müller, C. Thermoelectric plastics: From design to synthesis, processing and structure-property relationships. *Chem. Soc. Rev.* **2016**, *45*, 6147–6164, doi:10.1039/c6cs00149a.
31. Tzounis, L.; Hegde, M.; Liebscher, M.; Dingemans, T.; Pötschke, P.; Paipetis, A.S.; Zafeiropoulos, N.E.; Stamm, M. All-aromatic SWCNT-Polyetherimide nanocomposites for thermal energy harvesting applications. *Compos. Sci. Technol.* **2018**, *156*, 158–165, doi:10.1016/J.COMPSCITECH.2017.12.030.
32. Karalis, G.; Mytafides, C.; Polymerou, A.; Tsirka, K.; Tzounis, L.; Gergidis, L.; Paipetis, A.S. Hierarchical Reinforcing Fibers for Energy Harvesting Applications - A Strength Study. *Key Engineering Materials* **2020**, *827* :252–7, doi:10.4028/www.scientific.net/KEM.827.252.
33. Karalis, G.; Tsirka, K.; Tzounis, L.; Mytafides, C.; Koutsotolis, L.; Paipetis, A.S.. Epoxy/Glass Fiber Nanostructured p- and n-Type Thermoelectric Enabled Model Composite Interphases. *Appl. Sci*. **2020**, *10*, 5352, doi:10.3390/app10155352.
34. Paluvai, N.R.; Mohanty, S.; Nayak, S.K. Synthesis and Modifications of Epoxy Resins and Their Composites: A Review. *Polym. - Plast. Technol. Eng.* **2014**, *53*, 1723–1758, doi:10.1080/03602559.2014.919658.

35. Gibson, R.F. A review of recent research on mechanics of multifunctional composite materials and structures. *Compos. Struct.* **2010**, *92*, 2793–2810, doi:10.1016/j.compstruct.2010.05.003.
36. De Luca, F.; Clancy, A.J.; Carrero, N.R.; Anthony, D.B.; De Luca, H.G.; Shaffer, M.S.P.; Bismarck, A. Increasing carbon fiber composite strength with a nanostructured "brick-and-mortar" interphase. *Mater. Horizons* **2018**, *5*, 668–674, doi:10.1039/c7mh00917h.
37. Gkikas, G.; Barkoula, N.M.; Paipetis, A.S. Effect of dispersion conditions on the thermo-mechanical and toughness properties of multi walled carbon nanotubes-reinforced epoxy. *Compos. Part B Eng.* **2012**, *43*, 2697–2705, doi:10.1016/j.compositesb.2012.01.070.
38. Qian, H.; Greenhalgh, E.S.; Shaffer, M.S.P.; Bismarck, A. Carbon nanotube-based hierarchical composites: A review. *J. Mater. Chem.* **2010**, *20*, 4751–4762, doi:10.1039/c000041h.
39. Bekas, D.G.; Paipetis, A.S. Damage monitoring in nanoenhanced composites using impedance spectroscopy. *Compos. Sci. Technol.* **2016**, *134*, 96–105, doi:10.1016/j.compscitech.2016.08.013.
40. Foteinidis, G.; Tsirka, K.; Tzounis, L.; Baltzis, D.; Paipetis, A.S. The role of synergies of MWCNTs and Carbon Black in the enhancement of the electrical and mechanical response of modified epoxy resins. *Appl. Sci.* **2019**, *9(18)*, 3757, doi:10.3390/app9183757.
41. Orfanidis, S.; Papavassiliou, G.; Paipetis, A.S. Microcapsule-based self-healing materials: Healing efficiency and toughness reduction vs. capsule size. *Compos. Part B* **2019**, 171, 78–86, doi:10.1016/j.compositesb.2019.04.030.
42. Qian, H.; Kucernak, A.R.; Greenhalgh, E.S.; Bismarck, A.; Shaffer, M.S.P. Multifunctional structural supercapacitor composites based on carbon aerogel modified high performance carbon fiber fabric. *ACS Appl. Mater. Interfaces* **2013**, *5*, 6113–6122, doi:10.1021/am400947j.
43. Han, J.H.; Zhang, H.; Chen, M.J.; Wang, D.; Liu, Q.; Wu, Q.L.; Zhang, Z. The combination of carbon nanotube buckypaper and insulating adhesive for lightning strike protection of the carbon fiber/epoxy laminates. *Carbon N. Y.* **2015**, *94*, 101–113, doi:10.1016/j.carbon.2015.06.026.
44. Sung, D.H.; Kang, G.H.; Kong, K.; Kim, M.; Park, H.W.; Park, Y. Bin Characterization of thermoelectric properties of multifunctional multiscale composites and fiber-reinforced composites for thermal energy harvesting. *Compos. Part B Eng.* **2016**, *92*, 202–209, doi:10.1016/j.compositesb.2016.02.050.
45. Han, S.; Chung, D.D.L. Through-thickness thermoelectric power of a carbon fiber/epoxy composite and decoupled contributions from a lamina and an interlaminar interface. *Carbon N. Y.* **2013**, *52*, 30–39, doi:10.1016/j.carbon.2012.08.071.
46. Han, S.; Chung, D.D.L. Carbon fiber polymer-matrix structural composites exhibiting greatly enhanced through-thickness thermoelectric figure of merit. *Compos. Part A Appl. Sci. Manuf.* **2013**, *48*, 162–170, doi:10.1016/j.compositesa.2013.01.008.
47. Li, C.; Sun, P.; Liu, C.; Xu, J.; Wang, T.; Wang, W.; Hou, J.; Jiang, F. Fabrication of flexible SWCNTs-Te composite films for improving thermoelectric properties. *J. Alloys Compd.* **2017**, *723*, 642–648, doi:10.1016/j.jallcom.2017.06.253.
48. Choi, J.; Lee, K.; Park, C.R.; Kim, H. Enhanced thermopower in flexible tellurium nanowire films doped using single-walled carbon nanotubes with a rationally designed work function. *Carbon N. Y.* **2015**, *94*, 577–584, doi:10.1016/j.carbon.2015.07.043.
49. Park, H.; Son, W.; Lee, S.H.; Kim, S.; Lee, J.J.; Cho, W.; Choi, H.H.; Kim, J.H. Aqueous chemical synthesis of tellurium nanowires using a polymeric template for thermoelectric materials. *CrystEngComm* **2015**, *17*, 1092–1097, doi:10.1039/c4ce02222j.
50. Wei, J.; Wen, X.; Zhu, F. Influence of Surfactant on the Morphology and Photocatalytic Activity of Anatase TiO2 by Solvothermal Synthesis. *J. Nanomater.* **2018**, *2018*, 1–7, doi:10.1155/2018/3086269.
51. Thilagavathi, T.; Geetha, D. Nano ZnO structures synthesized in presence of anionic and cationic surfactant under hydrothermal process. *Appl. Nanosci.* **2014**, *4*, 127–132, doi:10.1007/s13204-012-0183-8.

52. von Lukowicz, M.; Abbe, E.; Schmiel, T.; Tajmar, M. Thermoelectric Generators on Satellites—An Approach for Waste Heat Recovery in Space. *Energies* **2016**, *9*, 541, doi:10.3390/en9070541.
53. ASTM INTERNATIONAL Standard Test Methods for Flexural Properties of Unreinforced and Reinforced Plastics and Electrical Insulating Materials. D790. *Annu. B. ASTM Stand.* **2002**, 1–12.
54. Roy, A.; Amin, K.R.; Tripathi, S.; Biswas, S.; Singh, A.K.; Bid, A.; Ravishankar, N. Manipulation of Optoelectronic Properties and Band Structure Engineering of Ultrathin Te Nanowires by Chemical Adsorption. *ACS Appl. Mater. Interfaces* **2017**, *9*, 19462–19469, doi:10.1021/acsami.6b12064.
55. Tsirka, K.; Karalis, G.; Paipetis, A.S. Raman Strain Sensing and Interfacial Stress Transfer of Hierarchical CNT-Coated Carbon Fibers. *J. Mater. Eng. Perform.* **2018**, *27*, 5095–5101, doi:10.1007/s11665-018-3532-2.
56. Liang, F.; Qian, H. Synthesis of tellurium nanowires and their transport property. *Mater. Chem. Phys.* **2009**, *113*, 523–526, doi:10.1016/j.matchemphys.2008.07.101.
57. Choi, J.; Lee, J.Y.; Lee, H.; Park, C.R.; Kim, H. Enhanced thermoelectric properties of the flexible tellurium nanowire film hybridized with single-walled carbon nanotube. *Synth. Met.* **2014**, *198*, 340–344, doi:10.1016/j.synthmet.2014.10.037.
58. Moriarty, G.P.; Wheeler, J.N.; Yu, C.; Grunlan, J.C. Increasing the thermoelectric power factor of polymer composites using a semiconducting stabilizer for carbon nanotubes. *Carbon N. Y.* **2012**, *50*, 885–895, doi:10.1016/j.carbon.2011.09.050.
59. Zaia, E.W.; Sahu, A.; Zhou, P.; Gordon, M.P.; Forster, J.D.; Aloni, S.; Liu, Y.S.; Guo, J.; Urban, J.J. Carrier Scattering at Alloy Nanointerfaces Enhances Power Factor in PEDOT:PSS Hybrid Thermoelectrics. *Nano Lett.* **2016**, *16*, 3352–3359, doi:10.1021/acs.nanolett.6b01009.
60. Marshall, G.J.; Mahony, C.P.; Rhodes, M.J.; Daniewicz, S.R.; Tsolas, N.; Thompson, S.M. Thermal Management of Vehicle Cabins, External Surfaces, and Onboard Electronics: An Overview. *Engineering* **2019**, *5*, 954–969, doi:10.1016/j.eng.2019.02.009.
61. Khaled, M.; Harambat, F.; Peerhossaini, H. Underhood thermal management: Temperature and heat flux measurements and physical analysis. *Appl. Therm. Eng.* **2010**, *30*, 590–598, doi:10.1016/j.applthermaleng.2009.11.003.
62. Inayat, S.B.; Rader, K.R.; Hussain, M.M. Thermoelectricity from Window Glasses. **2012**, *2(1)*, srep00841, doi:10.1038/srep00841.
63. Lu, Z.; Zhang, H.; Mao, C.; Li, C.M. Silk fabric-based wearable thermoelectric generator for energy harvesting from the human body. *Appl. Energy* **2016**, *164*, 57–63, doi:10.1016/j.apenergy.2015.11.038.

5.2 Carbon fiber / epoxy composite laminates as through-thickness thermoelectric generators

Abstract

This research study demonstrates a carbon fiber reinforced polymer (CFRP) composite laminate with an embedded thermoelectric (TE) enabled glass fiber (GF) ply. The TE-enabled GF functional ply was purposely laminated to create a structural through-thickness thermoelectric generator (TEG). Simultaneously, the highly conductive carbon fiber (CF) reinforcing phase served as electrodes for the device. Tellurium nanowires (NWs) were incorporated in various mass ratios in a PEDOT:PSS matrix to produce different TE pastes. The TE pastes were deposited on the GF fabrics via a facile blade coating technique. The highest power factor (57.2 μW/m·K^2, in-plane Seebeck coefficient +189 μV/K) was exhibited by the coating formed by the paste with a specific mass ratio of 1:1 (Te NWs to PEDOT:PSS). The TE-enabled GF plies were employed for the manufacturing of both 10-ply unidirectional (UD), and cross-ply composite laminates. The UD laminate generated a TE voltage (V_{TEG}) of 8.4 mV and a TE current (I_{sc}) of 597.4 μA for 100 K through-thickness temperature difference (ΔT) *i.e.*, a maximum power of 1.3 μW. The temperature sensing capability of the TEG-laminate was also demonstrated. 3-point bending tests indicated a ca. 10 % decrease in flexural properties with the integration of the TEG functionality for the UD configuration.

Keywords: Seebeck effect; Large-scale thermal energy harvesting; Carbon fiber reinforced polymer composites; Functional coatings; Multifunctional composite laminates; Through-thickness; Thermoelectric generator; Temperature sensor

Highlights:

- TE-enabled GF functional ply with 57.2 μW/m · K^2
- through-thickness TEG-CFRP laminate device with 1.3 μW power output
- through-thickness TEG-CFRP laminate device with 0.1 W/m^2 power density
- multifunctional CFRP laminate with fast response temperature sensing capabilities

Graphical Abstract

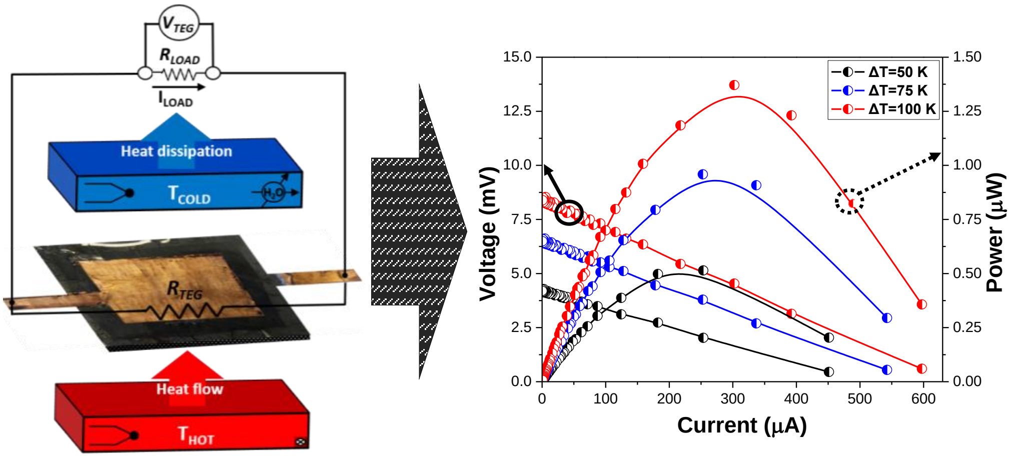

5.2.1 Introduction

Globally, research and development have been focused on alternative and sustainable energy sources which can respond to the enormous energy demands caused by vast human activity. Meanwhile, supplementary green solutions for energy generation could further reduce greenhouse gases and contribute towards the climate neutrality policy milestone by 2050 [1]. Energy harvesting concepts can utilize unlimited and diverse renewable energy sources from the natural environment, converting them directly to exploitable electrical power [2]. Some indicative approaches towards this auspicious direction are the broad implementation of self-powered energy harvesting applications based on, *e.g.* solar radiation, vibrations, thermal energy, *etc.* [3].

Recovery of the wasted heat from the transportation sector and industrial processes is one possible way of permitting the transformation from a fossil fuel-based era to a low-carbon society [4]. Thermoelectric (TE) energy conversion is based on the Seebeck effect, which provides the principles for converting thermal gradients (ΔT) directly into electrical voltage (ΔV), corresponding to electric power generation and thus avoiding combustion and emissions [5]. The magnitude of the Seebeck effect is expressed by the Seebeck coefficient (S), referred to as $\mathrm{S} = \Delta V/\Delta T$ and is related to the material's internal density of states resulting in positive (p-type) or negative (n-type) values, depending on the electronic behavior of the semi-conductor material [6,7]. The Seebeck coefficient is employed to estimate the power factor-$PF = \sigma \cdot \mathrm{S}^2$ (PF), which is equal to the product of the electrical conductivity (σ) and the Seebeck coefficient squared. This quantity is beneficial for the direct comparison of various materials' TE efficiency. The overall TE performance is classified by the dimensionless figure of merit-$ZT = (\sigma \cdot \mathrm{S}^2) \cdot \mathrm{T}/\kappa$ (ZT), where T is the absolute temperature and κ the thermal conductivity. Consequently, the combination of high electrical conductivity and

Seebeck coefficient, coupled with low thermal conductivity, leads to an optimum thermoelectric efficiency [8].

Low-bandgap semiconductors, *e.g.* Te, Bi_2Te_3, Sb_2Te_3, Bi_2S_3, *etc*., and their alloys, are classified as well-established TE inorganic materials [9–11]. Nanocomposite organic-inorganic hybrids perspective is highly recommended by the research community. The organic part offers the necessary electrical conductivity enhancement and flexibility in this approach, thus enriching the range of potential efficient TE coatings utilization [12]. Additionally, the combination of the nanostructured inorganic part offers a crystalline structure with grain boundaries, allowing the simultaneous sustainment of the high Seebeck coefficient and the further decrease of the thermal conductivity due to the increase of scattering centers of phonons by shortening of the phononic mean free path [13,14]. As a result of the aforementioned synergistic effects, the thermal conductivity of low-dimensional materials can become significantly lower than that of their bulk counterparts without negatively affecting the electrical conductivity nor the Seebeck coefficient [15,16].

Thermoelectric generators (TEGs) can harvest the ambient low-grade thermal energy losses to provide practical, fully energy-autonomous solutions for a wide application range, which require a power supply from micro Watts up to several hundreds of Watts scale [2,17]. Typical TEG devices consist of single-type or p- / n-type multiple thermoelements interconnected electrically in series and thermally in parallel. Research has been focused on improving the TE performance at the material level, since the conversion efficiency of the present TEG devices is 3-5 % requiring large applied thermal gradients [18]. Various TEG designs have been reported operating upon a wide range of available ΔT between a heat source and a heat sink, resulting in the creation of an electric current due to the diffusion of electrons and holes with a direction from the hot side to the cold one [19–22].

Progress in research of TEG modules / devices also includes more complex flexible [23,24] and wearable [25,26] architectures based on highly efficient durable TE nanocomposite films. Moreover, a variety of scientific publications refer to improvements in TE efficiency of bulk nanocomposites [27,28], as well as structural fiber reinforced polymer (FRP) composites [29,30].

FRP composites are categorized as advanced construction materials widely used in aerospace, automotive, renewable energy, *etc*.. In the recent decade, nanotechnology improvements and incorporation of nanomaterials consist critical factors for further development in the field of advanced structural composites. FRPs offer the potential for flexible design and novel manufacturing approaches with significantly improved specific properties, *i.e.* enhanced fracture toughness, interfacial adhesion, electrical and thermal properties [31–34]. Furthermore, a diversity of added functionalities may be included in FRPs presenting a multifunctional structural character. Representative previous studies exhibited advanced multifunctional composites with smart structural self-monitoring assessment and damage self-sensing [35,36], self-healing potential [37], massless electrochemical energy storage [38,39], thermal energy management [40,41], piezoelectric and thermoelectric energy harvesting perspectives [42,43].

In particular, the improvement of bulk structural polymer composite's TE efficiency has concerned research groups. In a previous study, Chung and colleagues [44] achieved the tailoring of the TE behavior in various directions of a laminate by creating p- and n-type carbon fiber laminae interlaminar interface junctions with a Seebeck coefficient of +82 μV/K. Han *et al.* employed ball-milled TE microparticles and carbon black as interlaminar fillers within a carbon fiber reinforced polymer (CFRP) laminate interfaces and reported a Seebeck coefficient of +110 μV/K [45]. Another relevant study displayed a polymer matrix-carbon fiber interfaces modification with micro-scale inorganic fillers resulting in a Seebeck coefficient of +163 μV/K [46].

Apart from their exceptional specific properties such as high specific strength and stiffness, carbon fiber (CF) reinforcements are also attractive due to their excellent conductive properties. This has also encouraged their utilisation as current collectors or counter electrodes upon electrochemical devices fabrication, as is reported in various studies [47,48].

In this study, we demonstrate for the first time purposely designed structural unidirectional (UD) and cross-ply 10-ply CFRP composite laminates which operate as through-thickness TEGs, *i.e.*, the temperature difference ΔT is applied along the thickness of the laminate, typically resulting in high temperature gradients. As should be noted, the through-thickness configuration is of particular interest as it may be readily applied in applications such as cooling circuits, superheated steam ducts, thermal insulation elements *etc*.. However, it is not easy to achieve at system level using planar elements such as laminae. Herein, we employ an architecture lamination configuration from nano-enabled lamina to manufacture a functional TE-enabled structural laminate. To this end, a p-type TE paste with a specific mass ratio of 1:1 Te nanowires (NWs) to PEDOT:PSS was developed. Subsequently, a glass fiber (GF) fabric was coated with the TE paste via a simple blade-coating and drying process. The resulted durable TE coatings exhibited an in-plane Seebeck coefficient of +189 μV/K, which corresponded to a power factor of 57.2 $\mu W/m \cdot K^2$. Scanning Electron Microscopy (SEM) was employed to inspect the microstructural characteristics of the tellurium coated GFs (GF-TE paste). Electrical and spectroscopic measurements (XRD and Raman) were performed to evaluate the properties of the TE properties of the functional GF fabrics. Eventually, the TE-enabled

GF laminae were used for the manufacturing of TEG-CFRP composite laminates. The UD and the cross-ply laminates could generate 1.3 μW and 0.5 μW respectively. The employed configuration comprised of a single thermoelement operation through-thickness at a ΔT of 100 K. The highly conductive CF tows were exploited as electrodes of the structural TEG device. The temperature self-monitoring ability of the TE-enabled laminate was also evaluated as an additional function. Finally, the mechanical properties of the proposed through-thickness TEG-CFRP laminates were tested and compared to conventional CFRP laminates standard 3-point bending tests. An average reduction of ~10 % in bending strength and flexural modulus values was determined for the TE-enabled laminates.

5.2.2 Experimental section

5.2.2.1 Materials

Telluric acid ($Te(OH)_6$, 98 % purity), L-Ascorbic acid (reagent grade with 99 % purity), cetyltrimethylammonium bromide (CTAB, ≥98 % purity) and Dimethyl sulfoxide (DMSO, ≥ 99 %, 78.13 g/mol) organic solvent were purchased from Sigma Aldrich. Poly(3,4-ethylenedioxythiophene)-poly(styrenesulfonate) – PEDOT:PSS conductive polymer screen-printing ink (Orgacon™ EL-P5015 with 2.5-5.5 % wt. solid content) was provided by Agfa. RS pro silver (Ag) conductive adhesive epoxy-based paste was supplied from RS Components. All chemicals were analytical grade and utilized as received without any further purification. Distilled H_2O, hereafter denoted as DI water, was used throughout all synthetic, dilution and cleaning procedures.

Unidirectional stitched carbon fiber (CF) fabric (UD, 300 g/m^2) with 0.33 mm ply thickness and unidirectional stitched glass fiber (GF) fabric (UD, 320 g/m^2) with 0.26 mm ply thickness received from Braca and Fibermax, respectively. The commercial Araldite LY 5052 / Aradur 5052 epoxy resin and amine-based hardener system by Huntsman was employed as the composite matrix with resin to hardener weight ratio 100:38 % w/w. Curing was conducted under pressure of 3 MPa at room temperature (RT) for 24 h and the post-curing at 100 ^{o}C for 4 h, resulting in T_g of 131 ^{o}C according to the manufacturer's technical datasheet. Copper (Cu) foil with a total thickness of ~500 μm was employed to create the external metallic electrodes for the TEG.

5.2.2.2 Development of the nanoparticle-based TE paste

Figure 67 illustrates the development steps for producing the TE pastes with the different Te NWs to PEDOT:PSS mass ratios. The nanostructured TE powder was synthesized following a surfactant-assisted chemical reduction reaction based on a previously reported synthetic route [49]. In more detail, in a reaction 3-necked round flask, 4.93 g of L-Ascorbic acid as the reducing agent was dissolved in 200 mL of DI water, followed by the addition of 0.1 g CTAB as the stabilization and nucleation agent. After the homogenization of the solution, 0.277 g $Te(OH)_6$ Te precursor was added to the vigorously stirred mixture. Then, the mixture was raised to 90 °C for 20 h and afterwards left to cool down at room temperature. The cleaning process consisted of centrifugation at 9000 rpm for 1 h and removing any unreacted constituents by pouring off the CTAB rich supernatant. The final product was collected with vacuum-assisted filtration through a PVDF membrane filter (pore size 45 μm). Subsequently, efficient TE pastes were produced to be deposited onto GF substrates. A thick, concentrated paste (200 mg/mL) was formed by fully dispersing in DI water the Te NWs powder via vigorous stirring for 30 min and mild bath sonication for 1 h at room temperature. Afterwards, 5 % DMSO was added into the commercial PEDOT:PSS paste to further improve the electrical conductivity by swelling the PSS molecules [50]. Thereafter, the shear force mixing process was performed via a mechanical overhead stirrer IKA EUROSTAR 20 high-speed digital with R 1389 (PTFE-coated) 3-bladed propeller for 15 min in order to thoroughly homogenize the TE paste. 3 different TE pastes with specific mass ratios of Te NWs to PEDOT:PSS were developed. Namely, the 1 to 1.25 (TE paste 1:1.25), the 1 to 1 (TE paste 1:1) and the 1.25 to 1 (TE paste 1.25:1).

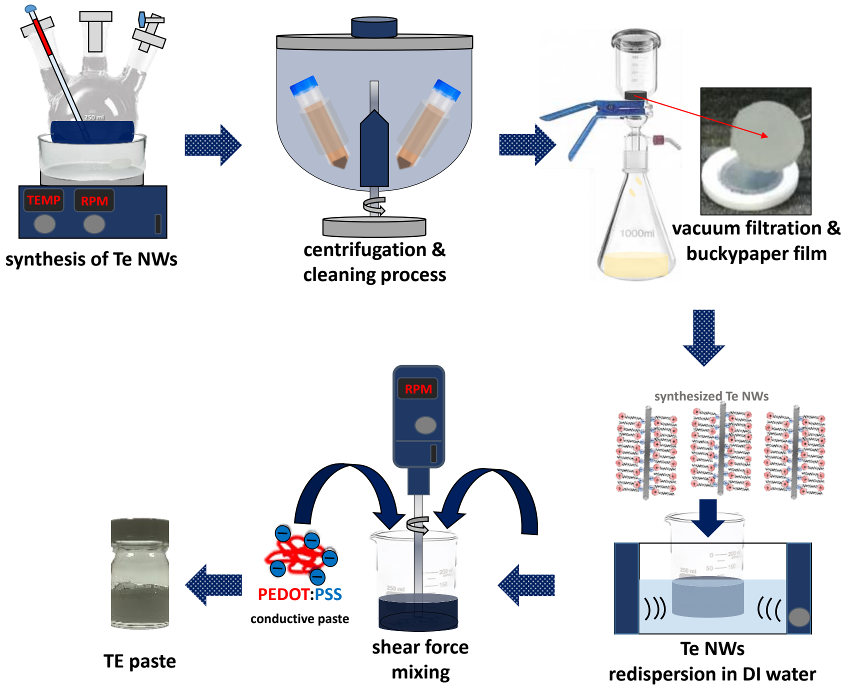

Figure 67. Illustration of the preparation steps for the development of the TE paste for coating applications. Particularly, a solvothermal reaction for the synthesis Te NWs powder was followed up by the cleaning process, resulting in a buckypaper film which was re-dispersed in DI water and then mixed with a PEDOT:PSS conductive paste in various mass ratios.

5.2.2.3 *Manufacturing of the through-thickness TEG-CFRP laminate*

In **Figure 68a,** the double-sided blade coating of the GF fibrous substrate with the TE paste (1:1) is schematically presented. The fibers were coated onto a hot plate at 120 °C and left for 30 min for the solvent to evaporate entirely. The distance between the heated GF substrate and the blade was fixed at 500 μm to deposit via a moving blade a proper quantity of TE paste to create a thick, continuous and homogeneous TE film from each side. The resulting 50×50 mm^2 TE-enabled GF fabric is shown in **Figure 68b**.

Figure 68c depicts the 10-ply CFRP laminate architecture designed to operate as a single-thermoelement through-thickness TEG device based on the properly integrated TE-enabled functional GF lamina. The dimensions of the manufactured through-thickness TEG-CFRP laminates where 50×50 mm^2 delimited by the coated TE-enabled GF ply required single thermoelement active area. Vitally important during the fabrication procedure is to avoid any possible short-cut between the highly electrically and thermally conductive bottom 8-ply CFRP internal electrode and the top single CF lamina internal electrode, where the TE-enabled ply is inserted. For this purpose, the strict alignment of all CF plies is necessary to create a functional, structural TEG device. All CFRP laminates were manufactured by hand lay-up, epoxy resin impregnation and thermopressing in UD and cross-ply laminations. Afterwards, slight sanding was performed to remove a thin dielectric epoxy resin layer of the top and bottom CFRP's surface in order to stabilize with conductive epoxy-based silver paste the external copper foil-based ohmic contacts, as shown in **Figure 68d**. Both the silver paste and the copper foil assist the acquisition of appropriate thermal contacts.

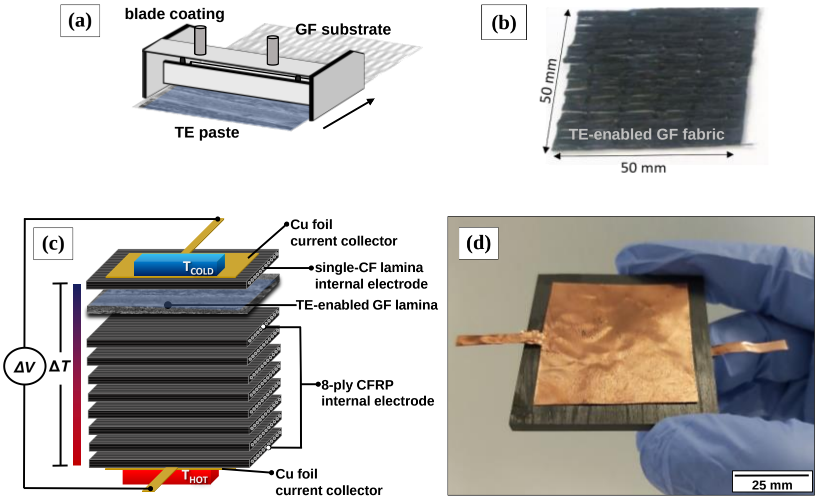

Figure 68. (a) schematic depiction of the blade coating process for the TE paste (1:1) double-sided deposition onto the GF fabric, **(b)** digital photo of the produced TE-enabled GF functional ply, **(c)** schematic illustration of the detailed lamination of the multifunctional CFRP and **(d)** digital photo of the manufactured 10-ply through-thickness TEG-CFRP laminate.

5.2.2.4 Characterization techniques

The morphology of the coated GF fabrics with the different TE pastes was investigated by field emission scanning electron microscopy (FESEM) utilizing a FEI NanoSem 200 (Netherlands) at an operational voltage of 5 KV.

4-probe sheet resistance measurements were conducted to determine the electrical resistivity values of the double-side blade-coated GF fabrics with the three different mass ratio TE pastes. A commercial measuring unit by Ossila Ltd (UK) was employed to calculate the electrical conductivity based on the following formula: $\sigma = 1/R_s \cdot L/A \cdot (\ln 2/\pi)$, where R_s is the measured 4-probe sheet resistance, L is the length and A is the cross-section of each sample. The fabricated coated films onto the fibrous substrates were typically 30-40 μm in thickness. This mean value was extracted from 10 measurements per sample with a digital caliper with a resolution down to 0.01 mm.

The corresponding Seebeck voltages were determined using a custom-made system. One side of the TE-enabled GF fabrics was placed onto a controlled heating aluminum block, and the other side to a heat sink kept at room temperature with water circulation. The temperature of the 2 blocks was constantly measured individually with K-type thermocouples to verify the achievement and stability of the thermal gradient. The temperature gradient across both sides of the specimens was varied, and the Seebeck coefficient was accurately calculated from the slope of the data curve in the plot of temperature difference versus output voltage. The in-plane generated TE voltage was measured across the silver paste deposited electrodes by Agilent 34401A6½ (USA) digital multimeter with a standard 2-probe method.

X-Ray diffractometry for the synthesized Te NWs buckypaper film was performed with the Bruker D8 ADVANCE (USA) in symmetric step-scan with a step $2\theta = 5°$ in transmission mode. The diffractometer operated at 40 KV and 30 mA with Kα radiation ($\lambda = 1.5406$ Å), diffraction angle (θ, $10° < 2\theta < 80°$) and a step size of 5°.

A Labram HR-Horiba (Japan) scientific micro-Raman system was used to identify the existing phases for the TE materials and the coated GF. The 514.5 nm line of an Ar^+ ion laser operating at a laser power of 1.0 mW at the focal plane and an optical microscope equipped with a 100× objective served to deliver the excitation light and collect the back-scattering Raman activity. All spectra were collected in the 90-2000 cm^{-1} range and were normalized to the highest intensity peak in each spectrum.

The TE output characteristics of the through-thickness TEG-CFRP laminates were measured using a variation of the abovementioned custom-made set-up. The laminate was placed between the hot and the cold metal block, which enabled the generation of the desired thermal gradients. For all measurements, the cold block was kept at room temperature (∼25 °C) via mild water circulation, while the hot block was heated at 75 °C, 100 °C and 125 °C via calibrated temperature-controlled resistors. The through-thickness TEG-CFRP device power output characteristics have been assessed using a custom-made fully automated system based on a LabVIEW-PC interface with a range of applied external load resistances from 1 Ohm to 10000 Ohm with discretion step down to 1 Ohm. All tests were performed at ambient conditions (1 atm and relative humidity: 40 ± 5 % RH).

3-point bending quasi-static tests according to ASTM D 790-03 standard were conducted using a 100 KN Universal Testing Machine by Jinan Testing Equipment IE Corporation (China). A loading speed of 1 mm/min was selected for testing the $58.8\times10.5\times\sim3.3$ mm^3 specimens. 6 specimens were tested for each of the through-thickness UD, the cross-ply TEG-CFRP laminates and the respective reference CFRP laminates. To minimize any plausible humidity absorbed by the specimens, they were conditioned overnight before testing by drying in an oven at 40 ^{o}C.

5.2.3 Results and Discussion

5.2.3.1 SEM investigations for the nanoparticle-based TE pastes coated onto GF fabric

Blade coating is a suitable printing technique to form relatively thick TE films onto fibrous substrates due to the capillary phenomena. At the same time, GFs are efficient as supporting scaffolds, so as to pertain structural stability to the functional TE films [30].

Figure 69 illustrates SEM images of the coated GF fabrics with the 3 TE pastes differentiated by the Te NWs mass into the PEDOT:PSS conductive polymer matrix. The morphological inspection discloses homogenous nanostructured features onto the microscale GF reinforcing phase. The satisfying adhesion properties between the thick films of the TE pastes and the fibrous substrate is elucidated by the continuously distributed nanostructures onto the GFs for all cases. As expected, the highest magnification image in **Figure 69c** reveals a comparatively to **Figure 69a-b** denser network of high aspect ratio typical 1D nanostructures with a diameter of a few nm [49], which resulted to the superior bulk TE properties of the 1.25:1 TE paste formulation. Additionally, the reinforcing GFs are buried within the TE films performing as a thermal blocker, resulting in an overall reduced thermal conductivity of the pillared-like structures. Moreover, the created continuous through-thickness films cover the areas between the stitched GF tows. Therefore, multiple bridging of interconnected TE paths is being introduced.

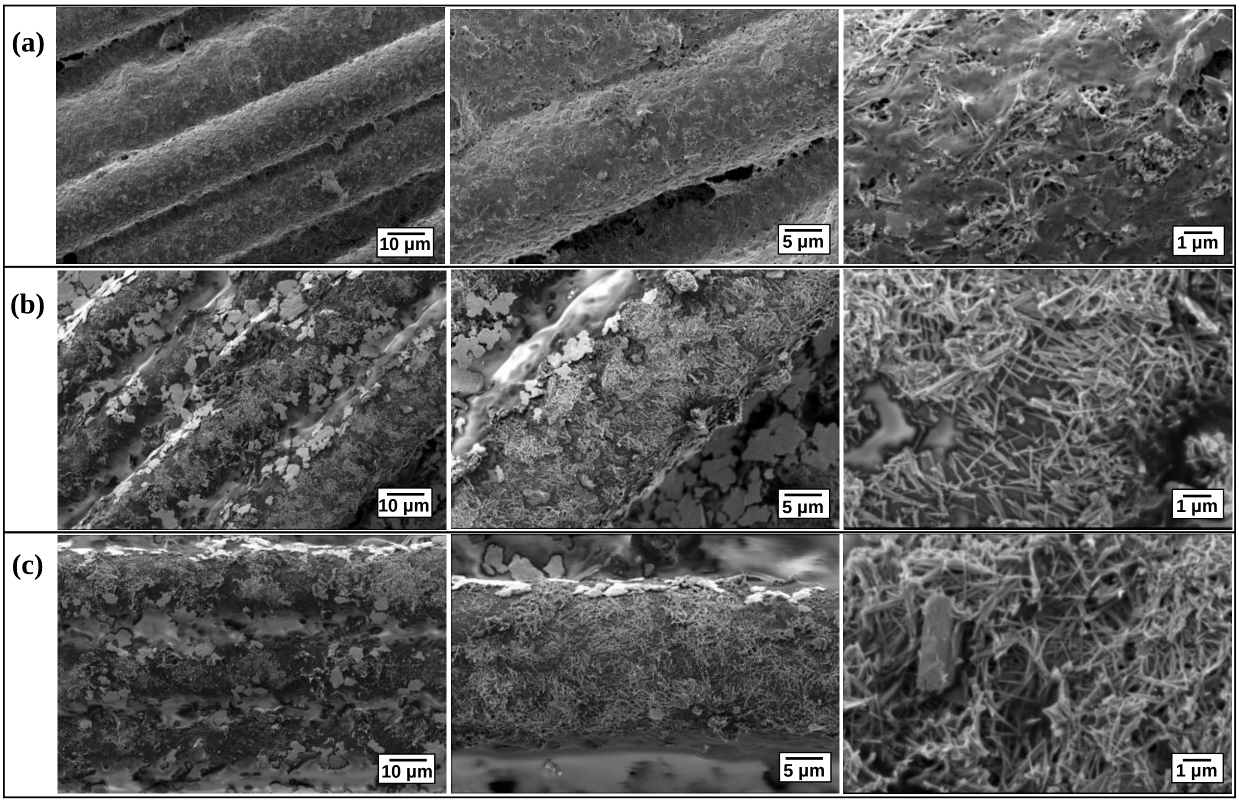

Figure 69. FESEM micrograph images at different magnifications for the double-sided blade-coated **(a)** GF fabric with TE paste (1:1.25), **(b)** GF fabric with TE paste (1:1) and **(c)** GF fabric with TE paste (1.25:1).

5.2.3.2 TE performance of the nanoparticle-based pastes coated onto GF fabric

4-probe sheet resistance measurements (**Figure 70a**) and the respective in-plane Seebeck voltage (**Figure 70b**) measurements were conducted to determine the electrical conductivity and the Seebeck coefficient values of the double-side blade-coated GF fabrics (25 mm×20 mm^2 specimens) with the 3 different mass ratio TE pastes. The mean output values were derived from TE measurements of 5 specimens for each TE paste.

Figure 70c summarizes the TE properties of the GF fabrics coated with the different mass ratio TE pastes (1:1.25, 1:1 and 1.25:1). Namely, the coated GF-TE paste (1:1) presented 1600 ± 2.42 S/m electrical conductivity at RT with +189 ± 4.2 μV/K Seebeck coefficient, corresponding to the maximum power factor of 57.2 μW/m·K^2 in comparison with 50.5 μW/m·K^2 for GF-TE paste (1:1.25) and 14.4 μW/m·K^2 for the 1.25:1. The positive values of the Seebeck coefficient indicate the p-type semiconducting character of the TE pastes measured at ΔT of 100 K.

It should be highlighted that the increase in nanoparticle (NP) content into the paste corresponds to a decrease of the electrical conductivity, while the Seebeck coefficient increases. The mentioned tradeoff relationship commonly appears in semiconductor TE materials upon tuning the doping concentration. Thus, a possible decrease in carrier concentration results in a decrease in the electrical conductivity and an increase of the Seebeck coefficient [9,49].

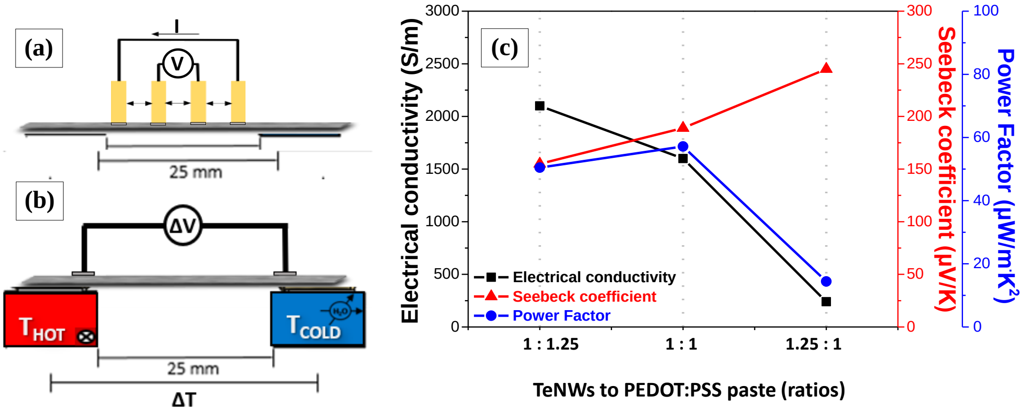

Figure 70. Schematic depiction of the in-plane **(a)** electrical, **(b)** TE measurements and **(c)** the respective values of the GF fabrics coated with TE pastes for different mass ratios.

The thermal conductivity value, ~0.2 W/m · K, of similar materials was utilized, as reported in the literature [16], to calculate the *ZT* values. *ZT* values equal to 0.11, 0.1 and 0.02 were calculated for the coated GFs with the TE paste (1:1), (1:1.25) and (1.25:1), respectively. The thermal to electrical energy conversion efficiency (η) is limited by the Carnot heat engine cycle efficiency. η was determined by the following equation [17]: $\eta = (T_H-T_C)/T_H \cdot \sqrt{(1+ZT)}-1/\sqrt{1+ZT}+(T_C/T_H)$, where T_H represents the temperature of the hot side and T_C is a steady temperature of a cold side. The calculated energy conversion efficiencies of the coated GF-TE paste (1:1), the GF-TE paste (1:1.25) and the GF-TE paste (1.25:1) at a ΔT of 100 K were 0.77 %, 0.68 % and 0.2 %, respectively. Consequently, the coated GF-TE paste (1:1) was selected as the TE-enabled functional GF fabric for further experiments, exhibiting the best TE values.

5.2.3.3 Spectroscopic analysis of the TE paste (1:1) onto GF fabric

The Te NWs have been characterized by XRD after their synthesis, as shown in **Figure 71a**. All the peaks seen in the XRD spectra could be indexed to the reference spectrum (No. 36-1452). Therefore, the synthesized Te NWs have a crystalline hexagonal structure with 3 atoms per unit cell and cell constants *a* and *c* equal to 4.46 Å and 5.92 Å, respectively. The XRD patterns recorded here agree with the reported literature for Te NWs [51].

The selected TE paste (1:1) was evaluated by Raman spectroscopy along with its constituent materials, namely Te NWs and PEDOT:PSS as presented in **Figure 71b**. Then, the paste was applied onto a GF, and the coated fabric was also assessed. The main vibrational modes of the TE paste (1:1) (blue plot) were identified as a double peak centered at 117 and 137 cm^{-1} that can be attributed to the A_1 and the E_2 vibrational modes of Te NWs [52]. These peaks were also present at the Te NWs spectrum (black plot) at 118, and 139 cm^{-1}, as well as in the TE coated glass fabric at 119 and 139 cm^{-1} (red plot). A minor intensity vibrational mode was found at 261 cm^{-1} in the TE paste (1:1) (blue plot) and the TE coated GF (red plot), which is a second-order vibration of Te NWs [51]. This band was found at 271 cm^{-1} at the spectrum of the Te NWs (black plot).

Another medium-intensity double peak was encountered between 1220 and 1680 cm^{-1} at the TE paste (1:1) spectrum (blue plot) and between 1050 and 1690 cm^{-1} at the TE coated GF (red plot). Furthermore, as expected, it was not present at the spectrum of the as-synthesized Te NWs (black plot). This complex double shoulder is very broad and can be assigned to the asymmetric C=C stretching vibrations, the C−C stretching and the symmetric (C=C)−O stretching of PEDOT. On the contrary, the contribution of PSS, being very weak, could not be observed in the spectra of the TE paste and the TE coated GF fabric (red plot) [53].

The spectrum of PEDOT:PSS presented several vibrational modes of very low intensity. The peak centered at 437 cm^{-1} can be attributed to the SO_2 bending, the bands at 578, 853, and 988 cm^{-1} are due to oxyethylene ring deformation, the band at 704 cm^{-1} is caused by symmetric C-S-C deformation, the band at 1128 cm^{-1} can be attributed to the C-O-C deformation, the peaks at 1259 and 1370 cm^{-1} can be assigned to C-C stretching, the band at 1431 cm^{-1} is due to C=C(-O) stretching, while the vibrational modes centered at 1496, 1541 and 1569 cm^{-1} are assigned to asymmetric C=C stretching [53]. However, these peaks did not seem to substantially contribute to the spectra of TE paste (1:1) (blue plot) and the TE coated GF fabric (red plot) as in the raw form, their intensities are too much lower in comparison to the rest of the peaks.

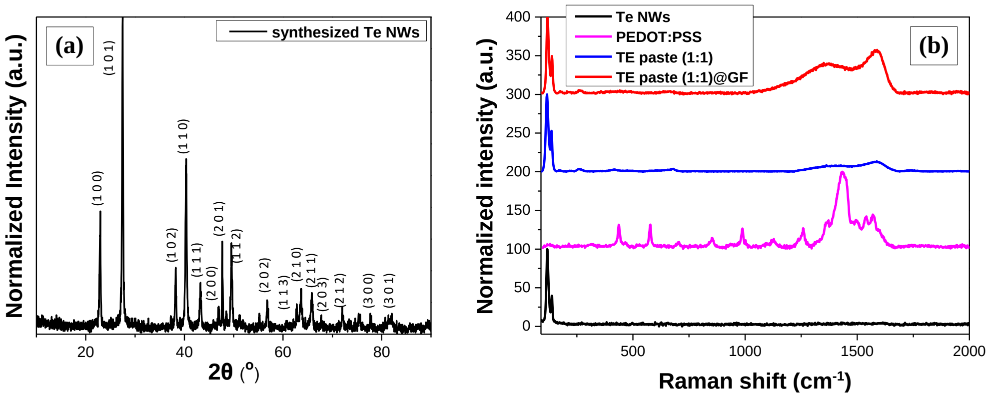

Figure 71. (a) XRD pattern of the synthesized Te NWs backypaper film and **(b)** normalized Raman spectra of the constituent TE materials as well as the coated GF with TE paste (1:1).

5.2.3.4 Power output characteristics of the through-thickness TEG-CFRP laminates

Figure 72a depicts the equivalent circuit of the through-thickness measurements configuration for the proposed structural TEG device. In contrast to conventional structural composites, a through-thickness TEG-CFRP multifunctional composite can effectively exploit the graphitized continuous CFs and contribute to the electrical and thermal properties of the laminate. Beyond their high electrical and thermal conductivity in both through-thickness and in-plane direction, they generally present relatively poor Seebeck coefficient values [44].

Figure 72b shows the comparison graph of the through-thickness electrical and TE response for the reference 10-ply UD and cross-ply CFRP laminates at a ΔT of 100 K. Indicatively, both reference CFRP composites exhibited a through-thickness electrical resistance in the range of 5–30 Ohm, while the through-thickness Seebeck TE voltage was as low as 0.3 to 0.4 mV at a through-thickness temperature gradient of 100 K. Similar findings have been pointed out by Chung and co-workers with a ~0.3 mV voltage from a cross-ply CFRP laminate at various curing pressures [45].

On the other hand, the 10-ply UD and cross-ply TEG-CFRP laminates exhibited TE voltages (V_{TEG}) of 8.4 ± 0.35 mV and 7.9 ± 0.48 mV with generated short-circuit current (I_{sc}) of 597.4 ± 22.4 μA and 220.2 ± 25.1 μA at a ΔT of 100 K, respectively. The TE output values result from independent measurements of 5 manufactured laminates for each category. The calculated maximum TE power output for the multifunctional UD TEG-CFRP laminate is ~1.3 μW and for the cross-ply TEG-CFRP laminate is ~0.5 μW according to the following equation [22]: $P_{max} = \Delta V^2/4 \cdot R_{TEG}$ at a ΔT of 100 K. The derived power density equals 0.1 W/m^2 and 0.05 W/m^2 for each case, respectively.

At this point, it is worth mentioning that the through-thickness internal electrical resistance (R_{TEG}) prior to the epoxy resin encapsulation was as low as 6.7 ± 0.4 Ohm for the UD lamination and 27.2 ± 0.7 Ohm for the cross-ply lamination measured at RT. After resin impregnation and thermal curing, the R_{TEG} values at RT were almost identical for both composite laminates, implying a chemically stable and non-reactive TE-enabled GF functional ply. Therefore, the overall improved TE power output of the 10-ply UD CFRP laminates depends strongly on the lamination sequence and the decreased R_{TEG} values, which are reflected in the improved TE efficiency at the composite level.

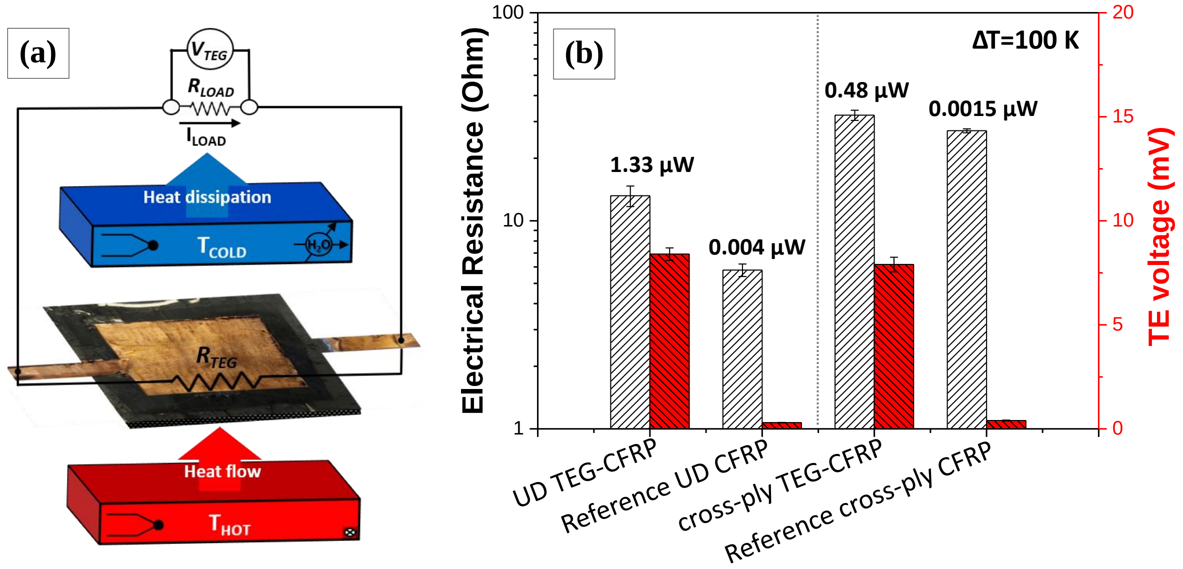

Figure 72. (a) Through-thickness measurement configuration and TEG equivalent circuit, **(b)** Electrical and TE response for the UD, and the cross-ply TEG laminates at 100 K Δ*T*.

The manufactured through-thickness TEG-CFRP laminates appear to be capable of thermal energy harvesting upon exposure to through-thickness temperature gradients under enforced cooling to sustain the by design desired Δ*T*, as shown in **Figure 73a**. Otherwise, the resulted power output appears to be inadequate. However, due to the TE response of the coated GF-TE paste (1:1), when the manufactured TEG-CFRP is exposed to a temperature difference between the bottom and the top side of the laminate in the through-thickness direction, a significant TE power is generated on account of Seebeck effect.

Figure 73b-c depicts the specific power output characteristics for the 10-ply UD CFRP laminates, and **Figure 73d-e** presents graphs for the respective 10-ply cross-ply CFRP laminates at various Δ*T*. Specifically, the plots show the output voltage-current (*V*-*I*), the output power-current (*P*-*I*), the output *V*-R_{LOAD} and the output *P*-R_{LOAD} curves with the application of different external load resistances (R_{LOAD}). The dots represent the experimentally measured values, while the continuous lines have been calculated by the following equation [49]: $P = I^2 \cdot R_{LOAD} = (V_{TEG}/(R_{TEG}+R_{LOAD})^2 \cdot R_{LOAD})$. For both 10-ply TEG-CFRPs, when the R_{LOAD} is equal to the experimental value of the R_{TEG}, the maximum TE power generation is being observed. As expected, the TE voltage output for the various applied R_{LOAD} was inversely proportional to the output current, resulting in the representative parabolic behavior.

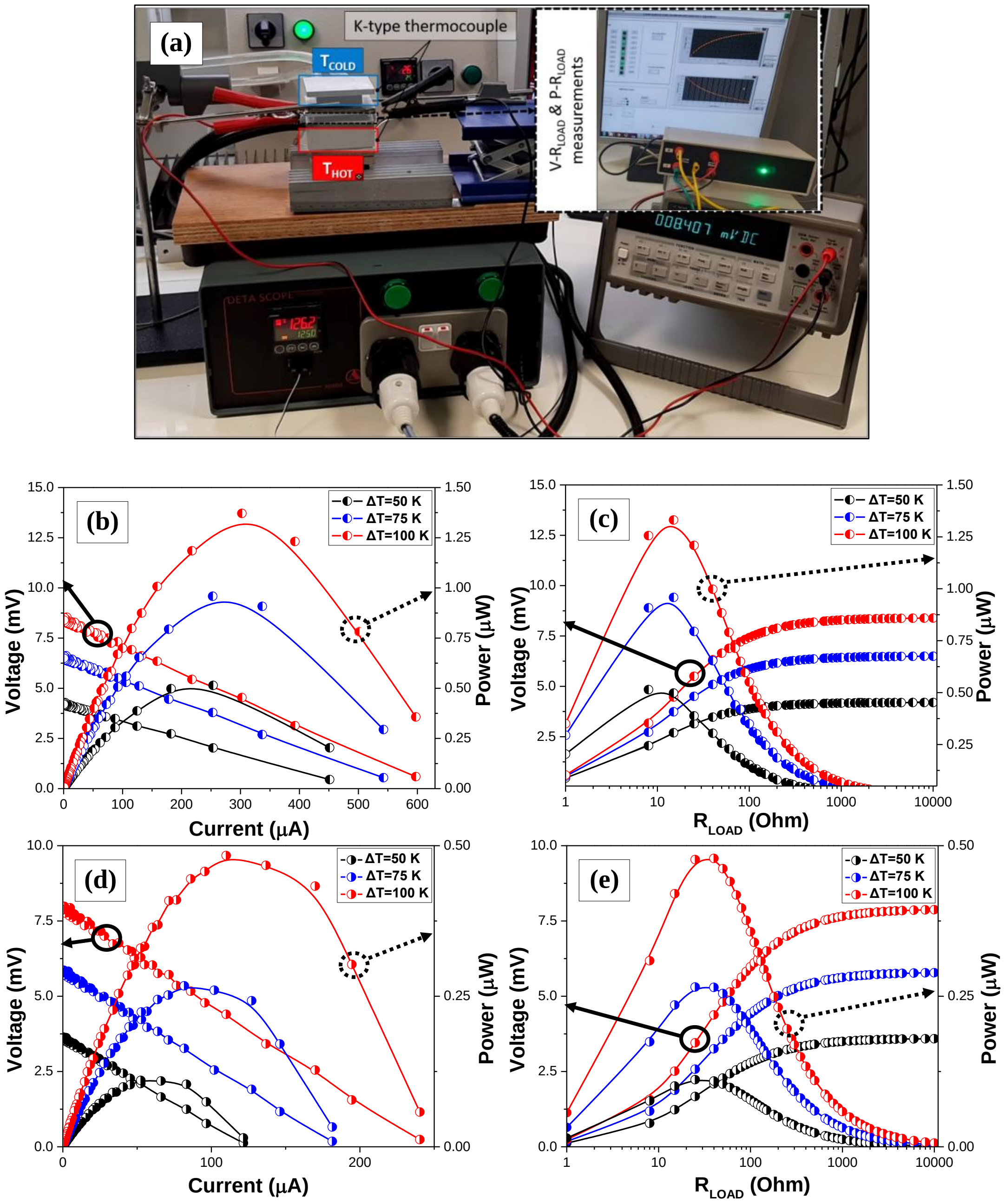

Figure 73. (a) Demonstration of the through-thickness TEG CFRP upon exposure to Δ*T* = 100 K, **(b, c)** power output characteristics for the UD TEG-CFRP and **(d, e)** power output characteristics for the cross-ply TEG-CFRP at Δ*T* of 50, 75 and 100 K.

A 55.5 % and a 58.2 % decrease in the through-thickness TE voltage values for the UD laminate (8.4 ± 0.35 mV) and the cross-ply laminate (7.9 ± 0.48 mV), respectively, were observed compared to the in-plane TE voltage (18.9 ± 0.22 mV) of the coated TE-enabled GF fabric. All measurements were performed at 100 K Δ*T*, but the interelectrode distance was extremely compact for the through-thickness ~0.3 mm (coated TE-enabled GF ply) compared to the 25 mm for the in-plane TE of the coated TE-enabled GF fabric *e.g.* [43].

Based on the above, it is evident that the manufactured multifunctional laminates possess the potential for thermal energy harvesting for various practical applications. The resulted values correspond to a single thermoelement structural TEG-laminate devices. As should be noted, the device efficiency can further improve using multiple in-series or in-parallel interconnected thermoelements in order to optimize the total TE power output in relation to the employed TE-enabled active area [25].

Further functionalities may also be imparted to the composite via the integration of the functional lamina. To this end, the temperature sensing abilities were also evaluated for the UD TEG-laminate (**Figure 74**). Typical temperature sensors are based on thermocouples or resistance elements [44,54]. **Figure 74a** presents the TE voltage as a function of time, which was attained at ca. 252 s to an applied temperature of 125 ^{o}C, upon exposure of the UD TEG-laminate to the respective ΔT. Similar dependency of temperature input to voltage response has been reported also in previous studies *e.g.* [54] related to self-powered temperature sensors concepts based on TEG devices.

Figure 74b demonstrates the TE voltage sensitivity of the through-thickness TEG-CFRP device exposed to an applied temperature of 125 ^{o}C during repeatedly heating-cooling cycles, revealing precisely the functioning, performance and response of the device as a temperature sensor. The laminate was repeatedly positioned on the 100 K temperature difference stage until it reached the hot stage temperature and then removed for 155 s. As can be seen, the TE voltage resulted in a 29.3 % decay every 155 s upon cooling by removing the laminate from the 100 K temperature difference stage. Reversible and almost identical TE voltage values fluctuation upon reposition and removal were measured for all the recorded heating-cooling cycles.

Figure 74c presents the generated TE voltage stability vs. time measurements at different applied temperatures of 75, 100 and 125 ^{o}C for a 10-ply UD through-thickness TEG-laminate. For each temperature difference, the TE power output was monitored for a total duration of 600 s. Remarkably steady TE voltage values have been observed, with corresponding power generation.

Summarizing, the integration of the TE-enabled functional lamina in the structural composite can additionally pertain the self-powered temperature sensing functionality without the need for embedded or externally adhered measuring sensors.

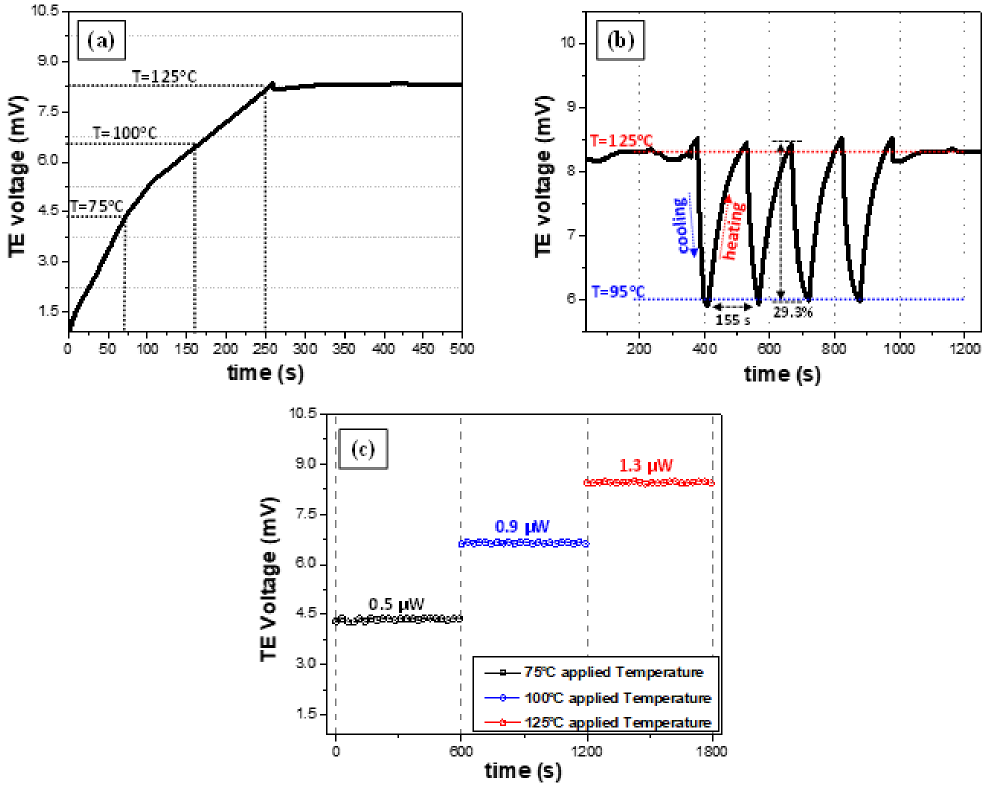

Figure 74. (a) TE response and **(b)** TE voltage variation of the CFRP-based thermocouple voltage exposed to an applied temperature of 125 °C during heating-cooling cycles, **(c)** TE power generation during time evolution upon different applied temperatures for the 10-ply UD CFRP laminates.

5.2.3.5 Evaluation of the through-thickness TEG-CFRP laminates mechanical performance

Figure 75 presents bar charts with the respective strength and modulus values (**Figure 75a**) and the corresponding optical microscopy images of the 3-point bending failed specimens (**Figure 75b-c**). More specifically, for the UD laminates, a bending strength of 1101.9 ± 23.2 MPa and a bending modulus of 46.7 ± 6.8 GPa for the TEG-laminate was measured. The values for the respective reference plain UD CFRP laminate were 1212.1 ± 21.4 MPa and 51.4 ± 6.1 GPa.

Concluding, the multifunctional laminate exhibited a deterioration in mechanical properties of 10 % in bending strength and 10.1 % in bending modulus compared to the reference CFRP laminate specimens. Although this property reduction is not negligible, it should be noted that the present work is focusing on demonstrating the functionalities and not in optimizing the mechanical performance.

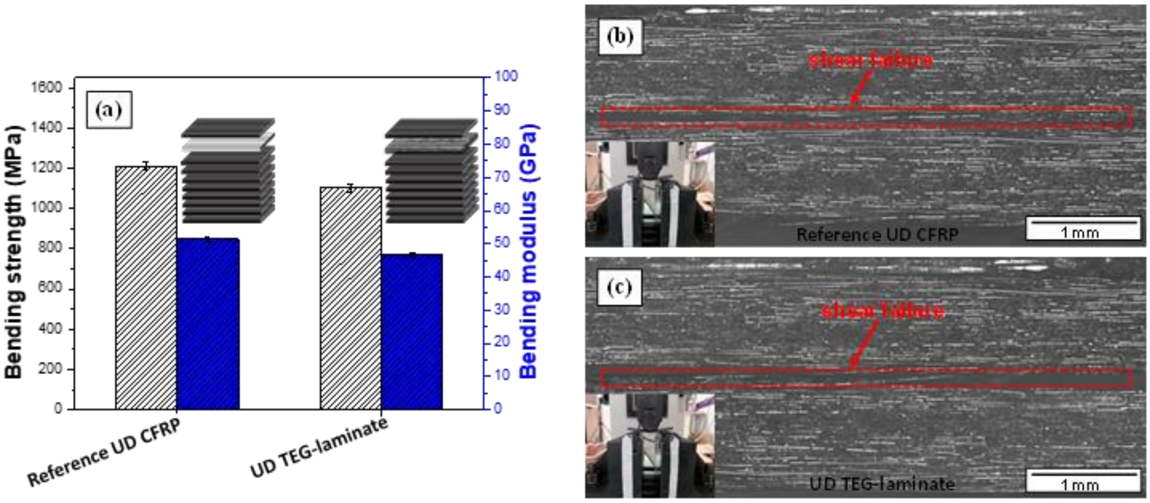

Figure 75. 3-point bending tests: UD reference CFRP *vs*. UD through-thickness TEG-laminate **(a)** bending strength and bending modulus, **(b, c)** indicative optical microscopy images of the respective failed specimens.

5.2.4 Conclusions

In this work we successfully manufactured CFRP composite laminates with through-thickness thermal energy harvesting capabilities, without considerable effect on the structural integrity of the laminate. The approach used in this work involved the design, manufacturing and testing of a functional TE-enabled GF system ply which was purposely laminated within a CFRP composite to create a structural through-thickness TEG architecture. The highly conductive CF reinforcing laminae were employed as structural electrodes for the device. In relation to the TE response, the UD lamination was found to be more efficient generating a maximum electrical power output of 1.3 μW at 100 K through-thickness temperature difference. Additionally, the UD TEG-laminate exhibited also temperature self-sensing capability with short response times.

Self-powered architectured composites allow for the realization of sustainable and self-sufficient smart structures. These are able to provide alternative energy as an electric power backup for battery-free low-power consuming electronic devices *e.g.*, wireless sensor nodes (WSNs) and Internet of Things (IoT) applications.

CFRPs with enhanced through-thickness thermoelectric power in the range of several μW are envisaged to harvest thermal energy at large-scale during their operational lifetime in the aerospace, automotive, aeronautics and renewable energy fields, where temperature gradients exist. Consequently, a route to self-powered recording of the exposure history of the component/ structure to thermal fields could be emerged, eliminating the need for external sensors as only the existing functional reinforcing phases perform also this task.

5.2.5 References

1. Zappa, W.; Junginger, M.; Broek, M. Van Den; Cover, C.L. Is a 100 % renewable European power system feasible by 2050 ? *Appl. Energy* **2019**, *233–234*, 1027–1050, doi:10.1016/j.apenergy.2018.08.109.
2. Wang, Z.L.; Wu, W. Nanotechnology-enabled energy harvesting for self-powered micro-/nanosystems. *Angew. Chemie - Int. Ed.* **2012**, *51*, 11700–11721, doi:10.1002/anie.201201656.
3. Xu, S.; Hansen, B.J.; Wang, Z.L. Piezoelectric-nanowire-enabled power source for driving wireless microelectronics. *Nat. Commun.* **2010**, *1*, 512–514, doi:10.1038/ncomms1098.
4. Martín-González, M.; Caballero-Calero, O.; Díaz-Chao, P. Nanoengineering thermoelectrics for 21st century: Energy harvesting and other trends in the field. *Renew. Sustain. Energy Rev.* **2013**, *24*, 288–305, doi:10.1016/j.rser.2013.03.008.
5. LeBlanc, S. Thermoelectric generators: Linking material properties and systems engineering for waste heat recovery applications. *Sustain. Mater. Technol.* **2014**, *1*, 26–35, doi:10.1016/j.susmat.2014.11.002.
6. Jin Bae, E.; Hun Kang, Y.; Jang, K.S.; Yun Cho, S. Enhancement of Thermoelectric Properties of PEDOT:PSS and Tellurium-PEDOT:PSS Hybrid Composites by Simple Chemical Treatment. *Sci. Rep.* **2016**, *6*, 1–10, doi:10.1038/srep18805.
7. Liu, J.; van der Zee, B.; Alessandri, R.; Sami, S.; Dong, J.; Nugraha, M.I.; Barker, A.J.; Rousseva, S.; Qiu, L.; Qiu, X.; et al. N-type organic thermoelectrics: demonstration of ZT > 0.3. *Nat. Commun.* **2020**, *11*, 1–9, doi:10.1038/s41467-020-19537-8.
8. See, K.C.; Feser, J.P.; Chen, C.E.; Majumdar, A.; Urban, J.J.; Segalman, R.A. Water-processable polymer-nanocrystal hybrids for thermoelectrics. *Nano Lett.* **2010**, *10*, 4664–4667, doi:10.1021/nl102880k.
9. Snyder, G.J.; Toberer, E.S. 1. Complex thermoelectric materials. *Nat Mater* **2008**, *7*, 105–114, doi:10.1038/nmat2090.
10. He, J.; Kanatzidis, M.G.; Dravid, V.P. High performance bulk thermoelectrics via a panoscopic approach. *Mater. Today* **2013**, *16*, 166–176, doi:10.1016/j.mattod.2013.05.004.
11. Zhang, B.Q.; Liu, Y.; Zuo, Y.; Chen, J.S.; Song, J.M.; Niu, H.L.; Mao, C.J. Colloidal synthesis and thermoelectric properties of cufese2 nanocrystals. *Nanomaterials* **2018**, *8*, doi:10.3390/nano8010008.
12. Jin, H.; Li, J.; Iocozzia, J.; Zeng, X.; Wei, P.C.; Yang, C.; Li, N.; Liu, Z.; He, J.H.; Zhu, T.; et al. Hybrid Organic–Inorganic Thermoelectric Materials and Devices. *Angew. Chemie - Int. Ed.* **2019**, *58*, 15206–15226, doi:10.1002/anie.201901106.
13. Russ, B.; Glaudell, A.; Urban, J.J.; Chabinyc, M.L.; Segalman, R.A. Organic thermoelectric materials for energy harvesting and temperature control. *Nat. Rev. Mater.* **2016**, *1*, doi:10.1038/natrevmats.2016.50.
14. Lu, Y.; Ding, Y.; Qiu, Y.; Cai, K.; Yao, Q.; Song, H.; Tong, L.; He, J.; Chen, L. Good Performance and Flexible PEDOT:PSS/Cu 2 Se Nanowire Thermoelectric Composite Films. *ACS Appl. Mater. Interfaces* **2019**, *11*, 12819–12829, doi:10.1021/acsami.9b01718.
15. Choi, J.; Lee, J.Y.; Lee, S.S.; Park, C.R.; Kim, H. High-Performance Thermoelectric Paper Based on Double Carrier-Filtering Processes at Nanowire Heterojunctions. *Adv. Energy Mater.* **2016**, *6*, 1–8, doi:10.1002/aenm.201502181.
16. Zaia, E.W.; Sahu, A.; Zhou, P.; Gordon, M.P.; Forster, J.D.; Aloni, S.; Liu, Y.S.; Guo, J.; Urban, J.J. Carrier Scattering at Alloy Nanointerfaces Enhances Power Factor in PEDOT:PSS Hybrid Thermoelectrics. *Nano Lett.* **2016**, *16*, 3352–3359, doi:10.1021/acs.nanolett.6b01009.
17. Mytafides, C.K.; Tzounis, L.; Karalis, G.; Formanek, P.; Paipetis, A.S. High-Power All-Carbon Fully Printed and Wearable SWCNT-Based Organic Thermoelectric Generator. *ACS Appl. Mater. Interfaces* **2021**, *13*, 11151–11165, doi:10.1021/acsami.1c00414.

18. Liu, L. Feasibility of large-scale power plants based on thermoelectric effects. *New J. Phys.* **2014**, *16*, doi:10.1088/1367-2630/16/12/123019.

19. Davoodabadi, M.; Vareli, I.; Liebscher, M.; Tzounis, L.; Sgarzi, M.; Paipetis, A.S.; Yang, J.; Cuniberti, G.; Mechtcherine, V. Thermoelectric energy harvesting from single-walled carbon nanotube alkali-activated nanocomposites produced from industrial waste materials. *Nanomaterials* **2021**, *11*, doi:10.3390/nano11051095.

20. Jung, K.K.; Jung, Y.; Choi, C.J.; Lee, J.M.; Ko, J.S. Flexible thermoelectric generator with polydimethyl siloxane in thermoelectric material and substrate. *Curr. Appl. Phys.* **2016**, *16*, 1442–1448, doi:10.1016/j.cap.2016.08.010.

21. Lu, Z.; Zhang, H.; Mao, C.; Li, C.M. Silk fabric-based wearable thermoelectric generator for energy harvesting from the human body. *Appl. Energy* **2016**, *164*, 57–63, doi:10.1016/j.apenergy.2015.11.038.

22. Karalis, G.; Tzounis, L.; Lambrou, E.; Gergidis, L.N. A carbon fiber thermoelectric generator integrated as a lamina within an 8- ply laminate epoxy composite : Efficient thermal energy harvesting by advanced structural materials. *Appl. Energy* **2019**, *253*, 113512, doi:10.1016/j.apenergy.2019.113512.

23. Suemori, K.; Hoshino, S.; Kamata, T.; Suemori, K.; Hoshino, S.; Kamata, T. Flexible and lightweight thermoelectric generators composed of carbon nanotube – polystyrene composites printed on film substrate Flexible and lightweight thermoelectric generators composed of carbon nanotube – polystyrene composites printed on film subst. **2014**, *153902*, doi:10.1063/1.4824648.

24. Zheng, Y.; Zhang, Q.; Jin, W.; Jing, Y.; Chen, X.; Han, X.; Bao, Q.; Liu, Y.; Wang, X.; Wang, S.; et al. Carbon nanotube yarn based thermoelectric textiles for harvesting thermal energy and powering electronics. *J. Mater. Chem. A* **2020**, *8*, 2984–2994, doi:10.1039/c9ta12494b.

25. We, J.H.; Kim, S.J.; Cho, B.J. Hybrid composite of screen-printed inorganic thermoelectric film and organic conducting polymer for flexible thermoelectric power generator. *Energy* **2014**, *73*, 506–512, doi:10.1016/j.energy.2014.06.047.

26. Kim, S.J.; We, J.H.; Cho, B.J. A wearable thermoelectric generator fabricated on a glass fabric. *Energy Environ. Sci.* **2014**, *7*, 1959–1965, doi:10.1039/c4ee00242c.

27. Liebscher, M.; Petra, P.; Voit, B.; Heinrich, G.; Stamm, M. Influence of a cyclic butylene terephthalate oligomer on the processability and thermoelectric properties of polycarbonate / MWCNT nanocomposites. **2014**, *55*, 5381–5388, doi:10.1016/j.polymer.2014.08.048.

28. Tzounis, L.; Liebscher, M.; Fuge, R.; Leonhardt, A.; Mechtcherine, V. P- and n-type thermoelectric cement composites with CVD grown p- and n-doped carbon nanotubes: Demonstration of a structural thermoelectric generator. *Energy Build.* **2019**, *191*, 151–163, doi:10.1016/j.enbuild.2019.03.027.

29. Karalis, G.; Mytafides, C.; Polymerou, A.; Tsirka, K.; Tzounis, L.; Gergidis, L.; Paipetis, A.S. Hierarchical Reinforcing Fibers for Energy Harvesting Applications - A Strength Study. *Key Engineering Materials* **2020**;827 :252–7, doi:10.4028/www.scientific.net/KEM.827.252.

30. Karalis, G.; Tsirka, K.; Tzounis, L.; Mytafides, C.; Koutsotolis, L.; Paipetis, A.S. Epoxy / Glass Fiber Nanostructured p- and n-Type Thermoelectric Enabled Model Composite Interphases, *Appl. Sci*. **2020,** *10*, 5352. https://doi.org/10.3390/app10155352.

31. Moaseri, E.; Karimi, M.; Baniadam, M.; Maghrebi, M. Enhancement in mechanical properties of multi-walled carbon nanotube–carbon fiber hybrid epoxy composite: effect of electrostatic repulsion. *Appl. Phys. A Mater. Sci. Process.* **2016**, *122*, 1–8, doi:10.1007/s00339-016-9600-2.

32. An, Q.; Rider, A.N.; Thostenson, E.T. Electrophoretic deposition of carbon nanotubes onto carbon-fiber fabric for production of carbon/epoxy composites with improved mechanical properties. *Carbon N. Y.* **2012**, *50*, 4130–4143, doi:10.1016/j.carbon.2012.04.061.

33. Baltzis, D.; Bekas, D.G.; Tzachristas, G.; Parlamas, A.; Karabela, M.; Zafeiropoulos, N.E.; Paipetis, A.S. Multi-scaled carbon reinforcements in ternary epoxy composite materials : Dispersion and electrical impedance study. *Compos. Sci. Technol.* **2017**, *153*, 7–17,

doi:10.1016/j.compscitech.2017.09.035.

34. Pozegic, T.R.; Anguita, J. V; Hamerton, I.; Jayawardena, K.D.G.I.; Chen, J.; Stolojan, V. Multi-Functional Carbon Fibre Composites using Carbon Nanotubes as an Alternative to Polymer Sizing. *Nat. Publ. Gr.* **2016**, 1–11, doi:10.1038/srep37334.

35. Bekas, D.G.; Paipetis, A.S. Damage monitoring in nanoenhanced composites using impedance spectroscopy. *Compos. Sci. Technol.* **2016**, *134*, 96–105, doi:10.1016/j.compscitech.2016.08.013.

36. Tzounis, L.; Zappalorto, M.; Panozzo, F.; Tsirka, K.; Maragoni, L.; Paipetis, A.S.; Quaresimin, M. Highly conductive ultra-sensitive SWCNT-coated glass fiber reinforcements for laminate composites structural health monitoring. *Compos. Part B Eng.* **2019**, *169*, 37–44, doi:10.1016/j.compositesb.2019.03.070.

37. Tsilimigkra, X.; Bekas, D.; Kosarli, M.; Tsantzalis, S.; Paipetis, A.; Kostopoulos, V. Mechanical properties assessment of low-content capsule-based self-healing structural composites. *Appl. Sci.* **2020**, *10*, doi:10.3390/APP10175739.

38. Asp, L.E.; Bouton, K.; Carlstedt, D.; Duan, S.; Harnden, R.; Johannisson, W.; Johansen, M.; Johansson, M.K.G.; Lindbergh, G.; Liu, F.; et al. A Structural Battery and its Multifunctional Performance. *Adv. Energy Sustain. Res.* **2021**, *2*, 2000093, doi:10.1002/aesr.202000093.

39. Fredi, G.; Jeschke, S.; Boulaoued, A.; Wallenstein, J.; Rashidi, M.; Liu, F.; Harnden, R.; Zenkert, D.; Hagberg, J.; Lindbergh, G.; et al. Graphitic microstructure and performance of carbon fibre Li-ion structural battery electrodes. *Multifunct. Mater.* **2018**, *1*, doi:10.1088/2399-7532/aab707.

40. Lee, J.; Ni, X.; Daso, F.; Xiao, X.; King, D.; Gómez, J.S.; Varela, T.B.; Kessler, S.S.; Wardle, B.L. Advanced carbon fiber composite out-of-autoclave laminate manufacture via nanostructured out-of-oven conductive curing. *Compos. Sci. Technol.* **2018**, *166*, 150–159, doi:10.1016/j.compscitech.2018.02.031.

41. Fredi, G.; Dorigato, A.; Fambri, L.; Pegoretti, A. Multifunctional structural composites for thermal energy storage. *Multifunct. Mater.* **2020**, *3*, 1–34, doi:10.1088/2399-7532/abc60c.

42. Wang, Z.; Kurita, H.; Nagaoka, H.; Narita, F. Potassium sodium niobate lead-free piezoelectric nanocomposite generators based on carbon-fiber-reinforced polymer electrodes for energy-harvesting structures. *Compos. Sci. Technol.* **2020**, *199*, 108331, doi:10.1016/j.compscitech.2020.108331.

43. Karalis, G.; Mytafides, C.K.; Tzounis, L.; Paipetis, A.S.; Barkoula, N. An Approach toward the realization of a through-thickness glass fiber/epoxy thermoelectric generator. *Materials.* **2021**, *14*(9), 2173. https://doi.org/10.3390/ma14092173.

44. Guerrero, V.H.; Wang, S.; Wen, S.; Chung, D.D.L. Thermoelectric property tailoring by composite engineering. *J. Mater. Sci.* **2002**, *37*, 4127–4136, doi:10.1023/A:1020083718789.

45. Han, S.; Chung, D.D.L. Through-thickness thermoelectric power of a carbon fiber/epoxy composite and decoupled contributions from a lamina and an interlaminar interface. *Carbon N. Y.* **2013**, *52*, 30–39, doi:10.1016/j.carbon.2012.08.071.

46. Han, S.; Chung, D.D.L. Carbon fiber polymer-matrix structural composites exhibiting greatly enhanced through-thickness thermoelectric figure of merit. *Compos. Part A Appl. Sci. Manuf.* **2013**, *48*, 162–170, doi:10.1016/j.compositesa.2013.01.008.

47. Yun, M.J.; Cha, S.I.; Seo, S.H.; Kim, H.S.; Lee, D.Y. Insertion of Dye-Sensitized Solar Cells in Textiles using a Conventional Weaving Process. *Sci. Rep.* **2015**, *5*, 1–8, doi:10.1038/srep11022.

48. Kjell, M.H.; Jacques, E.; Zenkert, D.; Behm, M.; Lindbergh, G. PAN-Based Carbon Fiber Negative Electrodes for Structural Lithium-Ion Batteries. *J. Electrochem. Soc.* **2011**, *158*, A1455, doi:10.1149/2.053112jes.

49. Karalis, G.; Tzounis, L.; Mytafides, C.K.; Tsirka, K.; Formanek, P.; Stylianakis, M.; Kymakis, E.; Paipetis, A.S. A high performance flexible and robust printed thermoelectric generator based on hybridized Te nanowires with PEDOT : PSS. *Appl. Energy* **2021**, *294*, 117004, doi:10.1016/j.apenergy.2021.117004.

50. Liu, J.; Wang, X.; Li, D.; Coates, N.E.; Segalman, R.A.; Cahill, D.G. Thermal conductivity and elastic constants of PEDOT:PSS with high electrical conductivity. *Macromolecules* **2015**, *48*, 585–591, doi:10.1021/ma502099t.

51. Park, H.; Son, W.; Lee, S.H.; Kim, S.; Lee, J.J.; Cho, W.; Choi, H.H.; Kim, J.H. Aqueous chemical synthesis of tellurium nanowires using a polymeric template for thermoelectric materials. *CrystEngComm* **2015**, *17*, 1092–1097, doi:10.1039/c4ce02222j.

52. Roy, A.; Amin, K.R.; Tripathi, S.; Biswas, S.; Singh, A.K.; Bid, A.; Ravishankar, N. Manipulation of Optoelectronic Properties and Band Structure Engineering of Ultrathin Te Nanowires by Chemical Adsorption. *ACS Appl. Mater. Interfaces* **2017**, *9*, 19462–19469, doi:10.1021/acsami.6b12064.

53. Farah, A.A.; Rutledge, S.A.; Schaarschmidt, A.; Lai, R.; Freedman, J.P.; Helmy, A.S. Conductivity enhancement of poly(3,4-ethylenedioxythiophene)- poly(styrenesulfonate) films post-spincasting. *J. Appl. Phys.* **2012**, *112*, doi:10.1063/1.4768265.

54. Yang, Y.; Lin, Z.; Hou, T.; Zhang, F.; Wang, Z.L. Nanowire-Composite Based Flexible Thermoelectric Nanogenerators and Self-Powered Temperature Sensors. **2012**, *5*, 888–895, doi:10.1007/s12274-012-0272-8.

Chapter 6

Electrothermal-enabled Fiber Reinforced Polymer Composites

Part of the results included in **Chapter 6** have been published at *Applied Materials & Interfaces* peer-reviewed scientific journal as part of the study "Printed Single-Wall Carbon Nanotube-Based Joule Heating Devices Integrated as Functional Laminae in Advanced Composites" and can be found under *https://doi.org/10.1021/acsami.1c10001*.

6. Electrothermal-enabled Fiber Reinforced Polymer composites

6.1 Printed Single-Wall Carbon Nanotube-Based Joule Heating Devices Integrated as Functional Laminae in Advanced Composites

Abstract

This work reports the design and fabrication of novel printed single-wall carbon nanotube (SWCNT) electrothermal Joule heating devices. The devices are directly deposited on unidirectional (UD) glass fiber (GF) fabrics. The GF-SWCNT Joule heaters were integrated during manufacturing as “system” plies in carbon fiber reinforced polymer (CFRP) composite laminates. Specific secondary functions were imparted on the composite laminate endowing thus a multifunctional character. The efficient out-of-oven-curing (OOC) of a CFRP laminate was demonstrated using a sandwich configuration comprising of a top / bottom GF-SWCNT system plies. A total power consumption of ~10.5 kWh for the efficient polymerization of the thermoset matrix was required. Infrared thermography (IR-T) monitoring showed a uniform and stable temperature field before and after impregnation with epoxy resin. Quasi-static 3-point bending and dynamic mechanical analysis (DMA) revealed a minor knock-down effect of the OOC-CFRP laminates properties compared to oven cured CFRPs, while the glass transition temperature (T_g) was almost identical. The OOC-CFRP laminates were efficient in providing additional functions such as de-icing and self-sensing highly sought in the energy and transport sectors *i.e.*, wind turbine blades or aircraft wings. The novel modular design provides unique opportunities for large-area applications via multiple interconnected arrays of printed devices.

Keywords: Printed heater; SWCNT; Electrothermal effect; Joule heating; Multifunctional Composites; Advanced FRP laminates; Out-of-Oven-Curing (OOC); De-icing; Smart materials

Highlights:

- Large-area, printed and highly-efficient SWCNT heater onto a glass fiber (GF) fabric
- CFRP electrothermal curing by seamless integrated glass fiber (GF) - SWCNT heater plies
- Efficient CFRP curing by a V_{bias} of 2 V to achieve a steady-state temperature of 90 °C
- Out-of-oven post curing by a V_{bias} of 2.3 V reaching a temperature of 130 °C
- Thermomechanical properties comparison between oven- and joule heater-cured laminates
- De-icing functionality of CFRPs by activation of the joule heater system-ply laminae

Graphical abstract

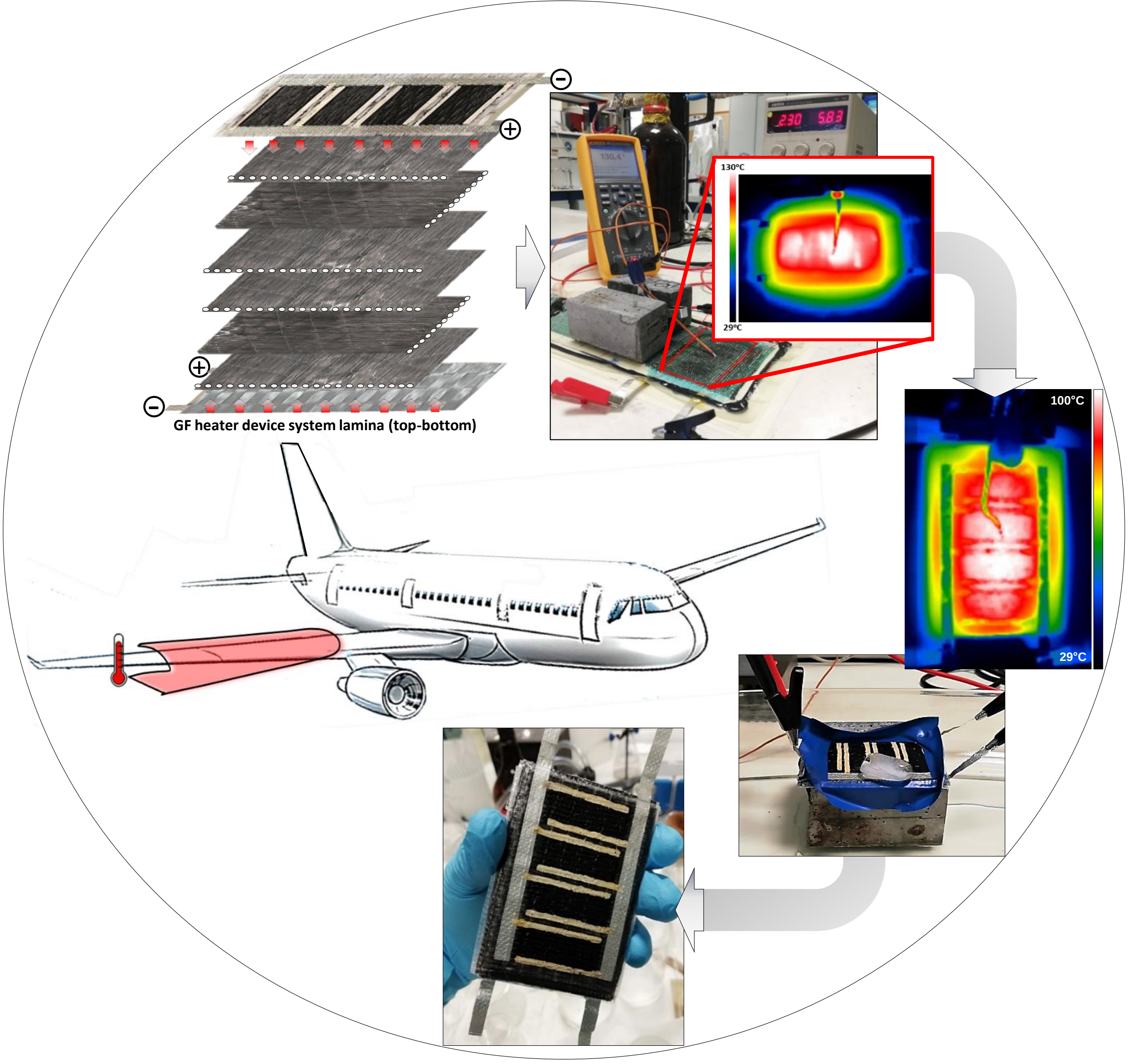

6.1.1 Introduction

Graphitic nanomaterials such as carbon nanotubes (CNTs) and Graphene (Gr) exhibit a unique combination of superior specific properties. These include among others both mechanical (*e.g.* stiffness and strength) and physical (*e.g.* electrical and thermal conductivity) properties [1–3]. For more than a decade, the incorporation of carbon nano allotropes in fiber reinforced polymer (FRP) composite materials is employed to exploit their exceptional properties. Two approaches have been employed and reported to date, *i.e. i)* the dispersion of carbon nano additives into the polymer matrix [4–6] and *ii)* direct growth *e.g.* via chemical vapor deposition (CVD) or solution based wet-chemical deposition / printing processes as hierarchical coatings onto the reinforcement phase [7–9]. Whereas the first "matrix" approach is directly aiming in improving matrix properties, the second "hierarchical" approach aims in directly improving the interface via the creation of a stronger/ tougher of functional interphase [10]. Among carbon allotropes, CNTs have been the most widely used nanomaterial for the production of multi-scale structural laminate composites with improved properties, *e.g.* fracture toughness [11], fatigue [12], interfacial adhesion strength [13–15], impact and energy absorption properties [16], electrical and thermal conductivity [17,18].

The potential seamless integration of various two dimensional (2D) constituents / devices into laminate composite structures as system plies, could be an ideal approach to realize multifunctional composites [19]. On the other hand, more complex design and implementation of carbon based micro-scaled or nanostructured materials within the bulk structure of composite materials could endow additional functions. Namely, smart non-destructive structural integrity evaluation [20] and damage sensing [21–23], structural energy storage and battery enabled composite devices [24], thermal energy storage [25] or thermal energy harvesting [26,27] are some of the functionalities that have been reported, which turn conventional structural materials into “multi-functional” composites. Nanoscale carbon allotropes have also been reported to act synergistically to improve other functionalities in “architecture” materials as in the case of self-healing [28,29], where concurrent physical and mechanical property recovery can be achieved [30].

The electrothermal, otherwise known as “Joule-heating” effect, has been widely studied by the research community from different scopes and in various sectors [31–33]. In principle, Joule resistive heating or Ohmic heating is the effect when electric current passes through an electrical conductor, resulting in heat generation. More specifically, the microscopic description of the Joule heating effect can be attributed to the inner interactions between electrons and atomic ions of every conductor. When voltage difference is applied between two points of a conductive network, an electric field is being generated, which accelerates charge carriers in the field direction, resulting in higher kinetic energy. Then, electrons collide within the conductor’s ions and the particles are being scattered. Under this atomic scale electronic charge carrier transport mechanism, electrical energy is converted to thermal energy [34,35]. As is well-known, Joule's first law states that the heating power generated by an electrical conductor is $P = I^2 \cdot R$, where P: Power (W), I: Current (A), R: Resistance (Ohm). According to the Ohmic conductor model, the conversion of electrical power into Joule-heating is $P = V^2/R$, where V (V) denotes the applied input voltage, or otherwise known as voltage bias (V_{bias}). Applications of resistive heating with numerous solutions amply exist in the market [36,37]. Nonetheless, there is a constant interest for the development of more energy-efficient thermal / heating technologies based on the Joule heating effect *e.g.* in demanding fields such as advanced FRP composites for curing [38], bonding [39] and de-icing applications [40].

Recent advances include the investigation of carbon materials *i.e.* CNTs [41,42] and electro-conductive carbon fiber (CF) textiles [43] as electro-thermal elements or systems. In the field of advanced structural composites, the incorporation of CNTs as highly electrically conductive one-dimensional (1D) nanomaterial imparts electrical conductivity in the composite at macroscopic scale (if only dielectric phases are present) provided the concentration is above the electrical percolation threshold. When percolation is achieved, the CNTs are forming an interconnected network with successive CNT-CNT resistive junctions forming random conductive paths. These can produce an efficient electrothermal effect. Xia *et al.* investigated electrically conductive percolated networks of graphene nanoplatelets formed within a thermosetting matrix to demonstrate the ability to act as integrated nano heaters for epoxy curing applying a DC voltage bias of 40 V. Under these conditions, the authors achieved a constant temperature of 100 °C for 240 min [44]. Shang *et al.* demonstrated a welded CNT / glass fiber tow system for the electrothermal resin curing with an applied voltage in the range of 21.2-26.5 V to achieve a thermal response of 100-125 ^{o}C [45]. In a previous study, a CNT web was applied as heating element to the outer surface of a CFRP to improve the de-icing efficiency without any influence on the mechanical properties, leading to uniform heating with an input voltage of 16 V [46]. Another study reported the electrothermal behavior of epoxy coatings with varying content of graphene nanoplatelets above the electrical percolation threshold. The graphene network was able to perform de-icing combined with low power consumption of 1–3 W, albeit at a high applied voltage 750-800 V [47]. Joule heating curing based on modified epoxy systems with graphitic fillers demand high external voltage input stimuli and present difficulties in processing due to high viscosity issues. On the other hand, CNT film-based or CF reinforcing fabric heating elements provide facile manufacturing combined with improved thermal distribution uniformity and reliability at lower power demands.

In this study, we report for the first time a novel design and fabrication process of a fully printed single wall carbon nanotube (SWCNT) based Joule heating device onto a unidirectional (UD) glass fiber (GF) substrate. A SWCNT aqueous dispersion was utilized for the 2D printing process of the electrothermal devices onto UD GF fabric substrates following a versatile, simple, low-cost and scalable mask-assisted blade coating deposition method. The fabricated GF heater "system" plies were integrated as top and bottom Joule heating devices within a 6-ply $[0/90]_s$ Carbon Fiber Reinforced Polymer (CFRP) composite laminate towards the implementation of out-of-oven-curing (OOC) and de-icing, self-sensing as secondary functions. The motivation of this work is based on the realization of multifunctional electrothermal CFRP structures relying on effective mass production, satisfactorily uniform and extremely responsive thermal distribution with a view to large-area applications using multiple interconnected arrays of printed heater devices. As presented herein, a seamless integration of 2D printed SWCNT heater devices onto conventional GF fibrous UD reinforcements could result in remarkably low power consumptions, compared with typical literature values for out-of-oven-curing of FRPs. The top and bottom Joule heating system plies enabled the curing and the post-curing process of the composite's thermoset matrix. The application of a V_{bias} of 4 V and 4.6 V, corresponding to 2.13 W and 2.82 W of power consumption was found to be sufficient for uniform electrothermal heating as validated by infrared thermography (IR-T). The recorded temperature profiles exhibited a remarkably steady temperature of 90 ^{o}C and 130 ^{o}C for the curing (90 min) and post-curing (180 min) process, respectively. CFRP laminates cured in a conventional manner using an oven in order to assess the total amount of power consumption and compare it further with the OOC-CFRP joule heating-enabled laminates. The thermomechanical behavior of the OOC-CFRP compared to conventionally cured CFRP laminates was tested via dynamic mechanical analysis (DMA) so as to evaluate the curing efficiency, while quasi-static 3-point bending was employed to evaluate the laminate's mechanical performance. Both cured systems exhibited almost identical properties. Furthermore, the de-icing potential of the multifunctional OOC composite laminates was assessed via testing their capability to melt a certain amount of ice placed onto the surface of the laminate up to detachment from the laminate. Efficient de-icing test was achieved using an applied voltage of 4.2 V for 8 min, or else 2.35 W of power consumption.

6.1.2 Experimental section

6.1.2.1 Materials

SWCNT in the form of powder were purchased from OCSiAl (TUBALL, Russia) with a carbon content >85 wt. %, SWCNT ≥75 wt. % with an outer mean diameter of 1.8 ± 0.4 nm, length >5 μm, and metal impurities <15 wt. %. Sodium dodecylbenzenesulfonate (M_w = 348.48 g/mol) abbreviated as SDBS was received from Sigma Aldrich. Distilled water (d-H_2O) was used for all the SWCNT dispersions prepared in this study. Silver (Ag) paste (ORGACON^{TM} Nanosilver Screen Printing Ink SI-P2000) was obtained from Agfa. Ag conductive tapes with conductive adhesive and a total thickness of ~500 μm were received from 3M™. All chemicals used for the cleaning procedures were analytical grade and used as received without further purification.

A unidirectional (UD) stitched carbon fiber (CF) fabric consisting of 12K filaments CF tows (T700 SC, Toray) with a ply thickness of 0.33 mm, as well as a UD glass fabric (GF) G320U (320 g/m^2) with a ply thickness of 0.26 mm were utilized for the FRP laminate composite manufacturing. A commercial epoxy resin (EPIKOTE™ Resin 828 LVEL) with amine-based hardener (EPIKURE™ Curing Agent 866) and catalyst (EPIKURE™ Catalyst 101) by Hexion was employed as the composite matrix (100:83:1.5 w/w) following a typical curing cycle of 90 °C for 90 min and post-curing at 130 °C for 180 min, as recommended by the supplier's technical data sheet.

6.1.2.2 Fabrication of the GF system ply Joule heating device

SWCNT with mass concentration of 2 mg/mL were dispersed in the presence of 10 mg/mL SDBS anionic surfactant via a tip-sonicator processor (UP400S by Hielscher). Specifically, SWCNT were added in a previously prepared SDBS aqueous medium of 100 ml for 60 min under stirring at 500 rpm. The SWCNT:SDBS (1:5) system was exposed to tip sonication for 90 min at 10 Watt power, using an ice cooled water bath. These dispersion parameters have been found to be sufficient in order to achieve a homogeneous and stable SWCNT dispersion. Subsequently, a mask-assisted wet chemical deposition / printing process was applied to deposit SWCNT films as joule heater resistors onto a glass fiber UD substrate employing a blade coating apparatus. Initially, a purposefully designed (CorelDRAW) patterned vinyl foil mask with adhesive was utilized for delimiting the specific areas of the heater device, which was attached onto the GF substrate. Then, the SWCNT dispersion was deposited via a moving blade fixed at 200 μm distance from the heated at 120 °C fibrous substrate, assisted by a hot plate for 30 min to fully evaporate the residual moisture and dry the SWCNT films. The GF fabric was placed onto a hot plate at 120 °C for 30 min for the simultaneous evaporation of water and drying of the SWCNT films. After drying, the vinyl mask was easily removed from the fibrous substrate and the desired pattern was formed. The production process of the patterned SWCNT films as joule heater device resistors (34×14 mm^2) onto the GF substrate is presented in **Figure 76a**.

In the next step, metallic contacts with a typical interdigitated electrode (IDE) like configuration were deposited in order to close the joule heater device circuit, resulting into an individual working device. For this purpose, Ag paste was carefully applied onto the specific desired regions with a syringe. The full device has been placed then in a vacuum oven at 150 °C for 30 min to allow the fully curing of the printed Ag IDE electrode (resulting into the highest possible electrical conductivity of the metallic Ag paste electrodes, according to the supplier's data sheet). Finally, two Ag tape stripes were properly adapted as depicted in **Figure 76b** to realize the full IDE geometry, allowing thus the current injection through the SWCNT 4 resistors upon applying an external voltage potential (V_{bias} or ΔV).

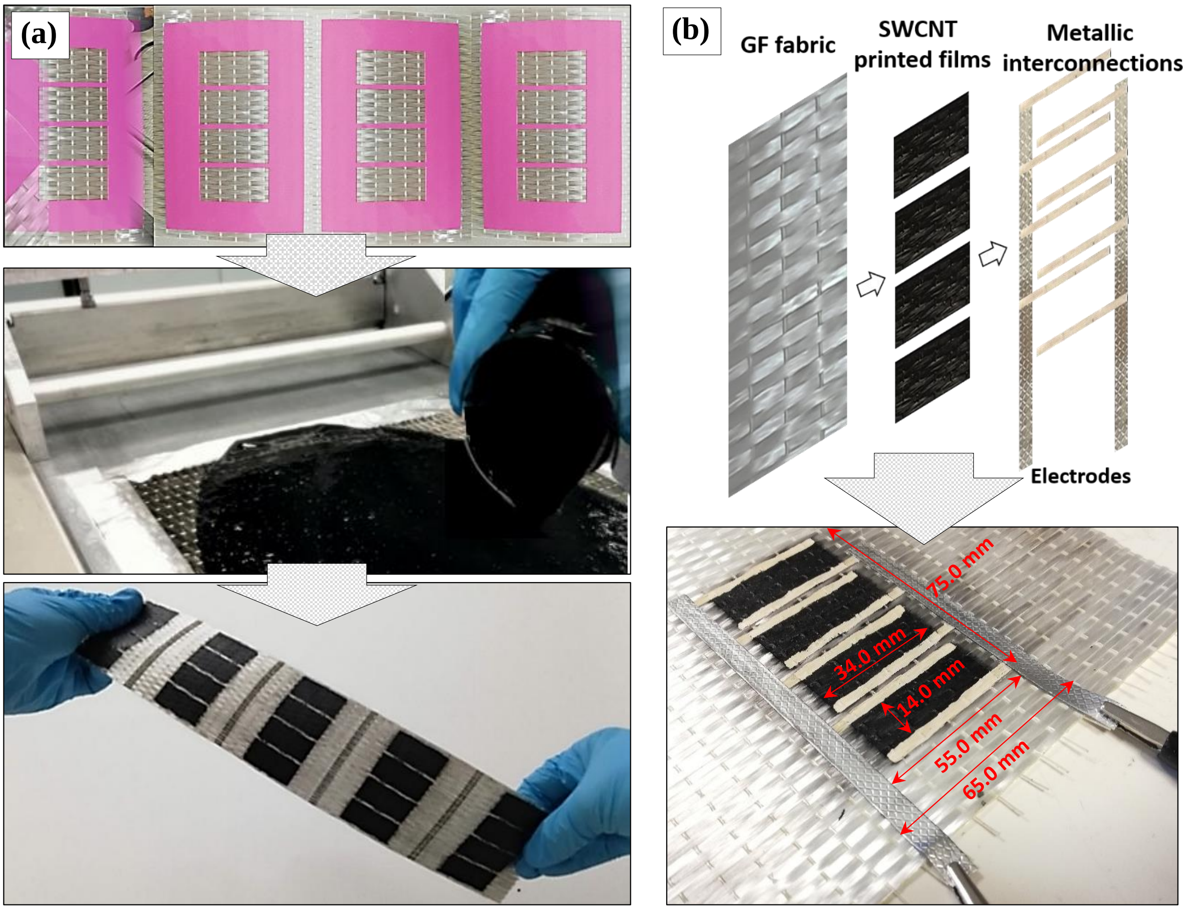

Figure 76. Fabrication of the system plies: **(a)** vinyl tape mask onto the GF fabric for the mask-assisted blade coating printing process resulting resistors / printed patterns after its removal and **(b)** schematic illustration of the process and photograph of the final device.

6.1.2.3 Lamination and out-of-oven curing process of the CFRP laminate

Figure 77a and **77b** depict the lamination of the $[0/90]_s$ manufactured composites, especially the ones that have been conventionally cured and post-cured using an oven (thermal transfer through a convection mechanism), as well as the OOC laminates by the integrated joule heater system plies, respectively (thermal transfer in the bulk FRP structure through a conduction mechanism). For the oven cured CFRP laminate manufacturing process, hereafter denoted as also as “reference” system, six CF plies were impregnated by hand lay-up with epoxy resin. Additionally, one bottom and one top UD GF ply were laminated. Subsequently, the laminate was transferred in oven for the curing (90 ^{o}C for 90 min) and post-curing (130 °C for 180 min) assisted by vacuum bagging. A lab-scale oven (VT 6025 Heraeus Thermoscientific) with vacuum supply up to 0.01 mbar of 25 L volume capacity and working temperature up to 200 °C at 1300 W and 230 V was used. On the other hand, the OOC-CFRP laminates were manufactured with a modified vacuum bagging technique in order to exploit the top / bottom GF system plies-Joule heating devices, as in detail shown schematically in **Figure S7** of the Supporting Information. For the activation of the SWCNT-based printed heaters onto the GF system laminae, two Xantrex XPH 18-10 DC power supply devices were used, each one capable of delivering a maximum power of 180 W at 18 V and 10 A, respectively. The dimensions of the manufactured 8-ply laminates where 75×65 mm^2. Critically important within the manufacturing procedure is to avoid any possible short-cuts between the SWCNT resistor films of the heater device, silver interconnections or electrodes with the extremely electrically conductive CF plies. Simultaneously, the dielectric GF laminae are successful in preventing any possible electrical contact between the SWCNT films of the top and bottom heater devices with the CF plies. As should be noted, the GF-SWCNT heater device electrical resistance (R_{heater}) values were measured before and after the resin impregnation and were found to be identical. Within the scope of this study was to prove that the proposed one-sided printed Joule heating devices served selectively as reliable electrical insulator and efficient symmetric electrothermal system during lamination process and subsequently.

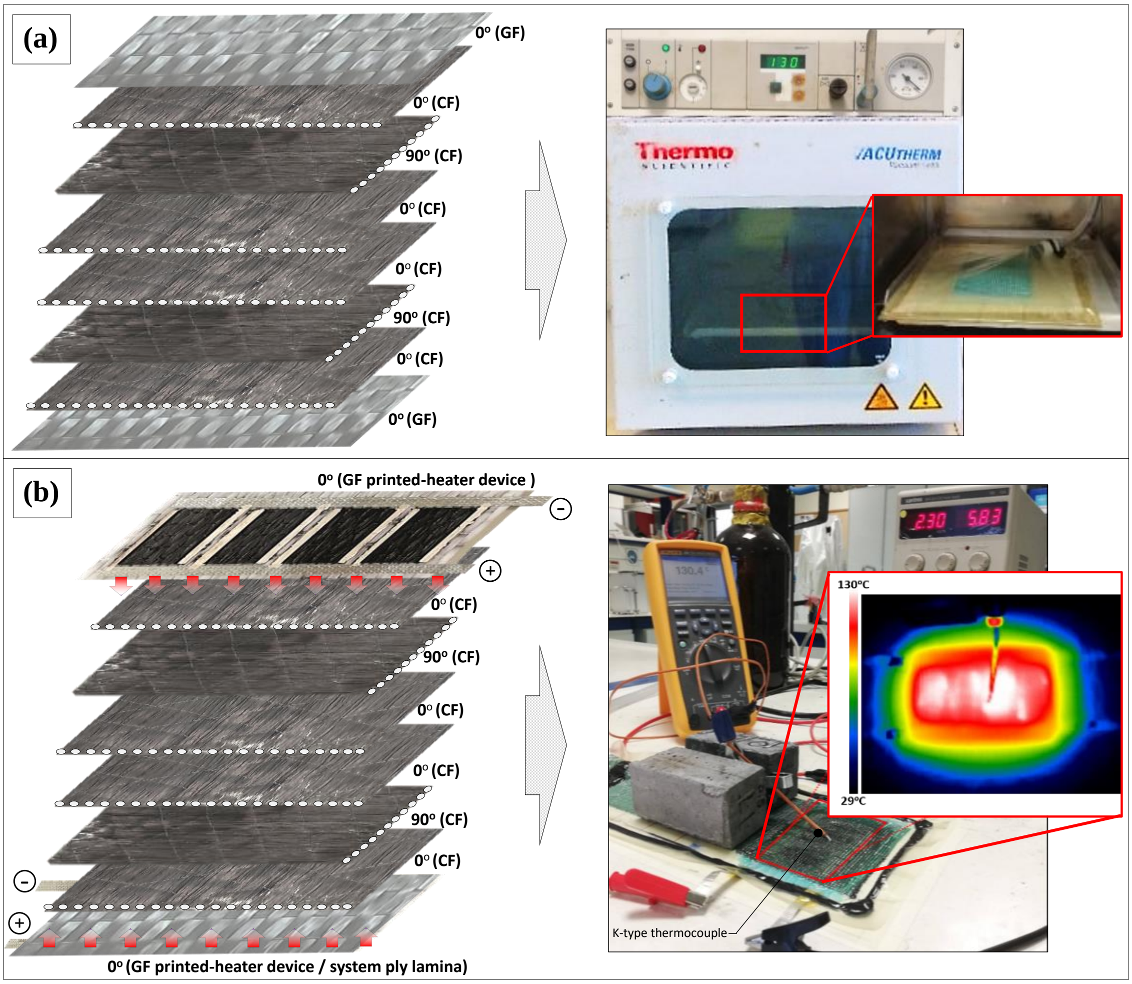

Figure 77. Schematic illustration of the composite lamination and manufacturing procedure via vacuum bagging technique for **(a)** the CFRP reference laminate cured / post-cured in an oven and **(b)** the OOC-CFRP laminate with simultaneously monitoring of the temperature (T) for the thermal curing / post-curing process.

6.1.2.4 Characterization techniques

The dynamic viscosity of the SWCNT ink / dispersion used for the blade coting printing process was measured with an NDJ-9S digital rotary viscometer.

The microstructural investigation of SWCNT coated GF fabric, as well as the nanomorphology of the SWCNT films was performed using an FEI NanoSem 200 operating at an accelerating voltage of 5 KV.

A Labram HR-Horiba scientific micro-Raman system was employed in order to identify the existing SWCNT characteristic fingerprints. The 514.5 nm line of an Ar^+ ion laser operating at a laser power of 1.5 mW at the focal plane was employed for the Raman excitation. An optical microscope equipped with a 100× long working distance objective served both for delivering the excitation light source, as well as collecting the back-scattered Raman emission. All Raman spectra were acquired in the 100-3500 cm^{-1} spectral range.

4-probe sheet resistance measurements were conducted to measure the electrical conductivity of the SWCNT:SDBS system / material, used for the Joule heater fabrication. More specifically, a SWCNT bucky paper film was prepared via a vacuum filtration process using the SWCNT:SDBS dispersion and sheet resistance measurements were performed on films with known geometrical characteristics following a process reported elsewhere [48]. A typical 4-probe technique was used employing a commercial 4-point probe electrical characterization apparatus (Ossila Ltd). The electrical conductivity was calculated from the following formula: $\sigma = 1/R_s \cdot L/A \cdot (\ln 2/\pi)$ where R_s is the measured 4-probe sheet resistance, L is the length and A is the cross-section of each bucky paper film sample. 2-probe electrical measurements were carried out using the Agilent 34401A digital multimeter with 6½ digits resolution.

Temperature measurements were performed via a Fluke 289 True RMS data-logging multimeter at a frequency of 1 Hz with a K-type thermocouple, which was surface mounted onto the top side of the investigated composite laminates (**Figure 77b**).

Thermal images were captured with a Seek Thermal Compact PRO Compact XR Imaging Camera IR Infrared Imager with a temperature working window of -40 to 330 °C.

The oven and power supply devices' power consumption were monitored via the VOLTCRAFT Energy Check 3000 power gauge. The consumption of the oven was monitored in real time throughout the curing and the post-curing process, so as to compare typical energies needed for the conventional polymerization processes with the novel approach presented in this work.

To eliminate the residual humidity absorbed by the laminates, all tested specimens were dried in an oven at 40 °C overnight prior to testing. 3-point bending quasi-static mechanical tests were conducted using a 100 KN Universal Testing Machine by JINAN TESTING EQUIPMENT IE CORPORATION, according to the ASTM D 790-03. A loading speed of 1 mm/min was employed for all tests. Two samples of 6 rectangular specimens of 50×10×~2.7 mm^3 were tested, one from the OOC-CFRP laminates and one from the conventionally oven cured laminate composites.

Dynamic mechanical analysis (DMA) was performed using a Q800 analyzer (TA Instruments, New Castle, US) in dual cantilever mode to determine the thermomechanical properties of OOC-CFRP laminates, as well as the oven cured "reference" CFRP laminates. Tests were carried out according to the ASTM D7028-07 with 3 specimens tested per grade for the cured laminates. More specifically, the samples were cut in flat rectangular strips (50 mm length, 10 mm width and ~2.7 mm thickness) and tested at a frequency of 1 Hz from 30 to 200 °C. The deformation amplitude was set at 15 μm and the heating rate was 3 °C/min.

6.1.3 Results and Discussion

6.1.3.1 Characterization of the SWCNT dispersion / ink and SWCNT film microstructure

Figure 78a illustrates the patterned SWCNT printed films onto a UD GF substrate reinforcing phase, focusing mainly on the micro-scale morphological inspection of the deposited films. The dynamic viscosity of the SWCNT:SDBS (1:5) ink used for the blade coating / printing process was 361.5 mPa · s measured at room temperature (RT). The SEM images shown in **Figure 78b** and **Figure 78c** at two different magnifications reveal the SWCNT film morphology and homogeneity. As can be observed, the SWCNT fully cover the GF surfaces creating a continuous film without any visible micro-aggregates (**Figure 78b**). This indicates a high-quality dispersion and deposition / printing process. Moreover, individual SWCNT are observed to be randomly distributed within a highly entangled network consisting of extended CNT-CNT junctions inducing the carrier transport conductive paths (**Figure 78c**). This is further anticipated *i)* to deliver an efficient charge transport upon applying an external potential, when the SWCNT films are operating as resistors of the final Joule heater device and *ii)* to induce a macroscopically homogeneous two dimensional (2D) thermal fields, via the Joule-heating effect and the carrier transport / collision underlying mechanism. This is indispensable for the efficient and homogeneous curing of epoxy resin in the composite laminates.

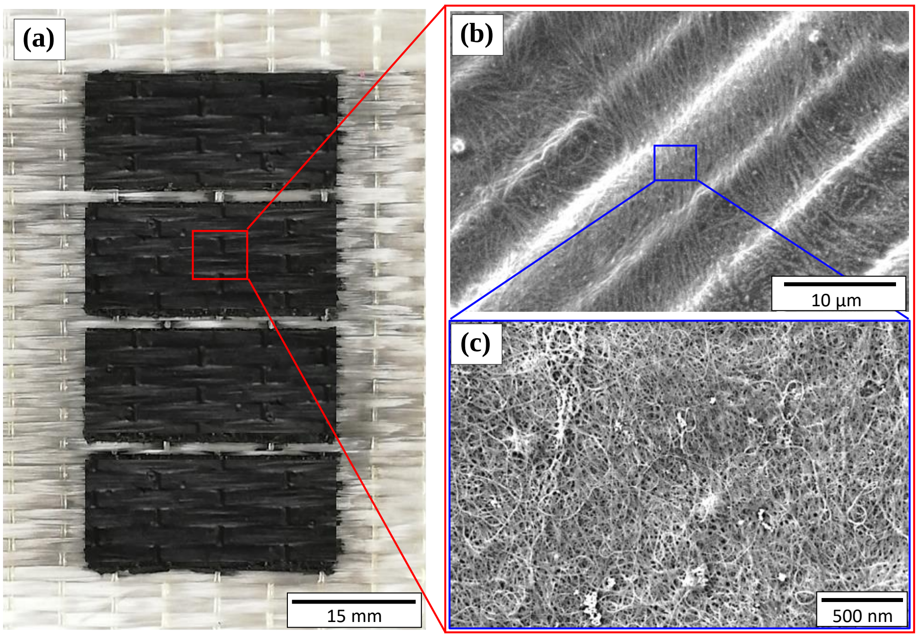

Figure 78. (a) A digital photo of the patterned-printed SWCNT films onto GF fabric and **(b, c)** the corresponding SEM images at two different magnifications.

6.1.3.2 Raman spectroscopic responses of the SWCNT powder and SWCNT printed films

Raman spectroscopy has been extensively employed for studying the graphitization degree and crystallite size of CNTs [49], as well as the defects and side-wall covalent or non-covalent interactions of CNTs with different functional groups [50]. Both pristine SWCNT in the form of powder (as received), as well as SWCNT printed onto the GF substrate using the SWCNT:SDBS ink exhibited the expected vibrational modes commonly found in SWCNT graphitic nanomaterials (**Figure 79**) [22]. The most prominent band of SWCNT located at ca. 1590 cm^{-1} denotes the graphitic or G-band with E_{2g} symmetry [14]. Both spectra are normalized relative to the main graphitic band. The radial breathing mode (RBM), which is a unique phonon mode of SWCNT, could be observed for both the SWCNT powder as well as the SWCNT film in the 120 cm^{-1} - 140 cm^{-1} spectral region. The RBM represents a bond-stretching out-of-plane phonon mode, where all carbon atoms move cohesively in the radial direction. It should be mentioned that the SWCNT film exhibits more peaks in the RBM region compared to the SWCNT powder, with the different RBM peaks known to be characteristic and attributed to different SWCNT diameters existing in the bulk of the material [51]. In this study, the SWCNT are the same in both studied samples. However, it could be envisaged that the SDBS dispersion process resulted in a high degree of SWCNT disentanglement, with single SWCNT randomly arranged in the film, exhibiting thus variable diameters detected in the Raman RBM corresponding region. On the other hand, the SWCNT as powder have shown a narrower distribution of SWCNT diameters with less peaks in the RBM region, which has been more specifically attributed to the strong Van der Waals forces, π-π stacking interactions, *etc.* [52]. The SWCNT film RBM peaks indirectly prove the high level and quality of SWCNT dispersion with SDBS surfactant molecules adsorbed onto the SWCNT surfaces. The dispersion process further disentangles the SWCNT, and the presence of SDBS provides the electrostatic repulsion forces which result in a stable SWCNT dispersion / ink over time. A photograph of the SWCNT ink three months after dispersion shown as inset in the Raman spectrum (**Figure 79**) is provided to confirm the ink stability. Another disorder-induced band appearing in the first order spectrum of the SWCNT is the D-band, at ca. 1341 cm^{-1}. The D-band is caused by either amorphous carbon or sp^3 carbon atoms at defect sites on the CNTs sidewalls [53]. The 2D band dominating the second order spectrum of the SWCNT was also distinctly observed. This band was located at ca. 2679 cm^{-1} as an overtone resulting from a double resonance process, and it is a symmetry allowed band which requires two phonons to be completed [54,55]. Finally, the intensity ratio of D- divided by G-band (I_D/I_G) is well-known and extensively used as a good indicator of the graphitization or the degree of disorder in CNTs [49]. The smaller I_D/I_G value indicates higher crystallinity or less amount of defects. The I_D/I_G was found 0.035 for the SWCNT powder, whereas 0.086 for the SWCNT film. The slight increase in the I_D/I_G for the SWCNT film could be attributed to defects that have been introduced to the SWCNT crystalline lattice, plausibly due to the tip sonication dispersion process, as reported elsewhere [9].

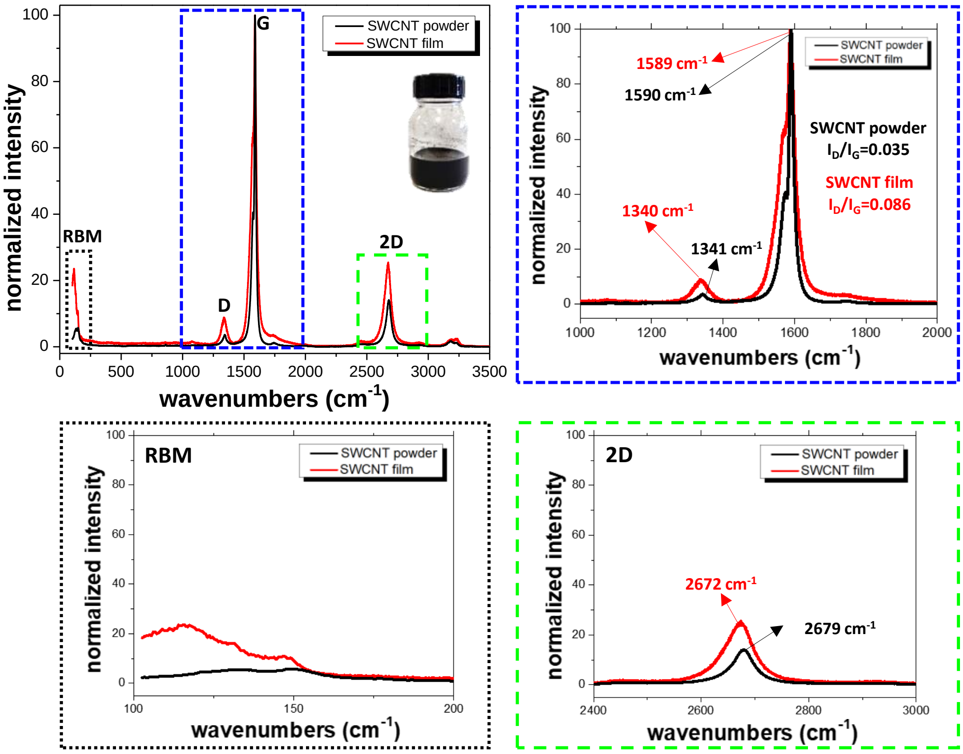

Figure 79. Raman spectrum of the SWCNT films and the pristine material (inset: photo of the SWCNT dispersion after 3 months of storage).

6.1.3.3 Electrothermal performance of Joule heater devices and OOC assessment of CFRP laminates

Figure 80a depicts the real Joule heater device printed onto the GF substrate comprising of 4 electrically interconnected SWCNT patterned films / resistors, as well as the device equivalent circuit. The resulting dry film thicknesses (t) of the SWCNT films were indirectly calculated by the formula of $R_s = \rho/t$ [56] and found in the range of ~11.6 μm, where R_s is the average value of the measured sheet resistance for each SWCNT film (3.16 Ohm/□), and σ is the bulk conductivity of SWCNT measured in the form of a "bulk" bucky paper films (2.72×10^4 S/m). The electrical conductivity of the produced SWCNT buckypaper film was derived by 4-probe sheet resistance measurements (Supporting Information - **Figure S8**). It is worth mentioning that the orientation of the UD fibrous substrate played an essential role in the fabrication of the GF system ply-Joule heating device and its electrical conductivity. The parallel orientation of the fiber with respect to the device favors the adhesion between the SWCNT films and the GF fibrous substrate, resulting in a total heater device resistance of ~0.7 Ohm (R_{heater}). Conversely, the transverse orientation of the device in relation to the fiber direction, increases substantially the internal resistance of the device to values of $R_{heater} \approx$ 50-60 Ohm. The superior performance of the parallel configuration (*i.e.*, the device is parallel to the reinforcing fibers) can be attributed to a minimized dry film thickness which in its turn correlates with the existence of more microscopic electrical discontinuities both within the SWCNT networks as well as to the interconnected printed SWCNT films. Concluding, the relative orientation directly affects the heater device performance, power consumption and the uniformity of the thermal distribution induced on the GF system ply-Joule heating device.

Figure 80b demonstrates the operation of the heater device in plain air during four "ON" and "OFF" cycles. The heater device performance, function and response upon being repeatedly exposed to an applied voltage bias of V_{bias} = 1.6 V is directly shown. As can be seen, the electrothermal effect results in a temperature rise of 125 °C. It is worth mentioning that no hysteresis or any temperature fluctuation phenomena are observed throughout the operational period of nearly 60 min.

Figure 80c depicts the average steady state temperature with respect to the applied voltage and power consumption of the GF-SWCNT Joule heating device operating in air (device active area of 65×55 mm^2 = 3575 mm^2). The power consumption P is given as a function of the resistivity of the heater and its dimensions as $P = V_{bias}^2 \cdot w \cdot t/\rho \cdot L$ [57] where V_{bias} is the input voltage, ρ is the electrical resistivity, L is the length, w is the width and t is the thickness of the resistive element.

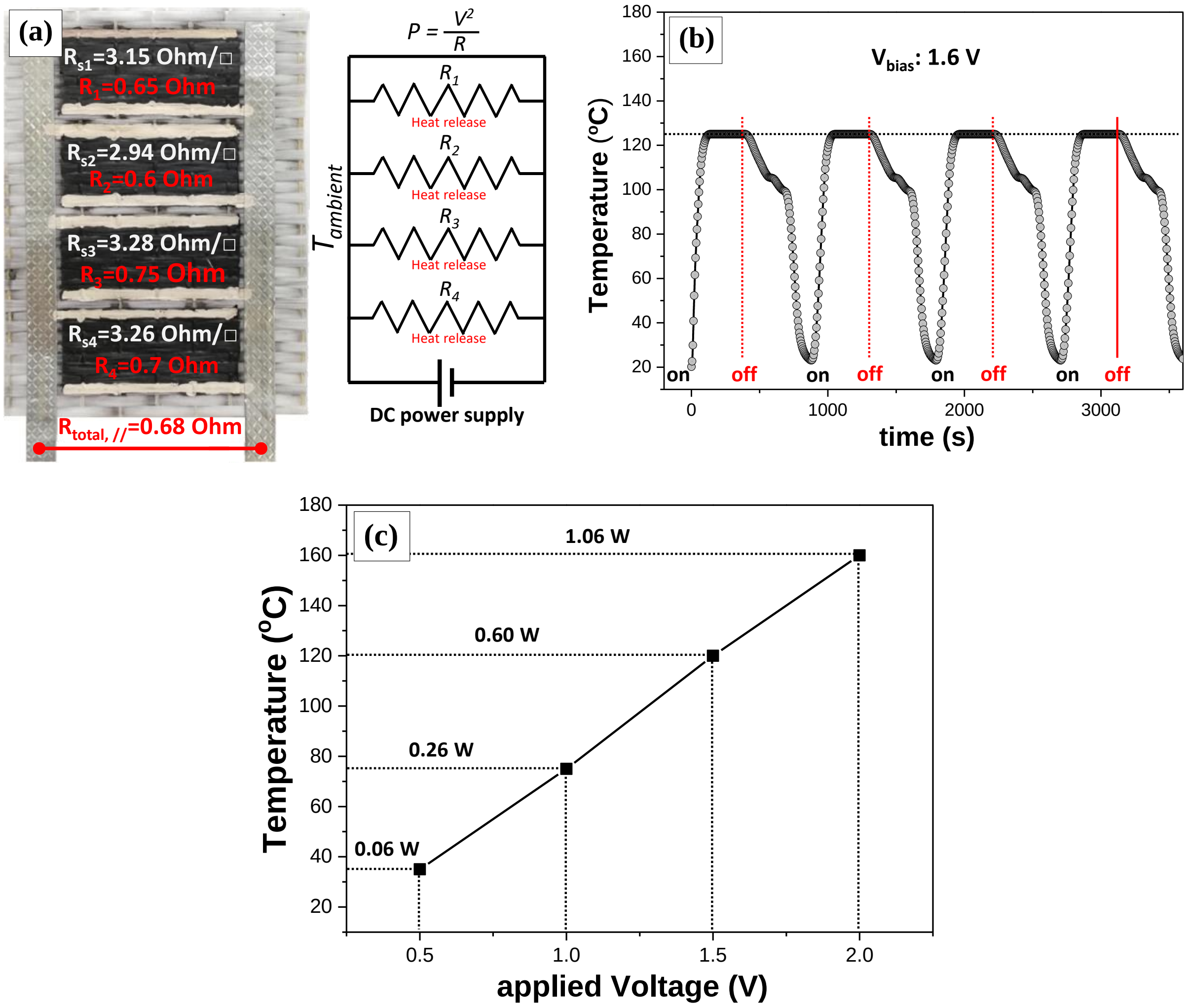

Figure 80. (a) Depiction of the SWCNT-based Joule heating device printed onto a GF substrate (insets: the experimentally measured specific electrical values) and the corresponding electrothermal equivalent circuit, **(b)** Joule heating device performance and temperature response under a V_{bias} of 1.6 V exposed to air for 1 hour of thermal-cooling cycles and **(c)** average steady state temperature with respect to the applied voltage and the respective power input (equal to the power consumption) of the GF-SWCNT Joule heating device, operating in ambient conditions.

Figure 81 shows the electrothermally generated temperature (T) *vs.* time (t), raised upon applying different V_{bias} (0.5 V, 1.0 V, 1.5 V, 2.0 V). For each curve, the power consumption per m^2 is also shown at steady state. A representative thermograph of the heater at V_{bias} = 1.5 V after t = 3 min of operation is also shown. At this input voltage value, the steady state temperature is 120 °C and the power consumption is 0.6 W. The temperature profile as assessed by IR-T is very uniform for each resistor element and in agreement with the temperature measured directly onto the heater surface by the thermocouple. The observed stability and homogeneity provide good evidence that the heater device could efficiently function for the proper OOC of FRPs, when integrated as top and bottom Joule heater system ply.

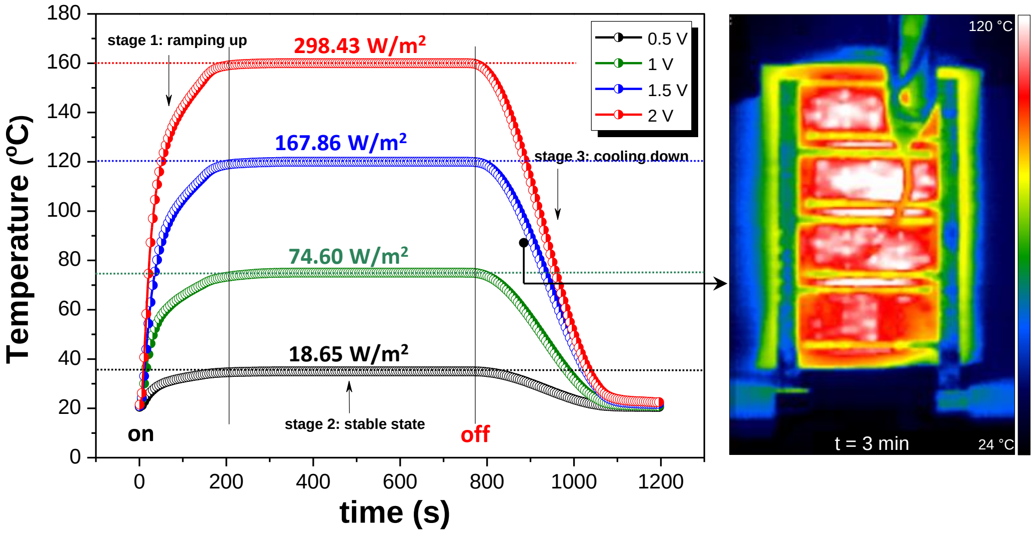

Figure 81. Temperature vs time for the Joule heating effect applying different V_{bias} inputs (0.5 V, 1.0 V, 1.5 V, 2.0 V) to GF-SWCNT joule heater device, showing the total power consumption per m^2 (W/m^2) and the temperature raised in each case. The IR-T image shown in the right hand-side upon applying a V_{bias} of 1.5 V at t = 3 min (power consumption per m^2 is 167.86 W/m^2) corroborates the temperature measured onto the surface of the heater ply by a thermocouple.

Figure 82 depicts the generated temperature (T) *vs.* time (t) for the total duration required for the curing (**Figure 82a**) and the post-curing process (**Figure 82b**) of the CFRP laminate, utilizing the integrated top and bottom GF-SWCNT joule heater system plies. The performance of the electrothermal devices as system plies after impregnation with epoxy resin did not affect their electrical resistance. The electrical resistance of the device is of critical importance for its electrothermal performance. However, slightly increased input voltages were necessary in order to achieve the same thermal imprint compared to the device operation in “air” (**Figure 82**). Since, the current mainly flows along the CNT film longitudinal direction, most heat was generated in this orientation. Heating mainly takes place between the SWCNT electrodes / resistors and does not spread outside the heater device area. It is also worth noting that during the recording the out-of-oven curing as well as the post-curing process, the temperature fluctuation was negligible. Representative thermographs of the curing and post-curing reveal a satisfactory heat distribution. It is expected thus that thermal energy is transferred throughout the whole CFRP by the top and bottom heater-enabled laminae, allowing an efficient electrothermal curing via the integrated Joule heater system plies. More specifically, when both heater system plies are operating for the curing (T = 90 °C @ V_{bias} = 2 V) and post-curing processes (T = 130 °C @ V_{bias} = 2.3 V), a power consumption of 2.13 W and 2.82 W is required, respectively. Indicatively, Lee *et al.* utilized a continuous-macroscale CNT film as surface heating element and succeeded the curing process with a requirement of 30 W for a composite laminate of 40×50×2 mm^3 [58]. Xu *et al.* achieved an in-situ curing and post-curing of a composite laminate (60×30×2 mm^3) with a fabricated CNT film and a total power consumption of ca. 100 W. In more detail, voltage input of 11.5 V and 13 V, correspond to 80 ^{o}C for 30 min and 120 ^{o}C for 2 h, respectively [59].

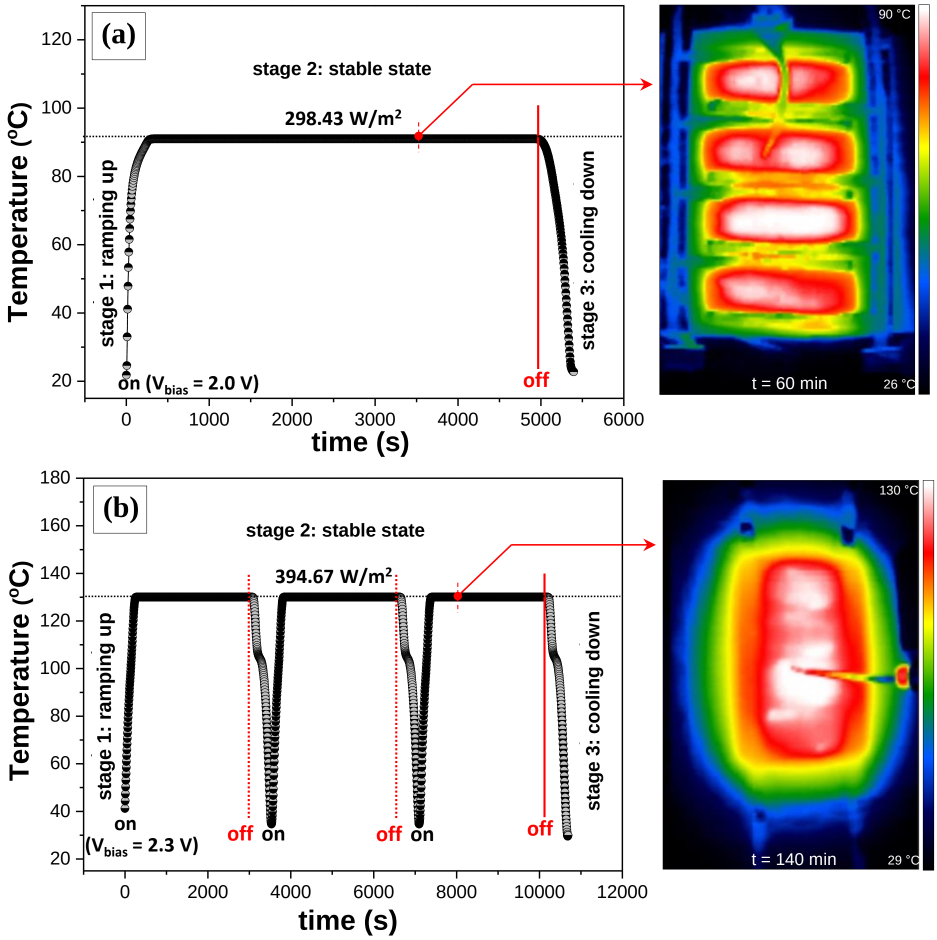

Figure 82. (a) Curing and **(b)** post-curing process via an electrothermal effect by applying different voltage inputs to activate both joule heater system laminae for different durations (the corresponding power consumption per m^2 for each heater operation is depicted). The thermal images in the right hand-side corroborate the temperature measured by the thermocouple in each case.

The most energy demanding stages during FRP composites manufacturing, especially referring to high-performance thermoset systems, are the thermal curing and post-curing procedures [60,61]. The OOC approach proposed in this study could potentially provide a more sustainable solution for energy efficient polymerization and curing / post-curing process.

Figure 83a presents the average steady state temperature of the integrated GF-SWCNT heaters, which were found to respond almost linearly to the applied external V_{bias}. This is in agreement with previous studies related to electrothermal devices [3,35,62]. Linear behavior with respect to V_{bias} is a prerequisite for the reliable function of the device and indicates good operation within the tested limits.

Figure 83b illustrates the power consumption over time for both oven and out-of-oven electrothermally cured CFRP laminates, exposed in both cases to 90 °C for 90 min for the curing, and 130 °C for 180 min for the post-curing process (a total duration of 270 min = 4.5 h for the curing / post-curing total thermal process). Photographs of the two differently cured FRPs are also shown as insets. Comparatively, the manufacturing of the OOC-CFRP laminates requires about 2 orders of magnitude lower power consumption with respect to the oven cured laminates (all power consumption measurement experimental details have been described in the Experimental section). As calculated from the monitored power throughout the curing and the post-curing process (**Figure 83b)**, for a total duration of 4.5 h required for the curing and post-curing process, the energy saving would be ca. 10.5 kWh in favor of the multi-functional Joule heater enabled OOC-CFRP structural laminate. Wardle and co-workers also reported approximately 2 orders of magnitude reduction of the electrical power consumption during a curing cycle of a CFRP laminate with 60×50×2 mm^3 dimensions, following an out-of-oven electrothermal curing manufacturing approach with a commercial CNT-based resistive heater [41].

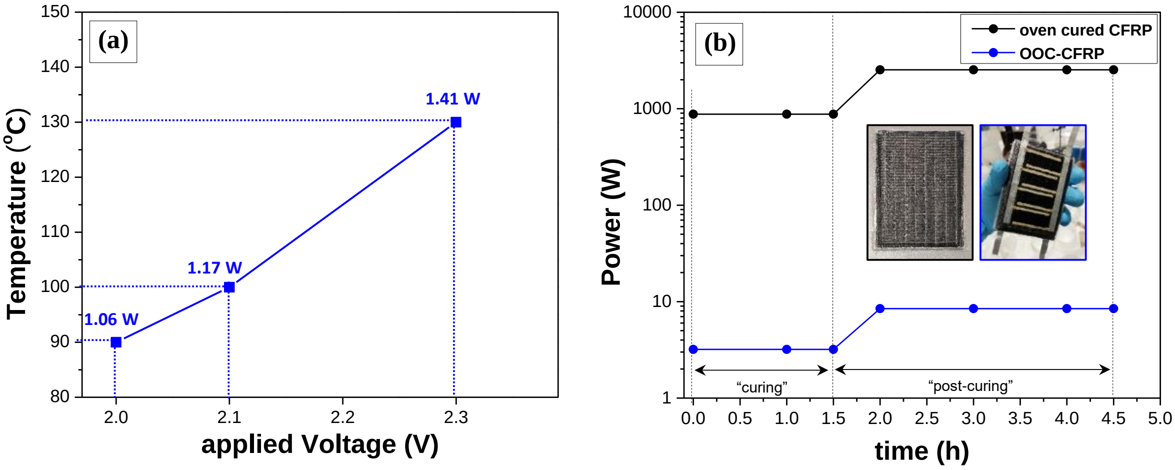

Figure 83. (a) Steady state temperature of the GF-SWCNT Joule heater system lamina, integrated into the CFRP laminate for the OOC process, with respect to the applied voltage (inset: the power input corresponding to the power consumption of the heater due to the electrothermal effect) and **(b)** comparison of the power consumption over time for both oven and out-of-oven cured CFRP laminates, exposed to 90 °C for 90 min and 130 °C for 180 min for the curing and post-curing process, respectively.

6.1.3.4 Mechanical analysis of the CFRP laminates

The mechanical properties of the OOC-CFRP laminates were evaluated using both quasi-static and dynamic tests. In particular, OOC-CFRP laminates compared to the oven cured laminates (reference) were tested with 3-point bending and with DMA in dual cantilever mode.

As can be observed in **Figure 84a**, an average 10.5 % reduction of bending strength and a 13.8 % reduction of flexural modulus were measured for the OOC-CFRP specimens compared to the reference ones. The bending strength was measured at 553.48 ± 13.23 MPa and the flexural modulus 38.7 ± 1.5 GPa for the OOC-CFRP. The respective values for the reference CFRP were 618.31 ± 11.45 MPa and 44.9 ± 1.3 GPa.

The glass transition temperature (T_g) of the specimens was determined via DMA. As is well known, the T_g of epoxy-based materials is indirectly linked to the extent of the resin curing [63]. Relatively, the T_g is a useful temperature indicator for quality control through curing degree quantification of epoxy matrix composite materials. The DMA plots shown in **Figure 84b** (temperature scan), demonstrate the temperature dependency of the FRPs' storage modulus and tan delta. A decrease of 9.2 % in the storage modulus was determined for the OOC-CFRP specimens. T_g values were calculated from the peak of the tan delta curve. The loss factor tan delta is a parameter that defines the specific loss of elastic energy and is at maximum at the temperature region near T_g. Accordingly, the shift of the tan delta values correlates directly with the polymer's T_g identification [6,64]. A relative shift of the tan delta curve was observed for the OOC-CFRP. Namely, the reference CFRP T_g value was 155.5 °C, compared to 153.6 °C for the OOC-CFRP laminate, which is deemed as negligible.

It can be concluded that the examined quasi-static 3-point bending and thermomechanical properties of the OOC-CFRP laminates present a slight knock-down effect compared to the oven cured CFRP laminates. As such, this indicates a similar thermally enabled curing process (curing and post-curing) realized in both CFRP laminates. The requirement of integrated metallic paste lines and Ag-tapes as electrodes for the Joule heater devices could be considered as points acting for plausible defect initiation and affecting thus the OOC-CFRP laminates mechanical and thermomechanical performance. The proper replacement of the aforementioned metallic electrodes without impact on the FRP mechanical properties would be able to eliminate the marginally lower static mechanical and thermomechanical values.

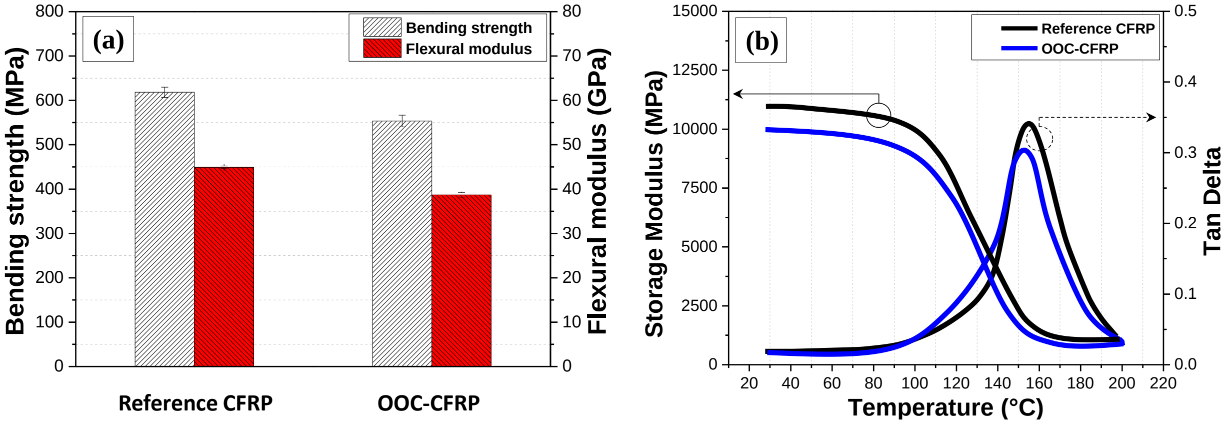

Figure 84. Comparison of **(a)** bending strength and flexural modulus with the corresponding standard deviations and **(b)** DMA plots for the reference CFRP (oven cured), as well as the OOC-CFRP.

6.1.3.5 De-icing functionality of the OOC-CFRP laminates

The de-icing functionality of the manufactured OOC-CFRP laminates was evaluated under a specific versatile protocol utilizing both heater system laminae of the multi-functional CFRP in operation. Specifically, an ice cube with a volume of 16 mL was placed onto the surface of the electrothermal CFRP, while the Joule heating GF-SWCNT system plies has been activated by a V_{bias} of 2.1 V applied on each using two separate DC power supplies. The total power consumption of the two heaters in operation has been calculated at 2.35 W (658.03 W/m^2), resulting into a steady state temperature of 100 °C onto the CFRP top ply surface (CFRP laminate dimensions: 75×65 mm^2). **Figure 85a** depicts some representative snapshots of the de-icing process at different time frames, while within a time period of 8 min most of the ice cube has been melted. In **Figure 85b** the temperature vs time plot illustrates the electrothermal effect – heating cycle for the de-icing function within a total duration of 8 min, namely from the time the heater was activates (ON) till the heater cooling stage.

Finally, one of the 2D printed heater devices seamlessly integrated in the multifunctional CFRP as system ply laminae was used as a temperature resistive sensor to identify the epoxy matrix glass transition temperature (T_g). This inherent function for the T_g self-sensing could be of utmost importance for the structural CFRP laminate, while it could be considered as an embedded sensor providing in-line or in service information recording in real time *i.e.*, the thermal history of the structural CFRP laminate, any thermal shocks during performance in the CFRP specific operational environment, *etc*.. The OOC-CFRP was placed onto a hot plate, and the temperature was increased at a controlled rate of 5 °C/min, from RT (25 °C) to 170 °C. The R_{heater} was monitored in-situ throughout the whole experiment in order to extract the real-time device's fractional electrical resistance change ($\Delta R/R_0$) shown in **Figure 85c**. At the same time, the surface temperature of the OOC-CFRP laminate was also verified with a K-type thermocouple. As can be observed, the $\Delta R/R_0$ of the temperature resistive sensor decreases until a minimum point at the 150-160 °C temperature range. This minimum point of the $\Delta R/R_0$ coincides with the T_g of the epoxy matrix experimentally measured by DMA (~155 °C), while from this point and up to 170 °C, the $\Delta R/R_0$ increases by ~9 %. As reported elsewhere [65], SWCNT electrical conductivity increases with temperature, leading thus to a decrease of the total device electrical resistance as also observed in our study. However, at higher temperatures and specifically near the epoxy matrix T_g region (~155 °C), the opposite device behavior regarding its internal electrical resistance has been experimentally determined. This could be directly attributed to the slight mobility of the crosslinked epoxy macromolecular chains above the T_g, affecting the carrier transport through the CNT-CNT junctions in the continuous SWCNT network of the printed device, as similarly interpreted elsewhere [66].

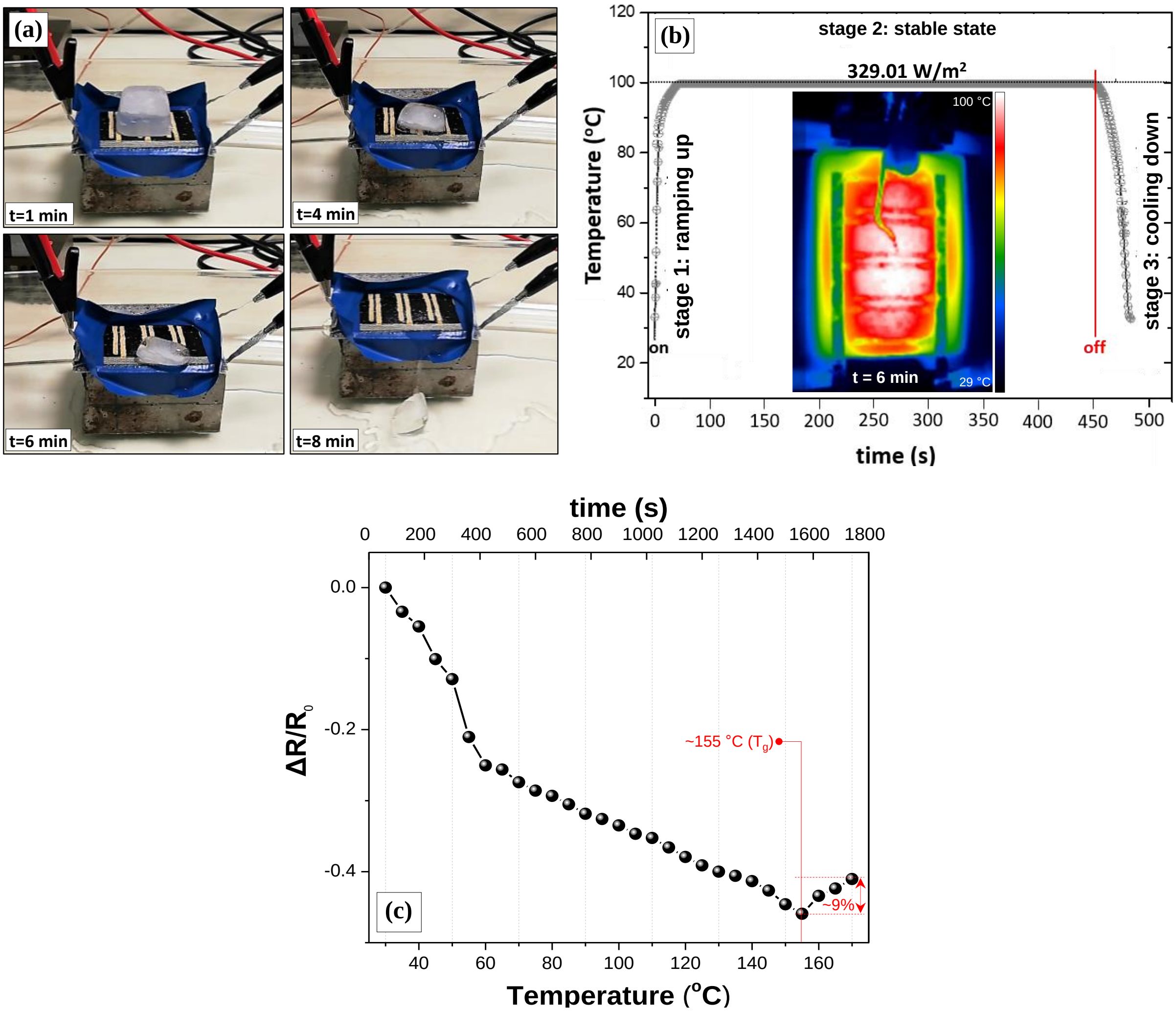

Figure 85. (a) De-icing process by activation of the top and bottom GF system plies-Joule heating devices and **(b)** Temperature vs. time plot showing the temperature electrothermal response of the heaters at an input voltage of V_{bias} = 2.1 V, applied using 2 separate DC power supplies on each heater system ply (the thermal image given as an inset denotes the temperature achieved onto the self-de-icing multifunctional CFRP, being in good agreement with the measurements logged during the whole de-icing experiment duration by a thermocouple). **(c)** The fractional electrical resistance change ($\Delta R/R_0$) of the heater device operating simply as a temperature resistive sensor monitoring in-situ the device internal resistance variation as a function of temperature, demonstrating the function of T_g self-sensing.

6.1.4 Conclusions

The efficient Joule heating electrothermal effect was demonstrated in multifunctional CFRP laminate composites by the seamless integration of 2D printed SWCNT heater devices fabricated onto conventional GF fibrous UD reinforcements. Water-processable SWCNT-based inks have been utilized for the heater fabrication offering several advantages as for instance *i)* process versatility and scalability towards large-area joule heating devices via multiple interconnected arrays *i.e.*, a roll-to-roll process on fibrous substrates, *ii)* transfer of the printing process and the heater design in other substrates for various applications *i.e.*, wearables, *etc*.. The novel SWCNT-based Joule heaters with the specific architecture fabricated herein showed extremely low device internal electrical resistance, resulting in a satisfactorily responsive and uniform thermal distribution imprint of the heater device in operation. The heater devices have been fully characterized in “air” at different driving voltages (V_{bias}), before being integrated into the multifunctional laminae composites.

Heater devices (GF-SWCNT) were integrated as top and bottom laminae in a $[0/90]_s$ CFRP laminate composite providing homogeneous temperature profiles and high temperatures over the total laminate area for the effective joule-heating enabled curing and post-curing processes. Relatively low voltages were required for the curing and post-curing processes, namely 2 and 2.3 V respectively applied on each heater ply, resulting in a total power consumption of ~10.5 kWh for the whole polymerization. Similar thermo-mechanical results as well as flexural properties were acquired by the OOC-CFRP laminates compared to the conventionally manufactured oven cures ones, indicating a successful out-of-oven curing. The de-icing efficiency of the multifunctional OOC-CFRP was also demonstrated in fully cured laminates by activating both of the two heater system ply laminae at a V_{bias} of 2.1 V, being able to reach a temperature of 100 °C onto the laminate surface that resulted further in the melting of an ice cube with specific volume (16 mL) within ~8 min. Finally, the heater device was used also for another specific functionality. The seamlessly integrated 2D printed SWCNT heater device was employed as a temperature resistive sensor. The real-time device’s fractional electrical resistance change ($\Delta R/R_0$) was monitored from room temperature (25 °C) up to 170 °C and was found to give a specific fingerprint corroborating the epoxy matrix glass transition temperature (T_g) determined by DMA, being an important self-sensing indicator for the laminate composite.

The multifunctional electrothermal CFRP manufactured and reported herein could be exploited for the cost-effective *i)* remote manufacturing or repairing, *ii)* retrofitting and/or reinforcement, *iii)* renovation purposes, *iv)* ice-protection of composite structures and *v)* for non-destructive testing (NDT) applications *i.e.*, inherent activation of integrated heater system ply devices to enable thermography and defect / crack identification, *etc*.. Moreover, it could be envisaged that the multifunctional-electrothermal FRPs could be further utilized for removing humidity, a known problem of FRP composite structures in their operational environment, since specifically epoxy is known to be polar polymer system absorbing remarkable amounts of moisture by time. Finally, the multifunctional-electrothermal FRPs could be utilized in the future to activate some encapsulated healing agents or for novel morphing / reshaping applications especially for thermoplastic matrix FRP composites.

6.1.5 References

1. Li, J.; Wang, Y.; Yue, T.-N.; Gao, Y.-N.; Shi, Y.-D.; Shen, J.-B.; Wu, H.; Wang, M. Robust electromagnetic interference shielding, joule heating, thermal conductivity, and anti-dripping performances of polyoxymethylene with uniform distribution and high content of carbon-based nanofillers. *Compos. Sci. Technol.* **2021**, *206*, 108681, doi:10.1016/j.compscitech.2021.108681.

2. Moaseri, E.; Karimi, M.; Baniadam, M.; Maghrebi, M. Enhancement in mechanical properties of multi-walled carbon nanotube–carbon fiber hybrid epoxy composite: effect of electrostatic repulsion. *Appl. Phys. A Mater. Sci. Process.* **2016**, *122*, 1–8, doi:10.1007/s00339-016-9600-2.

3. Karim, N.; Zhang, M.; Afroj, S.; Koncherry, V.; Potluri, P.; Novoselov, K.S. Graphene-based surface heater for de-icing applications. *RSC Adv.* **2018**, *8*, 16815–16823, doi:10.1039/c8ra02567c.

4. Ma, P.C.; Siddiqui, N.A.; Marom, G.; Kim, J.K. Dispersion and functionalization of carbon nanotubes for polymer-based nanocomposites: A review. *Compos. Part A Appl. Sci. Manuf.* **2010**, *41*, 1345–1367, doi:10.1016/j.compositesa.2010.07.003.

5. Gkikas, G.; Barkoula, N.M.; Paipetis, A.S. Effect of dispersion conditions on the thermo-mechanical and toughness properties of multi walled carbon nanotubes-reinforced epoxy. *Compos. Part B Eng.* **2012**, *43*, 2697–2705, doi:10.1016/j.compositesb.2012.01.070.

6. Baltzis, D.; Bekas, D.G.; Tzachristas, G.; Parlamas, A.; Karabela, M.; Zafeiropoulos, N.E.; Paipetis, A.S. Multi-scaled carbon reinforcements in ternary epoxy composite materials : Dispersion and electrical impedance study. *Compos. Sci. Technol.* **2017**, *153*, 7–17, doi:10.1016/j.compscitech.2017.09.035.

7. Boura, O.; Diamanti, E.K.; Grammatikos, S.A.; Gournis, D.; Paipetis, A.S. Carbon nanotube growth on high modulus carbon fibres: Morphological and interfacial characterization. *Surf. Interface Anal.* **2013**, *45*, 1372–1381, doi:10.1002/sia.5292.

8. Kwon, Y.J.; Kim, Y.; Jeon, H.; Cho, S.; Lee, W.; Lee, J.U. Graphene/carbon nanotube hybrid as a multi-functional interfacial reinforcement for carbon fiber-reinforced composites. *Compos. Part B Eng.* **2017**, *122*, 23–30, doi:10.1016/j.compositesb.2017.04.005.

9. Karalis, G.; Tsirka, K.; Tzounis, L.; Mytafides, C.; Koutsotolis, L.; Paipetis, A.S. Epoxy / Glass Fiber Nanostructured p- and n-Type Thermoelectric Enabled Model Composite Interphases, *Appl. Sci*. **2020**, *10*, 5352. https://doi.org/10.3390/app10155352.

10. Galiotis, C.; Paipetis, A. Definition and measurement of the shear-lag parameter, β, as an index of the stress transfer efficiency in polymer composites. *J. Mater. Sci.* **1998**, *33*, 1137–1143, doi:10.1023/A:1004357121802.

11. An, Q.; Rider, A.N.; Thostenson, E.T. Electrophoretic deposition of carbon nanotubes onto carbon-fiber fabric for production of carbon/epoxy composites with improved mechanical properties. *Carbon N. Y.* **2012**, *50*, 4130–4143, doi:10.1016/j.carbon.2012.04.061.

12. Vavouliotis, A.; Karapappas, P.; Loutas, T.; Voyatzi, T.; Paipetis, A.; Kostopoulos, V. Multistage fatigue life monitoring on carbon fibre reinforced polymers enhanced with multiwall carbon nanotubes. *Plast. Rubber Compos.* **2009**, *38*, 124–130, doi:10.1179/174328909X387928.

13. Mei, H.; Zhang, S.; Chen, H.; Zhou, H.; Zhai, X.; Cheng, L. Interfacial modification and enhancement of toughening mechanisms in epoxy composites with CNTs grafted on carbon fibers. *Compos. Sci. Technol.* **2016**, *134*, 89–95, doi:10.1016/j.compscitech.2016.08.010.

14. Tsirka, K.; Tzounis, L.; Avgeropoulos, A.; Liebscher, M.; Mechtcherine, V.; Paipetis, A.S. Optimal synergy between micro and nano scale: Hierarchical all carbon composite fibers for enhanced stiffness, interfacial shear strength and Raman strain sensing. *Compos. Sci. Technol.* **2018**, *165*, 240–249, doi:10.1016/j.compscitech.2018.07.003.

15. Karakassides, A.; Ganguly, A.; Tsirka, K.; Paipetis, A.S.; Papakonstantinou, P. Radially Grown Graphene Nanoflakes on Carbon Fibers as Reinforcing Interface for Polymer Composites. *ACS Appl.*

Nano Mater. **2020**, doi:10.1021/acsanm.9b02536.

16. Zhao, M.; Meng, L.; Ma, L.; Ma, L.; Yang, X.; Huang, Y.; Ryu, J.E.; Shankar, A.; Li, T.; Yan, C.; et al. Layer-by-layer grafting CNTs onto carbon fibers surface for enhancing the interfacial properties of epoxy resin composites. *Compos. Sci. Technol.* **2018**, *154*, 28–36, doi:10.1016/j.compscitech.2017.11.002.

17. Pozegic, T.R.; Anguita, J. V; Hamerton, I.; Jayawardena, K.D.G.I.; Chen, J.; Stolojan, V. Multi-Functional Carbon Fibre Composites using Carbon Nanotubes as an Alternative to Polymer Sizing. *Nat. Publ. Gr.* **2016**, 1–11, doi:10.1038/srep37334.

18. Karakassides, A.; Karakassides, A.; Konstantinidou, M.; Paipetis, A.S.; Papakonstantinou, P. Enhanced out of plane electrical conductivity in polymer composites induced by CO2 laser irradiation of carbon fibers. *Appl. Sci.* **2020**, *10*, doi:10.3390/app10103561.

19. González, C.; Vilatela, J.J.; Molina-Aldareguía, J.M.; Lopes, C.S.; LLorca, J. Structural composites for multifunctional applications: Current challenges and future trends. *Prog. Mater. Sci.* **2017**, *89*, 194–251, doi:10.1016/j.pmatsci.2017.04.005.

20. Grammatikos, S.A.; Kordatos, E.Z.; Matikas, T.E.; David, C.; Paipetis, A.S. Current injection phase thermography for low-velocity impact damage identification in composite laminates. *Mater. Des.* **2014**, *55*, 429–441, doi:10.1016/j.matdes.2013.09.019.

21. Bekas, D.G.; Paipetis, A.S. Damage monitoring in nanoenhanced composites using impedance spectroscopy. *Compos. Sci. Technol.* **2016**, *134*, 96–105, doi:10.1016/j.compscitech.2016.08.013.

22. Tzounis, L.; Zappalorto, M.; Panozzo, F.; Tsirka, K.; Maragoni, L.; Paipetis, A.S.; Quaresimin, M. Highly conductive ultra-sensitive SWCNT-coated glass fiber reinforcements for laminate composites structural health monitoring. *Compos. Part B Eng.* **2019**, *169*, 37–44, doi:10.1016/j.compositesb.2019.03.070.

23. Pavlopoulou, S.; Grammatikos, S.A.; Kordatos, E.Z.; Worden, K.; Paipetis, A.S.; Matikas, T.E.; Soutis, C. Continuous debonding monitoring of a patch repaired helicopter stabilizer: Damage assessment and analysis. *Compos. Struct.* **2015**, *127*, 231–244, doi:10.1016/j.compstruct.2015.03.014.

24. Johannisson, W.; Ihrner, N.; Zenkert, D.; Johansson, M.; Carlstedt, D.; Asp, L.E.; Sieland, F. Multifunctional performance of a carbon fiber UD lamina electrode for structural batteries. *Compos. Sci. Technol.* **2018**, *168*, 81–87, doi:10.1016/j.compscitech.2018.08.044.

25. Fredi, G.; Dorigato, A.; Fambri, L.; Pegoretti, A. Multifunctional structural composites for thermal energy storage. *Multifunct. Mater.* **2020**, *3*, 1–34, doi:10.1088/2399-7532/abc60c.

26. Karalis, G.; Tzounis, L.; Lambrou, E.; Gergidis, L.N.; Paipetis, A.S. A carbon fiber thermoelectric generator integrated as a lamina within an 8-ply laminate epoxy composite: Efficient thermal energy harvesting by advanced structural materials. *Appl. Energy* **2019**, *253*, 113512, doi:10.1016/j.apenergy.2019.113512.

27. Karalis, G.; Mytafides, C.K.; Tzounis, L.; Paipetis, A.S. ; Barkoula, N. An Approach toward the realization of a through-thickness glass fiber/epoxy thermoelectric generator. *Materials*. **2021**, *14*(9), 2173. https://doi.org/10.3390/ma14092173.

28. Bekas, D.G.; Baltzis, D.; Paipetis, A.S. Nano-reinforced polymeric healing agents for vascular self-repairing composites. *Mater. Des.* **2017**, *116*, 538–544, doi:10.1016/j.matdes.2016.12.049.

29. Tsilimigkra, X.; Bekas, D.; Kosarli, M.; Tsantzalis, S.; Paipetis, A.; Kostopoulos, V. Mechanical properties assessment of low-content capsule-based self-healing structural composites. *Appl. Sci.* **2020**, *10*, doi:10.3390/APP10175739.

30. Kosarli, M.; Foteinidis, G.; Tsirka, K.; Bekas, D.G.; Paipetis, A.S. Concurrent recovery of mechanical and electrical properties in nanomodified capsulebased self-healing epoxies Concurrent recovery of mechanical and electrical properties in nanomodified capsule-based self-healing epoxies. *Polymer.* **2021**, *227*, 123843, doi:10.1016/j.polymer.2021.123843.

31. Kim, M.; Sung, D.H.; Kong, K.; Kim, N.; Kim, B.J.; Park, H.W.; Park, Y. Bin; Jung, M.; Lee, S.H.;

Kim, S.G. Characterization of resistive heating and thermoelectric behavior of discontinuous carbon fiber-epoxy composites. *Compos. Part B Eng.* **2016**, *90*, 37–44, doi:10.1016/j.compositesb.2015.11.037.

32. Liebscher, M.; Tzounis, L.; Junger, D.; Dinh, T.T.; Mechtcherine, V. Electrical Joule heating of cementitious nanocomposites filled with multi-walled carbon nanotubes: Role of filler concentration, water content, and cement age. *Smart Mater. Struct.* **2020**, *29*, doi:10.1088/1361-665X/abc23b.

33. Chung, D.D.L. Self-heating structural materials. *Smart Mater. Struct.* **2004**, *13*, 562–565, doi:10.1088/0964-1726/13/3/015.

34. Liu, S.; Li, Y.; Shen, Y.; Lu, Y. Mechanical performance of carbon fiber/epoxy composites cured by self-resistance electric heating method. *Int. J. Adv. Manuf. Technol.* **2019**, *103*, 3479–3493, doi:10.1007/s00170-019-03707-0.

35. Zhou, B.; Han, X.; Li, L.; Feng, Y.; Fang, T.; Zheng, G.; Wang, B.; Dai, K.; Liu, C.; Shen, C. Ultrathin, flexible transparent Joule heater with fast response time based on single-walled carbon nanotubes/poly(vinyl alcohol) film. *Compos. Sci. Technol.* **2019**, *183*, 107796, doi:10.1016/j.compscitech.2019.107796.

36. Parent, O.; Ilinca, A. Anti-icing and de-icing techniques for wind turbines: Critical review. *Cold Reg. Sci. Technol.* **2011**, *65*, 88–96, doi:10.1016/j.coldregions.2010.01.005.

37. Ibrahim, Y.; Kempers, R.; Amirfazli, A. 3D printed electro-thermal anti- or de-icing system for composite panels. *Cold Reg. Sci. Technol.* **2019**, *166*, 102844, doi:10.1016/j.coldregions.2019.102844.

38. Slobodian, P.; Riha, P.; Olejnik, R.; Matyas, J. Accelerated shape forming and recovering, induction, and release of adhesiveness of conductive carbon nanotube/epoxy composites by joule heating. *Polymers.* **2020**, *12*, doi:10.3390/POLYM12051030.

39. Athanasopoulos, N.; Kostopoulos, V. Resistive heating of multidirectional and unidirectional dry carbon fibre preforms. *Compos. Sci. Technol.* **2012**, *72*, 1273–1282, doi:10.1016/j.compscitech.2012.04.018.

40. Tarfaoui, M.; El Moumen, A.; Boehle, M.; Shah, O.; Lafdi, K. Self-heating and deicing epoxy/glass fiber based carbon nanotubes buckypaper composite. *J. Mater. Sci.* **2019**, *54*, 1351–1362, doi:10.1007/s10853-018-2917-9.

41. Lee, J.; Ni, X.; Daso, F.; Xiao, X.; King, D.; Blanco, T.; Kessler, S.S.; Wardle, B.L.; Jose, S. Advanced carbon fiber composite out-of-autoclave laminate manufacture via nanostructured out-of-oven conductive curing Out-of-Oven. *Compos. Sci. Technol.* **2018**, *166*, doi:10.1016/j.compscitech.2018.02.031.

42. Yao, X.; Falzon, B.G.; Hawkins, S.C.; Tsantzalis, S. Aligned carbon nanotube webs embedded in a composite laminate: A route towards a highly tunable electro-thermal system. *Carbon N. Y.* **2018**, *129*, 486–494, doi:10.1016/j.carbon.2017.12.045.

43. Hayes, S.A.; Lafferty, A.D.; Altinkurt, G.; Wilson, P.R.; Collinson, M.; Duchene, P. Direct electrical cure of carbon fiber composites. *Adv. Manuf. Polym. Compos. Sci.* **2015**, *1*, 112–119, doi:10.1179/2055035915Y.0000000001.

44. Xia, T.; Zeng, D.; Li, Z.; Young, R.J.; Vallés, C.; Kinloch, I.A. Electrically conductive GNP/epoxy composites for out-of-autoclave thermoset curing through Joule heating. *Compos. Sci. Technol.* **2018**, *164*, 304–312, doi:10.1016/j.compscitech.2018.05.053.

45. Shang, Y.; Shi, B.; Doshi, S.M.; Chu, T.; Qiu, G.; Du, A.; Zhao, Y.; Xu, F.; Thostenson, E.T.; Fu, K.K. Rapid Nanowelding of Carbon Coatings onto Glass Fibers by Electrothermal Shock. *ACS Appl. Mater. Interfaces* **2020**, *12*, 37722–37731, doi:10.1021/acsami.0c09549.

46. Yao, X.; Hawkins, S.C.; Falzon, B.G. An advanced anti-icing / de-icing system utilizing highly aligned carbon nanotube webs. *Carbon N. Y.* **2018**, *136*, 130–138, doi:10.1016/j.carbon.2018.04.039.

47. Redondo, O.; Prolongo, S.G.; Campo, M.; Sbarufatti, C.; Giglio, M. Anti-icing and de-icing coatings

based Joule ' s heating of graphene nanoplatelets. *Compos. Sci. Technol.* **2018**, *164*, 65–73, doi:10.1016/j.compscitech.2018.05.031.

48. Stamm, M.; Kirsten, M.; Simon, F.; Ma, E. The interphase microstructure and electrical properties of glass fibers covalently and non-covalently bonded with multiwall carbon nanotubes. *Carbon N. Y.* **2014**, *3*, doi:10.1016/j.carbon.2014.02.069.

49. Charisiou, N.D.; Tzounis, L.; Sebastian, V.; Hinder, S.J.; Baker, M.A.; Polychronopoulou, K.; Goula, M.A. Investigating the correlation between deactivation and the carbon deposited on the surface of Ni/Al 2 O 3 and Ni/La 2 O 3 -Al 2 O 3 catalysts during the biogas reforming reaction. *Appl. Surf. Sci.* **2019**, *474*, 42–56, doi:10.1016/j.apsusc.2018.05.177.

50. Tzounis, L.; Debnath, S.; Rooj, S.; Fischer, D.; Mäder, E.; Das, A.; Stamm, M.; Heinrich, G. High performance natural rubber composites with a hierarchical reinforcement structure of carbon nanotube modified natural fibers. *Mater. Des.* **2014**, *58*, 1–11, doi:10.1016/j.matdes.2014.01.071.

51. Yonezawa, S.; Chiba, T.; Seki, Y.; Takashiri, M. Origin of n type properties in single wall carbon nanotube films with anionic surfactants investigated by experimental and theoretical analyses. *Sci. Rep.* **2021**, *11*, 1–9, doi:10.1038/s41598-021-85248-9.

52. Tzounis, L.; Hegde, M.; Liebscher, M.; Dingemans, T.; Pötschke, P.; Paipetis, A.S.; Zafeiropoulos, N.E.; Stamm, M. All-aromatic SWCNT-Polyetherimide nanocomposites for thermal energy harvesting applications. *Compos. Sci. Technol.* **2018**, *156*, 158–165, doi:10.1016/J.COMPSCITECH.2017.12.030.

53. Tzounis, L.; Liebscher, M.; Fuge, R.; Leonhardt, A.; Mechtcherine, V. P- and n-type thermoelectric cement composites with CVD grown p- and n-doped carbon nanotubes: Demonstration of a structural thermoelectric generator. *Energy Build.* **2019**, *191*, 151–163, doi:10.1016/j.enbuild.2019.03.027.

54. Dresselhaus, M.S.; Dresselhaus, G.; Saito, R.; Jorio, A. Raman spectroscopy of carbon nanotubes. *Phys. Rep.* **2005**, *409*, 47–99, doi:10.1016/j.physrep.2004.10.006.

55. Tsirka, K.; Karalis, G.; Paipetis, A.S. Raman Strain Sensing and Interfacial Stress Transfer of Hierarchical CNT-Coated Carbon Fibers. *J. Mater. Eng. Perform.* **2018**, *27*, 5095–5101, doi:10.1007/s11665-018-3532-2.

56. Zhang, D.; Ryu, K.; Liu, X.; Polikarpov, E.; Ly, J.; Tompson, M.E.; Zhou, C. Transparent, conductive, and flexible carbon nanotube films and their application in organic light-emitting diodes. *Nano Lett.* **2006**, *6*, 1880–1886, doi:10.1021/nl0608543.

57. Zhao, W.; Li, M.; Zhang, Z.; Peng, H. Carbon nanotubes based composites film heater for de-icing application. *14th Eur. Conf. Compos. Mater.* **2010**, *14*, 1–8.

58. Lee, J.; Stein, I.Y.; Kessler, S.S.; Wardle, B.L. Aligned Carbon Nanotube Film Enables Thermally Induced State Transformations in Layered Polymeric Materials. **2015**, doi:10.1021/acsami.5b01544.

59. Xu, X.; Zhang, Y.; Jiang, J.; Wang, H.; Zhao, X.; Li, Q.; Lu, W. In-situ curing of glass fiber reinforced polymer composites via resistive heating of carbon nanotube films. *Compos. Sci. Technol.* **2017**, doi:10.1016/j.compscitech.2017.06.001.

60. Song, Y.S.; Youn, J.R.; Gutowski, T.G. Life cycle energy analysis of fiber-reinforced composites. *Compos. Part A Appl. Sci. Manuf.* **2009**, *40*, 1257–1265, doi:10.1016/j.compositesa.2009.05.020.

61. Friedrich, K.; Almajid, A.A. Manufacturing aspects of advanced polymer composites for automotive applications. *Appl. Compos. Mater.* **2013**, *20*, 107–128, doi:10.1007/s10443-012-9258-7.

62. Shobin, L.R.; Manivannan, S. Enhancement of electrothermal performance in single-walled carbon nanotube transparent heaters by room temperature post treatment. *Sol. Energy Mater. Sol. Cells* **2018**, *174*, 469–477, doi:10.1016/j.solmat.2017.09.041.

63. Wang, B.; Yang, B.; Wang, M.; Zheng, Y.; Hong, X.; Zhang, F. Effect of Cutting Temperature on Bending Properties of Carbon Fibre Reinforced Plastics. *IEEE J. Sel. Top. Quantum Electron.* **2019**, *26*, 394–401, doi:10.1515/secm-2019-0019.

64. Loos, M.R.; Coelho, L.A.F.; Pezzin, S.H.; Amico, S.C. Effect of carbon nanotubes addition on the

mechanical and thermal properties of epoxy matrices. *Mater. Res.* **2008**, *11*, 347–352, doi:10.1590/S1516-14392008000300019.

65. Nakai, Y.; Honda, K.; Yanagi, K.; Kataura, H.; Kato, T.; Yamamoto, T.; Maniwa, Y. Giant Seebeck coefficient in semiconducting single-wall carbon nanotube film. *Appl. Phys. Express* **2014**, *7*, doi:10.7567/APEX.7.025103.

66. Gao, B.L.; Thostenson, E.T.; Zhang, Z.; Chou, T. Sensing of Damage Mechanisms in Fiber-Reinforced Composites under Cyclic Loading using Carbon Nanotubes. **2009**, *100191*, 123–130, doi:10.1002/adfm.200800865.

6.2 Supporting Information

Figure S7 depicts the vacuum bagging configuration for the manufacturing of the OOC-CFRP laminate assisted by the thermal activation of the 2 (top and bottom) GF system plies-Joule heating devices. The set-up is very simple consisting of 2 DC power supply electronic devices with the respective Cu-based wirings for the GF heaters electrodes, a data-logging multimeter for temperature measurements with a K-type thermocouple, an Infrared camera for temperature monitoring and all the required components and the auxiliary material (release film, single breather, sealant tape and high-temperature vacuum bag) for the manufacturing procedure.

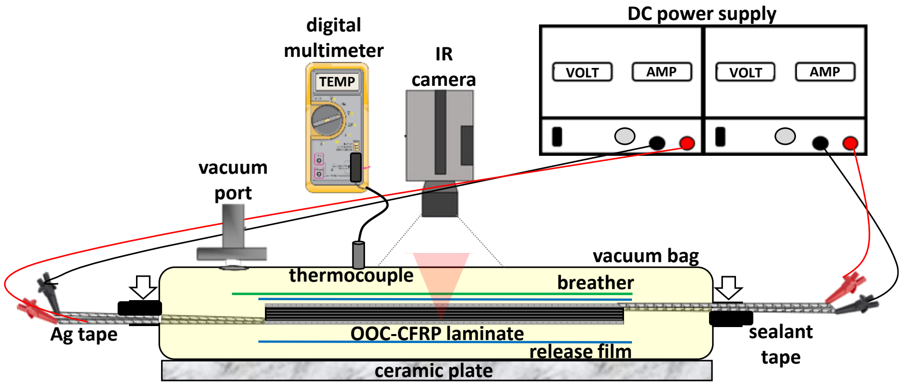

Figure S7. Schematic of the vacuum bagging process for the manufacturing of the OOC-CFRP laminate.

Figure S8 illustrates the "bucky paper" film of 40-50 μm thickness derived from vacuum-assisted filtration with a PVDF filter membrane (47 mm diameter and 0.45 μm pore size) which was left drying overnight. This film was employed for electrical measurements via typical 4-probe technique. *I–V* curves for the SWCNT buckypaper material showed an expected linear relationship between the applied voltages and current passes through the conductive network.

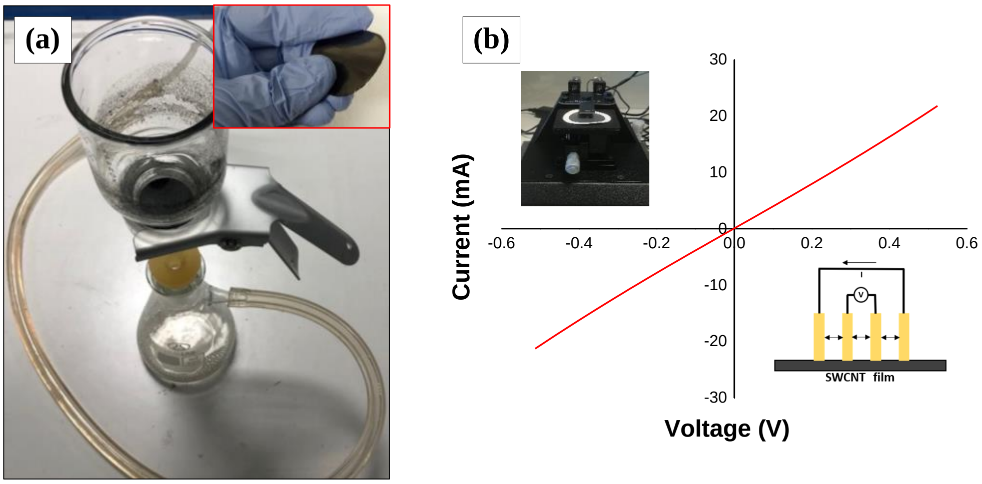

Figure S8. (a) The process of vacuum filtration for production of a SWCNT buckypaper film and **(b)** *I-V* curve of the corresponding film.

Chapter 7

Conclusions and Outlook

7. Conclusions and Outlook

The main results and the respective prospects arose from this research are presented comprehensively below.

Conclusions: Initially, the synthesis and formulation process of hybrid inorganic-organic nanomaterials with tuned transport properties that affect their overall TE behavior has been pointed out. Te NWs were synthesized in aqueous solution medium and characterized with advanced techniques in detail. More precisely, the corresponding spectroscopic, morphological, electric, carrier transport and TE characteristics were assessed for the produced pristine and hybrid nanomaterials. During the solution post-processing stage, the synthesized Te NPs were employed for the hybridization with different ratios of PEDOT:PSS solution, resulting in an efficient TE film with a *PF* of 102.42 μW/m · K^2. Also, Drude model validated theoretically the enhanced carrier filtering properties. Consequently, the aforementioned hybrid TE ink was utilized for the design and fabrication via shadow-mask assisted wet-chemical deposition printing technique of an efficient flexible TE module, as the building block of a TEG device. Moreover, the novelty of this work is based on the comparison of flexible TEGs with different materials as the metallic junctions of the device, as both conventional Ag metallic interconnections and SWCNT-based interconnections were extensively tested. In more detail, the electrical power output of the flexible TEGs was ~4.5 μW when exposed at an in-plane ΔT of 100 K and were evaluated with bending cycle experiments. Furthermore, thermal stability over time measurements were conducted for the TEG device with SWCNT-contact as the metallic junctions. The experimental findings indicate optimized flexibility especially when the Ag-junctions have been replaced with SWCNT printed metallic contacts, as well as remarkable device thermal stability over time upon operation at ΔT of 100 K in ambient atmosphere (**Chapter 2**).

Afterwards, hierarchical single GFs with Te NWs-based coatings illustrated 19.4 % enhanced tensile strength, resulting in epoxy resin matrix model composites with functional nanostructured interphases with 8.9 % enhanced IFSS based on SFFT. The respective p-type TE-enabled model composites exhibited a Seebeck coefficient value of +76.5 μV/K. Additionally, the fabrication of p-type and molecular doped n-type SWCNT-based TE-enabled model composites consisting of coated GF tows embedded in epoxy resin matrix was presented. The corresponding morphological, thermogravimetric, spectroscopic and TE measurements were assessed in order to characterize the produced functional interphases. Furthermore, the stress transfer at the interface of the coated GFs was studied by tow pull-out tests. In more detail, GF tows coated with either p-type or n-type SWCNT model composites were utilized as the thermoelements and exhibited a Seebeck coefficient of +16.2 μV/K and -28.4 μV/K, respectively. The aforementioned model composites were serially interconnected via Cu foil to realize a p-n junction creating a single pair TEG demonstrator, produced a voltage output of 4.46 mV upon being exposed to a ΔT of 100 K (**Chapter 3**).

Subsequently, the manufacturing and evaluation of in-plane TEG-enabled GFRP laminates consisting of coated GF fabrics with p- and n-type SWCNT-based films was reported for the first time. A fast and facile blade coating technique was employed for the fabrication of the coated GF fabrics, which exhibited a Seebeck coefficient of +23 μV/K and -29 μV/K with 60 $\mu W/m \cdot K^2$ and 118 $\mu W/m \cdot K^2$ *PF* values, respectively. The respective morphological, spectroscopic, electric and TE measurements were assessed for the detailed characterization at material level. The resulting TE-enabled GF fabrics (4 p-type coated GFs, 4 n-type coated GFs) and 8 GFs as insulators were impregnated with epoxy resin by hand lay-up. Simultaneously, the functional laminae were properly electrically in series interconnected within a configuration of a p-n TEG. The lamination process for the thermal curing and post-curing of the thermoset matrix was occurred via thermopressing. The produced 16-ply $[0/90]_{4s}$ balance symmetric TEG-enabled GFRP laminate was evaluated both from the functional and mechanical perspective. The maximum electrical power of 2.2 μW was generated upon a 16-ply multifunctional GFRP being exposed to ΔT of 100 K, as a demonstration of an inherently operating TEG structural device. Moreover, the structural integrity of the multifunctional GFRP laminate was tested by 3-point bending coupled with on-line SHM by exploiting the produced steady state TE I_{sc} at 80 K in-plane ΔT record. The respective reference GFRP laminate composite compared to the TEG-enabled GFRP laminate were tested in terms of mechanical performance via quasi-static 3-point bending and DMA according to their standards. As an illustration of practical thermal energy harvesting application an 8-ply GFRP multi-TEG laminate was manufactured, able to succeed 11.4 μW power at a ΔT of 75 K. The generated TE power was enough for powering-up a commercial step-up boost converter (ALD-EH4295) and activate a green LED at about 28 min (**Chapter 4**).

Thereafter, a 10-ply GFRP composite laminate, operating as a structural through-thickness TEG was demonstrated. A flexible p-type inorganic-organic hybrid TE material was synthesized presenting a *PF* value of 58.88 $\mu W/m \cdot K^2$. The corresponding electrical and spectroscopic measurements were assessed in order to identify the produced Te NWs with the added SWCNT dispersion during growth. An aqueous TE ink for coating purposes was prepared by redispersing properly the synthesized nanomaterial. Then, a GF ply was coated with the TE ink via a simple dip-coating and oven-drying process. SEM was employed for the inspection of the microstructural special characteristics of the coated GF with Te NWs-SWCNT. Eventually, the TE-coated GF ply was purposely laminated to manufacture a TEG-GFRP composite laminate capable of generating 54.22 nW TE power output from a single thermoelement at a through-thickness ΔT of 100 K. Furthermore, the mechanical properties of the proposed through-thickness TEG GFRP laminates were tested within a 3-point bending configuration in correspondence to the reference plain cross-ply GFRP laminates. A minor reduction ~11.5 % of bending strength and flexural modulus was displayed. In a similar context, a 10-ply CFRP composite laminate, operating as a structural through-thickness TEG was elucidated. A durable p-type TE paste-based film was developed presenting a Seebeck coefficient of +189 μV/K, which corresponds a *PF* value of 57.2 $\mu W/m \cdot K^2$. SEM was employed for the inspection of the microstructural special characteristics of the coated GF-TE paste functional plies. The electrical and spectroscopic measurements were assessed in order to identify both the synthesized TE nanomaterial, as well as the TE paste properties. The TE paste was utilized for double-sided blade coating onto GF reinforcing fabrics, as the substrate. Eventually, the single-functional plies were purposely integrated to manufacture UD and cross-ply 10-ply through-thickness TE-enabled CFRP composite laminates. The highly conductive CF reinforcing phase was exploited as the internal junctions of the device. Regarding to their TE response, the UD lamination was found to be more efficient presenting a TE voltage of 8.4 mV allowing a TE current of 597.4 μA at an applied through-thickness ΔT of 100 K. As a result, a maximum electrical power output of 1.3 μW was generated, coupled with a fast response temperature sensing capability. Moreover, the mechanical properties of the proposed through-thickness TE-enabled CFRP laminates were tested within a 3-point bending configuration in correspondence to the reference plain UD CFRP laminates. A minor reduction of bending strength and flexural modulus (ca. 10%) was displayed indicating only a marginal knock-down effect (**Chapter 5**).

Finally, the novel design and fabrication of printed SWCNT-based electrothermal Joule resistive heating devices directly onto the GF reinforcing fabrics are being reported. SWCNT powder was surfactant-assisted dispersed in aqueous solution medium and characterized to evaluate the pristine and the resulting printed material. The SWCNT dispersion was further utilized for the printing process of the novel-patterned Joule heater devices onto GF substrates via a facile blade coating technique. The fabricated GF system plies-Joule heating devices were integrated within a 6-ply $[0/90]_s$ CFRP composite laminates for the implementation of specific secondary functions. More precisely, OOC of a CFRP laminate was succeeded based on a configuration of a top and bottom

GF system plies-Joule heating devices proper incorporation to accomplish the curing and the post-curing process of the thermoset matrix. According to their electrothermal response, a total amount of 4 V and 4.6 V applied voltage which corresponds to 2.13 W and 2.82 W power consumption is sufficient for the creation of a uniform and stable temperature state of 90 ^{o}C curing for 1.5 h and 130 ^{o}C post-curing for 3 h, respectively. Comparatively to the manufactured OOC-CFRP laminate via vacuum bagging, the conventional way of CFRP laminate polymerization process by oven was assessed in respect to the total amount of power consumption. In more detail, contrasted with the relative values of the existing literature, the herein reported values elucidate an ultra-low power consuming approach for manufacturing of FRP structures. Besides, the thermomechanical behavior of the OOC-CFRP laminates and the corresponding conventionally oven cured CFRP laminates evinced almost identically through quasi-static 3-point bending and DMA tests. The multifunctional OOC composite laminates exhibited a responsive de-icing capability with an applied voltage of 4.2 V, which is equivalent to 2.35 W power consumption operating for 8 min. Lastly, the capability of the OOC-CFRP laminate for T_g self-sensing was illustrated (**Chapter 6**).

Outlook: Overall, this study could provoke the spark for a new era for the integration of functional nanomaterials as bulk and flexible “electronic devices” for thermal energy harvesting and management by advanced structures in optimized areas with specific geometries and complex shapes. In general, future research directions that enforce advancements in nanostructured materials and emerging additive manufacturing methods should be prioritized. Moreover, advanced process monitoring, control and in-situ characterization techniques are needed to automatically optimize the printing procedures to achieve the desired final properties.

More precisely, the properties of nano-scaled materials vary significantly, as expected from their diversity in chemical-electronic structures, from zero to small band gaps to large band gaps. Therefore, numerous opportunities exist for formulating high-performance inks and printing functional devices. The rapid development of nanoparticle synthesis has accelerated progress in preparing advanced nanomaterials with controlled nanostructures. By using bottom-up or top-down approaches, functional nanomaterials have been synthesized with a high yield and fast production speed. However, the commercial production (*i.e.* 10–100 kg quantity level) of high-performance nanomaterials remains a major challenge, since industrial large-scale methods combining high-quality with low cost are yet to be developed. For functional inks processing, the individual components (*e.g.* solvents, surfactants, polymers and binders) play critical roles in determining the quality of inks, and thus innovations in ink additives can further improve the performance of printed devices. For instance, surfactants can greatly reduce the interfacial tension and form steric and/or provide electrostatic stabilization for nanomaterials within solution-processed inks. Nevertheless, the residual surfactant in printed devices often limits the overall functionalities of the nanomaterials, which requires post-treatments to remove the surfactant. Accordingly, one practical need for the large-scale applications is the development of compatible ink additives without compromise the overall performance of the printed devices. A possible solution is the development and utilization of semiconducting/ conducting nano-surfactants, realizing a promising approach for preparing organic-free functional inks. Additionally, novel molecular or ionic additives could be employed to enhance the device total performance *e.g.* in thermoelectrics. In order to further improve the charge-energy carrier transport of printed nanomaterials-based devices, techniques that could align the nanostructured networks with minimal defects are highly desirable. The dispersions of nanoparticles have shown a fascinating diversity of liquid crystal phases, *i.e.* forming orientationally or positionally ordered structures. The aforementioned approach, combined with directed assembly tools capable of additive printing processes, has been proposed to tune the device performance in terms of thermal and electrical properties. Moreover, innovative approaches of post-treatments (*e.g.* microwave treatment) have also demonstrated great potential in improving the performance of the resulted solution-processed nanoparticle-based films.

The TE-enabled FRP laminates are envisaged to harvest thermal energy at a large-scale during the operational lifetime of the advanced composites employed in the civil, aerospace and automotive sectors, where ΔT exist arbitrary or by design (*e.g.*, piping systems). The generation of thermoelectricity using structural engineering materials will represent a breakthrough in multifunctional materials rendering them an attractive technology for future zero energy consumption structures. Simultaneously, research in efficient electrothermal resistive heating via Joule effect exploitation permit the realization of low electrical resistance devices with a satisfactorily uniform and extremely responsive thermal distribution. The aforementioned effect can be exploited by the integrated devices within a FRP laminates for the remote manufacturing, repairing or ice-protection and self-sensing of composite structures. Automated large-scale continuous printing techniques optimization and industrialization for production of fibrous reinforcing system functional laminae is expected to realize beyond the state-of-the-art multifunctional high strength to weight ratio structural components.

List of Publications

During these past 3 years, results of the present research have been contributed to the following publications, both at peer-review journals as well as at peer-review international conferences.

Papers:

1. Tsirka K., **Karalis G.**, Paipetis A.S.. Raman Strain Sensing and Interfacial Stress Transfer of Hierarchical CNT Coated Carbon Fibers. *Journal of Materials Engineering and Performance*. pp 1–7, 2018. Available from: *https://doi.org/10.1007/s11665-018-3532-2.*

2. Karalis G., Tzounis L., Lambrou E., Gergidis L.N., Paipetis A.S.. A carbon fiber thermoelectric generator integrated as a lamina within an 8-ply laminate epoxy composite: Efficient thermal energy harvesting by advanced structural materials. *Applied Energy*. 2019;253:113512. Available from: *https://doi.org/10.1016/j.apenergy.2019.113512.*

3. Karalis G., Mytafides C., Polymerou A., Tsirka K., Tzounis L., Gergidis L., Paipetis A.S.. Hierarchical Reinforcing Fibers for Energy Harvesting Applications - A Strength Study. *Key Engineering Materials.* 2020;827 :252–7. Available from: *https://doi.org/10.4028/www.scientific.net/KEM.827.252.*

4. Karalis G., Tsirka K., Tzounis L., Mytafides C., Koutsotolis L., Paipetis A.S.. Epoxy/Glass Fiber Nanostructured p- and n-Type Thermoelectric Enabled Model Composite Interphases. *Applied Sciences.* 2020, *10,* 5352. Available from: *https://doi.org/10.3390/app10155352.*

5. Mytafides C., Tzounis L., **Karalis G.,** Formanek P., Paipetis A.S.. High-Power All-Carbon Fully Printed and Wearable SWCNT-Based Organic Thermoelectric Generator. *Applied Materials & Interfaces.* 2021, 13 (9), 11151–11165. Available from: *https://doi.org/10.1021/acsami.1c00414.*

6. Karalis G., Mytafides C., Tzounis L., Paipetis A.S., Barkoula N-M.. An Approach toward the Realization of a Through-Thickness Glass Fiber/Epoxy Thermoelectric Generator. *Materials.* 2021, 14(9), 2173. Available from: *https://doi.org/10.3390/ma14092173.*

7. Karalis G., Tzounis L., Mytafides C., Tsirka K., Formanek P., Stylianakis M., Kymakis E., Paipetis A.S.. A high performance flexible and robust printed thermoelectric generator based on hybridized Te nanowires with PEDOT:PSS. *Applied Energy*. 294 (2021) 117004. Available from: *https://doi.org/10.1016/j.apenergy.2021.117004.*

8. Karalis G., Tzounis L., Tsirka K., Mytafides C., Voudouris Itskaras A., Liebscher M., Lambrou E., Gergidis L.N., Barkoula N-M., Paipetis A.S.. Advanced Glass Fiber Polymer Composite Laminate Operating as a Thermoelectric Generator: A Structural Device for Micropower

Generation and Potential Large-Scale Thermal Energy Harvesting. *Applied Materials & Interfaces.* 2021, 13 (20), 24138–24153. Available from: *https://doi.org/10.1021/acsami.1c04527.*

9. Mytafides C., Tzounis L., **Karalis G.**, Formanek P., Paipetis A.S.. Fully printed and flexible carbon nanotube-based thermoelectric generator capable for high-temperature applications. J. Power Sources. 507 (2021) 230323. Available from: *https://doi.org/10.1016/j.jpowsour.2021.230323.*

10. Karalis G., Tzounis L., Dimos E., Mytafides C., Liebscher M., Karydis-Messinis A., Zafeiropoulos N.E., Paipetis A.S.. Printed Single-Wall Carbon Nanotube-Based Joule Heating Devices Integrated as Functional Laminae in Advanced Composites. *Applied Materials & Interfaces*. 2021, 13 (33), 39880–39893. Available from: *https://doi.org/10.1021/acsami.1c10001.*

11. Karalis G., Tzounis L., Tsirka K., Mytafides C., Liebscher M., Paipetis A.S., Carbon fiber/epoxy composite laminates as through-thickness thermoelectric generators. *paper under revision.*

<u>Conferences</u>:

1. «ECCM18» Athens-Greece, 24-28 June 2018 with oral presentation «CFRPs with Embedded Carbon Fiber TEG Module as Energy Harvester Device» **Karalis G.**, Tzounis L., Paipetis A.S..

2. «12th Hellenic Polymer Society International Conference» University of Ioannina-Greece, 30 September-3 October 2018 with poster "Carbon fiber thermoelectric module fabrication, integration, experimental and simulated power generation in 8-ply laminate epoxy composites" **Karalis G.**, Tzounis L., Lambrou E., Gergidis L.N., Paipetis A.S..

3. «6th International Conference on Multifunctional, Hybrid & Nanomaterials (HYMA2019)» Sitges-Spain, 11-15 March 2019 with oral presentation "Enhanced thermoelectric properties of reinforcing fibers covered with nanoparticle-based hierarchical coatings" **Karalis G.**, Tsirka K., Tzounis L., Paipetis A.S..

4. «12th Panhellenic Scientific Conference on Chemical Engineering» Athens-Greece, 29-31 May 2019 with oral presentation "Numerical Modeling of Thermoelectric Devices Based on Complex Materials with Carbon Fiber for Efficient Energy Harvesting" Lambrou E., Gergidis L.N., Tzounis L., **Karalis G**., Paipetis A.S..

5. «9th EASN International Conference on Innovation in Aviation & Space» Athens-Greece, 3-6 September 2019 with oral presentation "Advanced thermoelectric concepts for the aviation industry" Tzounis L., Tsirka K., **Karalis G.**, Mytafides C., Polymerou A., Paipetis A.S..

6. «18th International Conference on Fracture and Damage Mechanics (FDM2019)» Rhodes-Greece, 16-18 September 2019 with oral presentation "Hierarchical Reinforcing Fibers for Energy Harvesting Applications - A strength study" **Karalis G.**, Mytafides C., Polymerou A., Tsirka K., Tzounis L., Gergidis L.N., Paipetis A.S..

7. «World Sustainable Energy Days 2021 - Hybrid Event» Wels-Austria, 21-25 June 2021 with oral presentation "Creation of a photo-thermal carbon fiber reinforced polymer" Mytafides C., **Karalis G.**, Barkoula N-M..

8. «6th International Virtual Conference of Engineering Against Failure (ICEAF)» 23-25 June 2021 with oral presentation "The Integration of a CNT-based Organic Thermoelectric Generator within a Carbon Fiber Reinforced Polymer Composite" Mytafides C., Tzounis L., Tsirka K., **Karalis G.**, Koutsotolis L., Lambrou E., Gergidis L.N., Paipetis A.S..

9. «6th International Virtual Conference of Engineering Against Failure (ICEAF)» 23-25 June 2021 with oral presentation "On Lateral and Axial Crushing Response of Filament Winding GFRP and Modified GFRP Tubes" Koutsotolis L., **Karalis G.**, Tiriakidou T., Tzounis L., Tsirka K., Mytafides C., Paipetis A.S..

10. «6th International Virtual Conference of Engineering Against Failure (ICEAF)» 23-25 June 2021 with oral presentation "A Carbon Fiber-Reinforced Polymer Composite with Embedded Photo-Thermal Energy Harvesting Capabilities" Mytafides C., **Karalis G.**, Tzounis L., Paipetis A.S., Barkoula N-M..